



**AALBORG UNIVERSITY**  
DENMARK

**Aalborg Universitet**

## **Floating Foundations for Offshore Wind Turbines**

Andersen, Morten Thøtt

*DOI (link to publication from Publisher):*  
[10.5278/vbn.phd.engsci.00175](https://doi.org/10.5278/vbn.phd.engsci.00175)

*Publication date:*  
2016

*Document Version*  
Publisher's PDF, also known as Version of record

[Link to publication from Aalborg University](#)

*Citation for published version (APA):*  
Andersen, M. T. (2016). *Floating Foundations for Offshore Wind Turbines*. Aalborg Universitetsforlag.  
<https://doi.org/10.5278/vbn.phd.engsci.00175>

### **General rights**

Copyright and moral rights for the publications made accessible in the public portal are retained by the authors and/or other copyright owners and it is a condition of accessing publications that users recognise and abide by the legal requirements associated with these rights.

- Users may download and print one copy of any publication from the public portal for the purpose of private study or research.
- You may not further distribute the material or use it for any profit-making activity or commercial gain
- You may freely distribute the URL identifying the publication in the public portal -

### **Take down policy**

If you believe that this document breaches copyright please contact us at [vbn@aub.aau.dk](mailto:vbn@aub.aau.dk) providing details, and we will remove access to the work immediately and investigate your claim.



# **FLOATING FOUNDATIONS FOR OFFSHORE WIND TURBINES**

**BY  
MORTEN THØTT ANDERSEN**

DISSERTATION SUBMITTED 2016



**AALBORG UNIVERSITY**  
DENMARK



---

---

# Floating Foundations for Offshore Wind Turbines

---

---

Ph.D. Dissertation  
Morten Thøtt Andersen

Dissertation submitted September 2016

---

Dissertation submitted: September, 2016

PhD supervisor: Professor Søren R.K. Nielsen  
Aalborg University

Assistant PhD supervisor: Associate Professor Peter B. Frigaard  
Aalborg University

PhD committee: Associate Professor Michael Rasmussen (chairman)  
Aalborg University

Project Manager Sébastien Gueydon  
Maritime Research Institute Netherlands

Professor Harry Bingham  
Technical University of Denmark

PhD Series: Faculty of Engineering and Science, Aalborg University

ISSN (online): 2246-1248  
ISBN (online): 978-87-7112-816-1

Published by:  
Aalborg University Press  
Skjernvej 4A, 2nd floor  
DK – 9220 Aalborg Ø  
Phone: +45 99407140  
aauf@forlag.aau.dk  
forlag.aau.dk

© Copyright: Morten Thøtt Andersen

Printed in Denmark by Rosendahls, 2016

---



# Contents

<b>Contents</b>	<b>v</b>
<b>Preface</b>	<b>ix</b>
<b>Curriculum Vitae</b>	<b>xi</b>
<b>Thesis Details</b>	<b>xiii</b>
<b>Abstract</b>	<b>xv</b>
<b>Resumé</b>	<b>xvii</b>
<b>Nomenclature</b>	<b>xix</b>
<b>1 Introduction</b>	<b>1</b>
1.1 Wind Energy . . . . .	3
1.2 Deep Water Offshore Wind Energy . . . . .	5
<b>2 State-of-the-Art</b>	<b>9</b>
2.1 Floating Foundation Archetypes . . . . .	10
2.1.1 Spar Buoy . . . . .	11
2.1.2 Semi-Sub . . . . .	12
2.1.3 TLP . . . . .	12
2.2 Market Review . . . . .	13
2.2.1 Technology Timeline . . . . .	14
2.3 The Future of FOWTs . . . . .	17
2.3.1 Bringing down LCOE . . . . .	17
2.3.2 Recommendations . . . . .	18
<b>3 Research Contribution</b>	<b>21</b>
3.1 Platform Hydrodynamics . . . . .	23

3.1.1	Slender Body Hydrodynamics . . . . .	24
3.1.2	Bluff Body Hydrodynamics . . . . .	24
3.1.3	Hybrid Modeling . . . . .	29
3.2	Mooring System Modeling . . . . .	30
3.2.1	Dynamic Mooring . . . . .	30
3.2.2	Multi-segmented Mooring . . . . .	32
3.3	Tower and RNA . . . . .	35
3.3.1	Tower Flexibility . . . . .	35
3.3.2	Emulated Turbine Loading . . . . .	38
3.4	Contextual Topics . . . . .	45
<b>4</b>	<b>Conclusion</b>	<b>47</b>
	<b>References</b>	<b>49</b>
<b>A</b>	<b>Hybrid Model Representation of a TLP Including Flexible Topsides in Non-Linear Regular Waves</b>	<b>55</b>
<b>B</b>	<b>Influence of Model Simplifications on Force in Surge for a Model-Scale Floating Foundation for Offshore Wind Turbines</b>	<b>77</b>
<b>C</b>	<b>Hydrodynamic Excitation Forces on Floating Structures with Finite Displacements</b>	<b>93</b>
<b>D</b>	<b>Incentive-based Financial Support Scheme for Immature Renewable Energy Systems</b>	<b>101</b>
<b>E</b>	<b>Verification and Validation of the New Dynamic Mooring Modules Available in FAST v8</b>	<b>109</b>
<b>F</b>	<b>Verification and Validation of Multisegmented Mooring Capabilities in FAST v8</b>	<b>123</b>
<b>G</b>	<b>Practical Low Cost Aerodynamic Thrust Emulation for Froude Scaled Wind Turbines</b>	<b>133</b>
<b>H</b>	<b>Fan Actuated Loading on Scaled Floating Offshore Wind Turbines</b>	<b>143</b>
<b>I</b>	<b>Auxiliary Publications</b>	<b>151</b>
I.1	Laboratory Testing and Energy Production of Scale 1: 35 Sigma Energy WEC . . . . .	151
I.2	Hydraulic Evaluation of Joltech’s GyroPTO for Wave Energy Applications . . . . .	151

I.3 The Inter Facility Testing of a Standard Oscillating Water Column (OWC) Type Wave Energy Converter (WEC) . . . . . 152



# Preface

This thesis has been produced during my Ph.D. study at Aalborg University from August 2013 to September 2016. I am truly happy to have been given the opportunity to stay at Aalborg University and evolve as a researcher and as a person. I have enjoyed the time and experiences as a Ph.D. student, but there are definitely a few people that have a big share in helping and guiding me through this process.

First of all I would like to thank my supervisors Søren and Peter for guiding me through the process, and for helping keeping me on track while still providing a lot of freedom for me to go explore and pursue ideas on my own. At the same time I would like to thank all my friends and colleagues at the Department of Civil Engineering. This thesis would not have been the same without the constructive feedback from the smart people in the blue section, the always flawless work by the technicians in the black section, or the helpful secretaries from the white section who often had to cope with my shortcomings with respects to administrative systems and procedures.

A big thanks also goes out to all my co-authors and people I have met along the way. Especially the great people of NREL who made my stay in Colorado such an unforgettable experience on both a personal and professional level. I would also like to extend a big thanks to the people of INORE. I thoroughly enjoyed meeting and befriending all the INOREans - many of whom will, without a doubt, impact the future of offshore renewables.

Lastly, I would like to thank my family for the unyielding support and for providing me with a platform to grow from. Most of all I would like to thank the two girls that mean the world to me; my lovely girlfriend Thilde, and our beautiful daughter Ellinor!

Morten Thøtt Andersen  
Aalborg University, September, 2016



# Curriculum Vitae

Morten Thøtt Andersen

**DATE OF BIRTH:**

August 11th 1986

**WORK ADDRESS:**

Department of Civil Engineering

Thomas Manns Vej 23

Room: 1.338

9220 Aalborg Ø, DK



**AFFILIATION:**

2015 to 2016

Board Member, PhD Board of the Doctoral School,  
Aalborg University

2014 to 2015

Board Member, International Network on Offshore  
Renewable Energy (INORE)

**ACADEMIC CAREER:**

2013 to present

Ph.D. Student, Division of Reliability, Dynamics and  
Marine Engineering, Aalborg University

2013

M.Sc. Structural and Civil Engineering, Aal-  
borg University

2011

B.Sc. Civil Engineering, Aalborg University

**EXPERIENCE:**

Work experience revolves around the fields connected to both physical and numerical modeling of marine structures. Relevant topics being: wave generation and analysis; model scaling and construction; micro-electronics; open source programming; marine hydrodynamics; mooring systems; wind turbine simulations; structural dynamics





# Thesis Details

**Thesis Title:** Floating Foundations for Offshore Wind Turbines  
**Ph.D. Student:** Morten Thøtt Andersen  
**Supervisors:** Prof. Søren R. K. Nielsen, Aalborg University  
Assoc. Prof. Peter B. Frigard, Aalborg University

The main body of this thesis consist of the following papers.

- [A] Wehmeyer, C., Ferri, F., Andersen, M. T., and Pedersen, R. R. (2014). "Hybrid Model Representation of a TLP Including Flexible Topsides in Non-Linear Regular Waves". *Energies*, 7(8):5047
- [B] Andersen, M. T., Hindhede, D., and Lauridsen, J. (2015). "Influence of Model Simplifications Excitation Force in Surge for a Floating Foundation for Offshore Wind Turbines". *Energies*, 8(4):3212
- [C] Andersen, M. T. and Nielsen, S. R. K. (2015). "Hydrodynamic Excitation Forces on Floating Structures with Finite Displacements". In *Proceedings of the Twenty-fifth (2015) International Ocean and Polar Engineering Conference*. International Society of Offshore & Polar Engineers
- [D] Andersen, M. T. and Frigaard, P. B. (2015). "Incentive-based Financial Support Scheme for Immature Renewable Energy Systems". In *Proceedings of the 11th European Wave and Tidal Energy Conference*. Technical Committee of the European Wave and Tidal Energy Conference
- [E] Wendt, F., Andersen, M. T., Robertson, A. N., and Jonkman, J. M. (2016). "Verification and Validation of the New Dynamic Mooring Modules Available in FAST v8". In *The Twenty-sixth International Offshore and Polar Engineering Conference, Rhodes, Greece*. ISOPE
- [F] Andersen, M. T., Wendt, F., Robertson, A. N., and Jonkman, J. M. (2016). "Verification and Validation of Multisegmented Mooring Capabilities in

FAST v8". In *The Twenty-sixth International Offshore and Polar Engineering Conference, Rhodes, Greece*. ISOPE

- [G] Andersen, M. T. and Ferri, F. (2016b). "Practical Low Cost Aerodynamic Thrust Emulation for Froude Scaled Wind Turbines". *Springer: Experimental Techniques*
- [H] Andersen, M. T. and Ferri, F. (2016a). Draft paper: "Fan Actuated Loading on Scaled Floating Offshore Wind Turbines". *To be submitted to: Journal of Marine Science and Engineering (ISSN 2077-1312)*

In addition to the main papers, the following publications have also been made. The publications revolve around experimental model scale testing, and have in that regard assisted the main works of the thesis. Note: Not all auxiliary publications are included in full length, and are not intended for evaluation but instead shows the themes and context of other published works.

- [I.1] Andersen, M. T. and Ferri, F. (2014). "Laboratory Testing and Energy Production of Scale 1: 35 Sigma Energy WEC"
- [I.2] Kramer, M. M., Pecher, A. F. S., Guaraldi, I., Andersen, M. T., and Kofoed, J. P. (2015). "Hydraulic Evaluation of Joltech's GyroPTO for Wave Energy Applications"
- [I.3] Andersen, M. T. and Thomsen, J. B. (2016). "The Inter Facility Testing of a Standard Oscillating Water Column (OWC) Type Wave Energy Converter (WEC)"

# Abstract

As the energy consumption continues to grow on a global scale, the supply needs to follow along. At times where political and environmental concerns are putting a strain on the conventional fossil fuel power sources, the focus has been shifting heavily towards the renewable energy sector. Wind energy is the oldest and one of the most technologically established renewable industries and is expected to answer this call of growing energy needs by contributing more and more to the energy mix in the future.

While land-based wind turbines are widespread, the market for offshore wind turbines have seen a rise since the humble beginnings in Vindeby, Denmark in 1991. This is partly due to the stronger and more stable wind resource at sea, and to the size of the current generation turbines that inhibit land-based transportation and cause concerns of visual and audible nuisance. To ensure continued development at current sites and to open up new markets, technologies for installation in deeper waters are becoming necessary. Bottom-fixed foundation types inherently have some limited feasibility as water depth increases, and hence an interest on floating foundations has emerged.

The idea of floating offshore wind turbines is a novel technology, that has come a tremendously long way since the first prototype installation less than a decade ago. A lot of the technologies have been adopted from the oil and gas industry, but still the system design differs drastically. Though lower targeted reliability levels hint at relatively cheaper structures, the coupled system dynamics of turbine/platform and lower profit margins in renewable energy necessitate an highly optimized design to be feasible.

In the work presented, efforts have been made to better understand the system properties of floating offshore wind turbines, and to improve both numerical and physical modeling techniques - and hence increase feasibility.

Numerical investigations highlight the effects of correctly modeling both the structural, the hydro- and the mooring dynamics. Every numerical result presented in the present work has been validated against experimental data from scaled model tests. A novel low cost device to emulate wind turbine loads in said scaled tests has been developed. This device allows for non-tactile excitation of floating wind turbines, and could assist the development of novel foundation types by allowing initial test campaigns to be conducted in wave basin facilities without wind generation capabilities. The numerical and physical investigations of floating wind turbines presented in this work should allow for more optimized early stage system designs and hence, improve the feasibility of these.

# Resumé

I takt med at det globale energibehov stiger, er det nødvendigt at forsyningen følger med. I tider hvor politiske og miljømæssige bekymringer øger presset på de konventionelle, fossile energikilder, flyttes fokus mere og mere mod vedvarende energi. Vindenergi er den ældste og en af de mest teknologisk modne industrier indenfor vedvandre energi, og forventes derfor at bidrage med en stadigt voksende andel i fremtidens energiforsyning.

Imens vindmøller på land er meget udbredte, er markedet for havvindmøller ligeledes vokset kraftigt siden den spæde start i Vindeby i 1991. Dette kan til dels tilskrives den stærkere og mere stabile vind over åbent vand, men også størrelsen på moderne vindmøller, der besværliggør transport på land og samtidig medfører bekymringer for visuelle og støjmæssige gener. For at sikre fortsat udvikling af etablerede områder samt åbne for nye markeder, er teknologier, der muliggør installation på dybere vand, nødvendige. Vindmøller funderet i havbunden har nogle åbenlyse økonomiske begrænsninger ved stigende vanddybder, og grundet dette er en interesse i flydende vindmøllefundamenter vokset frem.

Idéen om flydende havvindmøllefundamenter er en forholdsvis ny teknologi der dog er kommet lang siden den første prototype blev installeret mindre end et årti siden. Mange af teknologierne er taget direkte fra olie-/gasindustrien, men stadig er designet drastisk anderledes. Selvom de mere lempelige krav til pålideligheden peger i retning af billigere strukturer, nødvendiggør den koblede vindmølle/platform systemdynamik og lavere profitmargin i vedvarende energi stramme rammer for optimering før et økonomisk rentabelt design kan opnås.

I det forelagte arbejde har indsatsen været lagt i at opnå en bedre systemforståelse af flydende vindmøllefundamenter, samt i at forbedre såvel numeriske som fysiske modelleringsværktøjer - alt sammen med målet at styrke

rentabiliteten af sektoren. Numeriske undersøgelser har fremhævet effekterne ved korrekt modellering af såvel den strukturelle dynamik, samt hydro- og forankringsdynamikken. Samtlige numeriske resultater præsenteret i det forelagte arbejde er blevet valideret imod data fra skalerede fysiske modelforsøg. Et nyskabende og kosteffektivt instrument for påføring af skalerede vindmøllelaster er blevet udviklet. Dette instrument muliggør berøringsfri belastning af flyende havvindmøllefundamenter, og vurderes at kunne assistere i udviklingen af nye fundamentstyper ved at gøre initierende modelforsøg mulige i bølgebassiner der ikke kan tilbyde skaleret vindbelastning. De numeriske og fysiske undersøgelser af flydende havvindmøller præsenteret i det forelagte tænkes at åbne op for mere optimerede design på et tidligere stadie og igennem dette forbedre rentabiliteten af disse.

# Nomenclature

## Abbreviations

BEM	Boundary Element Method, pp. 25, 26, 29
BLDC	Brushless DC, p. 39
CAPEX	Capital Expenditure, pp. 12, 17
CFD	Computational Fluid Dynamics, p. 23
DoF	Degree of Freedom, pp. 21, 23, 24, 33, 35, 42, 43
ESC	Electronic Speed Controller, p. 39
EWEA	European Wind Energy Agency, pp. 6, 18
FLS	Fatigue Limit State, p. 35
FOWT	Floating Offshore Wind Turbine, pp. 7, 10, 11, 13–18, 21–24, 30, 35, 38, 42, 45
HITZ	Hitachi Zosen, p. 16
IFS	Incentive-based Financial Support, p. 45
LCOE	Levelised Cost of Energy, pp. 7, 17, 18
MHI	Mitsubishi Heavy Industries, p. 15
NREL	National Renewable Energy Laboratory, pp. 22, 30, 39, 40, 42
O&M	Operation & Maintenance, p. 12
OPEX	Operational Expenditure, pp. 12, 17
PSD	Power Spectral Density, p. 38
PWM	Pulse-Width Modulation, p. 39
R&D	Research & Development, pp. 13, 19
RNA	Rotor Nacelle Assembly, pp. 4, 14, 35, 38, 39
Semi-Sub	Semi-Submersible Platform, pp. 10, 12, 14, 15, 26, 30, 31
TLB	Tension-Leg Buoy, pp. 10, 12
TLP	Tension-Leg Platform, pp. 10, 12, 14, 35, 38
ULS	Ultimate Limit State, pp. 35, 38

## Latin Nomenclature

$A$	Body area, p. 24
$C$	Frequency dependent hydrodynamic damping, p. 25
$C_a$	Added mass coefficient, p. 24
$C_d$	Drag coefficient, p. 24
$d$	Significant body dimension, p. 24
$F_D$	Drag force, pp. 24, 29
$F_e$	Wave excitation force, p. 25
$F_I$	Inertia force, p. 24
$h_r$	Causal impulse response function, p. 25
$H_r$	Frequency response function, p. 25
$k$	Wave number, p. 27
$K_h$	Hydrostatic stiffness, p. 25
$K_m$	Mooring stiffness, p. 25
$L$	Wave length, p. 24
$m$	Structural mass, p. 25
$m_\infty$	Added mass at infinite high frequencies, p. 25
$T$	Wave period, p. 25
$u$	Fluid coordinate, p. 24
$v$	Body coordinate, p. 24
$V$	Body volume, p. 24

## Greek Nomenclature

$\omega$	Wave/Excitation angular frequency, pp. 27, 28
$\omega_0$	Angular eigenfrequency, pp. 27, 28
$\phi$	Fluid velocity potential, p. 24
$\rho$	Fluid density, p. 24



# 1 | Introduction

The motivation for the present thesis is in all sense the growing energy need of the world - and the push to change the global energy mix. Figure 1.1 shows the global energy flow in 2011. The total energy use is 534000 PJ, though this total does not add up from the figure due to different statistical uncertainties [LLNL, 2016]. This figure is expected to grow vastly over the coming years. The International Energy Agency expects a growth in solely the demand for electricity by 70% by 2040 [International Energy Agency, 2015].

This massive growth can be explained by the ever growing consumptions in the developed countries, but also greatly attributed to the rapidly growing middle class of emerging markets. The global middle class was in 2009 esti-

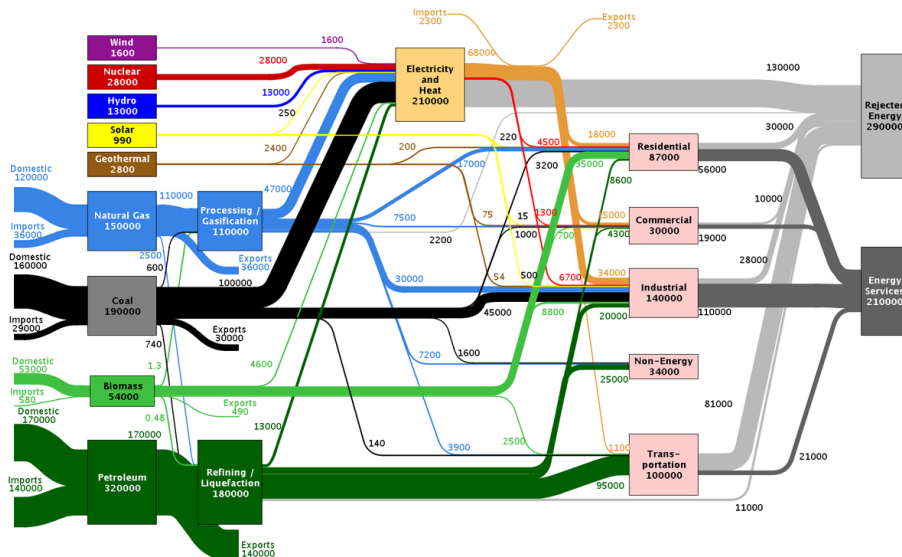


Fig. 1.1: World energy flow in 2011 (PJ) [LLNL, 2016]

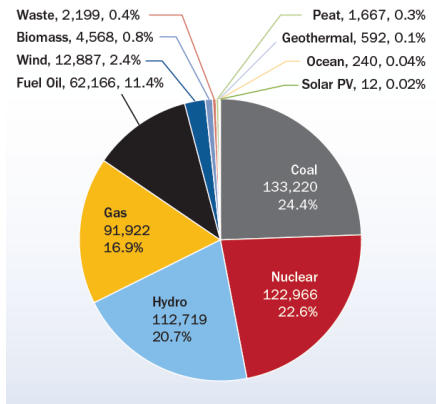


Fig. 1.2: European power mix in 2000 (MW). Renewable sources represents under 25% of the total power [EWEA, 2016b]

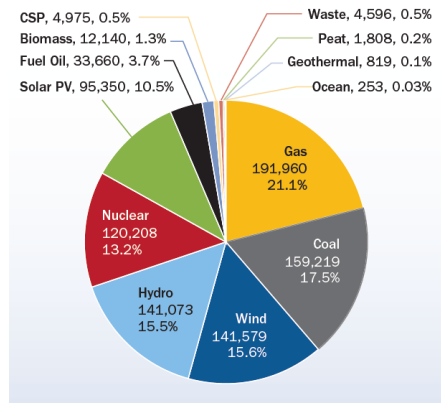


Fig. 1.3: European power mix in 2015 (MW). Renewable energy contribution has increased to over 44% [EWEA, 2016b]

mated at 1.8 billion people. This number is expected to increase to 3.2 billion by 2020 and 4.9 billion by 2030 [OECD Observer, 2012].

Globally, the energy mix does still rely greatly on fossil fuels. This posts a multitude of well known concerns. These are summed up in three main topics quite well by MacKay [2008]. Firstly, though predictions on climate change vary, a move away from fossil fuels will help limit the emission of greenhouse gases. Secondly, the global society needs an energy source once the fossil fuels inevitably are depleted. Thirdly, the security of supply for sovereign states helps ensure political stability. Two secondary points needs to be taken into considerations as well. One being the environmental impact from the more polluting conventional energy sources, and the other being the possibility of growth and job creation in the young renewable energy sectors. All of these points individually make for strong political agendas to push from fossil fuels towards renewables.

On an European scale this movement have been strong in the last 20-30 years. Figure 1.2 and 1.3 shows the change in energy mix of the EU member states over the last 15 years, where the contribution from renewable energy have risen from 25% to 44% [EWEA, 2016b]. Special attention should be given to the single energy source with the largest increase in energy mix contribution; wind power.

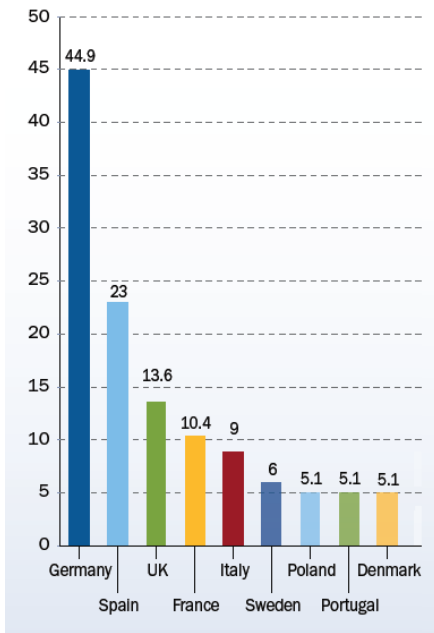


Fig. 1.4: Market share of installed wind power capacity in GW by EU member states - excluding countries with a capacity lower than 5 GW [EWEA, 2016b]

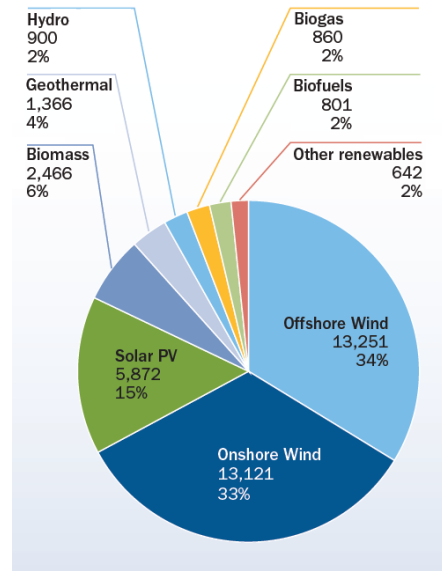


Fig. 1.5: Investments by EU member states in clean energies in 2015 (million EUR) [EWEA, 2016b]

## 1.1 Wind Energy

As one of the main contributors to the renewable energy sector in the EU, wind energy have seen tremendous growth over the recent years. In 2015 12.8 GW of wind power capacity was installed, pushing the total capacity to 142 GW. The 12,800 MW accounts for 44% of all energy production installed in 2015. As seen in figure 1.4, Germany remains the leading country in the EU when it comes to installed wind power with a total capacity of 45 GW, and representing 47% of all new installations in 2015. Though only being in third place when it comes to installed capacity, the UK managed to attract 12.6 bn EUR of investments in wind energy projects in 2015, which accounts for 48% of all wind energy investments - or, according to figure 1.5, 32 % of all clean energy investments that year [EWEA, 2016b].

Figure 1.6 shows the steady increase in wind turbine installations. Note that as the onshore wind energy projects seem to have found a more constant installation rate, the offshore projects are increasing almost year-by-year, ac-

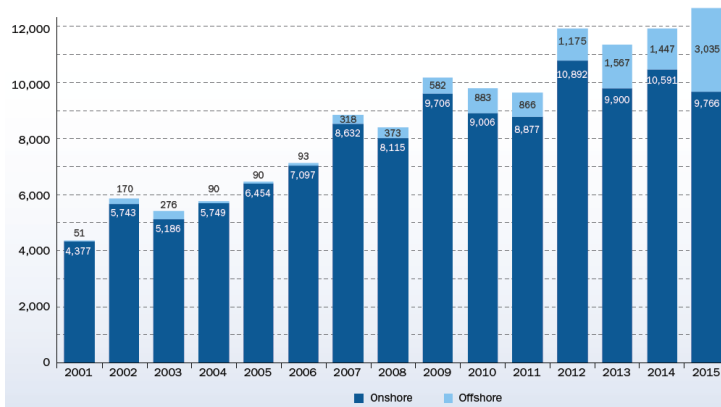


Fig. 1.6: Annual amount of installed MW of wind power in the EU [EWEA, 2016b]

counting for roughly 24% of all installed capacity in 2015. This is partly because of the UK's heavy commitment in the sector of offshore wind energy installations.

Though the installation costs of offshore wind turbines exceeds those of onshore, there are still plenty of drivers for this move into the oceans. A more contextual reason is the fact that as turbines become larger and larger, the visual and audible nuisance perceived by the public is greatly reduced. One of the more logistical benefits is the fact that the transportation over land is also limited by weight, width and length of the Rotor Nacelle Assembly (RNA) and blades respectively. When that is said, the main driver for offshore installations is probably the resource. The larger wind fetches and low shear surface of the open sea contribute to higher and more stable wind speeds; implying a significant untapped wind energy resource [EWEA, 2009].

Due to the favorable shallow water conditions of the North Sea, this is by far the most exploited offshore area accounting for almost 70% of the of the cumulative installed offshore capacity [EWEA, 2016a]. This is because of the sites with favorable combinations of a good wind resource, shallow water depths and a relatively short distance to shore for multiple countries with the required political will. The high rate of development of these suitable project locations have forced the industry to look beyond the obvious sites, and instead try to find acceptable compromises. The average grid-connected wind farm in 2015 was installed at 27.1 m of water and 43.3 km from shore. The distance to shore is primarily driven by the large amount of German installations in 2015, which had an average distance to shore of 52.6 km. In

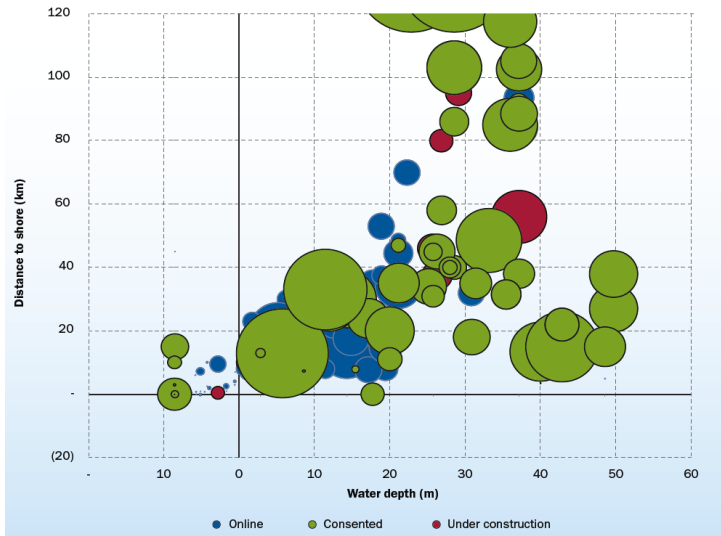


Fig. 1.7: Average water depth and distance to shore for bottom-fixed offshore wind turbine parks in the EU. Circle size indicates relative rated capacity [EWEA, 2016a]

comparison the UK projects was only 9.2 km from shore on average [EWEA, 2016a].

The compromise between the costs of installing in deeper waters and installing further from shore is depicted in figure 1.7. It is seen that where most of the already connected wind farms are at 20 m water depth or below and less than 40 km from shore, some of the consented projects have been designed at locations of either greater water depth or significantly longer distances to shore. It is possible that the distance to shore is not a major disadvantage in all cases since they might be able to utilize the existing undersea grid from older projects. Still, both the distance to shore and the installation water depth are seen as cost drivers.

## 1.2 Deep Water Offshore Wind Energy

While the offshore wind industry in some European countries thrive with access to a plethora of suitable locations, a lot of other counties - both in Europe and world wide - have limited access to shallow waters. This is the case for countries along the western coast of Europe facing the Atlantic, and countries in and around the Mediterranean Sea as seen in figure 1.8. Globally, other locations with desirable offshore wind resources but limited shallow waters

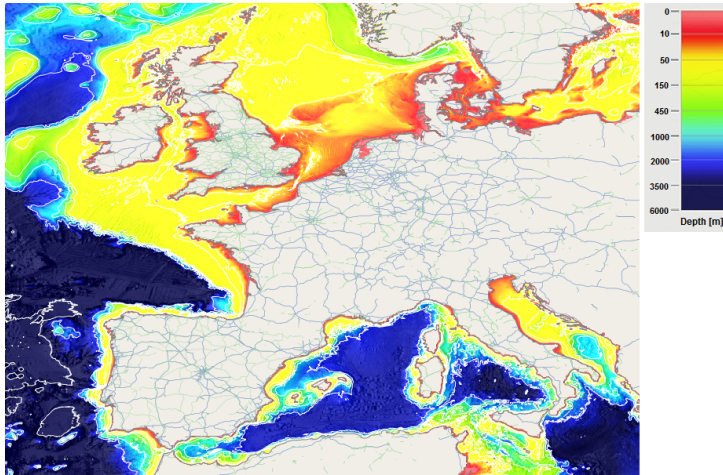


Fig. 1.8: European bathymetry map [EMODnet, 2016]

can be found around Japan and the western coast of the US. More countries with coast lines at continental shelves could be mentioned, but in the current context only countries with the present technology and political benevolence required for harnessing the deep sea wind resource are listed.

Different definitions have been made for defining *deep water*. Multiple definitions can be found across literature, but in the more modern works the transition from *intermediate waters* and *deep waters* are generally located at 50 or 60 m, which will also form the basis in the presented work. When applying this term to the regions mentioned above, the magnitude of the potential but yet untapped energy resources becomes evident. The share of offshore wind resource in >60 m of water for Europe, USA, and Japan, is estimated to 80%, 60% and 80% respectively [Carbon Trust, 2015].

Conventional foundation types have thrived in the shallow waters. Mainly the monopile foundation have carried the industry and is still the preferred foundation type in the EU accounting for 80% of the total cumulative installed capacity, and an impressive 97% of the installed European capacity in 2015 [EWEA, 2016a]. Even though technological improvements have and will make conventional foundation types like monopiles and jacket structures possible in deeper and deeper waters, some drastically new approach needs to be taken in order to feasibly harness the wind energy in the deeper waters. An extensive work carried out in 2012 by a task force under European Wind Energy Agency (EWEA) have identified multitude of challenges

in harnessing deep offshore wind energy. The task force consisted of leading companies and researchers in the deep offshore sector, and goal was to list challenges and recommendations for the industries as well as the politicians in the EU [Athanasia and Genachte, 2013]. Some of the recommendations are summarized below.



- Deep offshore designs are necessary to unlock the promising offshore market potential in the Atlantic, Mediterranean and deep North Sea waters.
- Deep offshore designs constitute an export opportunity. As deep offshore capacity increases, expertise, skills and technologies developed in Europe can be exported across the globe, initially to Japan and the US.
- The energy produced from turbines in deep waters in the North Sea alone could meet the EU's electricity consumption four times over.
- Deep offshore designs are competitive in terms of the Levelised Cost of Energy (LCOE) with bottom-fixed foundations in more than 50 m water depth. The technology is still at a very early stage of development and in order to achieve commercial and large-scale deployment, the sector must overcome technical, economic and political challenges.
- If the challenges are overcome, the first deep offshore wind farms could be installed and grid connected by 2017.

[EWEA, 2013]



When mentioning *deep offshore designs*, the implicit meaning is generally interpreted as a reference to Floating Offshore Wind Turbines (FOWTs). As mentioned above the LCOE of floating turbines is estimated to be competitive with that of conventional bottom-fixed designs in waters above 50 m in depth. Both the academic and industrial world have embraced the daunting task of solving the engineering obstacles in taking a massive structure under

heavy loads and putting it on a floating foundation. The following chapters will focus on the state of the art from two angles; the state of the art in terms of different designs and prototypes, and later discuss the approaches used to numerically and experimentally model these different and complex systems.



---

## 2 | State-of-the-Art

When the early bottom-fixed foundations moved offshore, a lot of know how from land based foundation designs could be used, but still new challenges arose from designing and operation in the marine environment. Here is has been a natural choice to seek information and learn from an older, well established industry renowned for its prowess in developing and designing offshore foundations; namely the O&G sector.

For floating foundation types, it is also an obvious first step to look at some of the designs used by the O&G industry. The large economic incentive from obtaining access to oil reserves, in waters where bottom-fixed towers are not

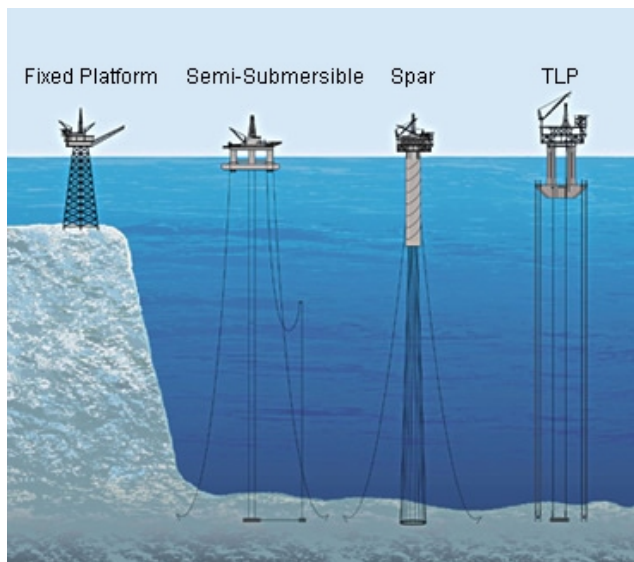


Fig. 2.1: The main concepts developed and used by the O&G sector [Fox Oil Drilling Company, 2016]



**Fig. 2.2:** The three archetypes of floating foundations adopted by the wind energy industry. From left: Spar buoy, Semi-Sub, TLP [DNV GL, 2016]

an option, have led to the development of multiple floating suitable foundation types. One testament to the economic feasibility of deep sea drilling is the Perdido platform operated by Shell, Chevron and BP at a water depth of 2450 m [Shell, 2010]. Figure 2.1 shows some of the three dominant typologies used in the O&G sector.

## 2.1 Floating Foundation Archetypes

The floating foundation types adopted by the wind energy sector can mainly be described as adhering to one of the following classes; Spar buoy types, Semi-Submersible Platform (Semi-Sub) types or Tension-Leg Platform (TLP)/ Tension-Leg Buoy (TLB) types. Figure 2.2 shows how these O&G concepts could look when adopted by the wind energy industry for FOWTs. This classification of only three main concepts is generally able to describe most designs, though every design use all three effects to some degree. A few concepts find themselves somewhat in-between two or more archetypes.

To obtain the needed stability required to support a structure such as a wind turbine three stabilizing effect can be used. These effects are naturally closely

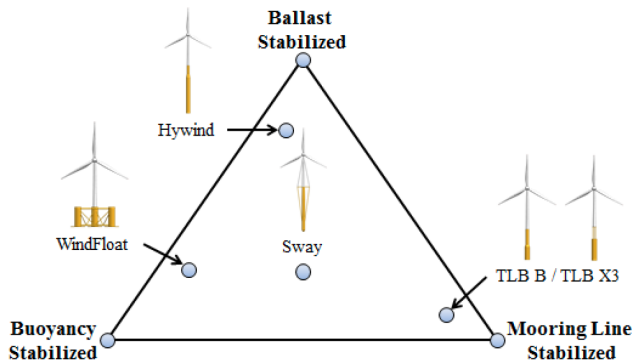


Fig. 2.3: Stabilizing effects utilized in the different FOWT concepts as discussed by [Butterfield et al., 2007]. A few selected designs are depicted for reference [Bjerkseter and Ågotnes, 2013]

linked to the three main concepts mentioned above. Figure 2.3 displays the three options available for a floating body to obtain stability [Butterfield et al., 2007]. The first option is to obtain stability via ballast. This is the effect utilized by the spar buoys, where the center of mass is moved far below the center of buoyancy. This provides a significant restoring moment when the structure is pushed out of equilibrium. The case of buoyancy stabilization is using the hydrostatic stiffness of piercing the water plane area in positions offset from the center-axis of the tower. This provides the restoring stiffness needed for the overall stability of the structure. The third and last alternative is to utilize the mooring in actively keeping the structure upright. This kind of structure is inherently unstable since the center of gravity is above the center of buoyancy. Therefore the taut mooring provides the righting moment by being connected to off-axis fairleads, and hereby transfers the wind turbine loads into the anchors below.

It is clear that there are some obvious differences between the main concepts and designs, and all have inherent pros and cons [Butterfield et al., 2007; Carbon Trust, 2015]. Nevertheless, ultimately they all serve the same purpose; to provide a stable platform for the wind turbine to operate off.

### 2.1.1 Spar Buoy

- |                            |                                 |
|----------------------------|---------------------------------|
| + Inherently stable        | - Large draft limits towing     |
| + Low wave exposure        | - Material usage                |
| + Simple structural design | - Floating turbine installation |

The biggest upside for the spar buoy is the inherently great stability. This

stability comes at a price; the draft. The deep hull provides challenges in launching the vessel from port, and handling the towing from port to site. Most concepts try to circumvent this issue by towing the structure at an inclined angle and then only adding the total ballast when arriving at site. Generally spar buoys are not suitable for installation in water depths of >100 m. Catenary moorings are well known and relatively simple to pre-install at site.

### 2.1.2 Semi-Sub

- + Inherently stable for towing
- + Low draft
- + Port installation of turbine
- Complex fabrication
- Active ballast system
- Structural mass

The Semi-Sub foundation has a large positive driver when it comes to Capital Expenditure (CAPEX). This is due to the fact that the turbine installation and testing can be done and finalized in port, and hence removes a lot of the expensive offshore operations during the commissioning phase. The only operations needed at sea is hooking the structure up to pre-installed anchors and grid cables. These anchors are often catenary, and thus become very long and expensive in deeper waters when a specific mooring compliance and station-keeping is required. The towing is also fairly straight forward due to the inherent stability of the assembled system and the low draft. This also means that the total system can be towed to port for more demanding tasks during Operation & Maintenance (O&M) - a crucial factor to consider when evaluating the Operational Expenditure (OPEX) during the structures lifetime.

### 2.1.3 TLP

- + Low material usage
- + Excellent stability
- + Cheap depth scaling due to taut mooring
- Inherently unstable
- Complex anchoring
- Bespoke vessel needed for installation





The TLP consists mainly of an almost fully submerged buoyant structure. Due to the small draft and the fact the the stability is obtained via the mooring system, these structures can be relatively small and light compared to the spar and Semi-Sub types. The TLB design is trying to strike a balance between the spar and the TLP, but is generally included in the latter category due to the need for tendons for adequate stability. For the TLP the inherently





unstable system will often require a bespoke vessel for assisting in installation. This also implies a greater risk of total system failure if one or more mooring lines should fail. The loads on the tendons and anchors are also significantly larger than in the other concepts, but the upside of this mooring configuration is that the taut mooring lines go vertically from seabed to fairlead and thus scales linearly with water depth.

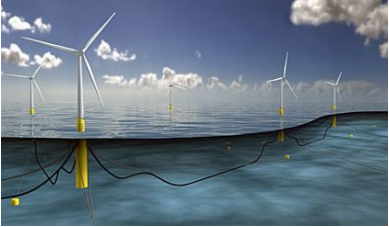

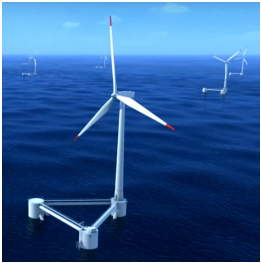
## 2.2 Market Review

The first FOWT concepts date back to the 1970s by works of e.g. Heronemus [1972], but the industry's participation in Research & Development (R&D) only started in the mid-1990s. As of summer 2016 there are currently more than 30 designs on the market. As illustrated in the following, the maturity of the different concepts range from R&D/demonstration stage where only numerical and experimental modeling is done, over pilot/prototype stages where either scaled or full scale models are deployed, and some even all the way to pre-production pushing for commercialization. Below a selected few events are listed to present a rough timeline of the market development [Carbon Trust, 2015; EWEA, 2013] .

## 2.2.1 Technology Timeline

- 2008** ... ● The worlds first FOWT is deployed by the Dutch company **Blue H**. The prototype consists of at TLP with a 80 kW turbine. Installation-site is in the Adriatic Sea at a water depth of 113 m, 22 km from the coast [Blue H, 2016].
- 
- 2008** ... ● Danish developer Floating Power Plant launches a multi-functional Semi-Sub platform. The **Poseidon 37** concept supports three smaller wind turbines along with wave energy conversion capabilities. Newer design-iterations only includes a single wind turbine, while still incorporating wave energy absorption capabilities [Floating Power Plant, 2016].
- 
- 2009** ... ● Statoil reaches a milestone in the **Hywind** project, and commissions the first full scale FOWT; a 2.3 MW Siemens turbine on a spar buoy off the coast of Norway. The spar has a draft of 100 m and is catenary moored in 200 m of water [Statoil, 2012].
- 
- 2011** ... ● Norwegian developer **Sway** deploys a pilot model. This spar-like concept is tethered to the seabed via a passive subsea yaw swivel. This allows the entire structure to yaw with the downwind turbine, in contrast to conventional fixed turbines where yaw motors in the RNA are used to orientate the rotor into the wind [Sway, 2016].
- 

- 2011** ... Principle Power deploys a full-scale 2 MW **WindFloat** prototype (WF1) 5km off the coast of Aguçadoura, Portugal. The Semi-Sub platform has the wind turbine placed on one of the three man columns, and utilizes active ballasting by pumping water from column to column as wind directions change [Principle Power, 2016].
- 
- 2013** ... The first North American grid connected FOWT is launched by University of Maine as a part of the DeepC consortium. The **VulturnUS** is a 1:8th-scale concrete Semi-Sub which employs a 20 kW turbine on 24 m of water off the coast of Castine, US [UMaine, 2016].
- 
- 2013** ... Following the nuclear accident in Fukushima in 2011, Japanese renewable research is intensified. Only two years later the Fukushima Offshore Wind Consortium installs the **Fukushima Mirai**; a compact Semi-Sub supporting a 2 MW downwind turbine [Fukushima OWC, 2016].
- 
- 2015** ... Another two years pass, and the massive **Fukushima Simpoo** is installed. This Semi-Sub supports the worlds largest FOWT; a 7 MW turbine by Mitsubishi Heavy Industries (MHI). This is currently still the largest floating concept in the world [Fukushima OWC, 2016].
- 

- 2016** ... ● The worlds first floating wind park begins construction, and is expected for installation within a year. The project called **Hywind** Scotland Pilot Park will consist of five turbines with a cumulative capacity of 30 MW installed in excess of 100 m water, 25-30 km off the coast near Aberdeen. The aim is to demonstrate the cost efficiency and reliability for future commercial parks [Statoil, 2016].
- 
- 2017** ... ● Commissioning of two **Ideol** projects is expected. The first is a 2 MW FOWT at the SEM-REV testing site at Le Croisic, France, at 33 m of water. For the second project Ideol has partnered up with Hitachi Zosen (HITZ) to commission two FOWTs with a cumulative capacity of 7.5 MW at an undisclosed location in Japan at around 50 to 100 m of water. This innovative floating concept utilizes a patented internally enclosed water column to dampen structure motions [Ideol, 2016].
- 
- 2018** ... ● Multiple **WindFloat** parks are planned for commission. The 25 MW WindFloat Atlantic in 90 m off the Portuguese coast. The 24 MW WindFloat Pacific in 300 m of water off the coast of Oregon, USA. Finally the Kincardine Offshore Wind Limited projects aims at installing eight 6 MW turbines of the Scottish coast near Aberdeen [Principle Power, 2016].
- 



## 2.3 The Future of FOWTs

From the timeline it is evident that the industry have gained tremendous momentum since the humble beginnings in 2008. While the massive investments prove a great deal of trust in the future of the floating offshore wind technology, deployment is still relying on subsidies to be feasible. The subsidies are widely used and established in the renewable sector, but still the floating offshore wind industry needs to compete with bottom-fixed wind turbines in terms of LCOE. For both floating and bottom-fixed turbines, the real target is getting the LCOE equal to or below that of conventional energy sources. That goal can be achieved by either waiting for the conventional prices to go up, or by lowering the LCOE from the renewable sources.

### 2.3.1 Bringing down LCOE

The inherent upsides of FOWTs are as mentioned many. An obvious example is the possibility of onshore/quay-side assembly and service - possibly lowering both CAPEX and OPEX. Though this might seem evident, the industry is still young and unproven, and hence the estimates for LCOE are still accompanied by some uncertainty. Multiple investigations have gone into comparing the different floating concept internally, and of course also comparing floating concepts to bottom-fixed designs.

Ebenhoch et al. [2015] have analyzed available literature and market data to establish an average target LCOE for bottom-fixed turbines of €135/MWh. When studying current concept's production claims, and taking their own less optimistic estimates into considerations, the average target for the floating turbines end up at €155/MWh. The economic model behind these figures suggests the transition from bottom-fixed to floating to currently be at around 100 m of water. Significantly deeper than suggested earlier.

The potential for competitiveness of floating turbines is highlighted by Carbon Trust [2015], estimating €130/MWh in commercial deployments, and possibly as low as €110/MWh for leading concepts. The bottom-fixed commercial projects in the UK are already on track with the 2020 target of €130 /MWh, and hence the floating concepts must have a steeper curve of improvements to be able to compete with bottom-fixed foundations on an equal footing.

Six conceptual FOWT designs have been analyzed by Myhr et al. [2014] and compared to bottom-fixed solutions. In general the LCOE of the floating

foundations are comparable the one of their bottom-fixed counter parts at intermediate waters from 50 - 150 m of water. Still, the presented LCOE of the different floating concepts range all the way from €82/MWh to €237/MWh for a commercial park 100 km offshore. This proves the nature of a market with the yet low level of concept maturity and high amounts of significant unknowns. The largest cost differences between the analyzed FOWTs is seen in the production costs and to a lesser extend in the mooring costs. The high manufacturing costs of the concepts is clearly influenced by design complexity, but primarily by steel prices - making low mass system more competitive.

### **2.3.2 Recommendations**

As mentioned above the floating turbine industry have to contentiously decrease LCOE in order to become a competitive player in the energy sector. The different archetypes have different needs of optimization and development, but common for all is the need for de-risking via better design tools and prototype deployments [Butterfield et al., 2007]. EWEA have listed 18 recommendations needed to aid deep water offshore wind in reaching maturity. These items span political, economic and technical recommendations. A selected few are quoted below.



Political recommendations:

- Public support for R&D should continue and increase to maintain European technology and market leadership in deep offshore designs.
- Access to financing should be ensured for deep offshore projects where a correct risk perception has been applied.

Technical recommendations:

- Modeling tools and numerical codes that simulate the whole structure's behavior should be developed and validated to allow for an improved design.
- More research must be done on mooring and anchoring systems with the industry benefiting from the experience of the oil and gas sector.

[EWEA, 2013]





---

## 3 | Research Contribution

The previous chapters have provided the motivation for the presented thesis. This chapter will illustrate the approach taken in the research, the methods applied and highlight a few of the main findings.

As seen from figure 3.1 the research has been conducted with focus being either mainly on a sub-component or on the full system. In the following the sub-systems will be explained. This segmented approach has been done in an effort to investigate the possibility for improvements in the different fundamental intrinsic parts of a FOWT.

While each investigation focuses on a specific and delimited part of the full system, a complex multi Degree of Freedom (DoF) system like a floating wind turbine cannot be solved by analyzing every sub-component individually. Each main component causes a change in response and excitation that will influence the total system behavior. Fully coupled models capable of this are known as aero-hydro-servo-elasto dynamic solvers. Referring to the inclusion of aerodynamics, hy-



Fig. 3.1: Scope of presented papers.

drodynamics, control strategy forces and structural dynamics. One solver among others capable of this, is the open source software FAST by National Renewable Energy Laboratory (NREL) [Jonkman and Buhl Jr, 2005; Jonkman, 2013]. Some of the following investigations have been made using FAST, and some have been made using simpler bare-bones models relying on the same governing equations. The amount of physical phenomena influencing the behavior of a FOWT is astonishing. Figure 3.2 shows many of the possible forces that would need to be accounted for. In the current work the main contributors are assumed to be; hydrodynamic performance and loading, mooring loads and response, and of course the aerodynamic loading on the turbine it self.

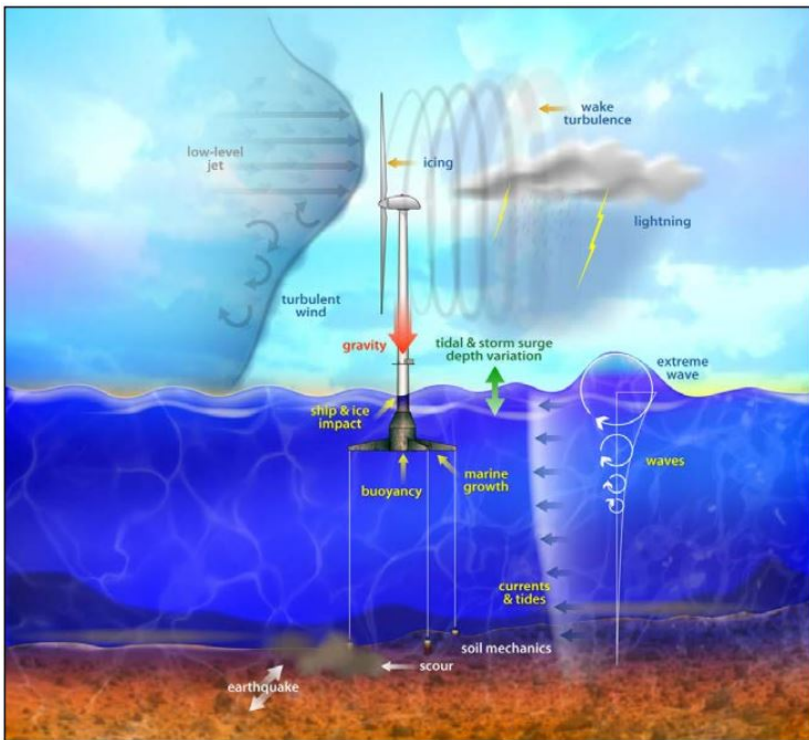


Fig. 3.2: The wide range of physical phenomena that needs to be captured by a model trying to capture the full system description [Jonkman, 2013]

### 3.1 Platform Hydrodynamics

The main component that sets a FOWT apart from any onshore land-based or offshore bottom-fixed turbine, is the floating platform on which it rests. The floating foundation is hence the primary component investigated in this thesis. The analysis of forces on, and motions of, floating bodies has been adopted from the naval and offshore O&G industry. The notation for the six rigid body DoFs of a floating system has hence also been adopted from the naval engineering and can be seen in figure 3.3 and 3.4.

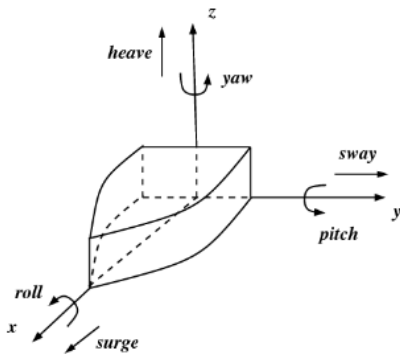


Fig. 3.3: Notation of the six degrees of freedom commonly used in naval architecture and marine engineering [Ardakani and Bridges, 2011]

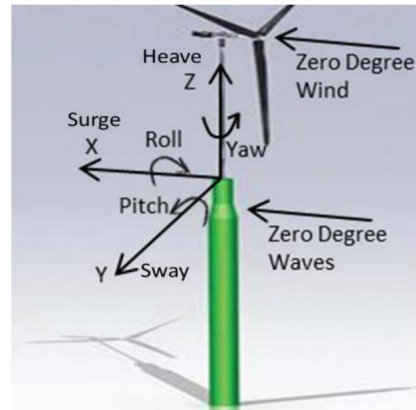


Fig. 3.4: Notation adopted from naval architecture applied to a floating wind turbine including definition of excitations [Browning et al., 2014]

For modeling the motions in these DoFs, different approaches can be taken. The hydrodynamics of the foundation can be characterized by two main classes: Slender bodies where the element geometry is significantly smaller than the dominating wave length, and bluff bodies that are large enough to cause wave diffraction. This distinction is made since these assumptions allow for simpler/lighter models either omitting the alteration of the wave field or omitting viscous forces by assuming potential flow. Computational Fluid Dynamics (CFD) models capable of including both wave diffraction, reflection and viscous forces are developed, but the computational heavy models become infeasible for the extent of simulated time analysis needed for the investigation of FOWTs. The slender and bluff body approaches will be elaborated in the following sections, where single DoF notation is used to illustrate the concepts.

### 3.1.1 Slender Body Hydrodynamics

Slender bodies are defined as bodies with  $d \ll L$ , where  $d$  is the significant body dimension and  $L$  is the wave length. This implies that the body causes no change to the passing wave front. Eq. (3.1) know as the Morison equation shows the Inertia force ( $F_I$ ) and Drag force ( $F_D$ ) components in phase with the fluid/system-relative acceleration and velocity respectively. The inertia force is included as the sum of the Froude Krylov force and the hydrodynamic mass force. Eq. (3.1) is simplified to a single DoF scalar equation.

$$F(t) = \underbrace{\rho V \ddot{u}(t) + \rho C_a V (\ddot{u}(t) - \ddot{v}(t))}_{F_I} + \underbrace{\frac{1}{2} \rho C_d A (\dot{u}(t) - \dot{v}(t)) |\dot{u}(t) - \dot{v}(t)|}_{F_D} \quad (3.1)$$

where,

$V$		Body volume	$\rho$		Fluid density
$A$		Body area	$u$		Fluid displacement
$C_a$		Added mass coefficient	$v$		Body displacement
$C_d$		Drag coefficient			

The slender body approach is usually not applicable as the sole hydrodynamic force description on FOWTs due to the large dimensions of most designs. Still, the definition of  $F_D$  can be included in other solutions as will be described later.

### 3.1.2 Bluff Body Hydrodynamics

The bluff body assumption is also commonly known as diffraction theory. As the name implies, this approach aims at describing the including the effects from both the incident and the scattered wave fields. The disturbed wave field is generated by wave diffraction and radiations due to structure motions. While this approach includes wave/structure interactions, it omits viscous forces since it is based on the assumption of an irrotational potential flow of an incompressible fluid.

$$\phi = \phi_i + \phi_d + \phi_r \quad (3.2)$$

$$\nabla^2 \phi = 0 \quad (3.3)$$

where,

$\phi$		Total velocity potential	$\phi_i$		Incident velocity potential
$\phi_d$		Diffraction velocity potential	$\phi_r$		Radiated velocity potential



The diffraction problem is solved means of the Boundary Element Method (BEM) also known as the panel method. In the works presented in this thesis either the proprietary WAMIT [Lee and Newman, 2006] or open-source Nemoh [Babarit and Delhommeau, 2015] numerical solvers have been used.

When assuming monochromatic linear wave loadings the governing time domain equation is described by Cummins [1962] and also presented in paper [C]:

$$(m + m_\infty) \ddot{v}(t) + \int_{t_0}^t h_r(t - \tau) \dot{v}(\tau) d\tau + Kv(t) = F_e \cos(\omega t), t > t_0 \quad (3.4)$$

and

$$v(t_0) = v_0, \quad \dot{v}(t_0) = \dot{v}_0 \quad (3.5)$$

$m$  is the structural mass, and  $m_\infty$  is the added mass at infinite high frequencies.  $\ddot{v}(t)$ ,  $\dot{v}(t)$  and  $v(t)$  indicates the acceleration, velocity and position of the platform respectively, and  $v_0$  and  $\dot{v}_0$  indicate the initial conditions at the time  $t_0$ .  $h_r(t)$  is the causal impulse response function for the radiation force.  $K$  represents the linear spring stiffness from hydrostatics and mooring system ( $K = K_h + K_m$ ).  $F_e$  is the amplitude of the external wave loading, and  $\omega = \frac{2\pi}{T}$  is angular frequency and  $T$  is the period of the monochromatic waves.

In the stationary state, where the response from the initial conditions has been dissipated, Eq. (3.4) should be reformulated as:

$$M \ddot{v}(t) + C \dot{v}(t) + Kv(t) = F_e \cos(\omega t) \quad (3.6)$$

where:

$$\left. \begin{aligned} M &= M(\omega) = m + m_h + \frac{1}{\omega} \text{Im}(H_r(\omega)) \\ C &= C(\omega) = \text{Re}(H_r(\omega)) \end{aligned} \right\} \quad (3.7)$$

$$H_r(\omega) = \int_0^\infty e^{-i\omega t} h_r(t) dt \quad (3.8)$$

$H_r(\omega)$  indicates the frequency response function obtained as the Fourier transform of  $h_r(t)$ .  $M(\omega)$  and  $C(\omega)$  indicates the total structural and hydrodynamic added mass as well as the radiation damping predicted by linear wave theory [Falnes, 2002].

### Stationary Body Excitation

As mentioned the platform for a floating turbine is often consisting of different geometries dominated by different force regimes. Investigation on surge excitation of a generic Semi-Sub has been conducted in paper [B]. The concept used is based on the design presented by Puche [2014], and can be seen in figure 3.5 at a Model scale ratio ( $\lambda$ ) of 1:80.

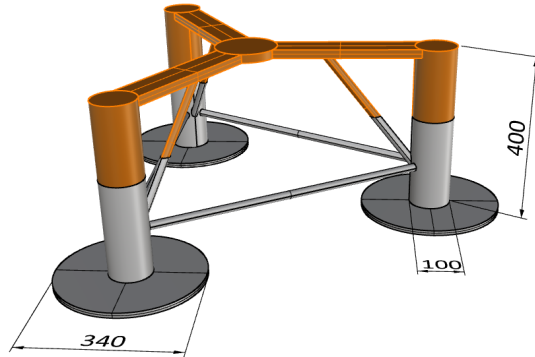


Fig. 3.5: Model scale platform used to assess influence of body geometry on structure excitation (mm) [C]

When a bluff body assumption is made for a complex geometry as the one presented, a full mesh of the structure is used to solve and obtain the frequency dependent excitation force, as well as added mass and radiation damping. The heave plates on the structure will have significant influence in heave (and to an extent in pitch and roll) where the geometry of the plate is a relatively significant part of the total structure. When observing the entire platform from the side, parallel to the water plane, this is not the case. In this dimension the heave plates are thin discs, and major influence on the fluid motion is not to be expected. This leads to the assumption that slender structural parts (e.g. heave plates and cross braces) of such a structure can be omitted from the linear diffraction analysis.

The computational requirements for solving the problems in BEM is proportional to the number of panels. Figure 3.6 shows how the exclusion of secondary slender parts reduces the number of mesh faces by a factor of 6. In paper [B] this led to a reduction in computational time of a factor of almost 50. It has also been shown that the numerical results from the simplified structure is actually describing the loads measured in wave tank testing better than when all structural parts are included. This leads to the assumption

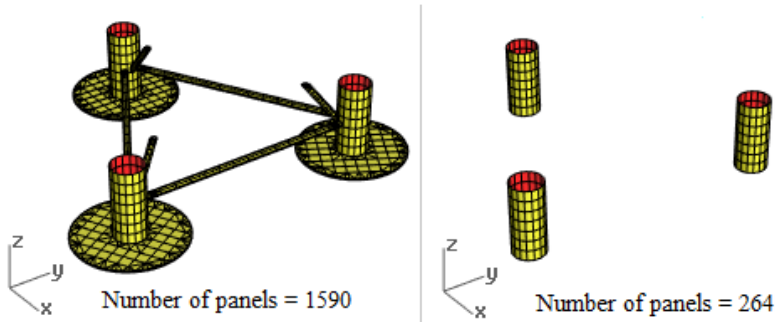


Fig. 3.6: Left: Full mesh of the entire wetted surface. Right: Simplified mesh consisting only of main columns [B]

that the slender bodies that lie outside the diffraction region, causes numerical noise when trying to assess the frequency dependent parameters to the platform in question.

### Displaced Body Excitation

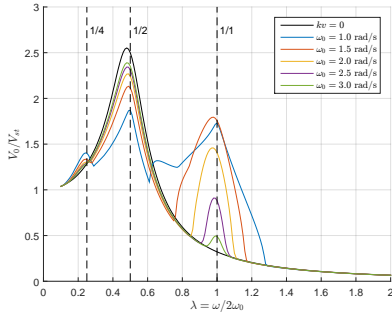
The loading in Eq. (3.6) refers to a structure fixed to a referential coordinate system. In reality the loading is applied at the displaced position  $x = v(t)$ . This will cause a phase change of magnitude  $kv(t)$  where  $k$  is the wave number of the selected sea-state. This implies that for compliant structures with significant finite displacements Eq. (3.6) should be reformulated as:

$$M \ddot{v}(t) + C \dot{v}(t) + K v(t) = F_e \cos(kv(t) + \omega t) \quad (3.9)$$

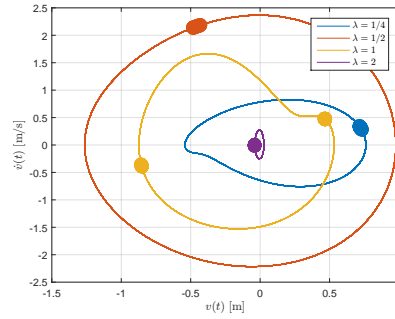
In paper [C] the influence of this excitation at a displaced position has been investigated. Figure 3.7 shows the dynamic amplification of different angular eigenfrequencies, and how they compare to the classic formulation where no phase change is considered, e.g.  $kv = 0$ .

The expected behavior of highest dynamic amplification at resonance ( $\omega = \omega_0$ ) is seen. Though for compliant structures with low stiffness and hence lower natural frequencies, lower motion amplitude is seen at resonance, but instead a higher response is observed at  $\omega = 2 \omega_0$ . When investigating the Poincaré map in figure 3.8 it is evident that the increased response is caused by a subharmonic resonance of order 2.

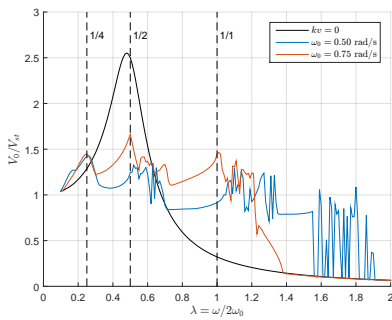
For the systems tested with even lower stiffness a less continuous dynamic amplification was found, see figure 3.9. When observing the subharmonic response of two neighboring excitation frequencies a 6th order subharmonic



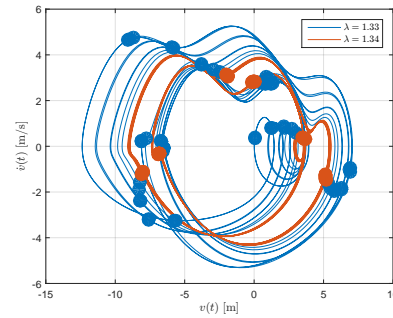
**Fig. 3.7:** Comparison between dynamic amplification of motion amplitude of different higher system natural angular eigenfrequencies [C]



**Fig. 3.8:** Poincaré map and trajectories as a function of  $\lambda$ . Harmonic and subharmonic response of order 2,  $\omega_0 = 2 \text{ rad/s}$  [C]



**Fig. 3.9:** Comparison between dynamic amplification of systems with a lower natural angular eigenfrequency [C]



**Fig. 3.10:** Poincaré map and trajectories as a function of  $\lambda$ . Subharmonic response of order 6 and fully chaotic response,  $\omega_0 = 0.5 \text{ rad/s}$  [C]

and even chaotic response was detected. It is unclear if this is due to numerical instability of it is an indication of a delicate system state. The investigation was conducted with a linear mooring assumption and would benefit from validation by physical model scale testing, as well as a more elaborate non-linear dynamic mooring description. The importance of dynamic mooring modeling is highlighted in paper [E] and [F] and will be discussed section 3.2.1. If the results are confirmed, the lower dynamic amplification at resonance is obviously positive, but the increased amplifications at  $\omega = 2 \omega_0$  can be important for designs that rely on having eigenperiods at around twice the wave peak periods.

### 3.1.3 Hybrid Modeling

One of the most promising hydrodynamic modeling approaches is referred to as hybrid modeling. This approach has been utilized in all hydrodynamic investigations of this thesis. The hybrid modeling strikes a balance between slender and bluff body assumptions by incorporating the perks of both. The inertial loads, impulse response function, frequency dependent added masses and radiation damping coefficients are found by BEM integration. This model is then extended to also include separate *drag members* that serve the purpose of accounting for the neglected viscous forces around parts of the structure. The additional viscous drag is calculated as  $F_D$  in Eq. (3.1).

The hybrid modeling approach has been applied in both the FAST based investigations (papers [E] and [F]) and the bare-bones models (papers [A] and [H]) with good accuracy of the hydrodynamic loading and response of the investigated foundations.

## 3.2 Mooring System Modeling

The correct description and design of mooring systems are paramount to a valid investigation of any FOWT concept. Until recently one of the leading software for modeling floating wind turbines FAST by NREL had very limited mooring modules available. This is due to the history of the software; coming from onshore design, to offshore bottom-fixed, and now fully floating design. Two new capabilities have recently been introduced into FAST. Firstly, multiple ways of coupling the mooring dynamics to the system solver, and secondly, allowing for multi-segmented mooring layouts while doing so.

### 3.2.1 Dynamic Mooring

Simple mooring designs rely on quasi-static assumptions. This allows the omission of dynamic coupling between mooring and system motions. This assumption is valid for stationary floating bodies, or bodies where the eigenfrequencies of the system are significantly lower than the exciting frequencies. These assumptions can not be made for FOWTs, especially as mooring designs needs to be more and more optimized.

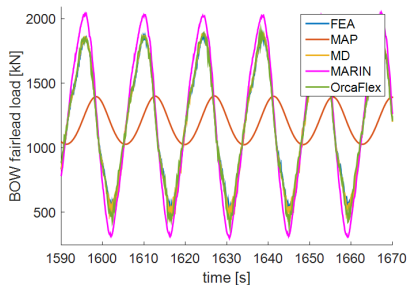


**Fig. 3.11:** OC4-DeepCwind Semi-Sub system as tested in the ocean basin at MARIN. Photo credit: Andy Goupee, University of Maine [E]

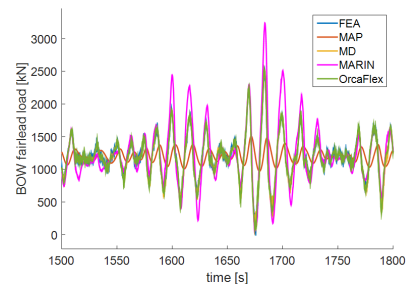
The work presented in paper [E] shows the inclusion and comparison of the

following mooring modules in FAST: MAP++, MoorDyn, FEAMooring and FAST/OrcaFlex. MAP++ is the only quasi-static solver in the list, earlier validated in Coulling et al. [2013]; Prowell et al. [2013]. MoorDyn is a lumped mass model with linear axial stiffness [Hall, 2015; Hall and Goupee, 2015], where FEAMooring is a finite-element based elastic rod model with consistent mass matrix [Bae, 2016]. OrcaFlex is a validated and renowned software for solving hydro- and mooring dynamics in the industry [OrcaFlex, 2016a,b]. The aim of the study was to validate the models against experimental data, and verify them against the trusted commercial tool OrcaFlex.

In figure 3.11 the 1:50 scale model setup tested at MARIN by the DeepCwind consortium. This model, known as the OC4 Semi-Sub, is a generic platform with a simple  $120^\circ$  symmetric catenary mooring layout [Robertson et al., 2012].



**Fig. 3.12:** Bow fairlead loads during regular waves [E]



**Fig. 3.13:** Bow fairlead loads during irregular waves [E]

Figure 3.12 and 3.13 shows the comparisons between the numerical models and the experimental data for regular and irregular waves respectively. For the regular waves a good agreement is seen between FEAMooring (FEA), MoorDyn (MD) and OrcaFlex. The quasi-static MAP++ is unable to accurately model the line tension. The same is the case for the irregular waves, where again the dynamic models outperform the quasi-static one.

The performance of both MoorDyn and FEAMooring is sound when compared to OrcaFlex. The agreement between the numerical models and the experimental was good when taking the limitations of linear hydrodynamic load calculation and inevitable small discrepancies of measurement data into account.

### 3.2.2 Multi-segmented Mooring

Floating platforms without mooring fairleads, such as the spar buoy, rely on ingenuity of mooring layout to obtain sufficient yaw stiffness. This is regularly done by using a delta connection for setting up a bridle mooring (also commonly known as a *crawfoot*) as seen in figure 3.14.

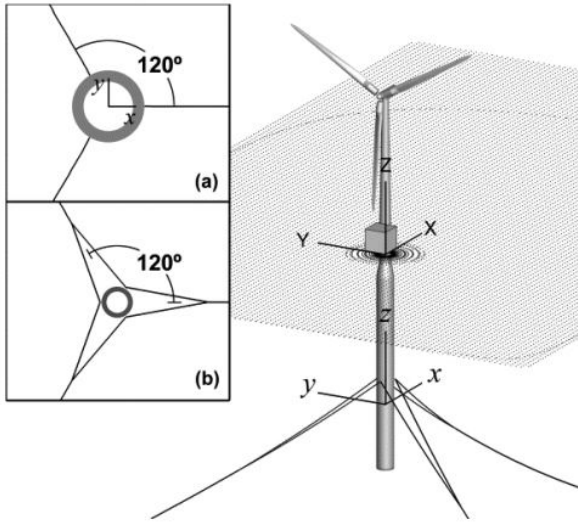


Fig. 3.14: OC3-Hywind spar buoy. (a) Median single line mooring approximation. (b) Full bridle mooring configuration [Quallen et al., 2013]



Fig. 3.15: OC3-Hywind spar buoy during testing at MARIN [Robertson et al., 2013]

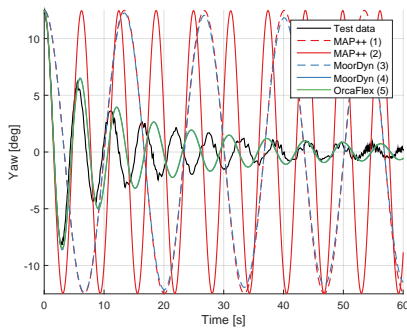
Paper [F] presents the efforts made to verify and validate the ability of modeling multi-segmented mooring layouts in FAST. Previously in FAST, mooring lines could only connect a fairlead directly to an anchor point, as shown in figure 3.14(a). This meant that for structures such as the spar buoy, additional artificial yaw stiffness and damping was needed to tune the system response in the numerical models. As in section 3.2.1, the numerical models were verified against OrcaFlex and validated against experimental data. Figure 3.15 shows the 1:50 scale spar buoy tested at MARIN. FEAMooring does not have multi-segmented capabilities and hence was omitted from this study.

To investigate the influence of mooring dynamics and bridle effects separately five different models were built for comparison:

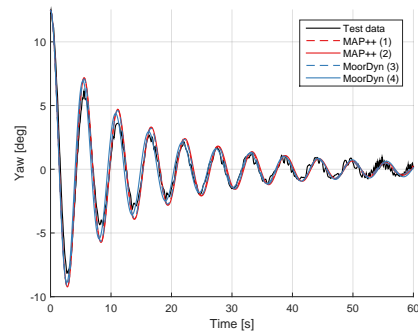


1. MAP++ with three single mooring lines (bisecting the bridle).
2. MAP++ with three multi-segmented bridle moorings.
3. MoorDyn with single mooring lines (as in 1, but with mooring dynamics via MoorDyn)
4. MoorDyn with multi-segmented bridle moorings (as in 2, but with mooring dynamics via MoorDyn)
5. OrcaFlex with multi-segmented moorings (as in 4, but using OrcaFlex) - considered the “benchmark” in the comparisons.

Due to the fact that the effect of this bridle mooring is most prominent in yaw, coupled with the fact that this DoF experiences very little yaw excitation, the validation by experimental data was quite tedious. Hence the model verification and validation was mainly carried out by means of yaw decay tests.



**Fig. 3.16:** Untuned yaw decay response. Models 4 and 5 are indistinguishable [F]



**Fig. 3.17:** Tuned yaw decay response. Model 5 omitted [F]

Figure 3.16 shows the untuned response of the five models. It is observed that the models including the bridle layout obtain a better estimate of the system yaw stiffness. Even more evident is the observation that only the combination of multi-segmented layout and a dynamic mooring solution is able to obtain acceptable estimates for the system damping. MoorDyn (4) and OrcaFlex (5) obtains effectively identical solutions, which is interpreted as a good verification. In figure 3.17 the same models have been tuned to fit the experimental system decay (OrcaFlex does not allow alterations to yaw stiffness and hence has been omitted). It is no surprise that all models can be tuned to match the response when changes are made to both linear stiffness, linear damping and

quadratic damping, but the interesting part is the amount of tuning needed. The quasi-static single line model (1) needs  $140e6$  Nm/rad linear stiffness,  $10e6$  Nm/(rad/s) linear damping and  $100e6$  Nm/(rad/s)<sup>2</sup> quadratic damping. Drastically better performance is seen by model (4) where only  $35e6$  Nm/rad linear stiffness and no additional damping is needed.

With the capability of directly modeling the delta connecting as is, a much better estimate for yaw stiffness has been determined. This is true for both the quasi-static solver MAP++, as well as MoorDyn and OrcaFlex. When including the dynamic mooring solutions from MoorDyn and OrcaFlex, as described above, a highly satisfying accuracy is seen in the system yaw damping. Alleviating the need for model tuning, and providing engineers the tools to directly model and investigate motions and loads in their mooring designs.

## 3.3 Tower and RNA

Even though the wind turbine as a separate structure is well understood, additional uncertainties are introduced when placing it on a moving foundation. The coupled dynamics of the system needs to be investigated and full system response needs to be taken into account. The wave loading will excite the structural dynamics of the tower to some extent depending on the concept design. For example when observing the pitch motion of the platform, the tower acts like a cantilever beam with some inherent additional inertia, damping and possibly loads as well. Continuously and/or amplified cyclic motions will impact the Fatigue Limit State (FLS) design of the FOWT, while the high peak forces will affect the Ultimate Limit State (ULS) design.

The wind turbine tower and RNA have in this not been the primary objective. The topside is regarded as an auxiliary system that, granted, inevitably will influence the full system dynamics. Paper [A] have accepted and worked by the premise of the topside being a passive point mass appendix as described as a cantilever Bernoulli Euler beam with no external load. Hence no aerodynamic damping is considered. Paper [G] and [H] investigates an approach to include the turbine loads. This is done by means of thrust force emulation at the nacelle height.

### 3.3.1 Tower Flexibility

Modern wind turbines are flexible structures. The design of FOWTs often allow for a low frequency component in the pitch motion; the motion mainly exciting the first tower fore-aft bending mode. For the TLP concepts this is not true. These structures are much stiffer in pitch due to the taut mooring cables, and hence aim at putting the pitch eigenfrequency of the structure above the wave load frequencies. The work presented in paper [A] revolves around determining the influence of the tower flexibility on the total system characteristics.

To investigate the influence of tower flexibility a numerical model has been developed. This model has been verified against commercial hydrodynamic software AQWA from ANSYS, and validated against experimental data obtained from 1:80 scaled model tests. AQWA does not allow for coupled structural and hydro-dynamics, and hence has only been used for verifying rigid body motions. Figure 3.18 shows a conceptual sketch of the 5 DoF system modeled. The physical model is shown in figure 3.19. This setup allowed for exchange of the tower part, and hence three distinct models were constructed:

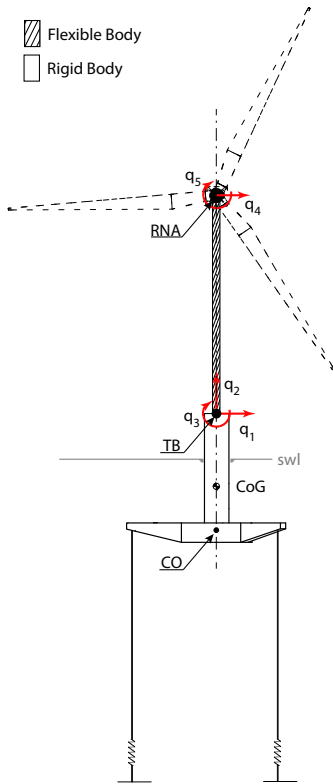


Fig. 3.18: Sketch of tested setup [A]

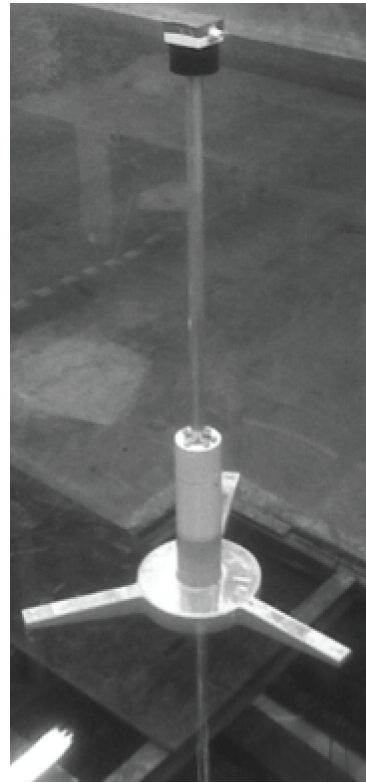


Fig. 3.19: 1:80 scaled model setup [A]

1. Flexible model: Physical tests incorporated a PVC tube as representation of the turbine tower. The structural stiffness of the tower was used in the numerical model.
2. Stiff model: Physical tested were conducted with a aluminum pipe used as tower. Again; this stiffness was adopted in to numerical model.
3. Very stiff / Quasi-rigid model: Not tested physically, but to allow for comparison to AQWA the numerical model was executed with a tower stiffness at orders of magnitude higher than the physical setups - hence the term *quasi-rigid*.

In figures 3.20 and 3.21 the numerical model is compared to measured time series. An overall good fit is seen in the main dynamics, but the accuracy still has room for improvements. Figure 3.22 shows the code-to-code comparison between the quasi-rigid numerical model and the rigid body solution

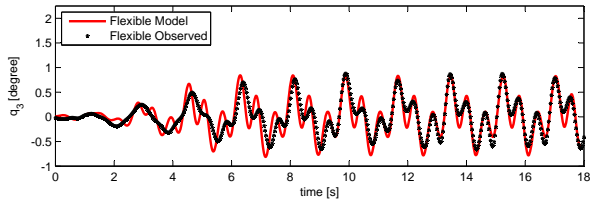


Fig. 3.20: Pitch response of the flexible numerical model under regular wave loading compared to the motions of the flexible model tests [A]

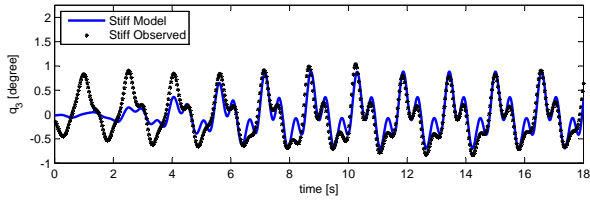


Fig. 3.21: Comparison between the pitch response of the stiff numerical model and the stiff physical setup in regular waves [A]

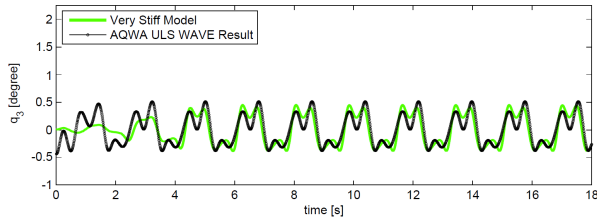


Fig. 3.22: Quasi-rigid numerical model compared to the rigid body solution from AQWA [A]

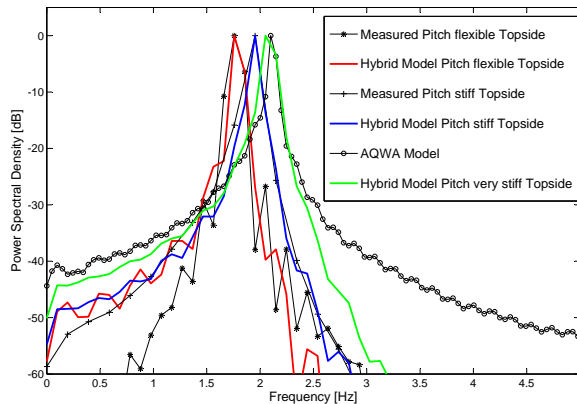


Fig. 3.23: FFT of pitch decay tests from the three numerical models, compared to physical and numerical realizations respectively [A]

obtained from AQWA. Again, the main dynamics are well described.

The Power Spectral Density (PSD) shown in figure 3.23 represents system pitch decay tests. The flexible and stiff models are compared to physical system decay tests, and the very stiff (quasi-rigid) model is compared to the rigid body decay found in AQWA. The numerical model is able to capture the response of all three investigated systems. As seen the peak-frequency of the spectrum is reduced by approximately 20% when flexibility is introduced. Further, the half-band width is decreased indicating a reduced modal damping.

The overall performance of the numerical model was satisfactory. In the PSD of the pitch decay tests it became evident that the flexibility of the tower can not be ignored. The flexible tower shifts down the frequency response of the entire structure, an effect that is not desirable for structures designed to have pitch eigenfrequencies above the wave excitation frequencies, such as TLPs.

### 3.3.2 Emulated Turbine Loading

While the approach of assuming the RNA as a lumped mass might be valid for ULS cases where the turbine is parked, it cannot be used to describe the aerodynamic loads introduced by an operating FOWT. This connected behavior between platform motions and turbine loads needs to be solved in a fully coupled numerical model.

When validating such a model the best tool is often good quality experimental data. An issue with model scaling of FOWTs is the fact that the system is not dominated by a single force regime. The aerodynamic drag forces on the turbine calls for Reynolds scaling, while the gravity dominated wave loads on the platform encourages Froude scaling. Table 3.1 shows the similarities and discrepancies of a few commonly scaled parameters.  $\lambda$  denotes the ratio between model and full scale.

The discrepancies in scaling of main kinematic and dynamic properties require ingenuity in designing properly scaled model tests. Options include mutating the blade cord to obtain correct aerodynamic properties, or increasing wind speed to achieve the desired behavior. These approaches are not trivial to carry out, and still limits the execution of floating turbine experiments to be conducted at wave basins with the capability of producing said wind fields and speeds [Robertson et al., 2013].

Parameter	Froude	Reynolds
Length	$\lambda$	$\lambda$
Rotation	1	1
Time	$\lambda^{1/2}$	$\lambda^2$
Velocity	$\lambda^{1/2}$	$\lambda^{-1}$
Acceleration	1	$\lambda^{-3}$
Mass	$\lambda^3$	$\lambda^3$
Force	$\lambda^3$	1

**Table 3.1:** Comparison of Froude and Reynolds scaling factors.  $\lambda$  is the ratio between model and full scale

In this work a different and more practical approach is presented. The decoupling of force regimes by removing the incoming wind, and instead exhaust wind from the RNA to emulate a precompiled thrust time series. This is of course not an optimal approach for final design since it neglects some properties of the spinning turbine, e.g. the gyroscopic effect. Still this method is expected to be useful for testing more designs at an early stage, at wave basins without wind field generation capabilities, at expectedly lower costs. In the following a system able to emulate the wind turbine thrust loads is presented and evaluated. Additional information can be found in paper [G]. Later the floating performance of the system presented in paper [H] will be summarized.

### Fixed Evaluation of Concept

Figure 3.24 depicts a sketch of the setup constructed and tested. The Brushless DC (BLDC) motor is scaled to match the thrust forces experienced of a 1:80 scale of the 5 MW reference turbine proposed by NREL [Jonkman et al., 2009].

Besides the motor, the nacelle houses an Electronic Speed Controller (ESC) and an Arduino Uno microcontroller. The Arduino receives a serial signal via USB and translates it into a Pulse-Width Modulation (PWM) servo signal for the ESC, which in turn controls the BLDC. This means that only DC power and a single USB cable is running internally inside the tower and hence not inhibit structural behavior in the same way a thick cable bundle hanging off the RNA would. This is a secondary effect in the fixed setup, but can be significant when the system is incorporated as a part of a floating test setup. The physical model of the RNA and load cell test rig can be seen in figure 3.25.

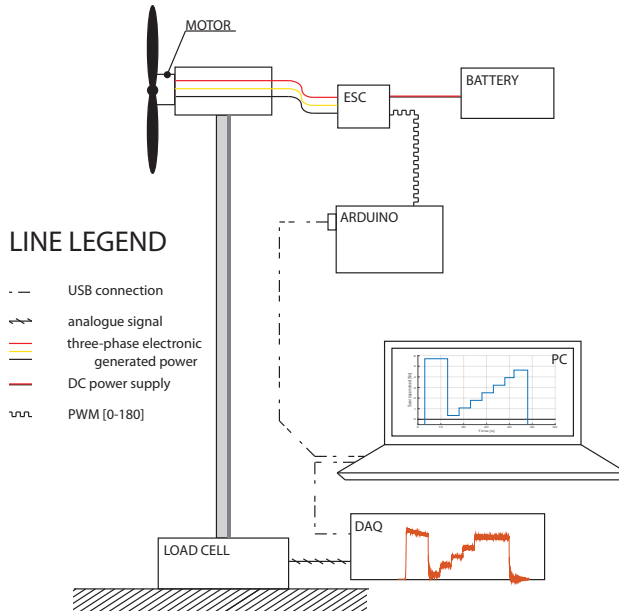
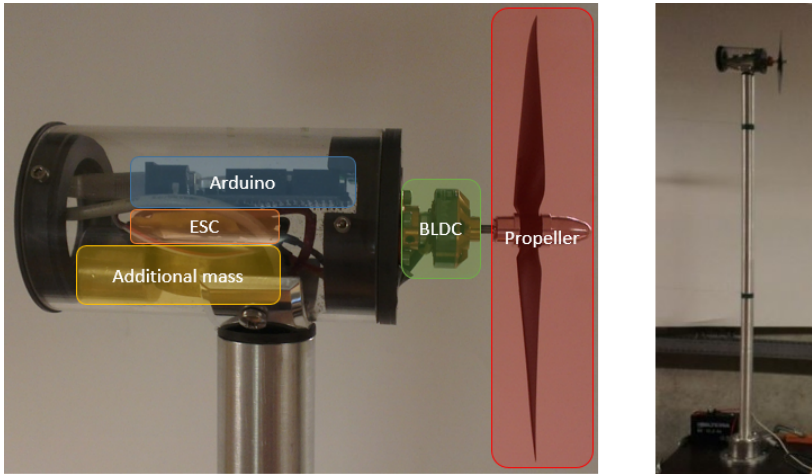


Fig. 3.24: Conceptual sketch of the thrust emulation system [G]

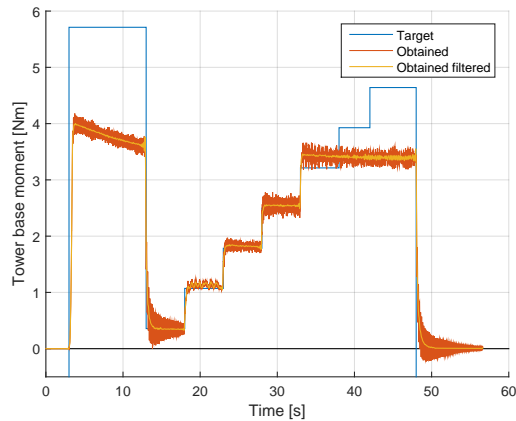
Since the tower bottom is the linking joint between the wind turbine and the platform, all loads are assessed at this point. This has been done in an effort to include the tower dynamics in the pre-simulated time series, and hence also being able to adopt the tower base node as the load and motion transferring joint between the wind turbine dynamics and the floating platform dynamics. Precompiled load time series have been scaled down to model scale and used to calibrate the real-time serial control signals used to adjust the fan thrust via the load data from the 6-axis load cell acting as the tower base mount. Figure 3.26 shows a step-function used for calibration as well as assessing the responsiveness of the system. Satisfactory performance is seen in the range of interest - the higher load range is intentionally outside the fan thrust potential to establish and document this limitation.

When the calibration is concluded, proper load time series of the tower base bending moment caused by the aerodynamic thrust can be simulated in FAST. Figure 3.27 shows the comparison between the prescribed pre-simulated load time series and the one captured in the test rig. The load history is from a 5 MW NREL reference wind turbine in 18 m/s turbulent winds [Jonkman et al., 2009]. Main load characteristics is reproduced well, but the require-



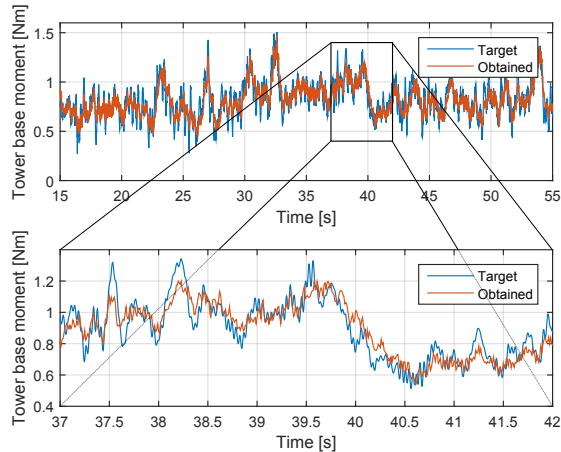


**Fig. 3.25:** Left: Physical content of the RNA. Right: Test rig setup with RNA and tower placed atop multi-axis load cell [G]



**Fig. 3.26:** Loads time series used for calibration [G]

ment of the speed up and down of the fan limits the high frequency content and any abrupt load changes.



**Fig. 3.27:** Time series comparison between requested and obtained tower base moments by use of thrust emulation setup [G]

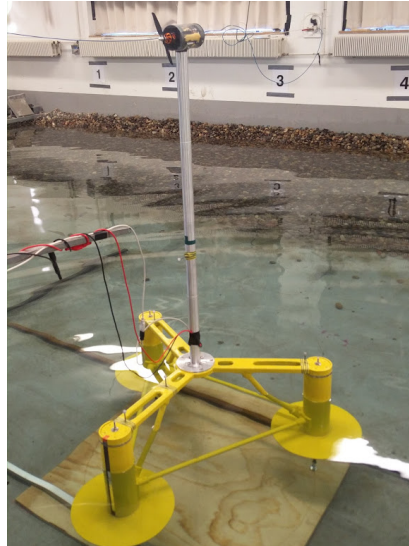
The thrust emulation system that has been constructed is capable of reproducing loads at the tower base comparable to those experienced by a scaled 5 MW NREL wind turbine. The small scale of 1:80 limits the accuracy of the fan thrust emulation setup due to the fact that time scale is compressed by approximately a factor 9, making it harder for the system to properly respond to high frequent and turbulent loads.

### Floating Application of Concept

The primary application of the thrust emulation system is on model tests of scaled FOWTs. This has been done in paper [H], where a 1:80 scaled foundation was tested in the wave basin. The foundation utilized taut but compliant mooring to get a simple mooring response, and was positioned in what would at full scale correspond to 50 m of water.

Figure 3.28 shows the setup from the wave basin. The body motions was assumed to be rigid and was captured by infra-red optical tracking. For comparison with the experimental data a 3 DoF (surge/heave/pitch) numerical model was constructed. This model was made with hybrid modeling of the hydrodynamic properties, and since tuned to the experimental free decay

tests by augmenting linear stiffness as well as linear and quadratic damping.



**Fig. 3.28:** Floating configuration used for testing the performance of the fan emulated aerodynamic loading on a floating foundation [H]

Initially both wind and wave loads were investigated as exemplified in Figure 3.29. Since the thrust emulation system was the aim of the investigation the combined tests were discarded with the aim of isolation the effects of wind loading. The strong coupling between the different DoF made this a necessity, but of course these combined load cases should be investigated once the thrust emulation is better understood and more established.

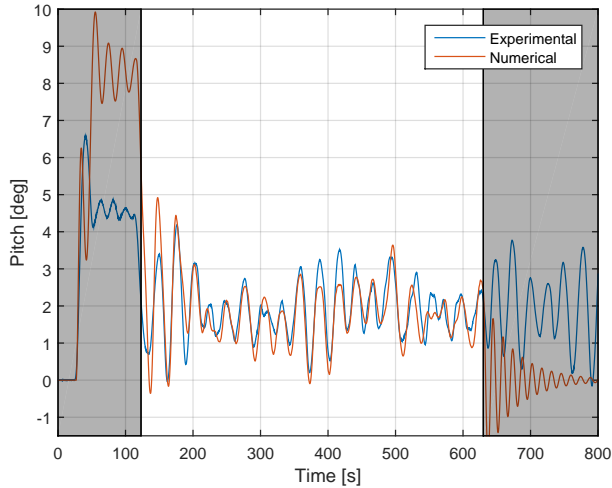
Since the pitch motion is the one primarily excited by the wind thrust this was chosen as the focus of the comparison. Load cases from both constant and turbulent winds were tested, see paper [H]. Figure 3.30 shows the recorded pitch of the physical model tests compared to the simulated pitch of the numerical model. The greyed out regions in the start and end of the comparison indicates areas where the comparison is not expected to match. In the first part the physical limitations of the fan system hinders the high loads requested. These high loads are requested in order to heat of the motor and are of course seen in the non-limited numerical model. In the last part of the simulation another discrepancy is seen. This is due to the fact that the load signal in the experiment was repeated, which was not the case for the numerical model and hence this returns to the equilibrium of  $0^\circ$  pitch. In the



Fig. 3.29: Floating foundation under combined wind and wave loads

middle part of the comparison a good similarity is seen between the experiments and the numerical simulations.

The good fit between the models is encouraging in terms of further investigation of the thrust emulation system. Though the quality of the fit rapidly degenerates when the load cases are dominated by high-frequency components. A more elaborate and stable calibration of the entire load emulation system would also be beneficial since both pre- and post-simulation calibration is needed for the current generation of the thrust emulation system. A revised version would be recommended to incorporate a tachometer to be able to use the fan RPM for load calibration. This would increase the stability and reproducibility of the system at the expense of a minor addition in the build complexity. The investigation shows that the system, either in its current state or in an updated version, can be applied to scaled models test where non-tactile loading is desired, and do so with good accuracy with the physical limitations of the system configuration.



**Fig. 3.30:** Time domain comparison between the physical and numerical models. The greyed out areas include expected discrepancies due to physical limitations [H]

### 3.4 Contextual Topics

While the previous sections all have addressed different topics of the technical recommendations listed in 2.3.2, work has also been performed in the more contextual, economic realm. Paper [D] discusses the current ways of supporting immature energy technologies such as FOWTs. While the wind turbine as such is a well investigated and thoroughly understood energy system, a wind turbine on a floating foundation is not. As an example it is to be expected that the control strategy of a floating turbine differs from the one of a bottom-fixed.

Current public subsidies often fall into one of two categories; One-time support, or feed-in tariffs. For wind turbines the latter is widely adopted. This means that the scale of the feed-in is a crucial part of the total wind project economy. The proposed Incentive-based Financial Support (IFS) scheme allows for public funding of energy concepts of a politically pre-determined amount, without having the subsidy being linearly proportional to the produced electricity.

The IFS excels in providing incentive for technology improvements, and hence might not be optimal for some well developed pre-commercial wind

energy projects. Still the concept of incentivizing production optimization over the first years of a project, might allow for less mature concepts to try out more exotic prototypes, e.g. vertical axis turbines or multi-rotor designs.

---

## 4 | Conclusion

It is evident that the world has a growing need for energy. At the same time it is also clear that this need can not be supplied solely by fossil fuels due to the finite amount available as well as the political/ethical implications such as pollution.

As shown the renewable energy sector has seen tremendous growth over the later years. One of the front runners has been the wind energy industry. Due to limited access to suitable areas on land the wind energy have moved into the open seas. Here the industry has struck a balance between the extract costs of operation offshore, and in turn harnessing a stronger and more stable wind resource. In an European context these suitable shallow water locations have limited the development of offshore to mainly north inhabit the North Sea.

To facilitate the access to clean wind energy across more coastal countries around the globe, development have gone into designing floating platform concepts for offshore wind turbines. These concepts have to a large extent inherited their design philosophies from the offshore oil and gas sector, summarized in three main categories: The spar buoy, the semi-submersible platform and the tension-leg platform. Since the first offshore deployed 80 kW floating turbine in 2008, the industry has gained enormous momentum and are now deploying pilot parks of multi-MW scale. This has only been possible by the means of massive public and private support in the improvements of modeling tools, enabling designers to continually optimize concepts and hereby lower the cost pr. installed MW.

The industry seems to have passed the infant stage where massive design alterations can drastically lower capital or operational expenditures. The current adolescent stage proposes that future cost saving needs to be found in fine-tuning well known concepts. This can only be done by de-risking designs

by means of creating and extending numerical tools to be able to capture and describe more physical phenomena with continued higher accuracy. These numerical models still rely heavily on scaled experimental model data, but hopefully the first generation of deployed offshore prototypes will provide even higher fidelity data for model validation.

The present work have presented efforts done in order to increase the already vast body of knowledge about modeling of floating offshore wind turbines. Fidelity of laboratory data used for numerical model calibration of hydrodynamic loads have been presented. Means of experimentally applying aerodynamic thrust loads at wave basin facilities without wind generation capabilities is shown, in the hopes that it will enable further access to model testing for less mature concepts.

It is evident from the present work that it, as expected, is difficult to pin point a single critical weak spot of the design of floating wind turbines. Instead, the target of greater design reliability and lower total cost can only be obtained by optimizing the vast amount of methods and sub-procedures used to describe such a complex dynamic structure. Though some concepts have reached early maturity, the battle for reaching these goals have only just been started. The renowned numerical tool FAST have recently obtained the capability of more complex and higher fidelity mooring design. The new features cover dynamic mooring analysis and multi-segmented mooring design. These new features have been verified and validation against state of the art experimental data and specialized industry leading mooring software, and very good accuracy has been found.

The future of floating offshore wind turbines still depend heavily on subsidies. The success of the industry relies on the momentum of design and deployment of full scale turbines going. Hopefully the improves made to numerical tools and testing facilities, made jointly by the industry and academia, can assist this process.



# References

- [Andersen and Ferri, 2014] Andersen, M. T. and Ferri, F. (2014). "Laboratory Testing and Energy Production of Scale 1: 35 Sigma Energy WEC".
- [Andersen and Ferri, 2016a] Andersen, M. T. and Ferri, F. (2016a). Draft paper: "Fan Actuated Loading on Scaled Floating Offshore Wind Turbines". *To be submitted to: Journal of Marine Science and Engineering (ISSN 2077-1312)*.
- [Andersen and Ferri, 2016b] Andersen, M. T. and Ferri, F. (2016b). "Practical Low Cost Aerodynamic Thrust Emulation for Froude Scaled Wind Turbines". *Springer: Experimental Techniques*.
- [Andersen and Frigaard, 2015] Andersen, M. T. and Frigaard, P. B. (2015). "Incentive-based Financial Support Scheme for Immature Renewable Energy Systems". In *Proceedings of the 11th European Wave and Tidal Energy Conference*. Technical Committee of the European Wave and Tidal Energy Conference.
- [Andersen et al., 2015] Andersen, M. T., Hindhede, D., and Lauridsen, J. (2015). "Influence of Model Simplifications Excitation Force in Surge for a Floating Foundation for Offshore Wind Turbines". *Energies*, 8(4):3212.
- [Andersen and Nielsen, 2015] Andersen, M. T. and Nielsen, S. R. K. (2015). "Hydrodynamic Excitation Forces on Floating Structures with Finite Displacements". In *Proceedings of the Twenty-fifth (2015) International Ocean and Polar Engineering Conference*. International Society of Offshore & Polar Engineers.
- [Andersen and Thomsen, 2016] Andersen, M. T. and Thomsen, J. B. (2016). "The Inter Facility Testing of a Standard Oscillating Water Column (OWC) Type Wave Energy Converter (WEC)".
- [Andersen et al., 2016] Andersen, M. T., Wendt, F., Robertson, A. N., and Jonkman, J. M. (2016). "Verification and Validation of Multisegmented Mooring Capabilities in FAST v8". In *The Twenty-sixth International Offshore and Polar Engineering Conference, Rhodes, Greece*. ISOPE.

- [Ardakani and Bridges, 2011] Ardakani, H. A. and Bridges, T. J. (2011). Shallow-water sloshing in vessels undergoing prescribed rigid-body motion in three dimensions. *Journal of Fluid Mechanics*, 667:474–519.
- [Athanasia and Genachte, 2013] Athanasia, A. and Genachte, A. B. (2013). Deep offshore and new foundation concepts. *Energy Procedia*, 35:198–209.
- [Babarit and Delhommeau, 2015] Babarit, A. and Delhommeau, G. (2015). Theoretical and numerical aspects of the open source bem solver nemoh. In *11th European Wave and Tidal Energy Conference (EWTEC2015)*.
- [Bae, 2016] Bae, Y. H. (2016). Development of a dynamic mooring module feam for fast v8. <https://nwtc.nrel.gov/FEAMooring>. Accessed: 2016-07-13.
- [Bjerkseter and Ågotnes, 2013] Bjerkseter, C. and Ågotnes, A. (2013). Levelised costs of energy for offshore floating wind turbine concepts.
- [Blue H, 2016] Blue H (2016). Historical development. <http://www.blueengineering.com>. Accessed: 2016-06-09.
- [Browning et al., 2014] Browning, J., Jonkman, J., Robertson, A., and Goupee, A. (2014). "Calibration and Validation of a Spar-Type Floating Offshore Wind Turbine Model Using the FAST Dynamic Simulation Tool". In *Journal of Physics: Conference Series*, volume 555, page 012015. IOP Publishing.
- [Butterfield et al., 2007] Butterfield, C. P., Musial, W., Jonkman, J., Scлавounos, P., and Wayman, L. (2007). *Engineering challenges for floating offshore wind turbines*. Citeseer.
- [Carbon Trust, 2015] Carbon Trust (2015). Floating Offshore Wind: Market and Technology Review. Technical report, Prepared for the Scottish Government.
- [Coulling et al., 2013] Coulling, A., Goupee, A., Robertson, A., Jonkman, J., and Dagher, H. (2013). "Validation of a FAST Floating Wind Turbine Model Using Data from the DeepCwind Semi-Submersible Model Tests". In *WIND-POWER 2013 Conf and Exhib, Chicago, IL*. AWEA.
- [Cummins, 1962] Cummins, W. (1962). The impulse response function and ship motions. Technical report, DTIC Document.
- [DNV GL, 2016] DNV GL (2016). Electrifying the future - third generation windpower. <https://www.dnvgl.com/technology-innovation/broader-view/electrifying-the-future/third-generation-wind-power.html>. Accessed: 2016-05-27.

- 
- [Ebenhoch et al., 2015] Ebenhoch, R., Matha, D., Marathe, S., Muñoz, P. C., and Molins, C. (2015). Comparative levelized cost of energy analysis. *Energy Procedia*, 80:108–122.
- [EMODnet, 2016] EMODnet (2016). European marine observing and data network - portal for bathymetry. <http://www.emodnet-bathymetry.eu>. Accessed: 2016-05-30.
- [EWEA, 2009] EWEA (2009). *Wind Energy - The Facts: a guide to the technology, economics and future of wind power*. Earthscan.
- [EWEA, 2013] EWEA (2013). Deep Water - The next step for offshore wind energy. Technical report, The European Wind Energy Association. ISBN: 978-2-930670-04-1.
- [EWEA, 2016a] EWEA (2016a). The European Offshore Wind Industry - Key trends and statistics 2015. Technical report, The European Wind Energy Association.
- [EWEA, 2016b] EWEA (2016b). Wind in Power - 2015 European statistics. Technical report, The European Wind Energy Association.
- [Falnes, 2002] Falnes, J. (2002). *Ocean waves and oscillating systems: linear interactions including wave-energy extraction*. Cambridge university press.
- [Floating Power Plant, 2016] Floating Power Plant (2016). The P37 Research and Demonstration Platform. <http://www.floatingpowerplant.com/>. Accessed: 2016-06-13.
- [Fox Oil Drilling Company, 2016] Fox Oil Drilling Company (2016). Drilling photos. <http://www.foxoildrilling.com/drilling-photos.html>. Accessed: 2016-06-09.
- [Fukushima OWC, 2016] Fukushima OWC (2016). Fukushima FORWARD. <http://www.fukushima-forward.jp/>. Accessed: 2016-06-13.
- [Hall, 2015] Hall, M. (2015). *"MoorDyn Users's Guide"*. Orono, ME: Department of Mechanical Engineering, University of Maine.
- [Hall and Goupee, 2015] Hall, M. and Goupee, A. (2015). "Validation of a Lumped-Mass Mooring Line Model with DeepCwind Semisubmersible Model Test Data". In *Ocean Engineering vol.104* 590-603.
- [Heronemus, 1972] Heronemus, W. E. (1972). *Pollution-Free energy from the offshore winds*. Marine Technology Society.

- [Ideol, 2016] Ideol (2016). Offshore Floating Wind. <http://ideol-offshore.com/>. Accessed: 2016-06-13.
- [International Energy Agency, 2015] International Energy Agency (2015). World energy outlook 2015 factsheet - global energy trends to 2040. [http://www.worldenergyoutlook.org/media/weowebiste/2015/WE02015\\_Factsheets.pdf](http://www.worldenergyoutlook.org/media/weowebiste/2015/WE02015_Factsheets.pdf). Accessed: 2016-06-06.
- [Jonkman et al., 2009] Jonkman, J., Butterfield, S., Musial, W., and Scott, G. (2009). Definition of a 5-mw reference wind turbine for offshore system development. *National Renewable Energy Laboratory, Golden, CO, Technical Report No. NREL/TP-500-38060*.
- [Jonkman, 2013] Jonkman, J. M. (2013). The new modularization framework for the fast wind turbine cae tool. In *51st AIAA Aerospace Sciences Meeting and 31st ASME Wind Energy Symposium, Grapevine, Texas*.
- [Jonkman and Buhl Jr, 2005] Jonkman, J. M. and Buhl Jr, M. L. (2005). Fast user's guide. *National Renewable Energy Laboratory, Golden, CO, Technical Report No. NREL/EL-500-38230*.
- [Kramer et al., 2015] Kramer, M. M., Pecher, A. F. S., Guaraldi, I., Andersen, M. T., and Kofoed, J. P. (2015). "Hydraulic Evaluation of Joltech's GyroPTO for Wave Energy Applications".
- [Lee and Newman, 2006] Lee, C.-H. and Newman, J. N. (2006). Wamit user manual. *WAMIT, Inc.*
- [LLNL, 2016] LLNL (2016). Lawrence Livermore National Laboratory - Energy Flow Charts. <https://flowcharts.llnl.gov>. Accessed: 2016-05-25.
- [MacKay, 2008] MacKay, D. (2008). *Sustainable Energy-without the hot air*. UIT Cambridge.
- [Myhr et al., 2014] Myhr, A., Bjerkseter, C., Ågotnes, A., and Nygaard, T. A. (2014). Levelised cost of energy for offshore floating wind turbines in a life cycle perspective. *Renewable Energy*, 66:714–728.
- [OECD Observer, 2012] OECD Observer (2012). An emerging middle class. [http://www.oecdobserver.org/news/fullstory.php/aid/3681/An\\_emerging\\_middle\\_class.html](http://www.oecdobserver.org/news/fullstory.php/aid/3681/An_emerging_middle_class.html). Accessed: 2016-06-06.
- [OrcaFlex, 2016a] OrcaFlex (2016a). <http://www.orcina.com/SoftwareProducts/OrcaFlex/>. Accessed: 2016-05-19.

- [OrcaFlex, 2016b] OrcaFlex (2016b). Orcaflex validation. <http://www.orcina.com/SoftwareProducts/OrcaFlex/Validation/index.php>. Accessed: 2016-05-19.
- [Principle Power, 2016] Principle Power (2016). Wind Float. <http://www.principlepowerinc.com/>. Accessed: 2016-06-13.
- [Prowell et al., 2013] Prowell, I., Robertson, A., Jonkman, J., Stewart, G., and Goupee, A. (2013). "Numerical Prediction of Experimentally Observed Scale-Model Behavior of an Offshore Wind Turbine Supported by a Tension-Leg Platform". In *Proc Offshore Technology Conf. OTC*.
- [Puche, 2014] Puche, F. V. (2014). Semi-submersible topside conceptual design: Transition piece.
- [Quallen et al., 2013] Quallen, S., Xing, T., Carrica, P., Li, Y., Xu, J., et al. (2013). Cfd simulation of a floating offshore wind turbine system using a quasi-static crowfoot mooring-line model. In *The Twenty-third International Offshore and Polar Engineering Conference*. International Society of Offshore and Polar Engineers.
- [Robertson et al., 2012] Robertson, A., Jonkman, J., Masciola, M., Song, H., Goupee, A., Coulling, A., and Luan, C. (2012). Definition of the semisubmersible floating system for phase ii of oc4. *Offshore Code Comparison Collaboration Continuation (OC4) for IEA Task*, 30.
- [Robertson et al., 2013] Robertson, A. N., Jonkman, J. M., Goupee, A. J., Coulling, A. J., Prowell, I., Browning, J., Masciola, M. D., and Molta, P. (2013). Summary of conclusions and recommendations drawn from the deepwind scaled floating offshore wind system test campaign. In *ASME 2013 32nd International Conference on Ocean, Offshore and Arctic Engineering*, pages V008T09A053–V008T09A053. American Society of Mechanical Engineers.
- [Shell, 2010] Shell (2010). Perdido overview. <http://www.shell.com/about-us/major-projects/perdido/perdido-an-overview.html>. Accessed: 2016-06-09.
- [Statoil, 2012] Statoil (2012). Hywind - the floating wind turbine. [http://www.statoil.com/en/TechnologyInnovation/NewEnergy/RenewablePowerProduction/Offshore/Hywind/Downloads/Hywind\\_nov\\_2012.pdf](http://www.statoil.com/en/TechnologyInnovation/NewEnergy/RenewablePowerProduction/Offshore/Hywind/Downloads/Hywind_nov_2012.pdf). Accessed: 2016-06-13.
- [Statoil, 2016] Statoil (2016). Hywind scotland pilot park. <http://www.statoil.com/en/TechnologyInnovation/NewEnergy/RenewablePowerProduction/Offshore/HywindScotland/>. Accessed: 2016-06-13.

- [Sway, 2016] Sway (2016). Concept. <http://www.sway.no>. Accessed: 2016-06-13.
- [UMaine, 2016] UMaine (2016). VoltrunsUS 1:8. <https://composites.umaine.edu/our-research/volturnus/>. Accessed: 2016-06-13.
- [Wehmeyer et al., 2014] Wehmeyer, C., Ferri, F., Andersen, M. T., and Pedersen, R. R. (2014). "Hybrid Model Representation of a TLP Including Flexible Toppides in Non-Linear Regular Waves". *Energies*, 7(8):5047.
- [Wendt et al., 2016] Wendt, F., Andersen, M. T., Robertson, A. N., and Jonkman, J. M. (2016). "Verification and Validation of the New Dynamic Mooring Modules Available in FAST v8". In *The Twenty-sixth International Offshore and Polar Engineering Conference, Rhodes, Greece*. ISOPE.

---

# Paper A

## Hybrid Model Representation of a TLP Including Flexible Topsides in Non-Linear Regular Waves

Christof Wehmeyer  
Francesco Ferri  
Morten Thøtt Andersen  
Ronnie Refstrup Pedersen

The paper has been published in  
*Energies*, 7(8):5047, 2014.





Article

## Hybrid Model Representation of a TLP Including Flexible Topsides in Non-Linear Regular Waves

Christof Wehmeyer <sup>1,\*</sup>, Francesco Ferri <sup>2</sup>, Morten Thøtt Andersen <sup>2</sup> and Ronnie Refstrup Pedersen <sup>1</sup>

<sup>1</sup> Rambøll Offshore Wind, Esbjerg 6700, Denmark; E-Mail: rrp@ramboll.com

<sup>2</sup> Department of Civil Engineering, Aalborg University, Sohngaardsholmsvej 57, Aalborg 9000, Denmark; E-Mails: ff@civil.aau.dk (F.F.); mta@civil.aau.dk (M.T.A.)

\* Author to whom correspondence should be addressed; E-Mail: CFW@ramboll.com; Tel.: +45-516-170-36.

Received: 23 May 2014; in revised form 2 July 2014 / Accepted: 7 July 2014 /

Published: xx

**Abstract:** The rising demand for renewable energy solutions is forcing the established industries to expand and continue evolving. For the wind energy sector, the vast resources in deep sea locations have encouraged research towards the installation of turbines in deeper waters. One of the most promising technologies able to solve this challenge is the floating wind turbine foundation. For the ultimate limit state, where higher order wave loads have a significant influence, a design tool that couples non-linear excitations with structural dynamics is required. To properly describe the behavior of such a structure, a numerical model is proposed and validated by physical test results. The model is applied to a case study of a tension leg platform with a flexible topside mimicking the tower and a lumped mass mimicking the rotor-nacelle assembly. The model is additionally compared to current commercial software, where the need for the coupled higher order dynamics proposed in this paper becomes evident.

**Keywords:** floating wind turbine; TLP; non-linear wave; physical model test; ultimate limit state wave load

### 1. Introduction

The Horizon2020 call [1] of the EU states explicitly that innovative substructure concepts, including floating platforms, are needed for water depths beyond 50 m, in order to push the development of

competitive low carbon energy generation. One focus is to reduce the overall project risks. However, such project risks can only be accounted for or avoided if known and if their impact can be assessed by applicable tools. Conventional tools used in the oil and gas (O&G) industry for the assessment of the extreme event response of floating structures neglect two important aspects, making them non-conservative when used for floating offshore wind turbines (FOWT). Considering that the offshore wind industry intends to install floating structures at a much shallower water depth than the offshore O&G industry, *i.e.*, in the order of 50 m, a first or second order wave theory approach might not be sufficient to describe realistic wave shapes. Therefore, a higher order wave theory seems necessary. Furthermore, wind turbines are dynamically sensitive structures. Even while the floating part can be considered more or less rigid, the flexibility of the slender tower supporting a heavy rotor-nacelle assembly (RNA) influences the structure's response significantly. The significance of this is highlighted in the recently released DNV offshore standard, J103 [2], for the design of floating wind turbine structures, which specifically addresses the importance of the flexibility of the tower for the correct simulation of pitch and roll motions. The relation between tower flexibility and response amplitude operator (RAO) shift has been pointed out by Matha [3] in recent years. A numerical model of a tension leg platform (TLP) was compared against measured responses from tests carried out within the DeepCwind framework in [4]. Besides decay tests and wind wave loading, their TLP was exposed to a number of regular waves. The software, as well as the tests considered linear waves, and a reasonable agreement was found. A numerical comparison to the physical model tests of the DeepCwind TLP was performed in [5]. An underestimation of the spectral amplitudes around the natural pitch frequency in regular waves without wind was found. It was suggested that this might be due to the harmonics in the physical wave realization coinciding with the pitch natural frequency. The current work investigates if it is possible to consider these effects by including the viscous wave excitation from higher wave harmonics for the surface-piercing, drag-dominated structural part.

In summary, the current work assesses how well a hybrid model, consisting of a linear potential theory wave excitation and viscous force non-linear wave excitation, can predict key parameters of an FOWT in intermediate water depths. Such environments are common in ultimate limit state analysis (ULS), and often, wave shapes deviate from the first or second order description. As this violates the linear theory, the hybrid model is, in the current work, compared to observations from wave-tank tests. The general problem was two-fold; the hybrid model should be able to simulate the behavior of a tethered floater exposed to non-linear waves, while also accommodating the influences of non-rigid topsides. The hybrid model is an extendable research tool forming the basis of an in-house development. Further benchmarking against available tools at a later stage is planned. It is essential to note that the work is not a design verification, but a tool validation. Even though the full tendon length could be modeled due to a deep section in the wave basin, the structure originally designed for a 100-m water depth was exposed to waves generated in approximately a 60-m water depth. This caused the waves to become non-linear and, hence, allowed the assessment of the performance of a hybrid model, including non-linear viscous wave force excitation.

## 2. Methods

The scope of this section is to detail the assumptions and methodologies used throughout the work. The objective of this study is to implement a numerical model of a floating wind turbine mounted on an industry-inspired TLP. The numerical model will be exposed to regular, non-linear extreme waves representing ultimate limit state (ULS) conditions. DNV J103 [2] suggests this option to assess the behavior of an offshore wind turbine structure in design conditions. The numerical model will then be validated against experimental tests. The tests were conducted in the 3D wave basin at Aalborg University on a 1:80 scale model; see Figure 1. A detailed description of the set-up and results can be found in [6].

**Figure 1.** The physical model of the floating offshore wind turbine (FOWT) tension leg platform (TLP).

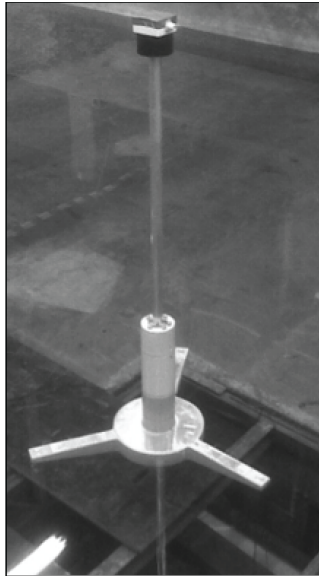
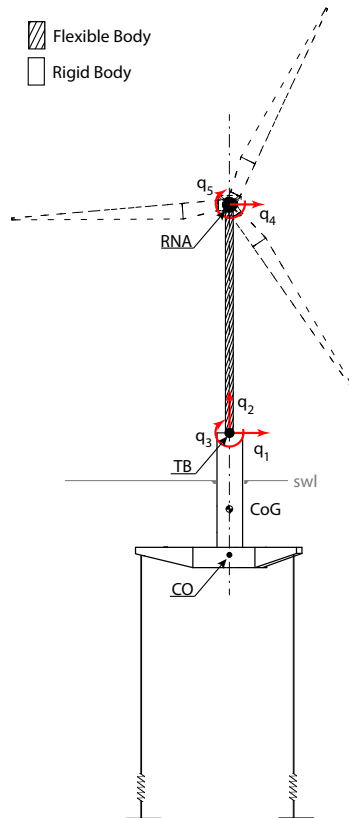


Figure 2 shows a sketch of the system under investigation, where the main elements are the TLP substructure (with the associated station-keeping system), the tower and the RNA.  $q$  is the 5 degrees of freedom (DOF) displacement vector, and  $q_1$  and  $q_2$  are the surge and heave motion of the structure, pointing in positive  $x$  and  $z$ , respectively. TB is the tower bottom, *i.e.*, the connection point between tower and substructure. swl is the still water line. CoG is the center of gravity of the TLP. CO is the elevation of the mooring attachment point projected onto the centerline of the structure.

**Figure 2.** Definition of the system's DOFs and key points. RNA, rotor-nacelle assembly; TB, tower bottom; swl, still water line.



Although both wave and wind loads excite the motion of the structure, the current validation focuses on the hydrodynamic response only. It is important to note that in actual ULS conditions, the wind load on the tower, as well as on the blades can become important during fault conditions.

Considering the construction method of the floater [6], it seems sensible to assume it to be rigid. However, as already mentioned in the previous section, the influence of tower flexibility on the dynamic response of the total structure cannot be neglected [3]. Therefore, the substructure model will be coupled with a flexible beam element connecting the RNA to the rigid substructure.

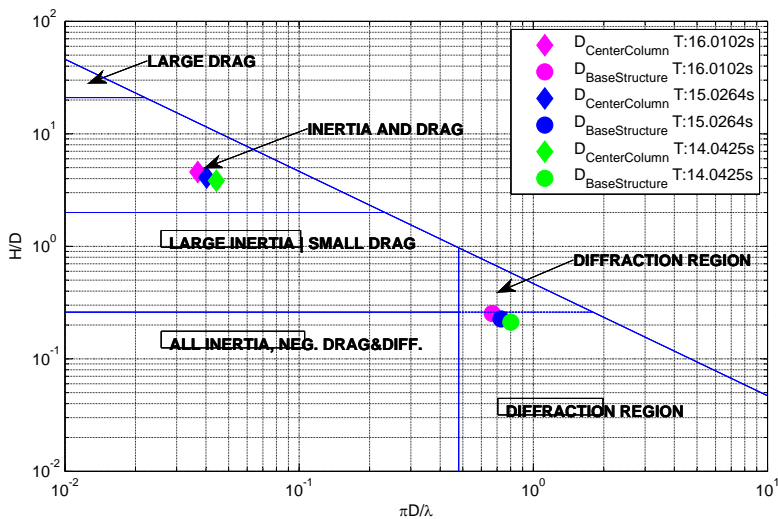
The substructure has trilateral symmetry about a vertical axis passing through its center. The dynamic response is studied in long crested, *i.e.*, 2D, incident waves, as has been done in the physical model test. The simplified model and the definition of the relative coordinate system are represented in Figure 2.

2.1. Numerical Model of the Substructure

The model will be based on a boundary integral equation method (BIEM) solution with additional hydrodynamic viscous drag terms according to Morison’s equation. This approach is believed to be more time efficient than complex numerical techniques, e.g., computational fluid dynamics. The need for an extra dissipative term related to viscous effects in the boundary layer is supported by the results of a non-dimensional analysis of the structure. Figure 3 shows that, based on the non-dimensional ratio between inertial and viscous loads, the flow regime changes along the vertical axis of the structure, and consequently, the use of BIEM plus a viscous drag term becomes necessary. Hence, the wave-body interaction is decomposed into four contributions:

- Wave excitation force: BIEM;
- Viscous drag forces;
- Radiation force;
- Hydrostatic force.

Figure 3. Non-dimensional ratios of inertial and viscous loads for dominating structural parts [7].



2.1.1. Wave Excitation Forces from Potential Flow

Wave excitation forces ( $F_{ex}$ ) are defined as the loads exerted on a submerged structure held in equilibrium position in waves.

The total excitation forces are expressed as a summation of the Froude–Krylov forces ( $F_K^i$ ) and the diffraction forces ( $F_D^i$ ). The index  $i$  represents the  $i$ -th degree of freedom. The Froude–Krylov forces are due to the undisturbed incident waves, while the diffraction forces are related to the modified wave

field generated by the structure. The forces are obtained from the integration of the linearized dynamic pressure distribution over the mean wetted surface. The complex frequency coefficients, describing the summation of those two forces, are obtained from the solution of the boundary integral equation problem using the commercial software, ANSYS AQWA [8]. The wave excitation force vector ( $F_{ex}$ ) is assessed in the time domain by convolution of the non-causal impulse response function (IRF) with the surface elevation time series for each DOF.

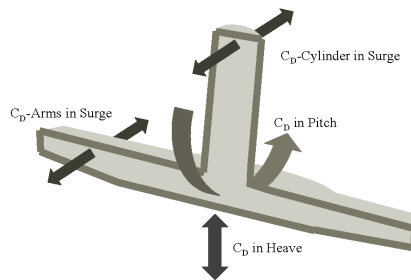
### 2.1.2. Viscous Drag Forces

Viscous energy dissipation, *i.e.*, flow separation, is likely to influence the motion of the system, due to the different flow regimes along the structure. This can be seen as an additional excitation force, as the wave particle velocity is likely to be higher than the body velocity, especially for the surface piercing part. The  $i$ -th viscous drag force ( $F_d^i$ ) used in the model is defined in Equation (1), where  $i$  refers to the drag force component, as shown in Figure 4.

$$F_d^i = -\frac{1}{2}\rho C_D^i A^i |u^i - u_0^i| (u^i - u_0^i) \quad (1)$$

where  $\rho$  is the water density,  $C_D$  is the drag coefficient,  $A$  is the cross-sectional strip area of the body, projected in a plane perpendicular to the velocity vector,  $u$  is the body velocity and  $u_0$  is the undisturbed particle velocity. The section-wise calculated drag force is integrated over the height and applied at the instantaneous force point of attack. As further explained in the Results section, the drag forces have been split into several contributions in order to account for the geometry changes.

**Figure 4.** Definition of the directions of drag coefficient application with respect to the structural cross-section.



### 2.1.3. Radiation Forces

The radiation force is the load exerted by the moving body in otherwise calm water. The total radiation load is composed of a part proportional to the acceleration of the body (added mass) and a part proportional to the velocity (radiation damping) of it. The time domain model is represented by the so-called fluid memory terms (IRF) and the matrix of added mass at infinite frequency. This term is related to the convergence of the integral, as detailed in [9]. Although the same convolution approach

can be used to evaluate the radiation force vector ( $F_{rad}$ ), it benefits the implementation to approximate the frequency response function by a system of first order ODEs. As presented in [9,10], a fifth or lower order system is enough to model a smooth response, as for the presented structure. The state space approximation of the radiation problem is obtained from a least squares fit of the radiation frequency response function. The freeware marine toolbox has been used for this purpose [10]. The selected model order is three.

#### 2.1.4. Hydrostatic Forces

The hydrostatic stiffness matrix of the rigid body is obtained from ANSYS AQWA.

#### 2.1.5. Numerical Model of the Station-Keeping System

A mooring system is required by every floating offshore structure for station-keeping purposes. Furthermore, for TLP-like structures, the mooring system compensates for the intrinsic instability of the system, providing a global positive restoring coefficient. For slender bodies, such as the tendons, it is possible to assume that the major load contributions come from stiffness along the axis of symmetry and from drag in the perpendicular direction. Nevertheless, due to the small cross-sectional area of the tendons used in the lab, it is possible to assume that their drag contribution is negligible, thus the mooring force reduces to a force proportional to the linear extension of the mooring cable. The mooring force  $F_m$  is detailed in the following equation:

$$F_{11} = PT + \left( \frac{3q_1}{LT} \sqrt{q_1^2 + LT^2} - LT \right) k \quad (2)$$

$$F_{22} = 3kq_2 \quad (3)$$

$$F_{33} = (kd_B^2 + 2kd_A^2)q_3 \quad (4)$$

$$F_{12} = \left( \sqrt{q_1^2 + LT^2} - LT \right) k \quad (5)$$

where  $F_{11}$ ,  $F_{22}$ ,  $F_{33}$  correspond to the uncoupled forces, given by a displacement in the relative DOF, while  $F_{12}$  is the heave mooring force induced by a displacement in surge.  $PT$  is the pretension at the equilibrium position;  $LT$  is the mooring cable length at the equilibrium position;  $k$  is the linear spring coefficient associated to the tendon's stiffness;  $d_B$  is the distance between bow fairlead and CO; and  $d_A$  is the distance between the port stern fairlead and CO projected in the xOz plane.

#### 2.1.6. Numerical Model of the Tower

In order to include the dynamic influence of a flexible tower into the model, a standard linear elastic Euler–Bernoulli beam element with four degrees of freedom ( $q_1$ ,  $q_3$ ,  $q_4$ ,  $q_5$ ) has been used, where the beam top end is connected to a lumped mass representing the RNA.

Only the first mode shape for each degree of freedom is used as a consequence of the ratio between lumped mass over beam mass. The resultant model of the tower has five DOFs: the surge ( $q_1$ ,  $q_4$ ) plus pitch ( $q_3$ ,  $q_5$ ) of the bottom and top, respectively, and a shared heave motion ( $q_2$ ); see Figure 2. Additionally, it is fully described by the mass and stiffness matrix. In addition to those matrices, a damping matrix is implemented to simulate the damping from the topside structure. Rayleigh damping

is used, and damping ratios are determined by decay tests. Definitions of the general mass, damping and stiffness matrices are given in [11], together with a comprehensive description of their derivation.

### 2.1.7. Combined Model

The above-mentioned loads are then assembled in a global system, where the equation of motion is given by:

$$M\ddot{q} = F_{rad} + F_m + F_{ex} + F_d + Kq \quad (6)$$

$M$  is the global mass matrix, combining the substructure mass matrix, the substructure added mass matrix and the topside mass matrix.  $K$  is the global stiffness matrix, combining the substructure hydrostatic stiffness matrix and the topside structural stiffness matrix.  $\ddot{q}$  is the acceleration vector and  $q$  the displacement vector.

The global mass and stiffness matrices are obtained from the summation of the sub-structure and tower matrices in the shared DOFs to ensure the dynamic coupling of the two bodies. The equation of motion is solved by the *ODE45* algorithm implemented in MATLAB [12].

### 2.2. Wave Model

In order to simulate ULS conditions, a proper wave model is needed. In deep water, the ULS waves can be represented with linear or non-linear waves of small order, such as first or second order Stokes waves. For severe waves in intermediate to shallow water, a higher order solution is needed. Based on the best fit with the experimentally observed wave shapes, a 30th order stream function wave theory is adopted [13]. Wave kinematics and surface elevations are obtained and subsequently applied in the hybrid model. Table 1 shows the applied regular wave parameters in the prototype scale.

**Table 1.** Wave parameters in the prototype scale.

Wave Parameters	Run 18	Run 17	Run 16
$H_{max}$ (m)	17.2	15.2	14.8
$T_{max}$ (s)	16.0	15.0	14.0

### 3. Results

The numerical results and their comparison with prior experimental measurements are presented in this section. In the first part, the model details are given. In the second part, the code-to-code and the code-to-experiment comparisons are presented. Three different stiffness set-ups of the hybrid model are used: very stiff, stiff and flexible; the first one is used in the code-to-code comparison and the other two in the code-to-experiment comparison. In both cases, the comparison is divided into two steps: first, the decay test response is presented, followed by the wave response in ULS conditions. The time series will have a predefined and constant color map:

- Red line: flexible model;
- Blue line: stiff model;



- Green line: very stiff/quasi-rigid model;
- Black line: reference signal (ANSYS AQWA and/or experimental results).

### 3.1. Parameters Definition

The prototype is a three-armed TLP structure, with an approximate total weight, including tower and turbine, of around 2,000 t, installed at a water depth of 100 m [6]. The topside mass is roughly 40% of the substructure mass. In order to include the viscous drag, it was assumed that four different viscous force contributions were sufficient. Figure 4 illustrates the idealized viscous drag contributions that are implemented in the model. These forces were included using the instantaneous relative velocities between body and water particle at specific locations. The  $C_D$  values for cylinders and for heave motions agree with common industry standards. For the heave motion, the obtained values were constant and were typical for separated flows at small  $KC$  numbers for angular parts [14]. Being a common practice in the offshore wind industry, the  $C_D$  values for the cylinder are calculated as a function of maximum undisturbed Reynolds number and maximum undisturbed  $KC$  number. More details can be found in [15].

Table 2 shows the applied drag coefficients. A  $KC$  relationship for the  $C_D$  in pitch was iteratively fitted and resulted in values similar to the ones in heave. The drag coefficient values for the projected area of the arms were iteratively fitted, as well. It is obvious that the  $C_D$  approximations for the lower part of the structure have been tailored to the structural layout and the respective assumptions. The estimated  $C_D$  value for the surface piercing cylinder in the surge direction, as well as the  $C_D$  in the heave and pitch direction agree well with values that can be found in the literature [14,16].

**Table 2.** Definition of applied drag coefficient values.

Direction	Structure part	$C_D$
Surge	Arms	1.1
Surge	Cylinder	1.8
Pitch	Base disc + arms	0.3 $KC$
Heave	Base disc + arms	3.3

### 3.2. Code-to-Code Validation

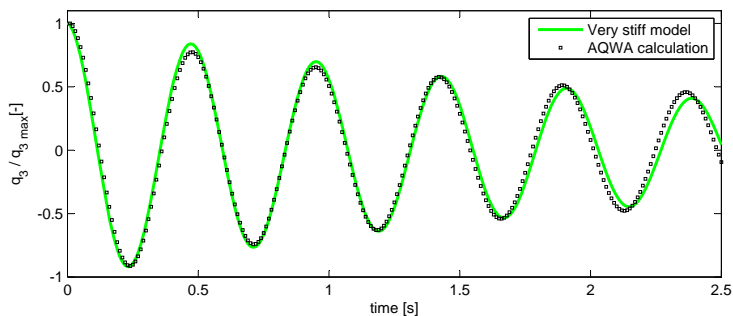
In order to validate the model, a code-to-code comparison with the commercial software, ANSYS AQWA, was carried out first. The results are presented hereafter for both the decay test and wave induced motion. The study focuses on the pitch response, being the one most affected by the tower flexibility, but results for the other DOFs are also presented in order to verify the response model. Since ANSYS AQWA models the entire structure as one rigid body, this can be used as a benchmark case to validate the hybrid model. In the hybrid model, the substructure is rigid, as well, and by applying a tower stiffness,  $EI$ , of orders of magnitude larger than the physical one, quasi-rigid body behavior is emulated.

*Energies* **2014**, *7*

### 3.2.1. Decay Test

Figure 5 shows the time series comparison between the rigid body response predicted by ANSYS AQWA and the hybrid model. The natural frequency of the rigid body motion predicted by the hybrid model is 2.05 Hz, where ANSYS AQWA predicts 2.10 Hz.

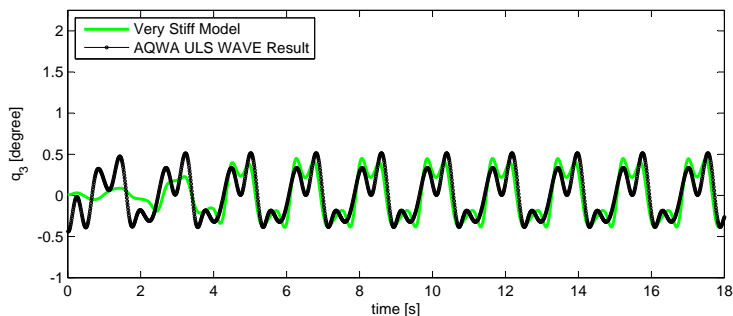
**Figure 5.** Code-to-code comparison between the hybrid model, including quasi-rigid topside layout pitch response and ANSYS AQWA pitch response in a decay test, normalized by the displacement in pitch at  $t = 0$ .



### 3.2.2. Regular Waves

A ULS design load case is generated with ANSYS AQWA, simulating rigid body behavior. The software generates second order regular Stoke waves. In order to mimic the physical test environment, the water depth matched the wave generation water depth in the wave tank, which, in turn, matched the water depth used in the numerical model for the generation of the stream function wave. Figure 6 shows the obtained results, and a good match is observed. The waves in the hybrid model are ramped for all cases, explaining the comparison convergence.

**Figure 6.** Code-to-code comparison between the hybrid model, including quasi-rigid topside layout pitch response and ANSYS AQWA pitch response under regular wave load conditions.



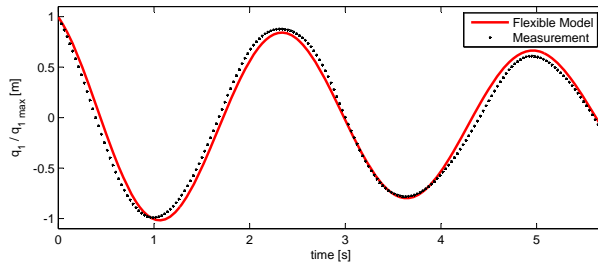
### 3.3. Physical Model Validation

Once a qualitative analysis of the hybrid model's capability was complete, the hybrid model was validated against experimental data. As previously mentioned, two different structural stiffness configurations form the basis of comparison, namely the stiff and flexible model [6]. The response will be evaluated in TB, as defined in Figure 2. TB has been selected as the point of comparison due to sensor location in the experimental setup. Consequently, only a single transformation from CoG to TB within the numerical model is required.

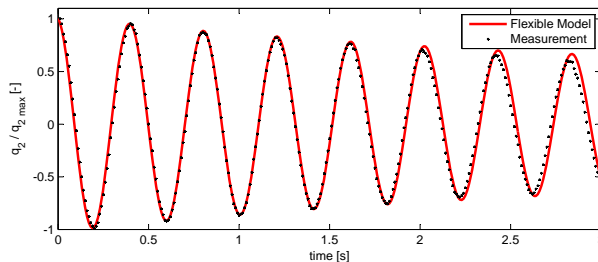
#### 3.3.1. Decay Test

The responses in surge and heave for the flexible tower system are shown in Figures 7 and 8, respectively. Figure 9 shows the pitch response comparison between flexible and rigid tower lay-outs, for both experimental and numerical models. Only the flexible model is used for the comparison of the decay in surge and heave, since the period in surge is orders of magnitude larger than that of the natural frequency of the tower bending mode, making the two models indistinguishable. This is also the case for the heave decay, since the axial stiffness of the tower is orders of magnitude higher than the vertical stiffness of the foundation and mooring.

**Figure 7.** Code-to-experiment comparison between the flexible hybrid model and experimental data in a surge decay test, normalized by the displacement in surge at  $t = 0$ .

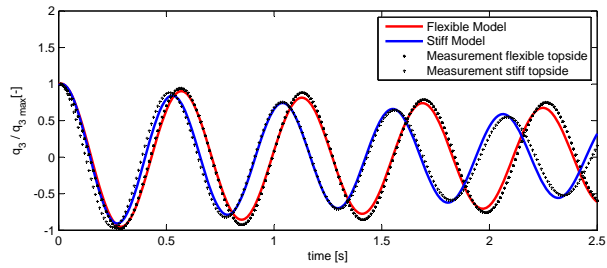


**Figure 8.** Code-to-experiment comparison between the flexible hybrid model and experimental data in a heave decay test, normalized by the displacement in heave at  $t = 0$ .



*Energies* **2014**, *7*

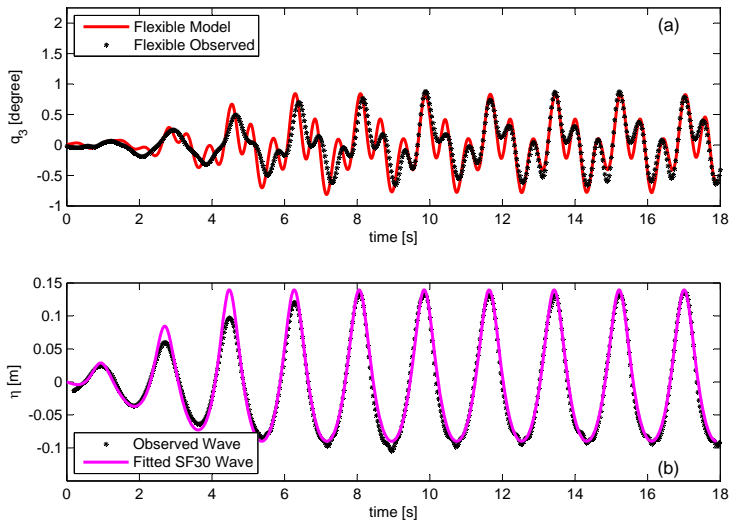
**Figure 9.** Code-to-experiment comparison between the flexible hybrid model and the stiff hybrid model and the experimental data in a pitch decay test, normalized by the displacement in pitch at  $t = 0$ .



### 3.3.2. Regular Waves

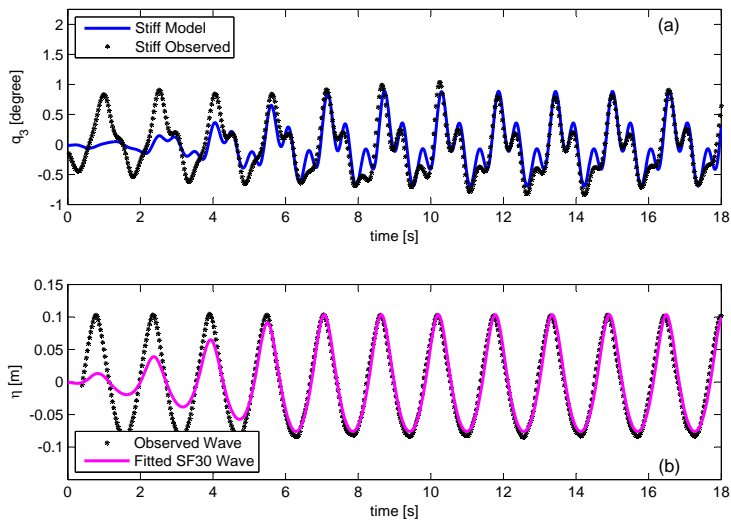
The numerical model was subsequently applied to three different wave conditions in accordance with the three largest sea states used in the physical model tests. Example time series plots for the upper and lower bounds, *i.e.*, flexible topside response to the highest wave and stiff topside response to the lowest wave, are given in Figures 10 and 11.

**Figure 10.** Code-to-experiment comparison between the flexible hybrid model and experimental data under regular wave load conditions. (a) Pitch motion comparison; (b) Surface elevation comparison.



*Energies* **2014**, *7*

**Figure 11.** Code-to-experiment comparison between the stiff hybrid model and experimental data under regular wave load conditions. **(a)** Pitch motion comparison; **(b)** Surface elevation comparison.



#### 4. Discussion

In order to gain an understanding of the model quality when compared with experimental results, cross-correlation coefficients and ratios between maximum and minimum values have been obtained, excluding the initial effects from the ramping up; see Tables 3 and 4. The correlation coefficients varied between 80%–96%, with an average of 88%. The ratios between the respective predicted minimum values and observed values showed good agreement. The maximum deviation was an 18% underestimation of the numerical model. An average deviation of 8% was found.

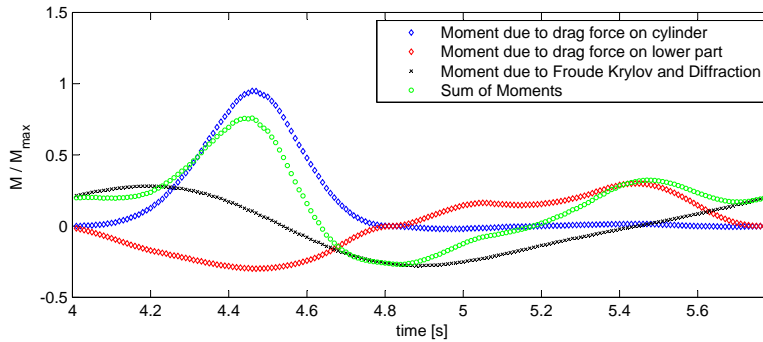
**Table 3.** Comparison of key data for the pitch motion of the flexible model. Experimental (Exp.) and numerical (Num.) data.

Flexible Model	Exp.	Num.	Exp.	Num.	Exp.	Num.
Run Number	18		17		16	
$H_{max}$ (m)	0.215		0.190		0.185	
$T_{max}$ (s)	1.79		1.68		1.57	
Min (degree)	-0.945	-0.993	-0.890	-0.857	-0.830	-0.747
Max (degree)	0.993	1.036	0.997	0.939	0.820	0.785
Min Ratio (-)	0.95		1.04		1.11	
Max Ratio (-)	0.96		1.06		1.04	
Correlation Coeff. (%)	92		80		82	

**Table 4.** Comparison of key data for the pitch motion of the stiff model. Experimental (Exp.) and numerical (Num.) data.

Stiff Model	Exp.	Num.	Exp.	Num.	Exp.	Num.
Run Number	18		17		16	
$H_{max}$ (m)	0.215		0.190		0.185	
$T_{max}$ (s)	1.79		1.68		1.57	
Min (degree)	-0.654	-0.792	-0.797	-0.730	-0.792	-0.740
Max (degree)	0.814	0.883	0.945	0.803	0.868	0.799
Min Ratio (-)	0.83		1.09		1.07	
Max Ratio (-)	0.92		1.18		1.09	
Correlation Coeff. (%)	86		95		95	

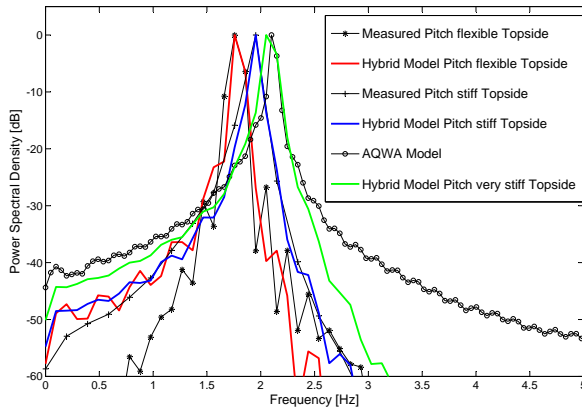
To obtain a better understanding of the force contributions, the pitch excitation moment was split into its single components for one period; see Figure 12. It is obvious that the horizontal drag force acting on the cylinder is the dominating load, *i.e.*, the combined total moment is dominated by the kinematics above the still water level impacting on the surface piercing part. The overturning moment is much larger than the moment induced by the loads acting on the lower part of the structure. The latter is, in fact, opposite, as the horizontal velocities are acting below the point of rotation. The diffractive part of the moment dominates the negative peak when the horizontal velocity components of the wave kinematics are close to zero. Hence, neither a pure potential flow approach nor a pure viscous force approach would be able to deliver the same degree of fit.

**Figure 12.** Illustration of the different wave load component contributions on pitch response.

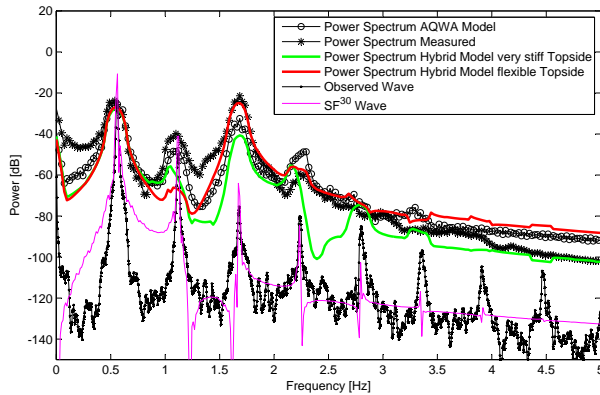
The hybrid model performs well when looking at the power spectra of the pitch decay responses; see Figure 13. Only a minor deviation is found for the very stiff model compared to the ANSYS AQWA response. For the regular wave pitch response spectra, the results are two-fold; see Figure 14. It becomes clear that the stream function wave cannot fully reproduce the laboratory waves, and in particular, the very high frequency components are underestimated. However, the influence on the structural response is negligible. The third order component is close to the pitch eigenfrequency of all structural layouts, and consequently, the dynamic amplification due to the flexibility of the topside becomes evident. The hybrid model matches the observed pitch response, whereas the very stiff model matches the results from the ANSYS AQWA model. Room for improvement can be found at the second order component; unlike the ANSYS AQWA model, the hybrid model lacks the inclusion of the second order sum frequency excitation force, explaining why both the flexible and very stiff models underestimate the responses, while the ANSYS AQWA model shows a better match.



**Figure 13.** Code-to-code and code-to-experiment power spectral density comparison of the pitch motion decay response for the quasi-rigid, stiff and flexible hybrid model.



**Figure 14.** Code-to-code and code-to-experiment power spectral density comparison of the pitch motion response for the quasi-rigid, stiff and flexible hybrid model under regular wave load conditions.



**5. Conclusions**

Non-linear waves are assumed to be relevant in the ULS analysis of FOWTs installed close to the minimum target water depth of ~50 m. The intention was to set up a resource-efficient tool, able to satisfactorily approximate pitch motions of a dynamically-sensitive FOWT resulting from a nonlinear

wave impact. As a numerical experiment, a hybrid model was developed, including linear potential theory forces and non-linear hydrodynamic viscous forces. The potential forces act thereby on the large volume part of the structure, whereas the viscous forces act on the cylindrical surface piercing part of the structure. Due to the violation of the potential flow approximations induced by wave non-linearity, the hybrid model needs to be validated by experimental tests. The  $C_D$  values applied in the hybrid model are used as tuning parameters. Considering that these are in sensible ranges, the overall match between the observations and the hybrid model is very good. To the authors knowledge, this is the first time a mildly-nonlinear approach has been assessed, comparing measured pitch responses to observed pitch responses excited by non-linear waves based on stream function theory. The term mildly-nonlinear describes the combination of linear radiation and wave scattering combined with additional non-linear terms, assuming small body motions. It was shown that the viscous drag contributions are an essential part of the response for the investigated structure, and it seems sensible to include those effects, as well, in subsequent irregular wave response analysis. Additionally, a code-to-code comparison was carried out and served as the performance verification for non-flexible topside configurations. It was shown that the hybrid model can be adopted to deliver more than satisfying results for different wave steepness values and different topside flexibilities. The model is thereby able to:

- Include the effects of regular, non-linear waves on an FOWT TLP structure;
- Include the effects of the dynamically-sensitive topside on the pitch response of an FOWT.

Comparing the maximum pitch values obtained by the rigid body simulation to those of the flexible topside simulation, the impact of the rigid body assumption becomes evident. Even though this appeared to be very structure specific, it underlines the importance of the correct implementation and furthermore proves that the rigid body assumption inherited from the O&G industry is not valid for FOWTs. It was not expected to obtain perfect fits, due to the complexity of the system and due to the simplifications. A higher fidelity model could be achieved by inclusion of the nonlinear Froude–Krylov force. When simulating irregular waves, second order diffraction forces might become relevant. However, the non-linear viscous contributions are expected to be of the same or higher significance, especially in severe seas for surface piercing parts, which are drag dominated. Considering the lateral extent of the structure, an integration of the instantaneous drag contribution over the wetted surface might lead to further improvement. However, the results already showed good agreement with the measured data. It is thereby concluded that the applied methodology is robust enough to be developed further. A natural next step is the assessment of key responses in irregular waves. Even though the general approach seems valid, a current limitation, and, therefore, incentive for future work, is the specific applicability of the model. Exchanging the potential flow coefficients is not a major challenge; however, the current drag coefficient implementation and the current mooring model makes the model case specific. Further development work, in order to make the model more generally applicable, *i.e.*, acceptable for different substructures and mooring configurations, is consequently planned.

#### Acknowledgments

The early stage PelaStar design by THE GLOSTEN ASSOCIATES was the genesis of the subject TLP. Their contribution to the project is gratefully acknowledged. The access to the wave laboratory of Aalborg University and the support by Aalborg University's staff provided an invaluable contribution.

#### Author Contributions

This work was planned and drafted by the C. Wehmeyer. The key methodology and subsequently implementation of the numerical model was done by C. Wehmeyer, however with invaluable input from the co-authors. The relevant experimental tests have been shared between F. Ferri and C. Wehmeyer. The contributions and the working atmosphere during the paper development is greatly appreciated.

#### Conflicts of Interest

The authors declare no conflict of interest.

#### References

1. *Call for Competitive Low-Carbon Energy*; Technical Report H2020-LCE-2014-1; European Commission: Brussels, Belgium, 11 December 2013.
2. *Design of Floating Wind Turbine Structures*; Offshore Standard DNV-OS-J103; Det Norske Veritas AS: Hovik, Norway, June 2013.
3. Matha, D. *Model Development and Loads Analysis of an Offshore Wind Turbine on a Tension Leg Platform, With a Comparison to Other Floating Turbine Concepts*; Subcontract Report NREL/SR-500-45891; National Renewable Energy Laboratory, Golden, CO, USA, February 2010.
4. Stewart, G.M.; Lackner, M.A.; Robertson, A.; Jonkman, J.; Goupee, A.J. Calibration and validation of a FAST floating wind turbine model of the deepwind scaled tension-leg platform. In Proceedings of the 22nd International Offshore and Polar Engineering Conference (ISOPE), Rhodes, Greece, 17–22 June 2012.
5. Prowell, I.; Robertson, A.; Jonkman, J.; Stewart, G.M.; Goupee, A.J. Numerical prediction of experimentally observed behavior of a scale-model of an offshore wind turbine supported by a tension-leg platform. In Proceedings of the Offshore Technology Conference, Houston, TX, USA, 6–9 May 2013.
6. Wehmeyer, C.; Ferri, F.; Skourup, J.; Frigaard, P. Experimental Study of an Offshore Wind Turbine TLP in ULS Conditions. In Proceedings of the Twenty-third (2013) International Offshore and Polar Engineering, Anchorage, AK, USA, 30 June–5 July 2013.
7. Chakrabarti, S.K. *Hydrodynamics of Offshore Structures*; WIT Press: Southampton, UK, 1987.
8. ANSYS AQWA, Version 15.0; ANSYS, Inc.: Canonsburg, PA, USA November 2013.
9. Yu, Z.; Falnes, J. State-space modelling of a vertical cylinder in heave. *Appl. Ocean Res.* **1995**, *17*, 265–275.
10. Perez, T.; Fossen, T.I. A Matlab Toolbox for Parametric Identification of Radiation-Force Models of Ships and Offshore Structures. *Model. Identif. Control: Nor. Res. Bull.* **2009**, *30*, 1–15.
11. Clough, R.W.; Penzien, J. *Dynamics of Structures*; Civil Engineering Series; McGraw-Hill Education: New York, NY, USA, 1993.

12. *MATLAB*, Version 7.13.0.564 (R2011b); The MathWorks Inc.: Natick, MA, USA, 2011.
13. Dean, R.G.; Dalrymple, R.A. *Water Wave Mechanics for Engineers and Scientists*; Advanced Series on Ocean Engineering-Vol2; World Scientific: Singapore, 1991.
14. Faltinsen, O. *Sea Loads on Ships and Offshore Structures*; Cambridge Ocean Technology Series; Cambridge University Press: Cambridge, UK, 1993.
15. *Design of Offshore Wind Turbine Structures*; Offshore Standard DNV-OS-J101; Det Norske Veritas AS: Hovik, Norway, October 2007.
16. Sumer, B.M.; Fredsøe, J. *Hydrodynamics around Cylindrical Structures*; Advanced Series on Ocean Engineering, V.12; World Scientific: Singapore, 1997.

© 2014 by the authors; licensee MDPI, Basel, Switzerland. This article is an open access article distributed under the terms and conditions of the Creative Commons Attribution license (<http://creativecommons.org/licenses/by/3.0/>).

---

# Paper B

## Influence of Model Simplifications on Force in Surge for a Model-Scale Floating Foundation for Offshore Wind Turbines

Morten Thøtt Andersen  
Dennis Hindhede  
Jimmy Lauridsen

The paper has been published in  
*Energies*, 8(4):3212, 2015.



Article

## **Influence of Model Simplifications Excitation Force in Surge for a Floating Foundation for Offshore Wind Turbines**

**Morten Thøtt Andersen**<sup>1,\*</sup>, **Dennis Hindhede**<sup>2,†</sup> and **Jimmy Lauridsen**<sup>2,†</sup>

<sup>1</sup> Department of Civil Engineering, Aalborg University, Sofiendalsvej 11, 9200 Aalborg SV, Denmark

<sup>2</sup> Department of Civil Engineering, Aarhus University, Inge Lehmanns Gade 10, 8000 Aarhus C, Denmark; E-Mails: dhi@ramboll.com (D.H.); lauridsen1988@gmail.com (J.L.)

† These authors contributed equally to this work.

\* Author to whom correspondence should be addressed; E-Mail: mta@civil.aau.dk; Tel.: +45-9940-8545; Fax: +45-9940-8552.

Academic Editor: John Ringwood

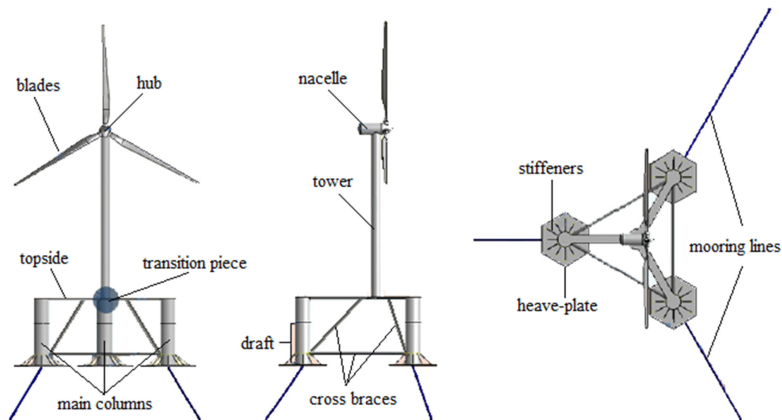
Received: 10 December 2014 / Accepted: 14 April 2015 / Published: 22 April 2015

**Abstract:** As offshore wind turbines move towards deeper and more distant sites, the concept of floating foundations is a potential technically and economically attractive alternative to the traditional fixed foundations. Unlike the well-studied monopile, the geometry of a floating foundation is complex and, thereby, increases the difficulty in wave force determination due to limitations of the commonly used simplified methods. This paper deals with a physical model test of the hydrodynamic excitation force in surge on a fixed three-columned structure intended as a floating foundation for offshore wind turbines. The experiments were conducted in a wave basin at Aalborg University. The test results are compared with a Boundary Element Method code based on linear diffraction theory for different wave force regimes defined by the column diameter, wave heights and lengths. Furthermore, the study investigates the influence of incident wave direction and stabilizing heave-plates. The structure can be divided into primary, secondary and tertiary parts, defined by the columns, heave-plates and braces to determine the excitation force in surge. The test results are in good agreement with the numerical computation for the primary parts only, which leads to simplified determination of peak frequencies and corresponding dominant force regime.

**Keywords:** wave force; surge; experimental; semi-submersible; offshore; floating foundation

## 1. Introduction

One of the most well-known and currently preferred renewable energy sources is wind power. The wind power resource is on average 50% higher offshore than onshore; however, the cost to install and run offshore wind power units is around double [1]. This has raised the challenge of optimizing the economical perspectives of offshore wind power. The generation of wind power is mainly located in areas within a distance of 5–50 km from the coastline, where the water depth is generally greater than 20 m. Studies have shown that the traditional fixed foundations will not be economically viable for offshore wind turbines in waters deeper than 30 m [2], which is why the concept of a floating foundation is a promising alternative. Four main concept types have been developed: semi-submersible, TLP, spar buoy and barge [3]. This paper will focus on the conceptual semi-submersible prototype, see Figure 1.



**Figure 1.** Conceptual semi-submersible prototype.

As conceptual designs of floating foundations are proposed, the evaluation of structural response is of high priority and a key element in the design [4]. This requires a fundamental determination and physical understanding of the wave force acting on the structure. One of the important parameters due to its high influence on hydrodynamic impact is the geometry. The dominating wave force regimes on cylindrical structures depend on the ratios of wave height to column diameter ( $H/D$ ) and of column diameter to wavelength ( $D/L$ ) [5]. For many reasons like separation, reflection, omni-directionality, three-dimensionality, turbulence, diffraction, refraction, flow-induced vibrations, *etc.*, a full structural design is beyond current computational capacity [6], so the current design philosophy for wave induced loads is often determined by empirical or first principle calculations of simple models and geometry (such as Morison [7]), which is why the validity of the applied methods for more complex structures is questionable [8].

In a recent test campaign on a semi-submersible 1/50 scale model in a wave basin, the recommendation was more research focusing on validation of the hydrodynamic loads by component-level tests [8]. Further, the modelling of wave loads by a definition of the wave spectrum is



seen as a sufficient approach to a given design. A frequency domain analysis shows that specific wave periods of regular waves and the direction of incident waves have significant effects on the excitation forces and motion of the structure [9]. The analysis of the global motion response for a semi-submersible floating wind turbine has previously been examined [10]. The study concluded that an uncoupled frequency domain analysis was sufficient to assess the global motion response as long as the aerodynamic forces were taken into account. For numerical evaluation of wave/structure interaction, the Boundary Element Method (BEM) is used to compute diffraction/radiation theory in related studies of wave force on a semi-submerged platform [11].

This paper deals with experimental analysis of the wave excitation force in surge on a conceptual prototype model of a semi-submersible foundation for an offshore wind turbine from Ramboll [12]. The concept is considered in three structural parts: columns (primary), heave-plates (secondary) and braces (tertiary). Because of the complex geometry, it is appropriate to analyse the excitation of wave induced loads on the structure in a component level test by analysing the influence of different parameters. The wave basin model test (Froude-based scale; 1/80) is conducted to observe and examine the wave load in surge. The model was fixed to simplify the influence of dynamic parameters by neglecting the motions.

The wave induced load is measured and compared with computed results of the diffraction/radiation problem in the open source BEM code, Nemoh [13], in order to obtain a feasible difference of simplified calculations of a complex geometric structure. Nemoh is based on linear diffraction theory, which neglects viscous effect. The diffraction effects are expected to be dominating due to the ratios  $H/D$  ( $0.01 < H/D < 1.5$ ) and  $D/L$  ( $\pi D/L > 0.5$ ), which make Nemoh applicable for the numerical computation. The model scaled experiment will together with the computed Nemoh results provide the basis of a parametrical analysis of the influence of a complex geometry on the excitation force in surge on a floating foundation prototype. Table 1 lists the parameter variation ranges.

**Table 1.** Parameters of tested wave set.

Parameter	Range	Ratio	Range
Wave height (H)	2 cm–16 cm	$\pi D/L$	0.05–1.26
Wave period (T)	0.4 s–2.5 s	(diffraction parameter)	
Wave length (L)	0.25 m–5.87 m	H/D	0.20–1.60
Incident wave direction ( $\theta$ )	0°–90°	(wave steepness)	

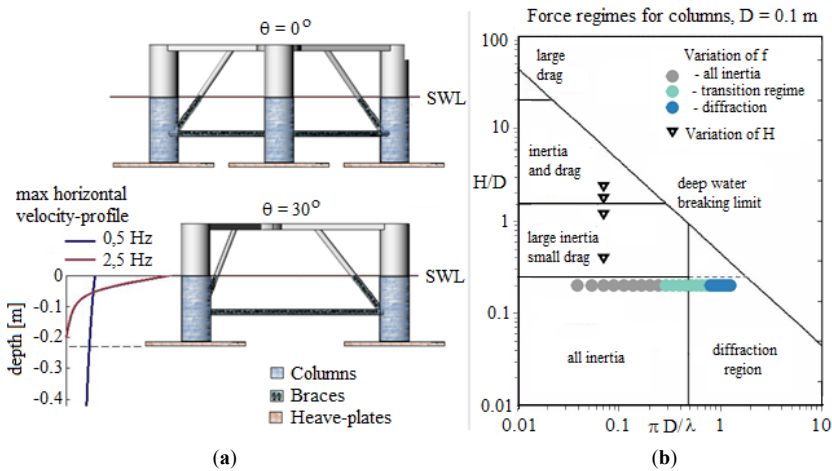
## 2. Method

### 2.1. Background

The comparison between measurements and Nemoh computation is, among other things, assumptions based on the validity of wave theories and dominant wave force regime. The experiments are a combination of variations in the parameters' wave frequency ( $f = 1/T$ ),  $\theta$ , H, and the geometrical modification by removing heave-plates and replacing them with cylinder plugs.

The variables H and f indicate the validity of wave theory in constant water depth (d) [8], where H, L and D determine the dominant force regimes [5]. The variation of f with constant H leads to an analysis of frequency dependable forces, whereas the variation of H with constant f leads to an analysis of contributions of viscous effects and omission of linear wave theory. Because the geometry of the

different structural parts affects the dominant force regime, it is appropriate to divide the structure into primary, secondary and tertiary parts based on their dominance, since the areas of wet surface (parts below Still Water Level (SWL)) and submerged volume are considered. In both cases, the columns are dominating since they are considered the primary structural part (see Figure 2a and Table 2). Figure 2b shows that by f-variation (scattered plot) the columns are within the inertia and diffraction area, where H-variation determines the significance of drag effects in dominant wave force regime. The ratio between the total frontal wet areas is  $A_{(\theta=0^\circ)} / A_{(\theta=30^\circ)} = 1.4$ , which might lead to potential shadow effects due to in-line positioning of columns in incident wave direction.



**Figure 2.** (a) Sub-divided frontal wet areas of model in incident wave direction, with illustration of velocity profile (b) Different wave force regimes of tested waves [5].

For low frequency waves, the maximum velocity profile is almost constant down the structure (see Figure 2a), which is why all structural parts are considered to be affected equally. For high frequency waves, the heave-plates have no influence because of the unaffected particles in depth. The viscous effects depend on the particle velocity and will primarily occur around the braces because of the small diameter and above the heave-plates because of the large horizontal area.

**Table 2.** Frontal wet areas (in incident wave direction), volume and force regime of wetted surface.

Structural part	Area distribution		Volume	Dominant effect	
	$\theta = 0^\circ$	$\theta = 30^\circ$		Low freq.	High freq.
Columns	74%	70%	69%	Inertia	Diffraction
Heave-plates	7%	6%	21%	Small drag	No influence
Braces	19%	24%	10%	Inertia	Small drag

## 2.2. Loads on Large Cylinders

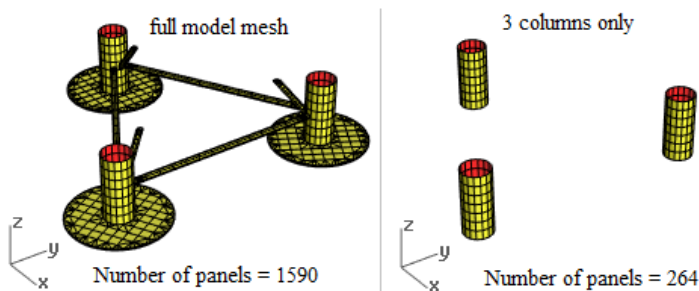
The forces of a flow acting on a body can be calculated as the pressure and shear forces integrated over the instantaneous wetted area. The solution can be found by solving the Navier-Stokes equations, which are a nonlinear set of differential equations. Today, there is no closed-form solution for the non-simplified equations, and the solution is commonly found by the use of Computational Fluid Dynamics (CFD). The major disadvantage of using CFD is the high demand of processing power and calculation time, since it is normal in hydrodynamics to make the simplifications, assuming incompressible, inviscid and irrotational flow. The potential theory follows these assumptions, and it is widely used in fluid mechanics despite its limitations [14].

When  $D/L$  becomes large, the columns will generate both reflected and diffracted waves which affect the incident wave. This process is, in general, termed diffraction and is important when the ratio  $D/L > 0.2$ , because it cannot be assumed anymore that the wave is not modified by the interactions with the body [8]. The total velocity potential ( $\varphi$ ) can be seen as the linear sum (1) of the incident wave potential ( $\varphi_w$ ), the scattered/diffracted wave potential ( $\varphi_s$ ) and radiated wave potential ( $\varphi_R$ ), which is zero due to fixation of model. The total velocity potential has to satisfy the Laplace equation (2) within the fluid domain, subjected to appropriate boundary conditions. McCamy & Fuchs [15] obtained the solution for diffraction force exerted on a circular cylinder and it is applicable as an analytical reference for lower and upper limits in terms of excitation force on one and three columns respectively:

$$\varphi = \varphi_w + \varphi_s + \varphi_R \quad (1)$$

$$\nabla^2 \varphi = 0 \quad (2)$$

Nemoh computes the linear partial differential equations of velocity potential by a boundary integral method and solves the Laplace Equation (2), where the 3-dimensional problem is described by a surface problem (panel method). For the computed results, a full model mesh (1,590 panels) and a mesh with primary structural parts only (three columns: 264 panels) are applied so as to observe differences, see Figure 3. A convergence analysis of panel size shows a divergence below 1%.



**Figure 3.** Meshes of the wetted structure applied in Nemoh (ratio in number of panels: ~6).

### 3. Experimental Setup

The experiments were conducted in a wave basin at The Hydraulic and Coastal Engineering Laboratory, Aalborg University, Denmark between 11/8-2014 and 26/9-2014. The software Awasy6 [16] controls the wave maker by inputs of  $f$  and  $H$ . Measurements of  $H$  by wave gauges are used in data processing. The tests were conducted with a water depth of 0.65 m and a temperature of  $\sim 20$  °C. Figure 4 illustrates the test setup. The wave maker is at one end of the basin with an absorbing gravel beach installed at the opposite end.

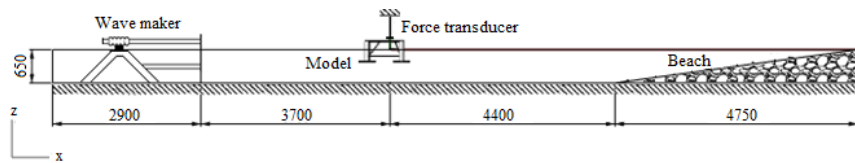


Figure 4. Illustration of experimental setup of wave basin [mm].

The paddle system is of the snake front type with translator movements. A Multi-Axis Force/Torque (FT) Sensor (ATI F/T: Delta IP65, 330-30: [http://www.ati-ia.com/products/ft/ft\\_models.aspx?id=Delta](http://www.ati-ia.com/products/ft/ft_models.aspx?id=Delta)) is mounted on top of the model and rigidly connected to the support by stiffeners. The FT measures all six components of force and torque from all three axes ( $x$ ,  $y$ , and  $z$ ).

The origin is placed at the centre of the structure at SWL, as seen in Figure 5. All results have the origin as point of reference. Froude-based scaling of a conceptual prototype is applied. Table 3 shows the model specifications.

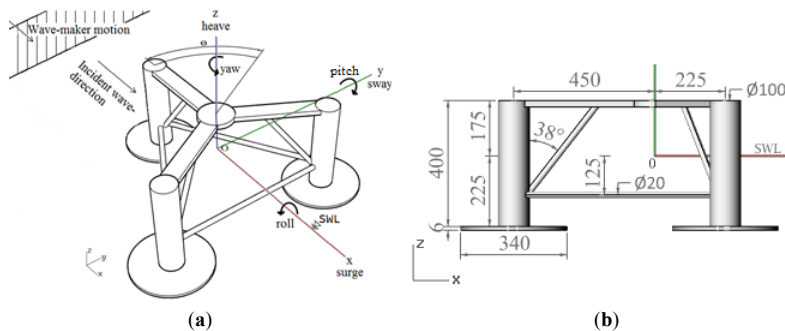


Figure 5. (a) Notation of DoFs according to [5]; (b) model dimensions [mm].

Table 3. Model specifications.

Scale: $\sim 1/80$	Model	Prototype
Weight	7.45 kg	3469 ton
CoG, $z_{(SWL=0\text{ m})}$	-37 mm	2.16 m
Draft	225 mm	18.00 m

Wave gauges are placed in the same distance from the wave maker as the model, but 2 m a side, see Figure 6.

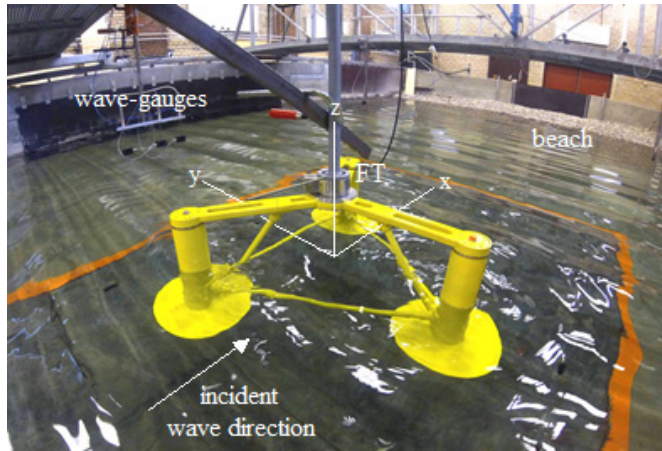


Figure 6. Picture of the model in the wave basin with illustration of the x-, y- and z-axis.

4. Results

For data processing, an FFT analysis of the measuring signal is applied in the determination of T, H and force amplitude in surge ( $F_x$ ). The results are presented in graphs showing the parameters  $\theta$ , f, H and modification of structure. All plots are normalized with respect to density ( $\rho$ ), gravity ( $g$ ), wave height (H), column radius (a) and water depth (d).

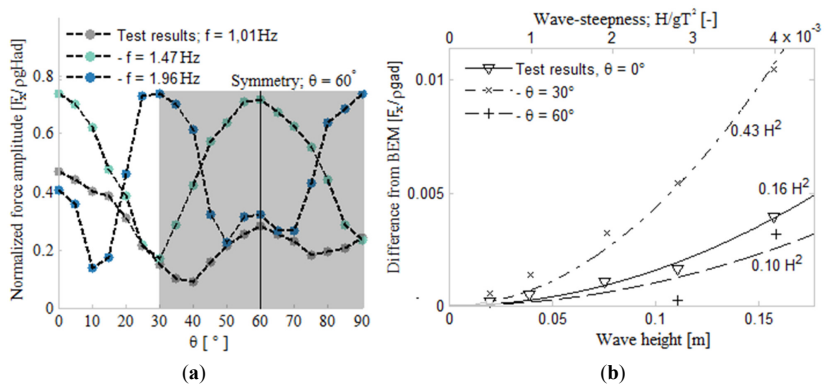
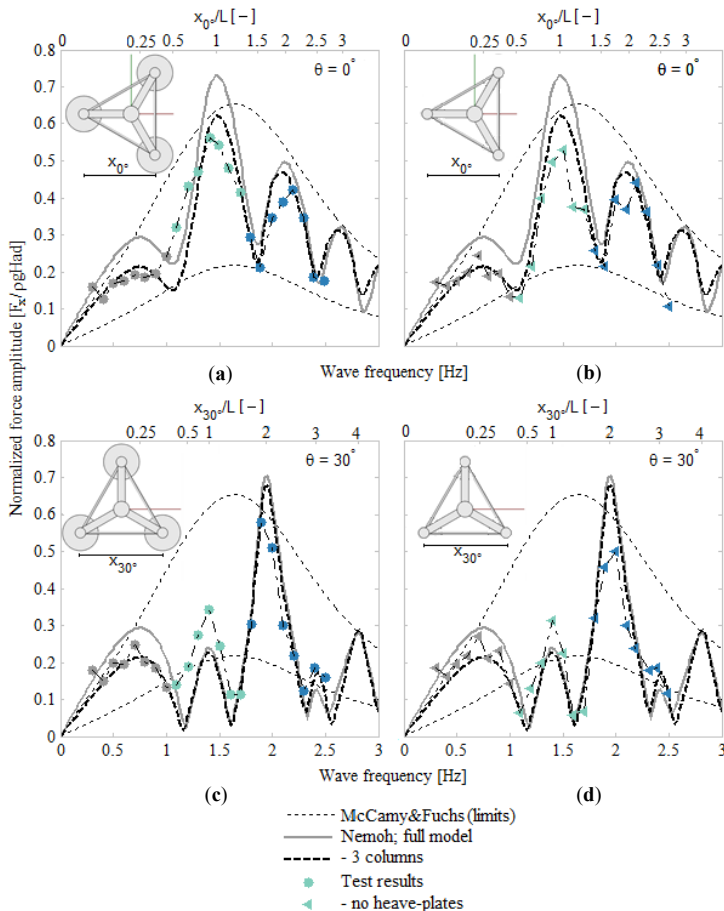


Figure 7. (a) Variation of  $F_x$  against  $\theta$  on model with heave-plates (b)  $F_x$ , difference between test results with heave-plates and Nemoh by increasing H.

As presented in Section 2, the scatter plot and test results symbols are linked to the variation of  $f$  (interval of 0.1 Hz) and, thereby, the dominant force regime, see Figure 2b. Figure 7a shows the normalized  $F_x$  by the influence of  $\theta$  with an interval of  $5^\circ$  and constant  $f$ . Peaks are observed around  $0^\circ$ ,  $30^\circ$ ,  $60^\circ$  and  $90^\circ$ . The tendency of the test results substantiate the expected axis of symmetry at  $60^\circ$ , with manual configuration of  $\theta$  taken into account. Figure 7b shows that by increasing  $H$  the test results diverge exponentially to Nemoh, which is due to violation of assumptions in potential theory. The influence of incident wave direction is considered to be caused by uncertainties in measurements, where non-symmetry affects the FT by moments around  $z$ -axis.



**Figure 8.**  $F_x$  force exerted at (a)  $\theta = 0^\circ$  (b)  $\theta = 0^\circ$ , - no heave-plates (c)  $\theta = 30^\circ$  (d)  $\theta = 30^\circ$ , - no heave-plates.

In Figures 8 and 9a,  $F_x$  is plotted by influence of  $\theta$ ,  $f$  and  $x_\theta/L$ , where  $x_\theta$  is the maximum distance (in the incident wave direction) between the columns. As expected, the local maxima and minima can be expressed by the ratio  $x_\theta/L$ , where maxima occurs at integers. The Nemoh-computed full model results diverge more to the test results at the peaks than with computation of primary structural parts only. The test results without heave-plates follow Nemoh better at local minima.

In Figure 9b, the normalized moment amplitude ( $M_z$ ) of excitation moment in yaw is plotted by influence of  $\theta$ ,  $f$  and  $x_{30^\circ}/L$ . The Nemoh computation of  $\theta = 0^\circ$  and  $60^\circ$  have  $M_z = 0$  due to symmetry, thus the test results diverge with a light increasingly small amplitude at higher frequencies. The moment amplitude for  $\theta = 30^\circ$  follows the Nemoh computation for the full model.

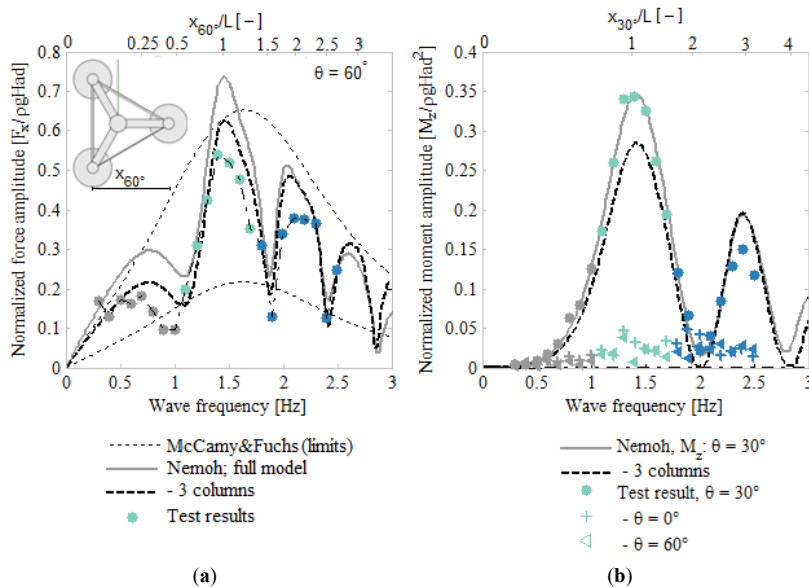


Figure 9. (a)  $F_x$  force exerted,  $\theta = 60^\circ$  (b) moment exerted in yaw,  $M_z$ .

5. Discussion

Figures 8 and 9a are a comparison of the frequency dependent excitation force for three different directions. The force is almost similar for low frequencies, but with higher frequencies it depends on the incident wave direction. The excitation force for  $0^\circ$  and  $60^\circ$  is generally in the range of lower and upper limits by the McCamy and Fuchs solution whereas the interval for  $30^\circ$  exceeds the lower limits due to a three-positioned placement of columns parallel to the incident wave direction. As seen in Figures 8 and 9a, the frequency for all local minima and maxima can be expressed by the geometric ratio  $x_\theta/L$ , which leads to a simple determination of peak frequency and peak force regime.

By determining the peak frequency and corresponding force regime, it is possible to solve excitation forces for peaks only and thereby decrease the number of equations ( $n_{EQ}$ ) significantly, see Equation (3):

$$n_{EQ} = (n_{DoFs} + n_{\theta}) \cdot n_f \quad (3)$$

where  $n_{DoFs}$ ,  $n_{\theta}$  and  $n_f$  is number of: DoFs, incident wave direction and frequencies.

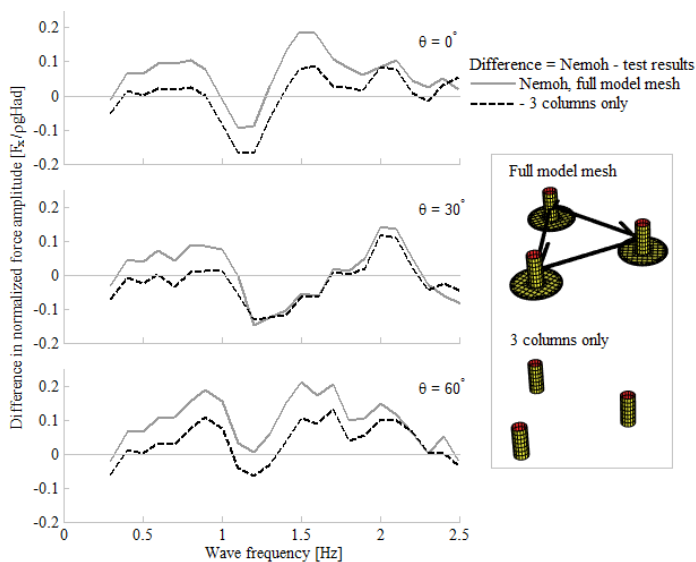
Table 4 shows the influence of  $n_f$  and number of panels in computation time. The number of panels is observed to affect the computation time with a factor of ~8 times the ratio between meshes where  $n_f$  affects it linearly.

**Table 4.** Duration of Nemoh computation for applied meshes and frequencies (where  $n_{DoFs} = n_{\theta} = 3$ ).

Mesh	Frequencies	Time *	Time [%]
Full model (1590 panels)	All ( $n_f = 150$ )	54.1 h	100%
3 columns (264 panels)	Peak ( $n_f = 8$ )	2.8 h	5.3%
	All ( $n_f = 150$ )	1.1 h	2.1%
	Peak ( $n_f = 8$ )	3.6 min	0.1%

\* Nemoh v2.01 [13] on an Intel® Core™ 3.00 GHz CPU with 4.00 GB installed memory.

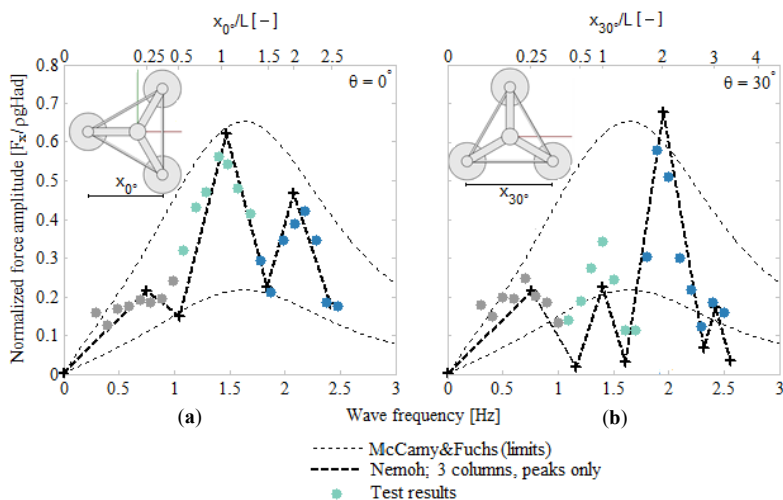
Figure 10 shows the difference between the Nemoh computed results of a mesh of the full model, a mesh of three columns only and the test results. As seen, the difference between computed results and test results is generally lower when only primary structural parts are computed. This is important because of the large difference in panels.



**Figure 10.** Difference between Nemoh-computed results and test results in normalized force amplitude.



Figure 11 shows the simple computation of the three-column mesh for peak frequencies only, which reduces the computation time to 0.1% of full model mesh for all frequencies (see Table 3). Despite the high reduction of computed panels and frequencies, the Nemoh computation is in good agreement with the test results. For the potential shadow effects in situation with in-line columns in incident wave direction ( $\theta = 30^\circ$ ), the yaw excitation ( $M_z$ ) of the structure is considered, see Figure 9b. The results show that  $M_z$  are close to zero for  $0^\circ$  and  $60^\circ$ , and the deviation could be due to a small error in the angle of the wave direction. For  $\theta = 30^\circ$ , a minimum close to zero is reached at  $x_{30^\circ}/L = 2$  and, thereby, indicates the shadow effect as negligibly small. This corresponds to the assumption of a no interference effect for an in-line placed cylinder in an oscillating flow when  $x_{30^\circ} > 4D$  [17]. Since there is no indication of shadow effects, the theoretical solution by McCamy and Fuchs including consideration of re-positioning of columns is applicable and sufficient.



**Figure 11.** Nemoh computation of 3-columned model mesh for local peak frequencies at incident wave direction of (a)  $\theta = 0^\circ$  (b)  $\theta = 30^\circ$ .

When increasing  $H$ , the excitation force moves towards the drag regime, cf. Figure 2b. Because the calculation is based on linear diffraction theory, no viscous effects are taken into account and an increasing deviation in respect to the wave height is expected. Figure 7b shows the normalized test result for a varying wave steepness at  $f = 0.5$  Hz in comparison with Nemoh. The test result deviates from Nemoh-computed results, which is considered to be primarily due to the increasing significance of the viscous effects and deviation from the linear wave elevation.

## 6. Conclusions

Because of the complex geometry, the determination of the hydrodynamic excitation force is doubtful due to the limitation of commonly used simplified methods. This paper shows good agreement between

the test results of the applied model and the calculated results obtained by applying diffraction theory in the open source BEM code, Nemoh. Furthermore, the agreement between the calculated results and the test results gets stronger when applying a simplified panel mesh consisting of primary structural parts only. The peaks are especially estimated significantly better. The average difference between Nemoh computations and test results are around 40% higher for full model mesh than for model mesh of primary structures only which have ~6 times fewer mesh panels. By simplifying the model mesh into primary structures, more realistic solutions are thereby achieved. This can be caused by mitigating effects due to non-achievement of ideal situations of full wave excitation force on secondary and tertiary structural parts (heave-plates and braces).

The peak frequencies can be predicted by the ratio of the distance between the columns (in the incident wave direction) and the wavelength, which is why the necessary frequencies for computation, and as such the computation time, can be reduced significantly. By computing peak frequencies and mesh of primary structures only, the computation time is reduced to 0.1% of full model mesh for all frequencies. The results by reduced computation demonstrate a significantly more effective method which shows good agreement with the test results.

For low frequencies, the result with heave-plates diverge more from the ideal situation solved by potential theory than the results without heave-plates. This is due to the disturbance of the particle motion and the presence of skin friction over the heave-plates. By considering the excitation moment in yaw, the shadow effects of columns in surge are observed as negligibly small. This supports the assumption of a no interference effect for an in-line placed cylinder in an oscillating flow when the distance between columns (in incident wave direction) is higher than four times the column diameter.

### Acknowledgments

The authors acknowledge the benevolence from Aalborg University, Department of Hydraulic and Coastal Engineering.

### Author Contributions

MTA drafted and planned the work; MTA, DH and JL conceived and designed the experiments; DH and JL performed experiments, analysed data and drafted the paper under supervision of MTA; MTA, DH and JL finalized the paper.

### Conflicts of Interest

The authors declare no conflict of interest.

### References

1. International Renewable Energy Agency (IRENA). *Renewable Energy Technologies: Cost Analysis Series, Volume 1: Wind Power*; IRENA: Bonn, Germany, 2012.
2. European Wind Energy Association (EWEA). *Deep Water; The Next Step for Offshore Wind Energy*; EWEA: Brussels, Belgium, 2013.

3. Jonkman, J.M. Dynamics of offshore floating wind turbines—model development and verification. *Wind Energy* **2009**, *12*, 459–492.
4. Hirdaris, S.; Bai, W.; Dessi, D.; Ergin, A.; Gu, X.; Hermundstad, O.A.; Huijsmans, R.; Iijima, K.; Nielsen, U.D.; Parunov, J.; *et al.* Loads for use in the design of ships and offshore structures. *Ocean Eng.* **2014**, *78*, 131–174.
5. Det Norske Veritas (DNV). *DNV-RP-C205; Environmental Conditions and Environmental Loads*; DNV: Høvik, Norway, 2010.
6. Sarpkaya, T. *Wave Forces on Offshore Structures*; Cambridge University Press: NewYork, NY, USA, 2010.
7. Morison, J.R.; O'Brien, M.P.; Johnson, J.W.; Schaaf, S.A. The force exerted by surface waves on piles. *Petroleum Transactions. Am. Inst. Mining Eng.* **1950**, *189*, 149–157.
8. NREL. Summary of Conclusions and Recommendations Drawn from the DeepCWind Scaled Floating Offshore Wind System Test Campaign. In Proceedings of the ASME 2013: 32nd International Conference on Ocean, Offshore and Arctic Engineering, Nantes, France, 9–14 June 2013.
9. Zhang, R.; Tang, Y.; Hu, J.; Ruan, S.; Chen, C. Dynamic response in frequency and timedomains of a floating foundation for offshore wind turbines. *Ocean Eng.* **2013**, *60*, 115–123.
10. Huijs, F.; Savenije, F.; de Bruijn, R. Concept design verification of a semi-submersible floating wind turbine using coupled simulations. *Energy Procedia* **2014**, *53*, 2–12.
11. Gao, Y.; Li, C.; Cheng, X. Research on foundation response of a tri-floater offshore wind. In *IOP Conference Series: Materials Science and Engineering*; IOP Publishing: Beijing, China, 2013; Volume 52.
12. Fernando, V.P. Semi-Submersible Topside Conceptual Design; Transition Piece. Master Thesis, Aalborg University, Esbjerg, Denmark, 2014.
13. LHEEA. Laboratoire de recherche en Hydrodynamique, Énergétique et Environnement Atmosphérique. Availale online: <http://lheea.ec-nantes.fr/doku.php/en/start> (accessed on 18 August 2014).
14. Massie, W.W.; Journée, J.M. *Offshore Hydromechanics*; Delft University of Technology: Delft, The Netherlands, 2001.
15. MacCamy, R.C.; Fuchs, R.A. *Wave Forces on Piles: A Diffraction Theory*; Technical Memorandum No. 69; Beach Erosion Board, U.S. Army Corps of Engineers, 1954.
16. AAU. Software for Wave Laboratories. Availale online: <http://www.hydrosoft.civil.aau.dk/awasys/> (accessed on 18 August 2014).
17. Frigaard, P.B.; Burcharth, H.F. *Wave Loads on Cylinders*; University of Aalborg: Esbjerg, Denmark, 1989.

© 2015 by the authors; licensee MDPI, Basel, Switzerland. This article is an open access article distributed under the terms and conditions of the Creative Commons Attribution license (<http://creativecommons.org/licenses/by/4.0/>).



---

# Paper C

## Hydrodynamic Excitation Forces on Floating Structures with Finite Displacements

Morten Thøtt Andersen  
Søren Rasmus Kjærshøj Nielsen

The paper has been published in  
*ISOPE*, ISBN:978-1-880653-89-0, 2015.



## Hydrodynamic Excitation Forces on Floating Structures with Finite Displacements

Morten Thøtt Andersen, Søren Rasmus Kjærshøj Nielsen  
Department of Civil Engineering, Aalborg University  
Aalborg, Denmark

### ABSTRACT

This paper aims to present an extended version of the classic linear wave excitation force theory. Linear wave theory implies that the wave load is applied in the referential state of the structure. In reality, the load is acting in the dynamically altered state. In the classic notation the wave excitation force is solely a function of time, hence the body is fixed in reference to the wave field. In this paper, the instantaneous position of the body is included in the calculation of the excitation force. Even though the displacement of the structure relative to a characteristic wavelength is generally small, it is demonstrated that the indicated nonlinear effect causes parametric instability at certain ratios between the wave frequency and the eigenfrequency of the structure. This calls for caution for structures designed to avoid resonance by having eigenfrequencies below the exciting wave frequencies.

**KEY WORDS:** Nonlinear wave excitation, Stability analysis, Parametric excitation, Mathieu equation

### INTRODUCTION

For floating offshore structures the wave excitation is commonly described via a boundary element integration of the linear potential field. This approach has proven useful, but one of the major assumptions is that the wave excitation occurs at the referential state of the structure. For a linearized frequency domain investigation of harmonic waves this carries no significant uncertainty since the effect is simply a phase shift of the wave train. When observing structures in the time domain, the continuously updated origin of excitation introduces a nonlinear effect that can occur even in harmonic monochromatic waves.

This paper is based in a project regarding a certain type of floating body, namely the foundation for a floating offshore wind turbine (FOWT). These structures often have a mooring system with very low stiffness in surge and sway in order to have the eigenfrequencies lower than the wave frequencies. The side ef-

fect of a soft mooring system is that large amplitudes of motion inherently can occur. This makes the general assumption about excitation at a fixed referential state seem questionable, hence this paper will discuss some of the implications. Figure 1 shows a sketch of a 1:80 scaled model of a semi-submersible foundation for a FOWT. The properties of this foundation will be used as an example throughout the paper - note that it is not important to focus on the exact model properties, but instead the relation between the system eigenfrequency and the excitation frequency is of interest.

Some incorporations of nonlinear wave excitation has been done within the field, but often the approach is done by modifying the wave spectrum to include a low frequency component or more generally by a quadratic transfer function, see e.g. Bayati et al. (2014), Chen and Duan (2007) and Pinkster (1980).

The work presented in this paper separates itself from prior nonlinear wave excitation effect in the way that it is not altering the frequency of the wave excitation, but instead demonstrates subharmonic response in cases of regular harmonic loading. It must be stressed that even though this paper uses model data from a FOWT the investigation and approach itself is in no way limited to any specific kind of floating body.

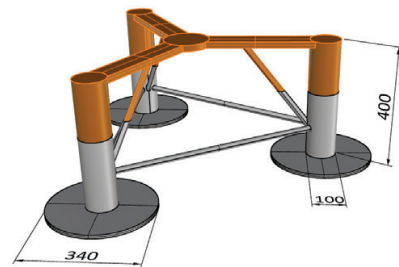


Figure 1: Semi-submersible foundation in scale 1:80. Dimensions in mm.

### EQUATION OF MOTION OF SYSTEM

Assuming monochromatic linear wave loadings the surge motion of the platform is described by the Cummins equation with a harmonic varying external excitation, Cummins (1962):

$$(m + m_h) \ddot{v}(t) + \int_{t_0}^t \dot{h}_r(t - \tau) \dot{v}(\tau) d\tau + K v(t) = F_e \cos(\omega t) \quad , \quad t > t_0 \quad (1)$$

and

$$v(t_0) = v_0 \quad , \quad \dot{v}(t_0) = \dot{v}_0 \quad (2)$$

$v(t)$  is the displacement of the platform, and  $v_0$  and  $\dot{v}_0$  indicate the initial conditions at the time  $t_0$ .  $m$  is the structural mass, and  $m_h$  is the added mass at infinite high frequencies.  $h_r(t)$  is the causal impulse response function for the radiation force, and  $K$  is the linear spring stiffness from the mooring system.  $F_e$  is amplitude of the external wave loading, and  $\omega = \frac{2\pi}{T}$  is angular frequency and  $T$  is the period of the monochromatic waves.

The loading in Eq. (1) refers to a structure fixed to a referential coordinate system. In reality the loading is applied at the displaced position  $x = v(t)$ . In the stationary state, where the response from the initial conditions has been dissipated, Eq. (1) should be reformulated as:

$$M \ddot{v}(t) + C \dot{v}(t) + K v(t) = F_e \cos(kv + \omega t) \quad (3)$$

where:

$$\left. \begin{aligned} M &= M(\omega) = m + m_h + \frac{1}{\omega} \text{Im}(H_r(\omega)) \\ C &= C(\omega) = \text{Re}(H_r(\omega)) \end{aligned} \right\} \quad (4)$$

$$H_r(\omega) = \int_0^{\infty} e^{-\omega t} h_r(t) dt \quad (5)$$

$H_r(\omega)$  indicates the frequency response function related to  $h_r(t)$ .  $M(\omega)$  and  $C(\omega)$  indicates the total structural and hydrodynamic added mass as well as the radiation damping predicted by linear wave theory, Falnes (2002).

Figure 2 shows the added mass and hydrodynamic damping introduced in Eq. (3) as obtained from a boundary element integration, LHEEA (2014). Due to the predominantly low angular frequencies considered in this study  $C(\omega)$  is unreasonably low. It is therefore chosen to replace  $C(\omega)$  and  $M(\omega)$  with the fixed values of  $C$  and  $M$  determined from physical model tests.

$k = k(\omega) = \frac{2\pi}{L}$  denotes the wave number and  $L$  is the wave length of the monochromatic waves. This is determined by the dispersion relation, Falnes (2002):

$$\frac{\omega^2 h}{g} = kh \tanh(kh) \quad (6)$$

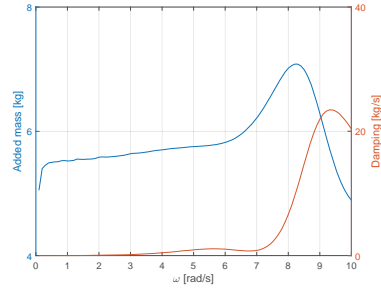


Figure 2: Frequency dependent added mass and damping coefficients for chosen model scale structure.

where  $h$  is the water depth, and  $g$  is the acceleration of gravity.

Eq. (3) is reformulated to the normalized form:

$$\ddot{v}(t) + 2\zeta\omega_0 \dot{v}(t) + \omega_0^2 v(t) = f_e \cos(kv + \omega t) \quad (7)$$

where:

$$\zeta = \frac{C}{2\sqrt{KM}} \quad , \quad \omega_0 = \sqrt{\frac{K}{M}} \quad , \quad f_e = \frac{F_e}{M} \quad (8)$$

$\zeta$ ,  $\omega_0$  and  $f_e$  indicate the modal damping ratio of the system, the undamped angular eigenfrequency and the normalized wave load amplitude.

### RESPONSE ANALYSIS

The importance of the correction of the load term in Eq. (3) depends on the relative magnitude of  $kV_0 = \frac{2\pi}{L}$  and  $\omega T = 2\pi$ , where  $V_0$  indicates the amplitude of motion of the platform. Hence, the criteria is determined by the magnitude of the fraction  $\frac{V_0}{L}$ . It turns out that under normal operation we have  $\frac{V_0}{L} \ll 1$ , indicating that the correction can be ignored for most angular wave frequencies. At resonance, where  $\omega = \omega_0$ , large amplitude  $V_0$  occurs. However, for specific discrete wave frequencies internal resonance may take place, also giving rise to large response. In order to analyze this phenomenon the following first order Taylor expansion in  $kv(t)$  is applied:

$$\cos(kv(t) + \omega t) = \cos(\omega t) - \sin(\omega t) kv(t) + O\left((kv(t))^2\right) \quad (9)$$

where  $O(\cdot)$  denotes the Landau symbol. Ignoring the remainder in Eq. (9), insertion of Eq. (9) in Eq. (7) provides:

$$\ddot{v}(t) + 2\zeta\omega_0 \dot{v}(t) + \omega_0^2 (1 + \kappa \sin(\omega t)) v(t) = f_e \cos(\omega t) \quad (10)$$



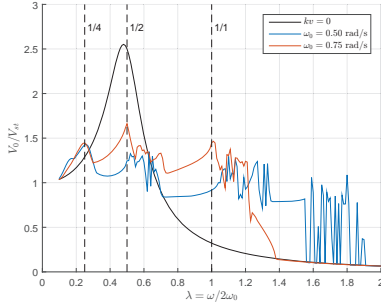


Figure 3: Amplitude response for the lower range of analyzed angular eigenfrequencies.

where:

$$\kappa = \frac{F_e k}{K} \quad (11)$$

Eq. (10) indicate an inhomogeneous Mathieu equation. Depending on the damping ratio instability in the homogeneous part of the equation may take place at angular wave frequencies fulfilling the following relations, Xie (2006):

$$\lambda = \frac{\omega}{2\omega_0} = 1, \frac{1}{2}, \frac{1}{3}, \frac{1}{4}, \dots \quad (12)$$

It should be noted that the infinite response predicted by the 1st order perturbation equation in  $kv$  will not happen in the underlying Eq. (7) because the load term is always limited to the interval  $[-f_e, f_e]$ . Nevertheless, increased response is expected at the indicated frequencies.

### NUMERICAL EXAMPLE

The following numerical investigations are performed for the surge direction as a single degree of freedom (SDOF) system governed by Eq. (7), rather than the approximate Eq. (10). All structural and hydrodynamic properties are based on numerical and experimental studies of the body shown in Figure 1.

The model damping ratio  $\zeta$  has been determined from experimental decay tests and hence  $C$  is given from Eq. (8).  $M$  is, due to the minor frequency dependence of the hydrodynamic added mass at low angular frequencies, fixed at an average value. The approximated parameters can be seen in Table 1.

As basis for comparison the dynamic amplification factor,  $D$ , for the SDOF with  $kv = 0$  is introduced, Clough and Penzien (1975):

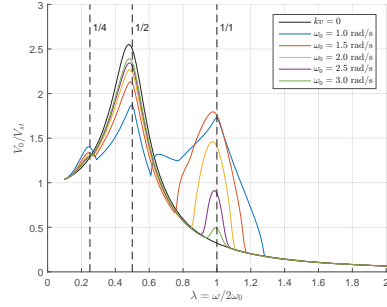


Figure 4: Amplitude response for the higher range of analyzed angular eigenfrequencies.

$$D = \frac{V_0}{V_{st}} = \frac{1}{\sqrt{(1 - \frac{\omega^2}{\omega_0^2})^2 + 4\zeta^2 \frac{\omega^2}{\omega_0^2}}}, \quad V_{st} = \frac{f_e}{\omega_0^2} \quad (13)$$

where  $V_{st}$  is the quasi-static amplitude at infinite low angular frequencies.

Figure 3 shows the dynamic amplification as a function of  $\lambda$ . The black curve indicates the linear harmonic response corresponding to  $kv = 0$  in Eq. (3). The dynamic amplification at resonance becomes equal to  $\frac{1}{2\zeta} = 2.5$ . The blue and red curves indicates the response of Eq. (3) for  $\omega_0 = 0.50$  rad/s and  $\omega_0 = 0.75$  rad/s. The irregular behavior at  $\lambda \approx 0.6, 1.2, 1.8$  is caused by jumps between the harmonic linear response and various subharmonic and chaotic attractors, which will be analyzed in the following discussion. Further, in case of orderly vibrations and for  $\lambda \approx 1, \frac{1}{2}, \frac{1}{4}$  the amplitude response deviates significantly from the linear harmonic response.

Figure 4 shows the similar results for higher angular eigenfrequencies. Again the black curve indicates the linear harmonic response corresponding to  $kv = 0$  in Eq. (3). The colored curves indicates the response of Eq. (3) for  $\omega_0 = 1$  rad/s to  $\omega_0 = 3$  rad/s. In these cases subharmonic or chaotic response are no longer present. However the parametric internal resonance as predicted by Eq. (10) is

Table 1: Structural and hydrodynamic parameters of the floating platform.

Parameter	Value	Unit	Parameter	Value	Unit
$M$	12.5	kg	$h$	0.7	m
$F_e$	25	N	$\zeta$	0.2	-
$\omega_0$	0.5 - 3	rad/s			

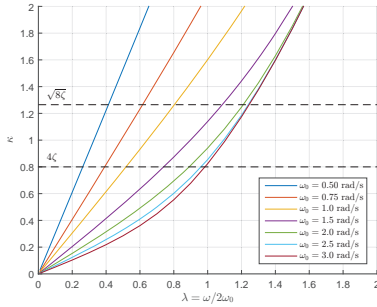


Figure 5: Limits under which parametric instability is not expected.

clearly visible, and it is noted that the effect diminishes with increasing eigenfrequencies - see the minor differences between the black and green curve on Figure 4. From a design standpoint is also interesting to observe that the dynamic amplification at resonance  $\lambda = \frac{1}{2}$  drop to a magnitude comparable to the amplification at  $\lambda = 1$ . This implies that structures with higher eigenperiods will be excited less a resonance than expected with the assumption  $kv = 0$  in Eq. (3).

### DISCUSSION

Figure 5 shows the instability driver,  $\kappa$ , over the range of tests presented. For low angular eigenfrequencies the stability limits given by Xie (2006) are reached before the resonance relation  $\lambda = \frac{1}{2}$ . This is in good accordance with the findings in figure 3 and 4.

In order to analyze the subharmonic and chaotic responses identified in Figure 3 and 4, the widely used Poincaré mapping is applied, as introduced by e.g. Moon (1987). The different maps include a periodic marker to detect subharmonics response as well as the trajectory of the motion.

Figure 6 shows the Poincaré map for the classic linear solution where  $kv = 0$ . The map depicts the larger response at resonance where  $\lambda = \frac{1}{2}$ , and the motion expectedly does not diverge from  $T_0 = T$ . Figure 7 shows the first three Poincaré maps where subharmonics are detected. For the example shown  $\omega_0 = 2$  rad/s which is a fairly stable solution when referring to Figure 4. It is observed that the amplified dynamics at  $\lambda = 1$ , corresponding to internal resonance, occurs as a subharmonic of the 2nd order, i.e.  $T_0 = 2T$ . The subharmonic motion of the system is only present when the dynamic amplification diverges from the linear  $D$  at values  $\lambda \simeq 1$ .

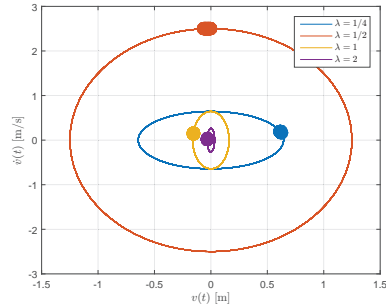


Figure 6: Poincaré map and trajectories as a function of  $\lambda$ . Harmonic response,  $kv = 0$ ,  $\omega_0 = 2$  rad/s.

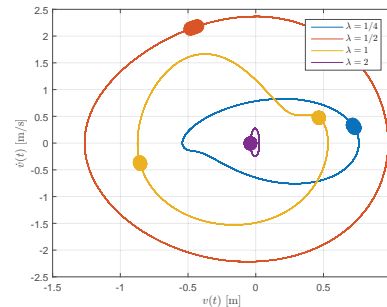


Figure 7: Poincaré map and trajectories as a function of  $\lambda$ . Harmonic and subharmonic response of order 2,  $\omega_0 = 2$  rad/s.

When observing the more unstable cases of the response of Eq. (3) the Poincaré mapping reveals an even more intriguing behavior as seen on Figure 8 and 9. Here the mapping depicts the behavior of a system where  $\omega_0 = 0.5$  rad/s.

On Figure 3 three distinct plateaus are detected at  $\lambda \simeq 0.4$ ,  $0.8$ ,  $1.4$  for  $\omega_0 = 0.5$  rad/s. In Figure 8 the Poincaré map reveals some complicated trajectories, or more interesting; that the subharmonic order increases by one for each new plateau at a higher  $\lambda$  value, i.e. adopting a  $T_0 = T$ ,  $T_0 = 2T$  and  $T_0 = 3T$  motion respectively. It is noted that the dynamic amplification is much more even over the range of  $\lambda$  than what is the case for the linear harmonic response,

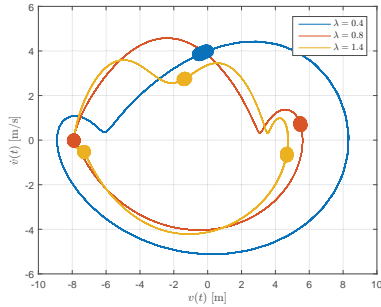


Figure 8: Poincaré map and trajectories as a function of  $\lambda$ . Harmonic and subharmonic responses of order 2 and 3,  $\omega_0 = 0.5$  rad/s.

despite the local irregularities.

When assessing the behavior in one of the irregular  $\lambda$ -regions, two neighboring simulations are chosen to exemplify and explain the large difference in dynamic amplification. Figure 9 shows two motions from an arbitrarily selected irregular area just before the third plateau of  $\omega_0 = 0.5$  rad/s on Figure 3. The two neighboring simulation shows a significant difference in dynamic amplification. In red the complex trajectory can be seen for  $\lambda = 1.34$ . In the Poincaré map it becomes evident that this complex behavior is merely a  $T_0 = 6T$  motion - a realization that is not easily captured in the visual inspection of the time series of the motion. In blue the trajectory can be seen for  $\lambda = 1.33$ . This trajectory is even more complex than what was the case for  $\lambda = 1.34$ . It is observed that the pattern never repeats itself implying that the motion is fully chaotic, i.e.  $T_0 \rightarrow \infty$ .

#### CONCLUDING REMARKS

When offshore structures are moving relative to a propagating monochromatic wave train the phase of the load is affected, resulting in a change of the displacement response. In the paper it is demonstrated that the indicated effect will diminish the amplitude response at resonance excitation. However, for some parametric values and at certain frequency ratios internal resonance may occur, which increases the response above the amplification predicted by the linear harmonic response. Furthermore it is demonstrated that some frequency ratios may lead to subharmonic and chaotic response. The study is a part of a larger project on mooring of offshore structures, and the next step will be to verify the findings in this paper by scaled model tests in a wave basin.

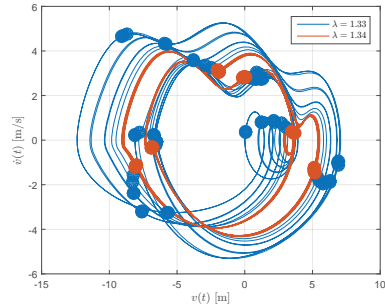


Figure 9: Poincaré map and trajectories as a function of  $\lambda$ . Subharmonic response of order 6 and fully chaotic response,  $\omega_0 = 0.5$  rad/s.

#### REFERENCES

- Bayati, I., Jonkman, J., Robertson, A. and Platt, A. (2014), The effects of second-order hydrodynamics on a semisubmersible floating offshore wind turbine, in 'Journal of Physics: Conference Series', Vol. 524, IOP Publishing, p. 012094.
- Chen, X. and Duan, W. (2007), *Formulation of low-frequency QTF by  $O(\Delta\omega)$  approximation*.
- Clough, R. W. and Penzien, J. (1975), *Dynamics of structures*, New York: McGraw-Hill.
- Cummins, W. (1962), *The impulse response function and ship motions*.
- Falnes, J. (2002), *Ocean waves and oscillating systems: linear interactions including wave-energy extraction*, Cambridge university press.
- LHEEA (2014), *Nemoh v2.0 - Open source BEM software*. <http://lheea.ec-nantes.fr/doku.php/emo/nemoh/start>.
- Moon, F. C. (1987), *Chaotic vibrations: an introduction for applied scientists and engineers*, Wiley-Interscience.
- Pinkster, J. A. (1980), *Low frequency second order wave exciting forces on floating structures*, TU Delft, Delft University of Technology.
- Xie, W.-C. (2006), *Dynamic stability of structures*, Cambridge University Press.



---

# Paper D

## Incentive-based Financial Support Scheme for Immature Renewable Energy Systems

Morten Thøtt Andersen  
Peter Bak Frigaard

The paper has been published in  
*EWTEC*, ISSN:2309-1983 (09B5-5-1), 2015.



# Incentive-based Financial Support Scheme for Immature Renewable Energy Systems

Morten Thøtt Andersen

Dept. of Civil Engineering, Aalborg University  
Sofiendalsvej 11, 9200 Aalborg SV, Denmark  
E-mail: mta@civil.aau.dk

Peter Bak Frigaard

Dept. of Civil Engineering, Aalborg University  
Sofiendalsvej 11, 9200 Aalborg SV, Denmark  
E-mail: pf@civil.aau.dk

**Abstract**—Most of today's renewable energy systems rely heavily on investments as well as public financial support. This support is often given by means of a higher sales price for each kWh produced, i.e. feed-in tariffs (FITs), green certificates or Renewable Obligation Certificates (ROCs), or by a fixed amount, being a percentage of the construction costs of the facility. All these ways of financing have different downsides. The feed-in tariff based kWh prices have some incentives to improve the technology, but enables infeasible solutions to stay financially supported even while R&D is in status quo. The fixed amount only helps with installation costs, which should not be an issue once the technology is sufficiently feasible. This means that the current ways of granting financial support all lack incentives for increasing production or decreasing construction costs. This paper presents a unique scheme for determining the level of support, based on production target curves. This incentive-based approach pushes development to constantly improve, and enables both investors and the general public to have a transparent view of which technologies are performing and improving the most, i.e. aiming for the steepest target curve.

**Index Terms**—Financial Support, Subsidies, IFS, Feed-in Tariffs, Cost of Energy

## I. INTRODUCTION

It is widely known that the world has a rising demand for energy, and that the call to fulfill this need is upon the established and upcoming renewable energy systems. The upcoming systems rely on investments and financial support throughout the R&D process where they still are infeasible at a commercial level. The need for financial support is applicable within all sectors of renewable energy, e.g. solar, biomass, wind, tidal and wave. Often the willingness to provide support for these emerging industries is present. The topic of the presented paper is a discussion on how to determine the terms for the support. The paper offers no political standpoints on the level of support, but is instead to be seen as a presentation of a technical tool for intelligent distribution of funding. The driving idea is a financial support scheme that offers incentive for technology progression, while still providing financial and political safety for governments and investors.

One of the larger upcoming renewable technologies is within the wave energy sector. The different concepts and prototypes are still all not economically feasible, due to high capital and operational expenditures (CAPEX/OPEX) and

therefore rely on financial support to continue development. Because of this, a fictive wave energy converter (WEC) will be used as an example in this paper. This is done to demonstrate how subsidies can be intelligently distributed to provide incentive for technology improvement with clear target trajectories. Note that this support scheme is far from limited to the wave energy sector. Within wave energy the financial support is often given by means of a higher sales price for each kWh produced, i.e. feed-in tariffs, green certificates, ROCs, or by financial installation support, being a percentage of the construction costs of the facility. All these ways of financing have different downsides. A comparison between the feed-in tariffs and the green certificates on a European scale have been conducted by [1] and [2]. The feed-in tariff based kWh prices have some incentive to improve the technology, but enables infeasible solutions to stay financially supported even while R&D is in status quo. This problem was also discussed by [3] who presented a two-part tariff design, and by [4] who presented a thorough investigation on four different main financial incentives valid for the US market. The financial installation support only helps with initial costs which should not be an issue once the technology is sufficiently feasible. This means that the current ways of granting financial support to a large extent lack incentives for improving technology, decreasing production costs and hereby reducing total cost of energy (CoE). This negates some of the investment issues presented by [5].

In Denmark, a unique scheme of determining the amount of financial support has been developed over the recent years. This scheme sets up a target curve for each individual technology or concept, and financial support is calculated on whether or not this target curve is met. The target for each energy plant is set from dividing each year into 10 minute intervals. If energy production in one of these  $\sim 52\,600$  intervals meets the given target, a bonus is given to the plant. This paper will describe the incentive-based financial support scheme in detail and how it brings higher incentives for continued development of technologies. It will also be described how this scheme enables both investors and the general public to have a transparent view of which technologies are improving the most, i.e. aiming for the highest target curve.

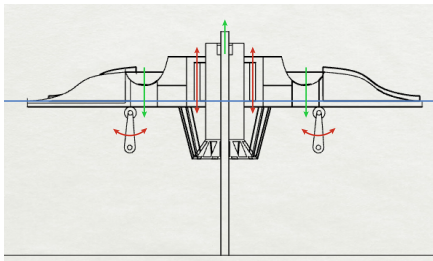


Fig. 1. Design sketch of WHOOPS.

## II. INTRODUCING WHOOPS

The Wave Heave Overtopping Oscillating Power System (WHOOPS) is a fictive WEC invented by *Clever Guys Inc.* Fig. 1 shows the working principle behind the system, where the red arrows indicated mechanical degrees of freedom and green arrows indicate flux outlets. Even though this device might not seem that optimal from an objective technical point of view, it has some financial characteristics, which are comparable to those of other devices. Without addressing the functionality of the design and power take-off (PTO) further, we will have a look at some other important technicalities:

- Location: Planned for North Sea installation.
- Effect: Estimated installed power is 800 kW.
- Production: Tank testing and numerical tests have been used to estimate a yearly production of 3,000 MWh.
- Lifetime: The WEC is planned to be running for 15 years.
- CAPEX: Structure and installation is expected to cost €2M.
- OPEX: Running production and operation and management (O&M) is assessed to amount to €0.1M/yr.

All the data are representing the commercial version of the WHOOPS device. It is to be expected that the a prototype (or demonstration plant) will not achieve these values in the first year(s). The chosen economical data of the demonstration device are much less appealing than the economic properties of the commercial version of the device. Nevertheless, experience shows that the economic reality for demonstration devices often are overestimated by optimistic device developers, and that the present estimates are close to what have been seen in real demonstration projects. Table I shows an estimated economical comparison between the final commercial model and the prototype. Note that the economical calculations are deliberately simplified not accounting for interest rates etc.

From Table I it is seen that the commercial version of the WHOOPS device might have an economical future. In

TABLE I  
ECONOMIC DATA OF THE WHOOPS DEVICE.

	Commercial	Prototype
CAPEX	€2M	€4M
OPEX/yr	€0.1M	€0.3M
Lifetime	15 yr	5 yr
Total cost	€3.5M	€5.5M
Production	3 000 MWh/yr	1 500 MWh/yr
Downtime	2%	10%
Total production	45 000 MWh	7 500 MWh
Device CoE	€78/MWh	€733/MWh
Market CoE	€50/MWh	€50/MWh
Required feed-in	€28/MWh	€683/MWh
Market value return	€2.25M	€0.375M
Required one-time support	€1.25M	€5.125M

a world with growing focus on renewable energy a feed-in tariff of €28/MWh does not sound unrealistic. On the contrary, when the economic key-figures are moved towards more realistic levels by say a venture capitalist, the incitement for investment crumbles completely. It would be difficult to defend the willingness to fund a technology that might operate at a CoE at ~15 times that of the market value. This leaves a promising project in a state where the prototype on paper seems economically underwhelming. In the following, it will be briefly presented how classic schemes of funding works, and how they would apply in the case of the WHOOPS device.

## III. CLASSIC FINANCIAL SUPPORT SCHEMES

Governmental bodies are still the major investors in immature energy technologies, providing up to 2/3 of the total investment in most devices. When directly distributing subsidies, governments have been prone to resort to one of the following schemes. The most simple support is in the form of an initial one-time payout to aid plant construction and installation. Secondly, it is custom within the sector to provide a production based support by the means of higher kWh rate, i.e. feed-in tariffs. Both methods have inherent strengths and weaknesses, which will be covered in the following. Please note that the presented paper will not cover the implications that subsidies might have on other political goals such as total carbon emissions etc. as presented by [6], [7].

### A. One-time support

Generally, the one-time support is given in the initial stage of demonstration to help fund the CAPEX. Construction and installation of wave energy converters are still a major part of the total expenses. This is partly due to the harsh environment of installation, and large forces that are sought to be harnessed. Some apparent considerations on one-time support include:

- + Total subsidy is well defined and hence cannot scale out of hand.
- + No need for complicated calculation of subsidy terms.



- Possibly large sums provided without a guaranty of project continuation.
- Subsidy offers no incentive for technology improvement.
- Possible public uproar against large sums to unproven technology.

#### B. Feed-in tariffs

The production based feed-in tariff is basically a promise to provide an additional €/MWh payment to compensate for the infeasible nature of the low market value of energy. The subsidy agreement is typically given on a time scale of 15-20 years. Since the subsidy is based on performance, they do encourage production of the plant in question. Though an often overlooked fact is that within the feed-in agreement period, a plant does not need to technologically improve to continue eligibility for funding. Thus eliminating the incentive for major device revisions. This means that a device might only be feasible within a feed-in bubble, which when burst, offers no good news for neither developer nor investor.

- + Industries are used to feed-in tariffs which might ease communication.
- + Ensures continued production and operation.
- Difficult to find a rate that satisfies all parties. The feed-in tariffs have been often seen in a range from €20/MWh to €500/MWh, with a typical value of €200/MWh.
- Plants that exceed production estimations can become a runaway drain in subsidy funds if no upper cap is established.
- Difficult to convey reason for significantly larger €/MWh prices to public, even though the total subsidy might be reasonable.
- Plant becomes feasible within the fed-in accounting, which can decelerate technology improvement.
- Uncertainty in level of future feed-in tariffs.

#### IV. IFS SCHEME

The incentive-based financial support (IFS) scheme is developed as a mean to provide a considerable financial support while still maintaining a demand for improvement. Based on case-by-case negotiation a total subsidy amount is fixed, but this total sum can only be unlocked by continuous technical development. As stated earlier, the IFS scheme breaks the year into 10 minute intervals. For each interval where a predetermined production target is met, a fraction of the total subsidy is paid to the developer. The production target is a function of e.g. met-ocean conditions which means that the developer does not need to hope for optimal/rare weather conditions to cover operational expenses. The target curves are individual for each device/concept and are to be estimated from e.g. scaled model test or numerical simulations. They have to be inherently ambitious to attract funding i.e. governmental bodies and/or venture capitalists. It is of paramount importance that the target curves are raised at a predetermined interval of either time or cumulative subsidy. For example, the target curve can be raised on a yearly basis,

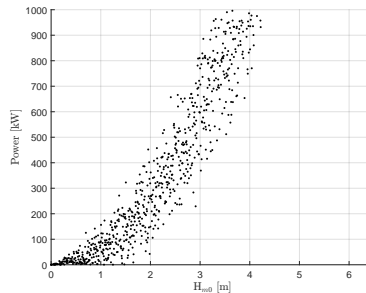


Fig. 2. Estimated production as a function of wave height.

or raised every time another 20% of the total subsidy has been paid. Another term to consider is how long time the developer has to claim the total subsidy. This is to be seen as a tool to urge the developer to utilize all steps of the target curves and hence drive technology forward.

Usually the condition of whether or not IFS target is reached, is determined from the amount of electrical power supplied to the grid. Another modulation of the IFS is that for really early stage devices, without much research in the PTO system, the target curves might only consider mechanical energy, if improvement in this property is the initial goal of the subsidy. It should be mentioned that when a device is under IFS funding, all produced energy can be sold freely to the grid on market terms, thus providing even further incentive for the developer.

- + Fixed total costs.
- + Incentive to strive for improvement in production.
- + Financial support is waived for projects unable to scale accordingly, leaving funds available to be used elsewhere.
- + Ability to compare confidence and outlook devices through target curve ambitions.
- + Possible to reward more immature technologies for capturing mechanical energy.
- + Low possibility for bad publicity since no terms manipulate market prices.
- Case-by-case negotiation.
- Settling terms regarding target curves.

#### A. Setting IFS target curves for WHOOPS

When setting up the production targets for our fictive WHOOPS device, we will first take a look at the performance that the *Clever Guys Inc.* has been able to obtain through numerical simulation and hopefully successful scaled model tests. Fig. 2 shows all the obtained data in full North Sea scale. Since WHOOPS is expected to be grid connected all

figures depicts the amount of energy fed to the public grid.

In the case of wave energy, the total power,  $P$ , is proportional to the wave period,  $T$ , and to the square of the significant wave height  $H_{m0}$ . We would like to only evaluate the production as a function of a single parameter, namely the wave height. When taking the correlation between wave period and wave height into account we end up with a good fit when using a relation of  $P \propto C H_{m0}^{2.08}$ , where  $C$  is a fitting constant. Fig. 3 shows this fitting applied to the production data. Note that the target curve has two distinct cutoffs at both the maximum rated power and a possible storm protection. This red target curve now serves as the benchmark for commercialization.

Through the negotiation between the funding body and the developer, and initial target curve for the first deployed prototype is need to be set. This is a balancing act between a healthy confidence need to impress the funding body, and still setting a goal that with good effort should be obtainable. The target curve is set high enough to show realistic potential of concept, and low enough to account for things as downtime, hydrodynamic efficiency, PTO-efficiency etc. The blue curve in Fig. 4 shows the initial target curve set for WHOOPS when deployed in real sea conditions. This target might seem unreasonably low, but it must be stressed that some immature technologies will encounter difficulties in e.g. downtime and efficiency while the working principle of the concept might still be on the right track.

The next step is to set up the aggressiveness of ambition by describing the path from the initial target curve to the commercial one. This process can be divided into any number of steps, but for WHOOPS an agreement was made on 5 individual steps. The steps which can be seen in Fig. 5 are distributed linearly in both fitting factor  $C$  and maximum rated power. Depending on the device, these values can be logarithmic, exponential, constant or as here linear. The aim is that the target curve fits the expected trajectory of the project development. The chosen target curves are now ready for implementation. If it again is assumed that 10 minute intervals are suitable for this technology, a short example is given in the following: The 1st (blue) target production for a  $H_{m0}$  of 3 m is calculated  $200 \text{ kW} \times \frac{1}{6} \text{ h} = 33.3 \text{ kWh}$ . This target is seen to increase to 100 kWh ( $600 \text{ kW} \times \frac{1}{6} \text{ h}$ ) for the 5th (red) and final target curve. Again, please note that these values are strictly used as example and should not be directly used as recommendations for real life targets.

To provide the WHOOPS device with at stable development economy, it is agreed upon that the total subsidy is to be split into five equal pools. When one pool is depleted after performance evaluation against the 1st target curve, the next pool is unlocked with a requirement of keeping up with the 2nd target curve. This process continues until the total subsidy is depleted. After this development phase is completed, it will

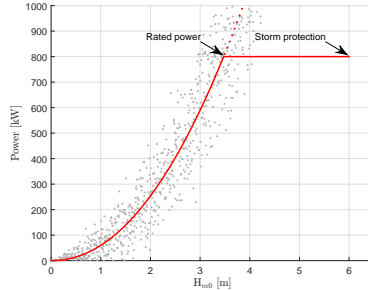


Fig. 3. Target curve for commercial device taking maximum rated power and storm protection into account.

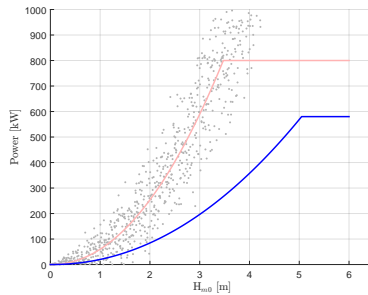


Fig. 4. Target curve for first iteration of prototype.

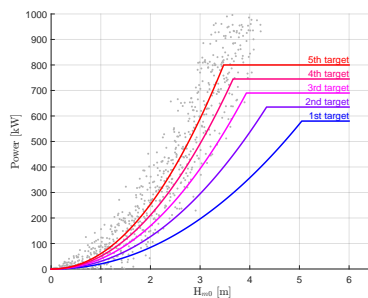


Fig. 5. Feather of suggested target curves.

be necessary that a new negotiation regarding the longer term subsidy of the WHOOPS plant is conducted.

## V. SCHEME COMPARISON

To compare the influence the different schemes for subsidies have on developers and policy makers, they will be applied to yet another test case involving the WHOOPS device. Since this one-time support to a large extent basically is another type of subsidy compared to the feed-in tariff type and the IFS scheme, it will not be covered in the following comparison.

The developers from *Clever Guys Inc.* and representatives from the governmental bodies in charge of handing out national subsidies have had a meeting. It is clear that both parties would like to see the WHOOPS device in a semi-commercial scale within a not too distant future. An agreement is made on the basis of a total subsidy of €5M over 5 years. The government agency quickly disregards the possibility of providing the subsidy as a one-time since it provides no promise of improvement of the WHOOPS technology. This means that the choice is between FIT and IFS.

Based on some of the data from Table I, and while taking device improvement into account, the feed-in tariff is set to €400/MWh. It is also suggested to look at the IFS target curves presented in section IV-A. If everything goes as estimated, the two solutions will amount to the same total subsidy after the 5 year period. Based on continuous device improvements, the cumulated subsidy can be seen in Fig. 6. The blue and red curves show the expected path of the total subsidy amount. The shaded areas depicts the subsidy if the device over- or under-performs during the period. For the FIT scheme this deviation could also be a symptom of a badly estimated feed-in value. It should be noted that for the FIT solution the total subsidy varies with unforeseen behavior. For the IFS scheme only the time, over which the subsidy is awarded, is affected, not the subsidy amount itself.

For the developer, both schemes bears a deal of incentive. Unless a maximum subsidy is agreed upon the FIT offer possibility for a higher total subsidy. The IFS scheme on average provides crucial support early in the process and the total subsidy is promised, given that the targeted production is met. Additionally, the developer is able to sell any produced power at market value.

For the subsidizing party, both schemes seem positive since the total subsidy is only paid if agreed improvements are met. Higher uncertainties in subsidy funds are seen when applying the FIT compared to the IFS scheme. Use of the IFS also avoid granting a €/MWh what is around 4 times that of the general market value.

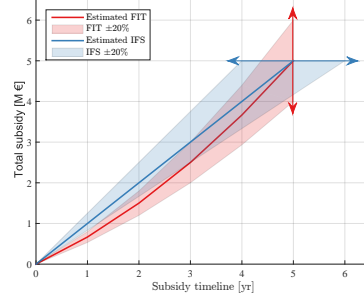


Fig. 6. Cumulative subsidy based on FIT and IFS respectively.

## VI. CONCLUSION

Most renewable energy systems needs support - especially during the start-up phase where large strides are being made on the device development. Multiple support schemes are already in place, mainly throughout Europe. This paper presents a new incentive based support scheme for immature renewable energy systems, referred to as IFS. IFS is capable of providing substantial financial support while still keeping the incentives to improve the proven production values. Furthermore, the use of IFS will, compared to traditional feed-in support, avoid having policy makers present €/MWh numbers grossly out of scale with market values. The subsidy is instead a production bonus based on production compared to performance targets. This means lesser risk for public discontent of subsidy distribution. The IFS has been used with success in Denmark. It is believed that it, if implemented in several countries, can and will promote a commercial breakthrough for renewable energy technologies such as wave and tidal energy systems.

## REFERENCES

- [1] M. Ringel, "Fostering the use of renewable energies in the european union: the race between feed-in tariffs and green certificates," *Renewable energy*, vol. 31, no. 1, pp. 1–17, 2006.
- [2] P. Menanteau, D. Finon, and M.-L. Lamy, "Prices versus quantities: choosing policies for promoting the development of renewable energy," *Energy policy*, vol. 31, no. 8, pp. 799–812, 2003.
- [3] J. A. Lesser and X. Su, "Design of an economically efficient feed-in tariff structure for renewable energy development," *Energy Policy*, vol. 36, no. 3, pp. 981–990, 2008.
- [4] J. G. Vining and A. Muetze, "Economic factors and incentives for ocean wave energy conversion," *Industry Applications, IEEE Transactions on*, vol. 45, no. 2, pp. 547–554, 2009.
- [5] R. Gross, W. Blyth, and P. Heptonstall, "Risks, revenues and investment in electricity generation: Why policy needs to look beyond costs," *Energy Economics*, vol. 32, no. 4, pp. 796–804, 2010.
- [6] C. Fischer and L. Preonas, "Combining policies for renewable energy: Is the whole less than the sum of its parts?" *Resource for the Future Discussion Paper*, no. 10-19, 2010.
- [7] M. Kalkuhl, O. Edenhofer, and K. Lessmann, "Renewable energy subsidies: Second-best policy or fatal aberration for mitigation?" *Resource and Energy Economics*, vol. 35, no. 3, pp. 217–234, 2013.



---

# Paper E

## Verification and Validation of the New Dynamic Mooring Modules Available in FAST v8

Fabian F. Wendt  
Morten Thøtt Andersen  
Amy N. Robertson  
Jason M. Jonkman

The paper has been published in  
*ISOPE*, ISBN:978-1-880653-88-3, 2016.



## Verification and Validation of the New Dynamic Mooring Modules Available in FAST v8

Fabian F. Wendt  
National Wind Technology Center, National Renewable Energy Laboratory.  
Golden, CO, USA  
Morten T. Andersen  
Department of Civil Engineering, Aalborg University.  
Aalborg, Denmark  
Amy N. Robertson, Jason M. Jonkman  
National Wind Technology Center, National Renewable Energy Laboratory.  
Golden, CO, USA

### ABSTRACT

The open-source, aero-hydro-servo-elastic wind turbine simulation software FAST v8 (created by the National Renewable Energy Laboratory) was recently coupled to two newly developed mooring dynamics modules: MoorDyn and FEAMooring. MoorDyn is a lumped-mass-based mooring dynamics module developed by the University of Maine, and FEAMooring is a finite-element-based mooring dynamics module developed by Texas A&M University. This paper summarizes the work performed to verify and validate these modules compared to other mooring models and measured test data to assess their reliability and accuracy. The quality of the fairlead load predictions by the open-source mooring modules MoorDyn and FEAMooring appears to be largely equivalent to that predicted by the commercial tool OrcaFlex. Both mooring dynamic model predictions agree well with the experimental data considering the given limitations in the accuracy of the platform hydrodynamic load calculation and the quality of the measurement data.

**KEY WORDS:** Floating offshore wind turbine; mooring dynamics; modeling; verification; validation; FAST; MoorDyn; FEAMooring

### INTRODUCTION

The analysis and design of a mooring system in floating offshore wind turbines requires reliable predictions of mooring line loads during a broad spectrum of environmental and operating conditions. Fatigue damage is often an important design driver for mooring systems, which makes the reliable prediction of load amplitudes even more important. Prior to the release of FAST v8.12.00a-bjj (October 6, 2015), the only mooring line module available in FAST was MAP++ (Masciola, Jonkman, and Robertson, 2013). MAP++ is a quasi-static mooring module that considers the average mooring line loads and nonlinear geometric restoring, but it does not consider any dynamics that are important for capturing the mooring line extreme and fatigue loads. Therefore, to improve the predictive capabilities in FAST for mooring line loads, recent development efforts have focused on coupling FAST v8 to two dynamic mooring line modules: MoorDyn and FEAMooring.

The improved predictive accuracy of these modules should allow FAST v8 to be used for effective mooring system design and analysis and thus enhance its use as a tool for the design and analysis of floating offshore wind systems.

This paper presents the two new dynamic mooring line modules that have been coupled to FAST, and it validates their load predictions against 1:50-scale wave tank test data obtained from the 2013 DeepCwind test campaign (Helder and Pietersma, 2013). This campaign was conducted at the Maritime Research Institute Netherlands (MARIN) under the direction of the University of Maine. Simulation results from the commercial maritime engineering software OrcaFlex, which has recently been interfaced to FAST v8, are added to the validation to verify the agreement of FAST's new dynamic mooring line modules with an established and widely used commercial design software. Further, the comparison of MoorDyn, FEAMooring, and OrcaFlex modeling results to the results obtained with MAP++ show the improvements that can be obtained with the mooring dynamics modeling capability compared to the quasi-static approach. Only wave cases are considered for the validation and verification conducted in this paper (no cases involved a turbine operating in wind).

### MOORING CODE DESCRIPTIONS

The following subsections describe the various mooring codes that will be examined in this paper.

#### MoorDyn

MoorDyn was developed by Matthew Hall at the University of Maine (Hall, 2015). It is based on a lumped-mass modeling approach that is able to capture mooring stiffness, inertia and damping forces in the axial direction, weight and buoyancy effects, seabed contact forces, and hydrodynamic loads from mooring motion using Morison's equation. Bending and torsional cable stiffness, as well as seabed friction, are not considered. Though not applied here, MoorDyn also allows for modeling segmented cables with multiline connection points (e.g., bridle configurations). MoorDyn has been successfully validated against wave tank test data from a previous 2011 test campaign of the DeepCwind system (Hall and Goupee, 2015).

This validation was conducted with a stand-alone version of MoorDyn as well as with a version that was coupled to a previous release of FAST. Presently, there is no direct coupling between MoorDyn and FAST's HydroDyn module, which means that all hydrodynamic line loads are computed in still-water conditions.

#### FEAMooring

FEAMooring is a finite-element-based mooring line code that was developed at Texas A&M University by Yoon Hyeok Bae (National Renewable Energy Laboratory, 2015). The utilized rod elements account for axial elastic stretching; axial structural damping; mass/inertia; seabed contact; geometric nonlinearities from large motion; buoyancy; and hydrodynamic drag, added mass, and inertia loads (the latter from Morison's equation). FEAMooring does not consider line bending or torsion, seabed friction, multisegmented mooring arrangements with line interconnections, clump weights, or buoyancy tanks. As with MoorDyn, wave kinematics are not considered for the calculation of the hydrodynamic line loads, meaning that the hydrodynamic load calculations assume still water. During its development, FEAMooring went through an internal verification at Texas A&M University, but it has not been validated against wave tank test data prior to the work presented in this paper.

#### MAP++

MAP++ is the previously available quasi-static mooring model available in FAST v8 that was developed by Marco Masciola while both at the National Renewable Energy Laboratory (NREL) and the American Bureau of Shipping (Masciola, Jonkman, and Robertson 2013). It is a relatively simple model that allows for a robust, first-pass evaluation of a mooring system by considering the average mooring line loads and nonlinear geometric restoring for both catenary and taut mooring systems. MAP++ simultaneously solves the nonlinear analytical catenary equations for individual lines with elastic stretching and the apparent weight of the lines in water as well as the force-balance equations at the line-to-line interconnection points (for two or more lines) where clump weights and buoyancy tanks may also be located. MAP++ also accounts for seabed friction. MAP++ does not consider any dynamic line loads (neither structural inertia nor hydrodynamic drag and inertia loads), nor does it consider line-bending stiffness and the three-dimensional shape of lines (each individual line in MAP++ lies within a vertical two-dimensional plane). MAP++ went through a thorough code-to-code verification, which was carried out at NREL as part of the verification of the new hydrodynamic capabilities available in FAST v8 (Wendt et al., 2015). Considering the given limitations of MAP++, we found that the platform motion itself can be predicted quite accurately by the coupled FAST v8-MAP++ modeling approach. Prior to this paper, MAP++ had been validated against wave tank test data on numerous occasions (Prowell et al., 2013; Coulling et al., 2013a; Colling et al., 2013b).

#### OrcaFlex

OrcaFlex is a comprehensive commercial maritime engineering tool that is widely used for the design and analysis of floating systems in the offshore industry. It contains a proprietary lumped-mass-based mooring line model that has been extensively verified and validated against real-world systems on multiple occasions (Orcina, 2015b). It is capable of computing wave-kinematics-induced cable loads, which are presently not included in MoorDyn and FEAMooring. The mooring modeling capabilities of OrcaFlex are described in Orcina (2015a). OrcaFlex has recently been interfaced to FAST v8 and is considered the benchmark solution in this paper.

## PLATFORM AND TURBINE MODEL

### Physical Model Tested in Wave Tank

The system being investigated in this study is the DeepCwind semisubmersible floating wind turbine that was tested at MARIN in 2013 (Helder and Pietersma, 2013), which builds on testing performed for a similar system in 2011.

Fig. 1 illustrates the geometry of the system, which was designed by the University of Maine. The same platform and mooring geometry (but at full scale) was used in the OC4-DeepCwind semisubmersible system examined within the International Energy Agency (IEA) Wind Task 30 Offshore Code Comparison Collaboration Continuation (OC4) project. Compared to OC4, only the scale and turbine changed: the OC4 project used the idealized NREL 5-MW turbine, and the 2013 tests used the MARIN stock wind turbine, which mimics the power, thrust, and torque characteristics of the NREL 5-MW turbine as best as possible at model scale but has slightly different scaled-mass properties. The appropriate power and thrust characteristics were achieved through special low-Reynolds-number-specific airfoils in combination with a modified chord length distribution (Goupee et al., 2015). A wave elevation sensor located at approximately 356.5 m on the port side of the system (full scale) was used to measure the wave elevation during the tank tests. A cable bundle that connects the measurement sensors installed on the floating system to the corresponding data acquisition system is shown in Fig. 1. The system tested at MARIN is being used in the IEA Wind Task 30 OC4 and Offshore Code Comparison Collaboration, Continued with data Correlation (OC5) project. Although only wave cases are used in this paper, wind-only and wind-plus-wave cases are being considered in OC5.



Fig. 1. DeepCwind semisubmersible system as tested in MARIN's ocean basin. Photo by Andy Goupee, University of Maine

### Numerical Platform Model

The numerical models of the DeepCwind system created in FAST v8 follow the properties of the ocean basin model as closely as possible. The numerical models were created at full scale; whereas the testing was done at 1:50 scale. (All results presented here are at full scale.)



The hydrodynamic platform model uses a hybrid combination of a potential-flow-based approach with additional viscous drag computed for all submerged members via FAST's hydrodynamics module (HydroDyn). The transverse and axial member drag coefficients were tuned using measurements from free-decay tests that were performed and can be found in Table 8 in the mooring section of this paper (the axial drag coefficients were used for the offset base columns). To match the linear damping characteristics of the model during small-amplitude free-decay oscillations, an additional linear damping matrix was included. Two preloads as well as an additional linear stiffness term in the surge direction, acting on the platform reference point (which is the intersection point of the tower-centerline/free surface), were introduced to model the influence of the measurement cable bundle (whose properties were not measured). The preloads were tuned based on the first regular wave test. Further details on the preload tuning for the first regular wave case are given in the validation section of this paper. The additional linear stiffness term was tuned to match the rigid-body surge eigenfrequency. The numerical values for the additional linear damping matrix, the additional stiffness matrix and the additional preloads that have been added to the platform model can be found in the appendix. The potential-flow model is based on frequency-dependent wave diffraction excitation and radiation added mass and damping matrices from WAMIT (2013). The HydroDyn model also considers the second-order sum- and difference-frequency wave-excitation loads derived from quadratic transfer functions, which were also computed via WAMIT. The utilized WAMIT model did not include an evaluation of the free-surface integral, which means that the sum-frequency potential term is only approximated here.

#### MOORING SYSTEM MODEL

The following section describes the analyzed catenary mooring system and its modeling in the investigated mooring modules.

#### Mooring System as Implemented in the Wave Tank

The mooring system installed in the 2013 MARIN tests examined here consisted of three equally spaced catenary mooring lines called BOW, PSA, and SBA (Fig. 2). In the ocean basin, waves propagate from the bottom to top of Fig. 2. The same mooring system was also used in the OC4-DeepCwind semisubmersible system (Robertson et al., 2014). Unlike many oil- and gas-related deepwater platform wave tank tests, where catenary mooring systems are modeled through truncated mooring configurations, the mooring system in MARIN's ocean basin was actually implemented in its full catenary configuration with significant portions of the lines resting on the seabed. Brass chains were used to ensure the correct underwater weight of the mooring lines. The mooring line loads were recorded through small load cells at the fairleads, and a small spring at the anchor point was introduced to ensure the correct axial stiffness of the mooring system during larger displacements (Helder and Pietersma, 2013). According to MARIN and visible in the test results, some level of hysteresis was present in the mooring system during the tests. This means that the displaced system does not necessarily return to its exact initial position. This hysteresis makes it difficult to assess the surge and sway position measurements because there is a certain level of uncertainty related to the corresponding equilibrium position.

The full-scale mooring line properties as described by MARIN are given in the upcoming table and figure. The three fairleads are equally spaced on a 40.87-m radius around the center of the platform and connect to the platform 20 m below the still-water line. The anchor points are based on a 837.6-m radius and are located at a water depth of 200 m.

Table 1. Mooring system properties as described by MARIN (Helder and Pietersma, 2013)

Line	Properties complete mooring line				Pretension [kN]
	Mass in air [ton]	Subm. weight [kN]	Stiffness [kN/m]	Length [m]	
BOW	105.1	901.7	893	835.50	1112
PSA	104.8	899.7	895	835.50	1148
SBA	104.9	905.1	900	835.50	1107

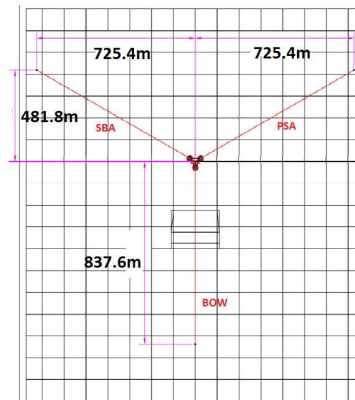


Fig. 2. Mooring system as installed (Helder and Pietersma, 2013)

#### Mooring System as Implemented in MAP++

The specifics of the mooring system geometry (anchor and fairlead positions and line length) used in MAP++ fall in line with what was described by MARIN in the previous section. The line diameter was calculated from the data given in Table 1, and the average value of all three mooring lines was assigned to each line in the MAP++ model. A similar approach was used for the cross-sectional axial line stiffness. The line properties that were used for all three lines in MAP++ are summarized in Table 2.

Table 2. MAP++-specific mooring system properties

Property	Assigned Value
Line diameter (m)	0.1389
Mass density per unit length in air (kg/m)	125.5935
Axial cross-sectional line stiffness (N)	748,608,000
Unstretched line length (m)	835.5

**Mooring System as Implemented in MoorDyn**

The MoorDyn model basically follows what was specified for the corresponding MAP++ model, but because of MoorDyn’s lumped-mass-based dynamic modeling approach, several additional parameters needed to be specified. The most important parameters are given in the following table.

Table 3. MoorDyn-specific mooring system properties

Property	Assigned Value
Internal, structural line damping coefficient (% critical)	5
Transverse added-mass coefficient (-)	0.865
Tangential added-mass coefficient (-)	0.269
Transverse drag coefficient (-)	1.404
Tangential drag coefficient (-)	0.213
Number of line segments (-)	20

The transverse and tangential hydrodynamic coefficients were based on values described for a previous MoorDyn validation project that was also based on the DeepCwind semisubmersible system (Hall and Goupee, 2015). In this previous validation project, the hydrodynamic coefficients were derived from the recommendations given in the corresponding DNV guidelines (DNV, 2013; DNV, 2007; DNV, 2004). The drag coefficients were prescribed considering the 1:50 scale of the model. The transverse drag coefficient has been increased from its initial value of 1.08, as described in Hall and Goupee (2015), to a value of 1.404. This was done to match the fairlead load amplitude predicted by MoorDyn to the corresponding fairlead load amplitude observed in the MARIN test data during the first regular wave test. The chosen line discretization of 20 subsegments for each line was based on a convergence study of the fairlead load signal.

**Mooring System as Implemented in FEAMooring**

Although the FEAMooring input parameters vary significantly from those used in MAP++ and MoorDyn, the parameters were set to be consistent with the equivalent input parameters in MAP++ and MoorDyn. The FEAMooring-specific parameters that were used are shown in the table below.

Table 4. FEAMooring-specific mooring system properties

Property	Assigned Value
Displaced mass per unit length (kg/m)	15.484
Inertia force per unit length normalized by acceleration (kg/m)	28.877
Drag force per unit length normalized by velocity squared (kg/m <sup>2</sup> )	99.791
Initial fairlead tension (N)	5E+04

The displaced mass per unit length (LD) in FEAMooring is related to the line diameter used in MAP++/MoorDyn:

$$LD = \pi \cdot d_{line}^2 \cdot \rho_{water} / 4 \tag{1}$$

where  $d_{line}$  is the diameter of the mooring line, and  $\rho_{water}$  is the density of the water in the wave tank (1,025 kg/m<sup>3</sup>).

The inertia force per unit length normalized by acceleration (LCI) in FEAMooring is related to the line diameter and transverse added-mass coefficient used in MoorDyn:

$$LCI = \rho_{water} \cdot C_i \cdot \pi \cdot d_{line}^2 / 4 \tag{2}$$

where  $C_i$  is the transverse mooring line inertia coefficient, which is calculated as  $C_i = 1 + C_{at}$ ; and the value for the transverse added-mass coefficient  $C_{at}$  is given in Table 3. The drag force per unit length normalized by velocity squared (LCD) is related to the line diameter and the transverse drag coefficient used in MoorDyn:

$$LCD = \rho_{water} \cdot C_{dt} \cdot d_{line} / 2 \tag{3}$$

The value for the transverse mooring line drag coefficient  $C_{dt}$  is given in Table 3.

The initial fairlead tension and the line length affect the axial deformation of the line elements in FEAMooring (especially important for tension-leg platforms). For ease of use with catenary moorings, where it is desirable to set the line length equal to the unstretched length, we found that doing so required setting a small pretension to avoid numerical problems in FEAMooring. The selected pretension equals approximately 4% of the mean fairlead load of the mooring lines. An alternative approach would be to set the initial fairlead tension (in the vertical direction) based on the difference between the platform buoyancy and floating wind system weight and consequently define the line length as the corresponding stretched line length. Both approaches were found to produce similar results.

Following the MoorDyn model, each line has been discretized into 20 subelements. Increasing the number of elements was not found to have a significant impact on the fairlead load signal.

**Mooring System as Implemented in OrcaFlex**

The OrcaFlex mooring system model is based on the MoorDyn mooring model discussed previously. The hydrodynamic coefficients specified for MoorDyn are also used in the OrcaFlex model, so carrying over the line properties and mooring system properties to OrcaFlex was a straightforward process. Each line has been discretized into 20 subsegments.

VALIDATION OF GLOBAL PROPERTIES

**Force-Displacement Curve**

The first step to validate the numerical mooring models was a comparison of the simulated versus measured force-displacement curve. This static analysis produced the same fairlead loads for all mooring line modules, which is why only the MAP++ results are shown in the following figure.

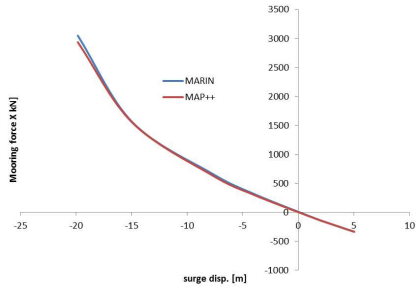


Fig. 3. Force-displacement curve validation

The simulation results for the static offset analysis shown in Fig. 3 agree well with the corresponding experimental results and capture the nonlinear geometric restoring for large platform surge offsets. The force displacement curve in Fig. 3 shows the total restoring force in the x-direction (sum of all three fairlead load x-components).

In these results and the results to follow, positive surge is defined upward in Fig. 2, positive sway is defined to the left in Fig. 2, and positive heave is defined opposite gravity. Positive roll, pitch, and yaw are rotations about the positive surge, sway, and heave directions, respectively.

#### Free-Decay-Based Damping and Frequency Analysis

In a second step, the damping and frequency characteristics of the floating platform were analyzed and compared to the corresponding values measured at MARIN (Table 5–Table 7). All frequency and damping values were derived from free-decay tests. The linear and quadratic damping coefficients ( $p$  and  $q$ ) were computed based on the algorithm described in Helder and Pietersma (2013). No significant differences in the free-decay platform response were found between the two dynamic mooring line modules, which is why only one set of simulated free-decay results are shown, labeled NREL.

Table 5. Natural frequencies of platform rigid-body modes

	Surge (Hz)	Sway (Hz)	Heave (Hz)	Roll (Hz)	Pitch (Hz)	Yaw (Hz)
MARIN	0.0094	0.0089	0.0571	0.0305	0.0308	0.0124
NREL	0.0092	0.0088	0.0575	0.0306	0.0301	0.0121
Delta (%)	-1.4230	-0.1438	0.8157	0.5512	-1.9953	-2.2144

Table 6. Linear damping of rigid-body modes,  $p$  coefficients as defined in (Helder and Pietersma 2013)

	Surge (-)	Sway (-)	Heave (-)	Roll (-)	Pitch (-)	Yaw (-)
MARIN	0.1095	0.0795	0.0094	0.0648	0.0579	0.1446
NREL	0.1109	0.0757	0.0090	0.0627	0.0578	0.1406
Delta (%)	1.3409	-4.7078	-3.4392	-3.2366	-0.0556	-2.7306

Table 7. Quadratic damping of rigid-body modes,  $q$  coefficients as defined in Helder and Pietersma (2013)

	Surge (1/m)	Sway (1/m)	Heave (1/m)	Roll (1/deg)	Pitch (1/deg)	Yaw (1/deg)
MARIN	0.1242	0.1265	0.2733	0.0625	0.0686	0.0165
NREL	0.1198	0.1146	0.2729	0.0707	0.0676	0.0433
Delta (%)	-3.4709	-9.3670	-0.1326	13.1207	-1.4166	162.653

The frequencies of the platform rigid-body modes agree very well between the experiment and simulation. The linear damping characteristics show good agreement as well because these values were tuned by prescribing a linear damping matrix in HydroDyn (main-diagonal elements of the linear damping matrix only). The quadratic drag was also tuned by adjusting the transverse and axial member drag coefficients of the platform members (values summarized in Table 8). Although it is unclear why, this tuning process yielded a single-sided axial member drag coefficient of 3.9, which is significantly lower than the double-sided drag coefficient of 4.8 that is oftentimes used to model viscous drag effects of heave plates. This single-sided drag coefficient of 3.9 is only applied to the bottom of the main columns. For this particular study, sway, roll, and yaw motion were not of major concern, which is why the resulting large discrepancies for these degrees of freedom in Table 7 were not addressed.

Table 8. Platform member drag coefficients

Property	Assigned Value
Transverse member drag coefficient (-)	1.2
Axial member drag coefficient, (applied at the bottom of the three offset base columns) (-)	3.9

#### VALIDATION OF SYSTEM RESPONSE

Two regular wave cases and two irregular wave cases were used to validate the response of the system to wave excitation. The first regular wave case was used to do some tuning of the system properties (preload and mooring drag coefficient), so only the second regular wave case and the irregular wave cases are strictly validation cases.

#### Regular Wave Case 1 (Height = 7.37 m, Period = 12.07 s)

The wave train used in the two regular wave simulations was based on the wave elevation signal measured during the experiment. The original wave elevation signal was band-pass filtered to its first-order component, and second-order wave terms were then numerically added to the first-order wave. This is a standard technique that was recently verified to produce reasonable results for regular wave cases within Phase Ib of the IEA Wind Task 30 OC5 project (Robertson et al., forthcoming). The simulation considers second-order sum- and difference-frequency excitation through quadratic transfer functions computed by WAMIT. A comparison between the simulated platform motion and the measured platform response during the experiment for the first regular wave case is shown in Fig. 4–Fig. 6. OrcaFlex results are not shown in the platform motion plots because the platform motion was externally prescribed for the OrcaFlex simulations. This is explained further at the end of this subsection.

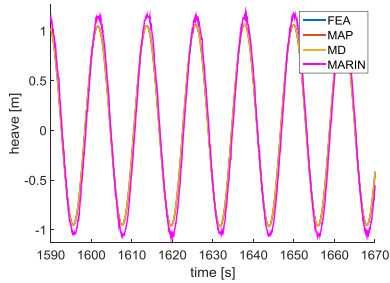


Fig. 4. Platform heave motion during regular wave case 1

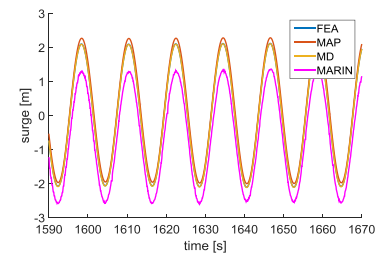


Fig. 5. Platform surge motion during regular wave case 1

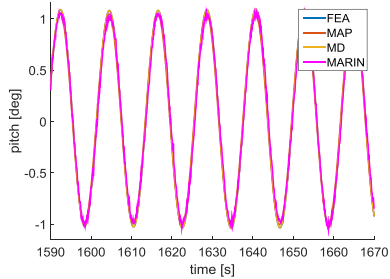


Fig. 6. Platform pitch motion during regular wave case 1

For all mooring modules, the platform motion agrees within reasonable limits with the experimental data. The heave motion is slightly underpredicted by the simulations, whereas the surge motion amplitude is slightly overpredicted. The assessment of the experimental surge mean value has proven to be difficult. The experimental surge mean value varies from one load case to another, which is potentially related to hysteresis effects in the mooring system or due to inconsistencies in

the optical surge position measurement. The initial surge position for this particular test case (prior to the influence of any waves) has been subtracted from the MARIN surge signal shown in Fig. 5. At this point, it is not clear whether the difference in the surge mean between simulation and experiment is related to drift effects that are potentially inaccurately captured by the FAST v8 hydrodynamics model or to measurement/hysteresis-related issues in the experimental data.

The corresponding mooring line loads are shown below. To reduce the number of plots shown in this paper, only one of the two lateral fairlead load signals is shown (SBL) in addition to the upstream fairlead (BOW). Because of the symmetry of the system, both lateral fairlead load signals behave relatively similar.

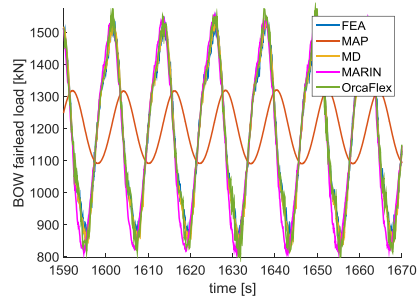


Fig. 7. BOW fairlead load signal during regular wave case 1

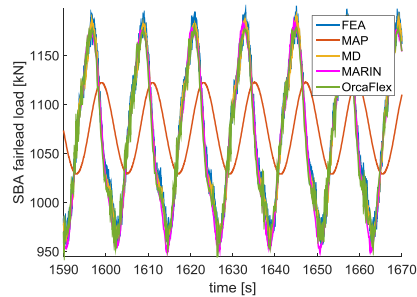


Fig. 8. SBA fairlead load signal during regular wave case 1

Very good agreement was found between the fairlead loads predicted by the simulation and the corresponding experimental data. FEAMooring (FEA) and MoorDyn (MD) basically predict the same fairlead loads. MAP++ (MAP) captures the mean load, but the phase and amplitude of the dynamic load components are very different. The fairlead load amplitudes predicted by MAP are significantly underpredicting the actual fairlead load amplitudes recorded during the experiment (MARIN). As previously mentioned, two preloads acting at the platform reference point were introduced to the FAST platform

model. The purpose of these preloads was to mimic the influence of the measurement cable bundle that was attached to the platform in the wave tank (and whose properties were not measured). The magnitude of these preloads was selected so that the fairlead load mean values for regular wave case 1 match the experimental data. Thus, the mean fairlead load level is captured accurately by all three mooring line modules.

In addition to the simulations performed in FAST, results from OrcaFlex are included here as well. To make the comparison consistent between FAST and OrcaFlex, the platform motion from the FAST v8 + MoorDyn simulation was used as input for OrcaFlex to achieve the exact same platform motion independent of the platform hydrodynamics model. (The new interface between FAST v8 and OrcaFlex was not used here.) This route was chosen due to discrepancies that were evident between FAST v8 coupled to OrcaFlex and FAST v8 standalone. The computation of hydrodynamic platform loads in OrcaFlex has several differences when compared to the approach used in HydroDyn. Because this paper is focused on the mooring system, prescribing the platform motion externally for OrcaFlex was the best option to achieve a direct comparison between OrcaFlex and the other mooring modules, without the need to explain and account for the differences that arise from varying approaches in the hydrodynamic platform load calculation. Because the platform motion was prescribed externally, no wave kinematics or platform hydrodynamics were computed within OrcaFlex. However, a capability that is unique to OrcaFlex (relative to MoorDyn and FEAMooring) is the computation of wave-kinematics-induced hydrodynamic loads on the mooring lines. To evaluate the influence of these load components on the global fairlead load signal, one simulation was run with still water, and an additional simulation was conducted that used the prescribed platform motion from FAST v8 + MoorDyn in combination with the OrcaFlex internal wave kinematics. However, no significant influence from the wave-kinematics-induced hydrodynamic line loads on the overall fairlead load signal was found (Fig. 9).

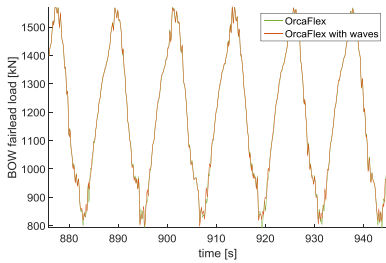


Fig. 9. Influence of the wave-kinematics-induced hydrodynamic line loads on the BOW fairlead load signal during regular wave case 1

The table below compares the averaged minima, the averaged maxima, and the overall mean values computed during the last 1,000 s of the simulation/experiment from the BOW fairlead load signal.

Table 9. BOW fairlead load statistics for regular wave case 1

	FEA	MD	MAP	ORCA	MARIN
Averaged maxima (kN)	1533.10	1531.08	698.21	1568.43	1553.55
Averaged minima (kN)	856.71	838.24	630.83	823.78	811.92
Mean (kN)	1194.69	1192.60	1199.37	1190.26	1182.63

These statistical metrics fall in line with what was discussed earlier for the time series plots and support the very good agreement among the three dynamic mooring line modules and the experimental data from MARIN.

### Regular Wave Case 2 (Height = 9.41 m, Period = 14.3 s)

The sea state prescribed for the second regular wave case is significantly more severe than the first. The corresponding platform motions from the experiment and the simulations are shown below.

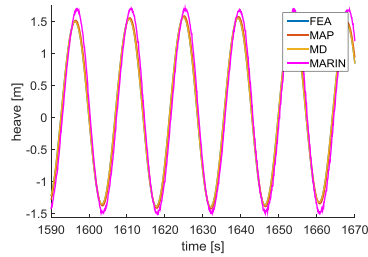


Fig. 10. Platform heave motion during regular wave case 2

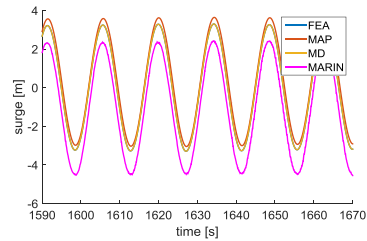


Fig. 11. Platform surge motion during regular wave case 2

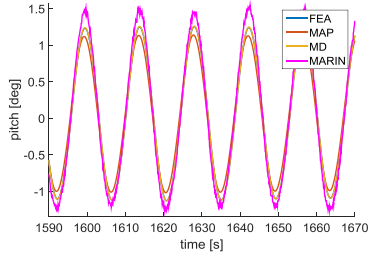


Fig. 12. Platform pitch motion during regular wave case 2

All FAST v8 simulations underestimated the platform motion amplitudes, and the platform pitch motion amplitude is most significantly underpredicted. A possible reason for this could be because the FAST v8 hydrodynamics model presently does not consider any wave stretching to the instantaneous free surface. An additional simulation using the OrcaFlex internal hydrodynamics model with vertical wave stretching, instead of prescribing the platform motion, showed an increase in the platform pitch motion amplitude. This points toward the influence of hydrodynamic drag components acting above the mean sea level position. The results from this additional OrcaFlex simulation are shown in Fig. 13.

A similar difference in the surge mean value between the experiment and simulations as discussed for the first regular wave case can also be found in the second regular wave case.

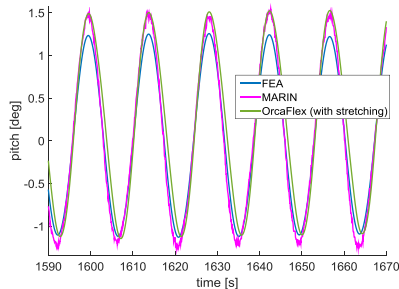


Fig. 13. Influence of wave stretching on the platform pitch response

The mooring line loads for the more severe regular wave case show larger differences between the simulations and experiment compared to what was shown for the first regular wave case. Because the mooring line loads are mainly controlled by the platform motion, these differences are at least somewhat expected. However, the consistency among MoorDyn, FEAMooring, and OrcaFlex is excellent. The BOW and SBA fairlead loads are shown below. As described for the first regular wave case, the platform motion of the OrcaFlex model was externally prescribed using the corresponding simulation results from the FAST+MoorDyn simulation.

The implementation of wave stretching into HydroDyn is planned for 2016, which will potentially reduce the differences in platform motion between the experiment and simulations and therefore also improve the agreement between the measured and predicted fairlead loads.

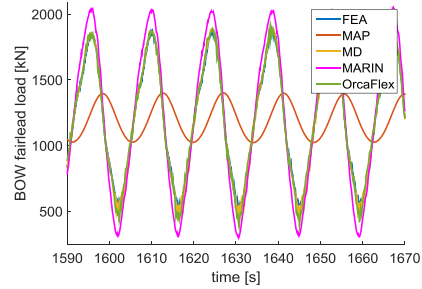


Fig. 14. BOW fairlead load during regular wave case 2

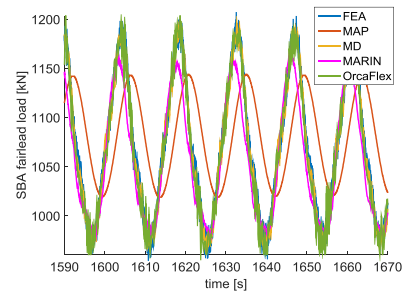


Fig. 15. SBA fairlead load during regular wave case 2

The averaged mean, maxima, and minima during the last 1,000 s of the BOW fairlead load signal further quantify the differences between predicted fairlead loads and the experimental MARIN data.

Table 10. BOW fairlead load statistics for regular wave case 2

	FEA	MD	MAP	ORCA	MARIN
<b>Averaged maxima (kN)</b>	1864.65	1871.58	721.76	1873.78	2052.64
<b>Averaged minima (kN)</b>	532.87	481.09	608.22	431.35	301.72
<b>Mean (kN)</b>	1189.43	1187.93	1198.18	1186.33	1204.31

### Irregular Wave Analysis

For the irregular wave case, the wave elevation signal from the experiment was directly used as input for HydroDyn, and no filtering

was applied. This approach was found to be favorable for irregular wave cases because it is difficult to adequately reduce an irregular wave elevation to its first-order component. The second-order WAMIT sum- and difference frequency quadratic transfer functions were not used for this case to avoid potentially double-booking the second-order components that are already present in the unfiltered wave elevation signal.

Two irregular wave load cases were simulated. Based on the results shown for the regular wave simulations, the analysis and discussion of the irregular wave results focuses on the load case with the more severe sea state: significant wave height = 10.5 m, peak-spectral wave period = 14.3 s, and peak-shape parameter = 3.0 based on a JONSWAP spectrum. The platform motion for the relevant degrees of freedom is shown in the figures below.

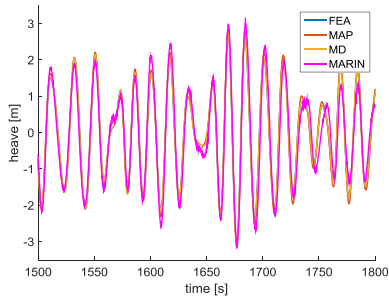


Fig. 16. Platform heave motion during severe irregular waves

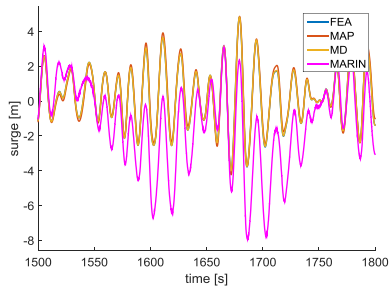


Fig. 17. Platform surge motion during severe irregular waves

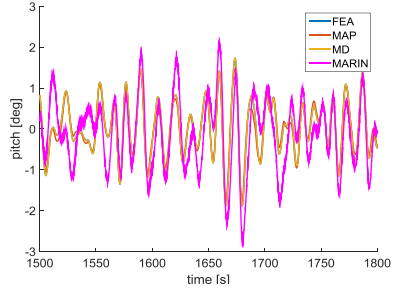


Fig. 18. Platform pitch motion during severe irregular waves

The predicted platform motions from the simulations follow the overall trend of the actual platform motion that was recorded during the measurement campaign. The differences between the simulations and experiment in the surge and pitch responses are assumed to be mainly related to the platform hydrodynamic load calculation. The FAST v8 simulation uses linear airy wave theory without any wave stretching. Especially for larger waves, nonlinear components in the wave kinematics become more important. These components are not captured by the utilized modeling approach. The same uncertainty regarding the mean value of the surge signal discussed for the regular wave load cases also applies to the irregular wave load cases, which means that the accuracy of the experimental surge mean value is potentially affected by hysteresis effects and artifacts in the optical surge position measurement.

The corresponding fairlead load signals for this severe sea state are shown below. As previously discussed for the regular wave cases, the platform motion in OrcaFlex was externally prescribed, using the results from the FAST+MoorDyn simulation.

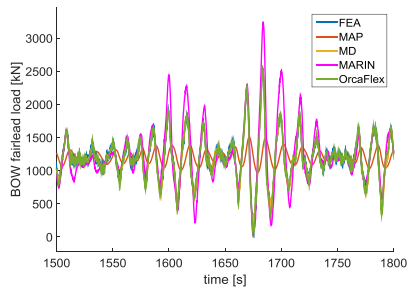


Fig. 19. BOW fairlead load during severe irregular waves

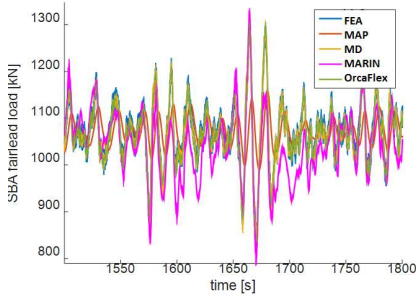


Fig. 20. SBA fairlead load during severe irregular waves

Considering the differences between the simulations and experiment in the pitch and surge motion, the mooring line loads are captured relatively well for all results, except for MAP, which captures only the means well. The differences between MAP and the dynamic mooring modules do not have a large influence on the resulting platform motions. MoorDyn, FEAMooring, and OrcaFlex also agree very well. Fig. 21 shows an extreme event during which the fairlead load drops to near zero (a slack line event). The successive load recovery predicted by MoorDyn, FEAMooring, and OrcaFlex agrees very well with the experimental data.

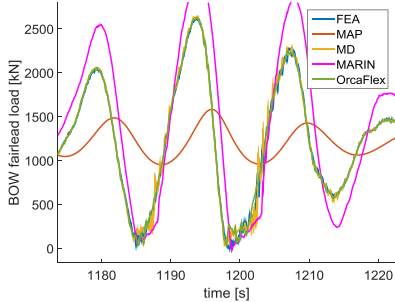


Fig. 21. BOW fairlead load during slack line tension events

Applying a rainflow-counting scheme over the BOW fairlead load time series yields the following load cycle mean value and amplitude histograms (Fig. 22–Fig. 23).

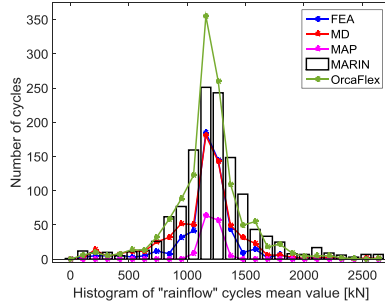


Fig. 22. Histogram of BOW fairlead rainflow cycle means

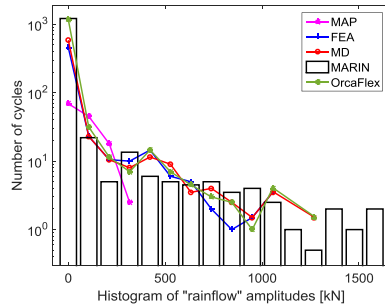


Fig. 23. Histogram of BOW fairlead load rainflow amplitudes

These histograms are useful to assess the capability of the mooring line modules to accurately predict the fatigue load spectra of the fairlead load signals. The two histograms were generated from the last 1,000 s of the BOW fairlead load signal. Because all mooring modules have a certain level of noise in their fairlead load time series output, a low-pass frequency-domain filter with a linearly ramped cutoff from 2.5–3 Hz was applied to all simulation results to reduce the impact of these high-frequency oscillations on the results of the rainflow count.

Based on Fig. 22, the dominant mean value of the fairlead load oscillations is accurately captured by all mooring line modules. The actual number of load cycles per mean value is slightly overpredicted by the OrcaFlex solution and slightly underpredicted by the MoorDyn and FEAMooring solution. The OrcaFlex solution contains the largest amount of high-frequency content around 1 Hz (Fig. 24). In the time domain, this manifests as small amplitude, high-frequency oscillations. These oscillations are responsible for the high number of OrcaFlex low-amplitude rainflow cycles shown in Fig. 23. The increased overall number of oscillations due to this small amplitude/high-frequency content is also clearly evident in Fig. 22, and it is probably related to the prescribed platform motion. OrcaFlex simulations that do not rely



on a prescribed platform motion did not show this high-frequency content.

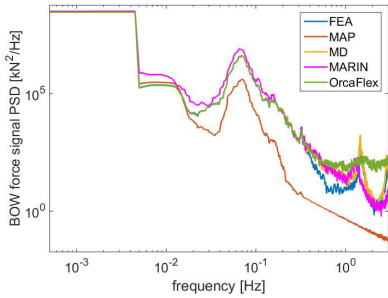


Fig. 24. PSD plot of BOW fairlead load signal (log-log scale)

The most extreme load amplitudes measured are not captured by any mooring line module. Though not presented here, the applied low-pass filter was investigated as a potential source for this issue, but it was not shown to have an effect on the number of high-amplitude fatigue cycles. Instead, very nonlinear steep waves were found to produce large surge motion amplitudes in the MARIN data that are not captured in the FAST simulations. One of these events is depicted in Fig. 17 (1,650–1,700 s). These steep waves extend far above the still-water line and introduce significant loads on the substructure. By modeling only the hydrodynamics up to the still-water line, these extreme loads are not accurately captured, which causes an underprediction of the mooring line extreme fatigue load amplitudes. Regardless, the general trend of the number of cycles per load amplitude curve is successfully predicted by all dynamic mooring line modules for the remainder of the load amplitude spectrum, which demonstrates their general usability as tools for the assessment of mooring line fatigue loads.

### CONCLUSIONS

Three dynamic mooring line modules and one quasi-static module have been validated against wave tank measurement data (without the turbine operating in wind). The quality of the fairlead load predictions by the open-source mooring modules MoorDyn and FEAMooring appear to be largely equivalent to what is predicted by the commercial tool OrcaFlex. All three mooring dynamic model predictions agree well with the experimental data considering the given limitations in the accuracy of the platform hydrodynamic load calculation and the quality of the measurement data. Although the mean loads and resulting platform motion are satisfactory, the quasi-static mooring module MAP++ was not able to adequately predict the fairlead load amplitudes during the investigated regular and irregular wave cases, as expected.

For the two regular wave cases, especially for the one with the smaller wave height, very good agreement was found between the simulations and the measured fairlead loads. The regular wave case with increased wave height showed modest differences between the simulations and experiment in the platform-surge and -pitch motion amplitudes, which led to differences in the corresponding fairlead load signals. These differences most likely originate from nonlinearities that are not accurately captured by the platform hydrodynamics model.

The analysis of an irregular wave case with severe waves also showed similar differences between the simulations and the experiment. Treating wave kinematics and hydrodynamic loads above the still-water level could potentially improve the simulation results. Besides the fact that a small number of rainflow cycles with large load amplitudes were not captured by the simulations, the fatigue spectrum of the fairlead load signal is sufficiently reproduced by all mooring dynamic modules. Extreme events with near-zero line tension and the following fairlead load recovery were also accurately predicted by all mooring dynamic modules.

The coupling of MoorDyn and FEAMooring to FAST v8 extends the capability of FAST for detailed mooring system design and analysis. Further, all mooring modules are very similar in terms of the required computational expenses, and they are not a major contributor to the required simulation time of FAST v8 floating offshore wind turbine simulations.

### ACKNOWLEDGMENTS

This work was supported by the U.S. Department of Energy under Contract No. DE-AC36-08GO28308 with the National Renewable Energy Laboratory. Funding for the work was provided by the DOE Office of Energy Efficiency and Renewable Energy, Wind and Water Power Technologies Office. The authors thank the University of Maine for supplying the MARIN data.

### APPENDIX

The tables below state the additional linear damping matrix, platform stiffness matrix, and preloads that have been added to the platform model to mimic the behavior of the model that was tested in the wave tank. For further comments on these parameters, please refer to the numerical platform model section.

Table 11. Additional linear platform damping matrix (N/(m/s), N/(rad/s), N-m/(m/s), N-m/(rad/s))

3.6665E+04	0	0	0	0	0
0	1.6017E+04	0	0	0	0
0	0	1.1802E+04	0	0	0
0	0	0	7.6802E+07	0	0
0	0	0	0	7.1399E+07	0
0	0	0	0	0	6.3425E+07

Table 12. Additional platform stiffness matrix (N/m, N/rad, N-m/m, N-m/rad)

5000	0	0	0	0	0
0	7000	0	0	0	0
0	0	0	0	0	0
0	0	0	0	0	0
0	0	0	0	0	0
0	0	0	0	0	0

Table 13. Additional preloads, acting on the platform (N, N-m)

Surge	Sway	Heave	Roll	Pitch	Yaw
14E4	1E4	0	0	0	0

## REFERENCES

- Coulling, A, Goupee, A, Robertson, A, Jonkman, J, and Dagher, H (2013a). "Validation of a FAST Floating Wind Turbine Model Using Data from the DeepCwind Semi-Submersible Model Tests," Proc. WINDPOWER 2013 Conf and Exhib, Chicago, IL.
- Coulling, A, Goupee, A, Robertson, A, Jonkman, J, and Dagher, H (2013b). "Validation of a FAST Semi-Submersible Floating Wind Turbine Numerical Model with DeepCwind Test Data," *J Renewable and Sustainable Energy* 5, 29-37.
- DNV (2013). DNV-OS-E301: Position Moorings, Høvik Norway: DNV.
- DNV (2007). DNV-RP-C205: Environmental Conditions and Environmental Loads, Høvik, Norway: Det Norske Veritas.
- DNV (2004). DNV-RP-F205: Global Performance Analysis of Deepwater Floating Structures, Høvik, Norway: V.
- Goupee, A, Kimball, R, Ridder, E, Helder, J, Robertson, A, and Jonkman, J (2015). "A Calibrated Blade-Element/Momentum Theory Aerodynamic Model of the MARIN Stock Wind Turbine," presented at ISOPE, Kona, HI. NREL/CP-5000-63568. Golden, CO: National Renewable Energy Laboratory.
- Hall, M (2015). MoodDyn User's Guide. Orono, ME: Department of Mechanical Engineering, University of Maine.
- Hall, M, and Goupee, A (2015). "Validation of a Lumped-Mass Mooring Line Model with DeepCwind Semisubmersible Model Test Data," *Ocean Engineering* 104: 590-603.
- Helder, J, and M Pietersma (2013). UMAINE—DEEPCWIND/OC4 SEMI FLOATING WIND TURBINE, 27005-1-OB. Wageningen, Netherlands: MARIN.
- Masciola, M, Jonkman, J, and Robertson, A (2013). "Implementation of a Multisegmented, Quasi-Static Cable Model," Proc Twenty-Third International Offshore and Polar Engineering, Anchorage, AK, USA, ISOPE, 1.
- National Renewable Energy Laboratory (2015). NWTC Information Portal (FEAMooring), October 12. <https://nwtc.nrel.gov/FEAMooring> (accessed Jan. 19, 2016).
- Orcina (2015a). OrcaFlex Features. October 22. <http://www.orcina.com/SoftwareProducts/OrcaFlex/Features/index.php> (accessed January 19, 2016).
- Orcina (2015b). OrcaFlex Validation. October 22. <http://www.orcina.com/SoftwareProducts/OrcaFlex/Validation/> (accessed Jan. 19, 2016).
- Prowell, I, Robertson, A, Jonkman, J, Stewart, G, and Goupee, A (2013). "Numerical Prediction of Experimentally Observed Scale-Model Behavior of an Offshore Wind Turbine Supported by a Tension-Leg Platform," presented at Offshore Technology Conference, Houston, TX. NREL/CP-5000-57615. Golden, CO: National Renewable Energy Laboratory.
- Robertson, A, et al. (2014). Definition of the Semisubmersible Floating System for Phase II of OC4. NREL/TP-5000-60601. Golden, CO: National Renewable Energy Laboratory
- Robertson, A, et al. (forthcoming). "OC5 Project Phase Ib: Validation of Hydrodynamic Loading on a Fixed, Flexible Cylinder for Offshore Wind Applications," Proc 13th Deep Sea Offshore Wind R&D Conference, Trondheim, Norway.
- WAMIT, Inc. (2013). WAMIT User Manual Version 7.0. Chestnut Hill, MA.
- Wendt, F, Robertson, A, Jonkman, J, and Hayman, G (2015). "Verification of New Floating Capabilities in FAST v8," Proc AIAA SciTech 2015. Kissimmee, FL: AIAA

---

# Paper F

## Verification and Validation of Multisegmented Mooring Capabilities in FAST v8

Morten Thøtt Andersen  
Fabian F. Wendt  
Amy N. Robertson  
Jason M. Jonkman  
Matthew Hall

The paper has been published in  
*ISOPE*, ISBN:978-1-880653-88-3, 2016.



## Verification and Validation of Multisegmented Mooring Capabilities in FAST v8

Morten T. Andersen<sup>1</sup>, Fabian F. Wendt<sup>2</sup>, Amy N. Robertson<sup>2</sup>, Jason M. Jonkman<sup>2</sup>, Matthew Hall<sup>3</sup>

<sup>1</sup>Department of Civil Engineering, Aalborg University  
Aalborg, Denmark

<sup>2</sup>National Renewable Energy Laboratory,  
Colorado, USA

<sup>3</sup>Department of Mechanical Engineering, University of Maine  
Orono, Maine, USA

### ABSTRACT

The quasi-static and dynamic mooring modules of the open-source aero-hydro-servo-elastic wind turbine simulation software, FAST v8, have previously been verified and validated, but only for mooring arrangements consisting of single lines connecting each fairlead and anchor. This paper extends the previous verification and validation efforts to focus on the multisegmented mooring capability of the FAST v8 modules: MAP++, MoorDyn, and the OrcaFlex interface. The OC3-Hywind spar buoy system tested by the DeepCwind consortium at the MARIN ocean basin, which includes a multisegmented bridle layout of the mooring system, was used for the verification and validation activities. This paper focuses on free-decay tests because the influence of the multisegmented moorings is most important for yaw motion, which is not excited by waves. All of the listed modules are able to represent the platform motion observed in the experimental data to a satisfactory degree. MoorDyn and the benchmark tool (OrcaFlex) yield almost indistinguishable results. But due to limitations of the system tested and data obtained, further work is needed to truly validate the multisegmented capability.

**KEY WORDS:** Floating offshore wind turbine; multisegmented mooring; modeling; verification; validation

### INTRODUCTION

Offshore wind turbines are designed and analyzed using simulation tools (i.e., computer design codes) capable of predicting the coupled dynamic loads and responses of the system to prescribed environmental conditions. As these turbines are moved to deeper waters, the substructure used to fix the system to the sea floor is replaced

by a floating platform constrained by moorings. For these floating systems, the ability to accurately predict the loads in the mooring lines is integral to the design process to ensure the safe operation of the offshore turbines.

Two tools that are commonly used for the design of floating offshore wind systems are the open-source aero-hydro-servo-elastic wind turbine simulation tool FAST, developed by the National Renewable Energy Laboratory (NREL), and FAST coupled to the commercial-software tool OrcaFlex. To achieve a more accurate estimation of the loads in the mooring lines without using OrcaFlex, the newest version of FAST (version 8) was updated to include two new mooring modules: MoorDyn and FEAMooring. These mooring modules are in addition to the previously available mooring module, MAP++. The two new mooring modules offer the capability of modeling the dynamics of the mooring lines, which greatly improves the accuracy of the mooring load predictions, as demonstrated in the verification and validation of these modules in (Wendt et al., 2016). In addition, MoorDyn offers the ability to model multisegmented lines, such as a bridle connection, which is important for some mooring configurations. MAP++ also offers the capability of modeling multisegmented moorings, but it does not consider the dynamics of the mooring lines. This paper focuses on verifying and validating the capabilities of FAST v8 in modeling systems that have multisegmented mooring designs, which is possible using either the MAP++ or MoorDyn mooring modules. (FEAMooring does not have this capability.)

The verification and validation of the multisegmented mooring capability was performed using the OC3-Hywind spar buoy system (Fig. 1) tested by the DeepCwind consortium at the MARIN ocean basin (Goupee et al., 2012). This system was chosen because the

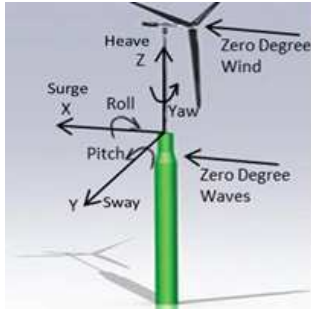


Fig. 1. Convention for degrees of freedom of the system.

platform relies on a multisegmented bridle layout of the moorings to obtain sufficient yaw stiffness, and both numerical and experimental data are available. Verification was accomplished by comparing simulations of the OC3-Hywind system with the two mooring modules (MAP++ and MoorDyn) to simulations performed in FAST v8 coupled to OrcaFlex. OrcaFlex (OrcaFlex, 2015a) is a comprehensive commercial maritime engineering tool that is widely used for the design and analysis of floating systems in the offshore industry, and the mooring line modeling capabilities have therefore already been extensively verified and validated (OrcaFlex, 2015b). Validation was then accomplished by comparing the simulations from all three models to measured test data from the DeepCwind test campaign (Goupee et al., 2012). The validation in this paper is limited to the use of free-decay tests because the influence of the multisegmented moorings is most important for yaw motion, which is not sufficiently excited in the wave tests. Due to limitations of the system tested and data obtained, further work is needed to truly validate the multisegmented capability.

Moreover, the comparison of the MoorDyn and OrcaFlex modeling results to the results obtained from MAP++ show the improvements obtained with the mooring dynamics modeling capability. In addition, the MAP++ and MoorDyn modeling results with the multisegmented mooring layout (Fig. 2) are compared to those from models that have single mooring lines (bisecting the bridle) and an additional yaw spring to augment the yaw stiffness, as has been considered in previous FAST-based studies of the OC3-Hywind system, to show the improvements obtained by the multisegmented modeling capability. But ultimately the aim is to circumvent the need for this by proper direct modeling of the multisegmented moorings via the new mooring capabilities in FAST v8.

The remainder of this paper is outlined as follows. The next section provides a description of the properties and differences among each of the mooring modules that are compared in the paper.

Then the properties of the OC3-Hywind system are given, along with the tuning that was needed to get the models of this system to better match the response seen during testing. Results are presented and discussed in terms of impact on verification and validation. Finally, conclusions are drawn, and recommendations based on the work are given.

## MOORING MODULE DESCRIPTIONS

### MAP++

MAP++ is the previously available quasi-static mooring model available in FAST v8 that was developed by Marco Masciola while both at the NREL and the American Bureau of Shipping (Masciola et al., 2013). It is a relatively simple model that allows for a robust first-pass evaluation of a mooring system by considering the average mooring line loads and nonlinear geometric restoring for both catenary and taut mooring systems. MAP++ simultaneously solves the nonlinear analytical catenary equations for individual lines with elastic stretching and the apparent weight of the lines in water as well as the force-balance equations at the line-to-line interconnections points (for two or more lines), where clump weights and buoyancy tanks may also be located. MAP++ also accounts for seabed friction, which is presently not considered by the two new dynamic mooring modules, MoorDyn and FEAMooring. MAP++ does not consider any dynamic line loads (neither structural inertia nor hydrodynamic drag and inertia loads), nor does it consider line bending stiffness and the three-dimensional shape of lines (each individual line in MAP++ lies within a vertical two-dimensional plane). MAP++ went through a thorough code-to-code verification, which was carried out at NREL as part of the verification of the new hydrodynamic capabilities available in FAST v8 (Wendt et al., 2015). MAP++ has also been validated against wave tank test data from test campaigns with singlesegment mooring lines (Wendt et al., 2016) (Coulling et al., 2013) (Prowell et al., 2013). Prior to this publication, MAP's multisegmented mooring line capabilities had not been validated against wave tank test data.

### MoorDyn

MoorDyn was developed by Matthew Hall at the University of Maine (Hall, 2015). It is based on a lumped-mass modeling approach that is able to capture mooring stiffness and damping forces in the axial direction, weight and buoyancy effects, seabed contact forces (without friction) and hydrodynamic loads from mooring motion using Morison's equation. Bending and torsional cable stiffness are not con-

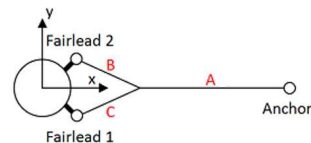


Fig. 2. Top view; conceptual sketch of bridle mooring configuration.

sidered. MoorDyn also allows for modeling segmented cables with multiline connection points (e.g., bridle configurations). Presently, there is no direct coupling between MoorDyn and FAST's HydroDyn module, which means that all hydrodynamic line loads are computed in still-water conditions. For a system without multiline connections, MoorDyn has been successfully validated against wave tank test data from a previous 2011 test campaign of the DeepCwind system (Hall and Goupee, 2015). This validation was conducted with a stand-alone version of MoorDyn as well as with a version that was coupled to a previous release of FAST. The verification and validation of this dynamic mooring module coupled to FAST v8 can be found in Wendt et al. (2016).

#### FAST-OrcaFlex

OrcaFlex is a comprehensive commercial maritime engineering tool that is widely used for the design and analysis of floating systems in the offshore industry. It contains a proprietary lumped-mass-based mooring line model that has been extensively verified and validated against real-world systems (OrcaFlex, 2015b). OrcaFlex is considered the benchmark solution in this paper.

#### MODEL DESCRIPTION

##### General Model Properties

The current model of the OC3-Hywind spar is based on the work of Browning et al. (2014). The experiments have all been conducted at 1:50 scale, but in the present paper all dimensions and results are reported in full-scale values. The DeepCwind tests of the OC3-Hywind were conducted with taut mooring, which will also be the case for the models presented in this paper. Table 1 shows some of the dominant characteristics of the system. Note that the values presented for the mooring are mainly from the DeepCwind test campaign. Changes to these values to better match the experimental data as suggested by Browning et al. (2014), are the platform displacement and the mooring line length, diameter, mass, and stiffness. Added mass and drag coefficients for the lines are standard values proposed by Hall (2015).

##### Model Configurations

FAST v8 models with five different mooring configurations were built for comparison:

1. MAP++ with three single mooring lines (bisecting the bridle).
2. MAP++ with three multisegmented bridle moorings.
3. MoorDyn with single mooring lines (as in 1, but with mooring dynamics via MoorDyn)
4. MoorDyn with multisegmented bridle moorings (as in 2, but with mooring dynamics via MoorDyn)
5. OrcaFlex with multisegmented moorings (as in 4, but with OrcaFlex) – considered the benchmark in the comparisons.

For simplicity, the capabilities of the five different model setups are listed in Table 2. To obtain comparable results, the quasi-static single

Table 1. Model properties of full-scale OC3-Hywind turbine concept.

<b>Wind Turbine</b>	
Tower-Base Height (above MSL)	10.0 m
Hub Height	89.6 m
Blade Length	61.5 m
Tower-Top Mass	394.5 $10^3$ kg
Tower Mass	303.1 $10^3$ kg
<b>Platform</b>	
Total Length	130.0 m
Draft	120.0 m
Diameter (of Main Draft)	9.4 m
Displacement	7947.8 m <sup>3</sup>
Platform Mass	7279.6 $10^3$ kg
Platform Roll and Pitch Inertia*	3966.2 $10^6$ kg m <sup>2</sup>
Platform Yaw Inertia*	98.6 $10^6$ kg m <sup>2</sup>
* Defined about the platform center of mass.	
<b>Mooring</b>	
Fairlead Depth	70.0 m
Fairlead Radius	5.2 m
Anchor Depth	200.0 m
Anchor Radius	445.0 m
Unstretched Single Line Length	450.5 m
Unstretched Line Length, A	423.6 m
Unstretched Line Length, B, and C	30.0 m
Line Diameter	90.0 $10^{-3}$ m
Mass per Length	13.5 kg/m
Cross-sectional Axial Stiffness (EA)	106.0 $10^9$ N
Transverse Added Mass Coefficient	1.0 -
Tangential Added Mass Coefficient	0.0 -
Transverse Drag Coefficient	1.6 -
Tangential Drag Coefficient	0.1 -

Table 2. Overview of model configurations

	Quasi-static	Dynamic
Single line	Model 1	Model 3
Multisegmented line	Model 2	Models 4 & 5

line model (1) needs an additional yaw spring-damper to augment the yaw response as has been used in previous FAST-based studies of the OC3-Hywind system. This is, to a lesser degree, also the case for Models 2 and 3. This yaw spring-damping will be described later.

**Model Calibration**

All models have been tuned with an additional platform heave damping of  $71 \times 10^3$  N-m/(rad/s) to better match the heave free-decay of the system (Browning et al., 2014). The different mooring configurations are expected to have a significant impact on the yaw stiffness and damping. As mentioned, the simplified mooring layout with a single line from anchor to fairlead can be tuned to closely match the behavior of a multisegmented mooring configuration (at least in terms of response of the spar). This paper will determine estimates for the required additional yaw stiffness and damping via physical system decay tests.

**RESULTS**

From the DeepCwind test campaign at MARIN, different data sets are available. These sets include decay tests, regular wave tests, irregular wave tests, as well as sets with different combinations of wind/waves. It is important to note that the models simulated via the FAST/OrcaFlex interface have both their moorings and hydrodynamics solved externally in OrcaFlex. This gives rise to some inherent minor discrepancies relative to the results with standalone FAST because the differences in the input are more extensive than only altering mooring configurations.

**Decay Tests**

Decay tests are useful for system identification and tuning. In the following they are used to display the simulated decay tests because they also grant information on how well the different model configurations are able to represent the system behavior.

**Translational Decay**

Fig. 3 and 4 show that all models calculate the translational free decay response of the system very well. The error in surge and heave natural frequencies is low, and the minor discrepancies at the end of each decay test can be explained by other degrees of freedom being excited; no pure single degree of freedom oscillation is maintained. In the heave decay, all models maintain the same oscillation; whereas in the surge decay, the dynamic mooring solvers match the experimental response slightly better than the quasi-static. This can be explained by the fact that the heave response is mainly driven by the hydrostatic stiffness of the system, and on the contrary, the surge stiffness is solely obtained via the mooring lines.

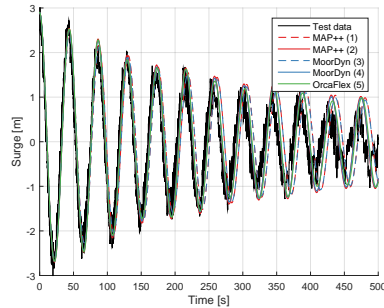


Fig. 3. Surge decay test.

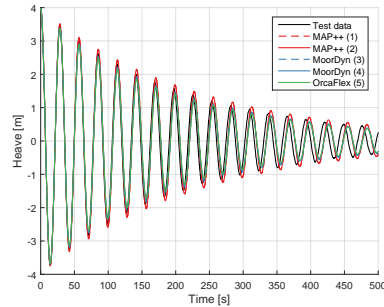


Fig. 4. Heave decay test.



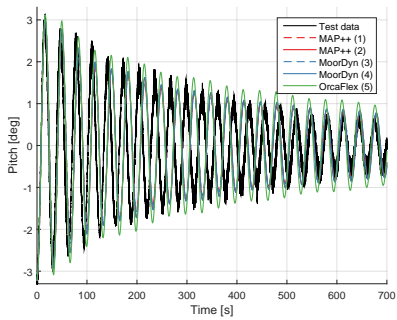


Fig. 5. Pitch decay test.

When observing the damping, all five models agree fairly well in the surge decay. The heave decay shows a little wider spread among the different models. There is, as expected, hardly any difference between the single/multisegmented mooring configuration. The main difference is observed between the quasi-static and the dynamic mooring solvers. Here the MAP++ simulations are slightly underdamped and the MoorDyn and OrcaFlex simulations are slightly overdamped compared to the measured data. This difference between the quasi-static and dynamic mooring solver is to be expected, and is a result of the extra damping captured by the mooring line drag. It should be mentioned that the two multisegmented dynamic solutions (Models 4 and 5), are practically indistinguishable.

#### Rotational Decay

Fig. 5 shows the decay of the system in pitch. Here, the mooring has very little influence on the motion of the system, which is mainly driven by the inertia versus the hydrostatic stiffness. The slight uneven changes of the amplitude during the decay can be explained by the fact that a pitching system of this type will almost certainly excite a small surge motion. The discrepancy between the damping of the four models running HydroDyn and the benchmark model running OrcaFlex, is mainly due to the differences in the viscous drag modeling. The member geometry and viscous drag coefficient definition in OrcaFlex and FAST v8 are inherently different, which makes the corresponding tuning procedure too tedious for the scope of this paper.

When observing the yaw decay in Fig. 6, a vastly bigger difference is seen among the different models. This is to be expected because the yaw stiffness and damping of the system is mainly, if not only, driven by the mooring system. At this point, we have not yet

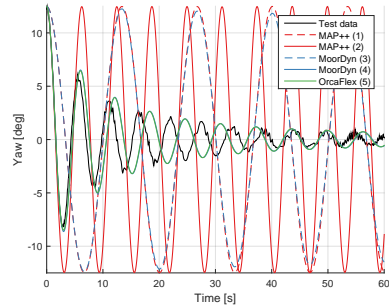


Fig. 6. Untuned yaw decay response. Models 4 and 5 indistinguishable.

applied any artificial yaw stiffness or damping. Fig. 6 serves to show the performance and inherent differences between the models. It is clearly seen that both the stiffness and damping are not well captured by the single line models (1 and 3). The quasi-static multisegmented simulation (Model 2) captures a better estimate of the stiffness of the system while still not obtaining any damping, as expected. The dynamic multisegmented solutions (Models 4 and 5) are once again in complete agreement, leaving the blue and green lines indistinguishable in the figure. They capture the damping of the system very well, but with small differences for the stiffness relative to the MARIN test data. This shows the benefit of direct modeling. The difference in yaw stiffness between the numerical models and the test data might be due to the cable bundle that hung from the system during tests, or the fact that the decay tests had significant motions in the surge and sway degrees of freedom (likely due to how the free-decay was initiated at MARIN).

To obtain better representations of the yaw response of the system, some additional tuning is done. For all systems, additional linear yaw stiffness, linear yaw damping and/or quadratic yaw damping were added. Because the damping is already well captured by the dynamic multisegmented simulations (Models 4 and 5), the adjustment of the stiffness in these models is straightforward. On the contrary, the tweaking of the linear and quadratic damping of the other models can be quite tedious. This is again seen as a clear benefit of the direct modeling of the physical system. The parameters needed to adjust each model are shown in Table 3. The damping values are found by visual fitting, and presented in the correct order of magnitude. Fig. 6 shows a minor difference between the damping of Models 1 and 3, and hence these will also have different additional tuning values if an even more precise estimate is needed.

Fig. 7 shows the response of the tuned models. They all obtain

Table 3. Additional yaw stiffness and damping applied to each model.

	Linear Stiffness	Linear Damping	Quadratic Damping
	N-m/rad	N-m/(rad/s)	N-m/(rad/s) <sup>2</sup>
MAP++ (1)	$140 \times 10^6$	$10 \times 10^6$	$100 \times 10^6$
MAP++ (2)	$35 \times 10^6$	$10 \times 10^6$	$100 \times 10^6$
MoorDyn (3)	$140 \times 10^6$	$10 \times 10^6$	$100 \times 10^6$
MoorDyn (4)	$35 \times 10^6$	-	-
OrcaFlex (5)	$(35 \times 10^6)$	-	-

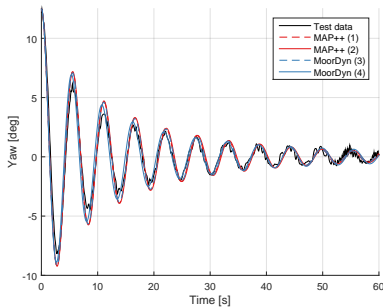


Fig. 7. Yaw decay test.

good representations of the desired behavior. Note that OrcaFlex is left out of the figure. This is due to the fact that in OrcaFlex it is not possible to make external changes to the hydrostatic stiffness in surge, sway, and yaw (hence why the linear stiffness for OrcaFlex in Table 3 is marked with parentheses). Due to the exact match between the multisegmented MoorDyn simulation and OrcaFlex for the un-tuned case, the adjustment of the models are expected to be identical.

Besides observing the motion response of the system, an important factor in the mooring design is the mooring line tension. Fig. 8 shows the mooring line tension at one of the anchors during a yaw decay from a large initial yaw angle (15 degrees). A purely numerical comparison was chosen because the measured mooring line tensions under the yaw decay were highly dominated by the system surge and sway motions, and hence not highlighting the differences between the models. To be able to compare all five models, the extra linear yaw stiffness of  $35 \times 10^6$  N-m/rad from was neglected from models 2, 4 and 5, and models 1 and 3 were instead tuned by  $105 \times 10^6$  N-m/rad. Fig. 8 shows a good match between multisegmented models, and a near perfect match between Models 4 and 5. The two quasi-static models both underestimate the tension in the mooring lines. The dominant underlying frequency in Fig. 8 is roughly twice that

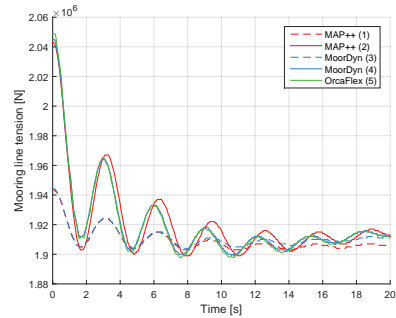


Fig. 8. Tension in mooring lines at anchor during yaw decay.

of Fig. 7 because the tension peaks at the peak of both the maximum and minimum yaw angles.

**Wave Tests**

When examining the system response in different sea states, not much difference is seen among the spar motions from the four FAST v8 models. This is to be expected because the difference in the mooring configurations have very little influence on the major system motions excited by the passing wave – surge, pitch, and heave. Fig. 9 shows the measured surge response from a regular wave test. The waves in the presented test had a wave height of 10.74 m and a period of 14.3 s, and the same realization of the wave time series was fed into each model. There are some differences in energy levels, but all models capture the same main dynamics of the system as those shown in the decay simulations.

**DISCUSSION**

In the surge, heave and pitch degrees of freedom, very little difference between the mooring configurations is seen. As stated earlier, the OC3-Hywind tests at MARIN was conducted with taut mooring, and the inherent properties of a taut moored spar buoy minimize the influence of the station keeping system. The interesting differences occur in the investigation of the yaw response of the system. Due to the inherently large yaw stiffness of the taut system, the only significant yaw motion is seen in the yaw decay tests, and hence the focus has been put in calculating this behavior.

Fig. 6 explicitly shows the main differences between the system properties captured when using a quasi-static or a dynamic mooring solver. It also highlights the influence of properly modeling the multisegmented bridle mooring configuration. It is evident that the combination of multisegmented mooring and a dynamic

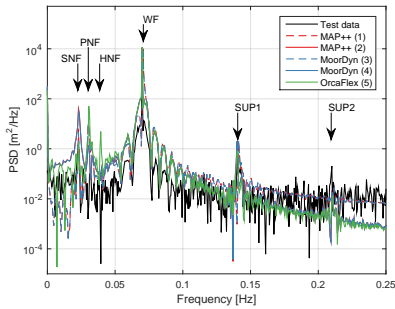


Fig. 9. Spectral density of the surge motion observed in regular waves. Annotation: Surge natural frequency (SNF), pitch natural frequency (PNF), heave natural frequency (HNF), wave frequency (WF), 1<sup>st</sup> wave super harmonic (SUP1) and 2<sup>nd</sup> wave super harmonic (SUP2).

mooring solver yields a good system description without tuning the system. This is a significant benefit when designing systems where experimental data is not available for response tuning.

While the dynamic multisegmented solver proves to describe the system well without tuning, Fig. 7 shows that all the models can of course be tuned to better match experimental data. While all models are able to match the response of the system, a difference is still seen in the anchor loads in Fig. 8, meaning that for mooring design, the dynamic multisegmented approach is suggested.

## CONCLUSION

Five different model configurations have been validated against wave tank measurement data. Two of these models (one single line and one multisegmented bridle configuration) use the dynamic mooring code MoorDyn coupled to FAST v8. The quasi-static mooring code MAP++, also coupled to FAST v8, is used for the next two models that use a single line and bridle mooring system configuration, respectively. The fifth model is a dynamic multisegmented bridle mooring model, relayed through the commercial tool OrcaFlex, coupled to FAST v8 - this last solution serves as a benchmark for the performance of the other models.

The investigation of the different models showed that the approach of modeling a multisegmented bridle system through a single mooring line, in combination with additional tuning of platform stiffness and damping, can achieve satisfactory results, but also that the direct modeling of the actual multisegmented mooring system yields far more desirable results (especially with respect to the predicted anchor/fairlead loads). The results obtained from dynamic multisegmented simulations were close to identical between the

open-source module MoorDyn and the commercial tool OrcaFlex, which serves as verification of MoorDyn's modeling capabilities.

For system motions not dominated by the mooring system, all five configurations described the system well, and little difference was seen between the models. The only true differences were observed in the fairly stiff yaw free-decay motion. Due to limitations of the system tested and data obtained, further work is needed to truly validate the multisegmented capability. To further investigate the influence of multisegmented mooring on floating wind turbine foundations in the future, a slack mooring layout combined with an operating wind turbine excited by misaligned turbulent winds could be of interest.

The introduction of multisegmented mooring capabilities in FAST v8 extends the capability of FAST for detailed mooring system design and analysis. Further, all mooring modules are very similar in terms of the required computational expenses, and they are not a major contributor to the required simulation time of FAST v8 floating offshore wind turbine simulations.

## ACKNOWLEDGEMENTS

For the NREL authors, this work was supported by the U.S. Department of Energy under Contract No. DE-AC36-08GO28308 with the National Renewable Energy Laboratory. Funding for the work was provided by the DOE Office of Energy Efficiency and Renewable Energy, Wind and Water Power Technologies Office.

## REFERENCES

- Browning, J., Jonkman, J., Robertson, A. and Goupee, A. (2014), "Calibration and Validation of a Spar-Type Floating Offshore Wind Turbine Model Using the FAST Dynamic Simulation Tool", in 'Journal of Physics: Conference Series', Vol. 555, IOP Publishing, p. 012015.
- Coulling, A., Goupee, A., Robertson, A., Jonkman, J. and Dagher, H. (2013), "Validation of a FAST Floating Wind Turbine Model Using Data from the DeepCwind Semi-Submersible Model Tests", in 'WINDPOWER 2013 Conf and Exhib, Chicago, IL', AWEA.
- Goupee, A., Koo, B., Lambrakos, K., Kimball, R. et al. (2012), "Model Tests for Three Floating Wind Turbine Concepts", in 'Proc Offshore Technology Conf.', OTC.
- Hall, M. (2015), "MoorDyn Users's Guide". Orono, ME: Department of Mechanical Engineering, University of Maine.
- Hall, M. and Goupee, A. (2015), "Validation of a Lumped-Mass Mooring Line Model with DeepCwind Semisubmersible Model Test Data", in 'Ocean Engineering vol.104 590-603'.
- Masciola, M., Jonkman, J., Robertson, A. et al. (2013), "Implementation of a Multisegmented, Quasi-Static Cable Model", in 'The Twenty-third International Offshore and Polar Engineering Conference, Anchorage, Alaska, ISOPE, Vol 1.

OrcaFlex (2015a), <http://www.orcina.com/SoftwareProducts/OrcaFlex/>. Accessed: 2016-01-23.

OrcaFlex (2015b), 'Orcaflex validation', <http://www.orcina.com/SoftwareProducts/OrcaFlex/Validation/index.php>. Accessed: 2016-01-23.

Prowell, I., Robertson, A., Jonkman, J., Stewart, G. and Goupee, A. (2013), "Numerical Prediction of Experimentally Observed Scale-Model Behavior of an Offshore Wind Turbine Supported by a Tension-Leg Platform", *in* 'Proc Offshore Technology Conf.', OTC.

Wendt, F., Andersen, M. T., Robertson, A. N. and Jonkman, J. M. (2016), "Verification and Validation of the New Dynamic Mooring Modules Available in FAST v8", *in* 'To be presented at The Twenty-sixth International Offshore and Polar Engineering Conference, Rhodes, Greece', ISOPE.

Wendt, F., Robertson, A., Jonkman, J. and Hayman, G. (2015), "Verification of New Floating Capabilities in FAST v8", *in* 'Proc AIAA SciTech 2015', American Institute of Aeronautics and Astronautics.

---

# Paper G

## Practical Low Cost Aerodynamic Thrust Emulation for Froude Scaled Wind Turbines

Morten Thøtt Andersen  
Fancesco Ferri

The paper is accepted in, and under review for  
*Experimental Techniques*, ISSN: 1747-1567, 2016.



# Practical Low Cost Aerodynamic Thrust Emulation for Froude Scaled Wind Turbines

Morten Thøtt Andersen<sup>1\*</sup> and Francesco Ferri<sup>1</sup>

## Abstract

For verifying the dynamics of floating structures, Froude scaled model tests are regularly conducted due to the proven accuracy of the scaled hydrodynamic behavior. When testing model scaled wind turbines, Reynold scaling is applied to ensure similarity of the drag dominated viscous forces on the blades. These two model laws conflict in the field of conceptual testing of floating offshore wind turbines where an even scaling of the entire model is not possible. This paper describes a method to circumvent this issue, by only scaling the aerodynamic thrust force of the turbine to match the Froude scaled floating foundation. This approach also alleviates the need for intricate generation of correctly scaled wind fields over the wave basin when testing. While this concept amounts to a much simpler model setup, one of the trade-offs is for example not being able to recreate the correct gyroscopic effect of the rotating turbine blades. In this paper the thrust emulation is conducted in a fixed position setup to verify the concept, but the application is aimed at installation of a floating foundation.

## Keywords

Aerodynamic Thrust; Floating Offshore Wind Turbines; Experimental Testing; Concept Verification

<sup>1</sup>Dept. of Civil Engineering, Aalborg university, Aalborg, Denmark  
\*e-mail: mta@civil.aau.dk

## Contents

<b>1</b>	<b>Introduction</b>	<b>1</b>
<b>2</b>	<b>Methods</b>	<b>2</b>
2.1	Setup description	2
2.2	Load time series	3
2.3	Algorithm	3
2.4	Calibration and System identification	4
<b>3</b>	<b>Results</b>	<b>4</b>
3.1	Tower Response	4
3.2	Fan Calibration	5
3.3	Frequency Sweep Test	5
3.4	Time Series Performance	5
<b>4</b>	<b>Analysis</b>	<b>6</b>
4.1	Discussion	6
<b>5</b>	<b>Conclusion</b>	<b>8</b>
	<b>References</b>	<b>8</b>

This provides ideal conditions for generation of wind power and hence the offshore areas are deemed a large untapped energy resource [1].

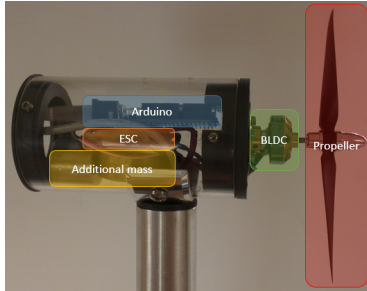
The issue with offshore wind turbines is that they require more elaborate foundation design than their onshore counterparts. Despite this the biggest wind farms in the world are placed in shallow to intermediate waters at water depths rarely exceeding 30 m [2]. Some countries have vast coastal areas that fall under this region, while some barely have any. With the growth of the wind energy sector these scarce locations are quickly getting populated, and the focus is shifting towards installation of offshore wind turbines in even deeper waters. These factors have led the investigation of the concept of floating offshore wind turbines (FOWTs).

This paper revolves around one of the technical issues of experimental testing floating offshore wind turbines. Scaled models tests are a valuable tool in determining and verifying the hydrodynamic behavior of any floating structure, but in the case where the FOWT is exposed to inertia dominated hydrodynamic loads and viscous drag dominated aerodynamic loads, the task of scaling is not trivial [3]. The correct scaling of inertial loads entails a constant Froude number, while the conservation of viscous forces is done by ensuring equality in Reynolds number. Both can not be obtained by the same scaling factors. In the present work the aim is to exclude the need for aerodynamic scaling and only mimic the thrust force exerted by the wind turbine on the floating foundation. In

## 1. Introduction

The benefits from installing wind turbines offshore as opposed to onshore are many. Some of the more contextual benefits come in the form of not causing visual and audible nuisance to populated areas. A more direct technical benefit is the high energy resource as the wind speeds at open seas are higher and more stable due to the lower surface shear and longer fetches.

## Practical Low Cost Aerodynamic Thrust Emulation for Froude Scaled Wind Turbines — 2/8



**Figure 1.** RNA including control components constructed to emulate wind turbine thrust load time series.

this way the entire model can be Froude scaled and coherent forces can be expected.

The thrust force excitation needs to be noninvasive on the dynamic response and movement range of the system in question. Hence, tactile excitation is no an option. Instead a fan is mounted at the position of the turbine, and the air exhausted in the upwind direction will be scaled to match the thrust force experienced of the chosen wind turbine/wind condition configuration. The idea of generating thrust by a fan is new, but not novel as explained and applied in [4, 5]. This paper will show a practical and inexpensive way of generating correctly scaled time series of aerodynamic thrust forces. The force time series are found from simulations of the NREL 5 MW wind turbine, and scaled down and applied to a 1:80 scaled model [6].

## 2. Methods

Physical models of floating wind turbines is complicated by the different scaling laws between wind and wave load. In order to avoid such issue, it is possible to generate a proper wind load by spinning a small low cost RC airplane motor. The main limitation of this thrust emulation approach is the absence of the aerodynamic damping and the gyroscopic effects of the longer and heavier spinning blades.

### 2.1 Setup description

The physical model system is Froude-scaled 1:80 from the NREL 5MW reference wind turbine. No aerodynamics are scaled; only the resulting force and bending moment caused by the rotor thrust are scaled. Masses, lengths, forces, moments and time are scales as in Tab. 1 [7].

Fig. 1 shows the fan assembly used in the work, and the present paper describes a practical approach to construct an equivalent system. The rotor nacelle assembly (RNA) contains the brushless direct current (BLDC) outrunner motor

Physical parameter	Scaling factor
Time	$\lambda^{0.5}$
Length	$\lambda^1$
Mass	$\lambda^3$
Force	$\lambda^3$
Moment	$\lambda^4$

**Table 1.** Froude scaling used in the paper, where  $\lambda = 1:80$ .

with blades, the micro-controller (MC) and the electronic speed controller (ESC). The motor is driven using a lead-acid battery pack. The RNA is installed on top of an aluminum pipe, representing the turbine tower.

The tower was constructed as stiff as possible in order to limit its influence on the RNA system. This choice is driven by the fact that the target time series is a moment at the base of the tower and not the actual thrust force. Therefore the tower dynamics are already included in the reference, and hence should not be introduced twice. For the system to be able to have the correct inertia properties if mounted on a floating foundation, some additional ballast have been placed inside the RNA to match the NREL 5MW. This mass will be removed in some tests to investigate its influence of the coupled system dynamics.

The RNA-tower system is fixed on top of a 6-axis force/torque-transducer. The load cell is capable of monitoring three linear forces plus three moments with respect to the selected coordinate system. The specification of the components used in the entire setup is given below:

- BLDC-motor: CF2805-14 2840KV
- ESC: 30 Amp, 6-16V
- Blade: 6×3E
- Power source: 6V 12Ah lead-acid battery
- MC: Arduino UNO - 16MHz, 8bit microcontroller
- 6-axis load cell: ATI Gamma IP68 F/T sensor
- Tower: 1085 × Ø35 mm Aluminum pipe
- RNA housing: 100 × Ø70 mm PVC pipe

The analogue signals from the 6-axis load cell is digitalised in a dedicated DAQ and the digital signal is recorded using the in-house developed software WaveLab [8]. The PC uses the hardware serial port (UART) to communicate with the MC, while the MC use a pulse width modulation (PWM) digital pin (PIN9) to send data to the ESC. The ESC accepts a standard servo PWM of 20 ms with a duty cycle in the range 5-10%. The schematic signal layout of the setup is shown in Fig. 2. In the physical system, as seen in Fig. 1, the Arduino MC and ESC are placed in the RNA. The power and control signal are wired inside the tower and comes out at the tower base. This is done in an effort to not have free hanging wires from the



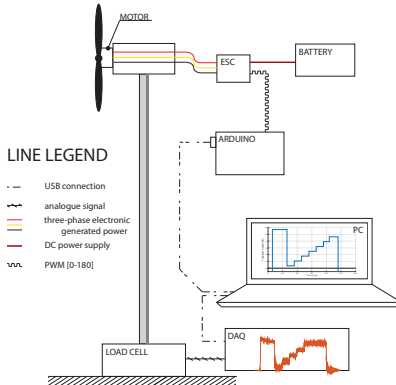


Figure 2. Schematic layout of the setup.

RNA that could lead to unwanted forces on, or damping of, the tower.

## 2.2 Load time series

The application of this force emulating system originates from the experimental investigation of fixed and floating wind turbines. Note that the layout is in no way limited to this application, but can be easily modified to exert forces and/or moments on any structure of choice. Only a force time series at the correctly scaled level is needed.

To assess the influence from a wind turbine on its foundation, the most critical component is the tower base bending moment. Simulated time series from a 5MW wind turbine in 18 m/s turbulent winds are carried out in FAST v8 [9, 10]. This is deemed as a representative test case, and is therefore used to demonstrate the capabilities of the thrust emulation system. The use of aero-servo-elastic coupled software allows the tower base bending moment to be a simple representation of the behavior of a more complex system. The base moment includes interaction between the structural dynamics, blade aerodynamics and generator control strategy.

The full scale simulation covers 10 min of data which leads to 68 s at model scale. This fairly short load time series was chosen to be representative, while still conserving battery capacity in between runs. The bending moment in this simulation peaks at  $61.7 \times 10^3$  kN-m, corresponding to approximately 1.51 N-m at model scale. At model scale, the center of the nacelle is at 1.12 m above the base of the tower, and hence only a peak thrust force of 1.35 N is needed. This value was used to define which motor/propeller-configuration was needed for the setup.

## 2.3 Algorithm

This section gives an elaborate description of the steps used to generate the requested thrust emulation time series in order to reproduce the conducted experiments. This includes functioning code used to build up the communication between the host computer and the MC, and between the MC and the ESC.

The first step is to prepare the MC. The MC is the interface between the host computer and the ESC. It handles translation of a serial integer signal into a servo PWM signal. Listing 1 shows the C++ code needed to handle this task. The MC communicates with the ESC using a PWM signal with a pulse width of 20ms. The Servo (motor) library has been used to form the signal. Once this code is uploaded to the Arduino, the MC will listen for serial communication as long as it is powered by the USB.

```

1 #include <Servo.h>
2 // Initialize servo object and variables
3 Servo ESC;
4 int servoPin = 9;
5 int val = 0;
6 // Attach the servo to the PWM pin, and
7 // start serial communication at 9600 bps
8 void setup() {
9     ESC.attach(servoPin);
10    Serial.begin(9600);
11 }
12 // If data is available, read it and send it
13 // to the ESC
14 void loop() {
15     if (Serial.available()) {
16         val = Serial.read();
17     }
18     ESC.write(val);
19 }
    
```

Listing 1. Arduino script for translating serial integer to servo PWM.

```

1 % Assign and open Arduino serial port
2 s1=serial('COM3');
3 fopen(s1);
4 % Write command to serial port
5 fwrite(s1,CmdVal,'uint8'); % Value 0-180
6 % Turn off fan and close communication
7 fwrite(s1,0,'uint8');
8 fclose(s1);
    
```

Listing 2. Serial control signal from Matlab.

When the MC is actively listening for serial communication, data can be written to it as if it was a file. The communication with the MC is handled using a USB (serial) port. Matlab is used to stream the data from the computer and the MC. The code used in the host computer is detailed in listing 2. Note that this is a condensed script, and that the command on line

5 is what should be looped over.

For the tests conducted, the following algorithm has been used:

1. Open the serial communication between the MC and the host computer
2. Switch the ESC and motor power on
3. Send hand-shake signal to the ESC
4. Send the target time series via serial communication
5. Shut down fan and close serial communication

The ESC has a built in feature that prohibits the fan from going directly from an unpowered idle state to spinning. This originates from a safety concern from the RC industry in order to prevent personnel injury if a system is accidentally connected to power while a high command value is provided. This is also why the initial value in listing 1 and the last command value in listing 2 are 0.

When the fully assembled system is powered on, the ESC will communicate its state through sound codes generated by high frequency vibration of a single coil in the motor. As the power is switched on, the ESC wakes up and gives a ready signal if the control signal is low enough. Before going to operational state a hand-shake signal is needed. The threshold for this will vary from system to system and can be found in the ESC specifications. For this setup a serial value of 40 was used. After an accepted hand-shake signal the ESC will make a sound indicating that it is now armed. For this system the fan cut-in happens a 70, meaning that the theoretical effective range of command values from zero to maximum load are the 110 integer values from 70 to 180.

#### 2.4 Calibration and System identification

Since the Arduino receives a 0-180 integer to command the rotational speed of the turbine, it is necessary to obtain a map that converts the required load to the appropriate integer value. Since the fan is only in operation at command values from 70 to 180, the obtained force is mapped to these values. In order to retrieve this information a multi-step calibration procedure is used. For each step the steady state condition is achieved prior to move to the next. The comparison between the steady state and the target at each step is used to build the interpolant.

Another important test to perform in order to characterize the model of the fan assembly is a frequency sweep test. In this test a number of unitary amplitude pure harmonic signals are sent to the fan, and the resultant torque at the base of the tower is measured. This test relies on the previous calibration procedure. Using this test it is possible to define a discrete bode diagram of the system, which can provide important insight in the model behavior.

When measuring the system response from sweep tests and

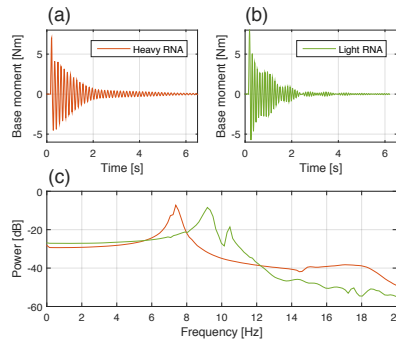


Figure 3. Tower decay with and without additional top-mass.

irregular load time series, influence from the tower dynamics on high-frequency vibrations are to be expected. Two different tower configurations are tested. Both setups have their natural frequency determined by decay tests of the tower motion. This information is linked to the interpretation of the other results from system excitation.

### 3. Results

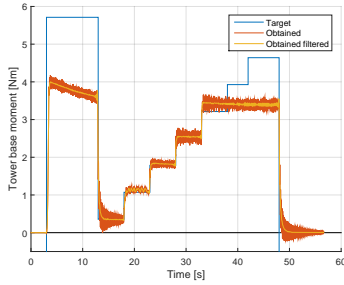
Section 2 explains how to practically set up a system capable of producing precompiled load time series. Since the loads are prescribed at the tower base, the tower dynamics needs to be taken into consideration. In all the results two different tower configurations are shown. One includes additional mass at hub height to match the properties of the NREL 5 MW reference wind turbine; the other excludes this mass to investigate the influence of less RNA inertia on the response of the system.

#### 3.1 Tower Response

Several decay tests were conducted on each setup. Fig. 3 shows the response of the two system configurations. As expected, the natural frequency of the system with the heavy topside is lower compared to its lighter counterpart. The first natural frequency of the systems are around 7.4 and 9.2 Hz respectively. For the lighter system a second mode is also excited around 10.5 Hz. The two first natural periods corresponds to 1.2 and 1.0 s at full scale, and should be compared to the reference turbine with a fore-aft mode period of around 3.1 s [6]. The system is modeled to have a higher stiffness to eliminate the coupling between load case dynamics and tower response. These natural frequencies will be monitored throughout the execution of the following test cases.

#### 3.2 Fan Calibration

In order to be able to map any given control signal to a physical load, a series of step tests were conducted to perform a



**Figure 4.** Load series used for calibration. Good agreement between targeted and obtained moment.

calibration of the fan controller. Fig. 4 shows the calibrated tower base moment performance of the system. As mentioned above, the desired coverage of the system is between 0 and 1.5 Nm, but even this small setup is able to produce more than twice that value. The zero load represents a command value of 70, and the target steps are 75, 85, 95 etc. The calibration is made from the lowest 4 plateaux since they cover the desired load range well with good accuracy. At command values above 110 the load is no longer linearly proportional to the command value. The applied linear calibration used for the presented setup is shown in (1).

$$CmdVal = 70 + \left\| \frac{1}{0.0714} M_{Twrbase} \right\| \quad (1)$$

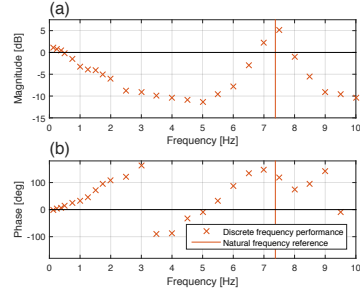
where,

$CmdVal$	Integer value of command value for the MC [-], $CmdVal \in 70 \leq N \leq 110$
$M_{Twrbase}$	Desired moment at tower base [Nm]

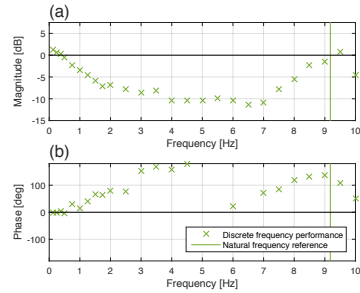
To remove the initial transients from the heat accumulation in the motor, the target is deliberately set at a value that forces the rotor into the highest obtainable workload. The calibration have been performed with every different setup combination of power source and blade diameter/pitch. The calibration shown in Fig. 4 is from the main configuration of a 6V lead-acid battery and with a  $6 \times 3E$  propeller. This configuration was chosen because of three main factors; the load range capability fits well with the desired loads, the peak effect from the power source is satisfactory, and a steady performance over time is achieved.

### 3.3 Frequency Sweep Test

When estimating the performance of the full system it is important to investigate the influence of the thrust fan vibrations on the tower structure. A sweep test has been conducted over a range of frequencies to examine the full system response.



**Figure 5.** Discrete bode diagram made from frequency sweep test with heavy RNA.



**Figure 6.** Discrete bode diagram made from frequency sweep test with light RNA.

Fig. 5 shows the bode diagram for the weighted system. The decreasing amplitude from 0.5 to 5 Hz is a symptom of the fact that the fan is not able to slow down and spin up again in between cycles. Note the significant amplification at the system response around the natural frequency mentioned earlier.

Fig. 6 shows the bode diagram for the lighter system. The performance is not significantly changed, but of course the system amplification is shifted to the natural frequency of the lighter configuration.

### 3.4 Time Series Performance

To test the time domain performance of the system a precompiled load time series simulation is sent to the motor via the MC and ESC.

Visual inspection indicates that the thrust emulation system is able to follow the prescribed load time series. Fig. 7 shows a snippet from an execution of one of these time series. The

Practical Low Cost Aerodynamic Thrust Emulation for Froude Scaled Wind Turbines — 6/8

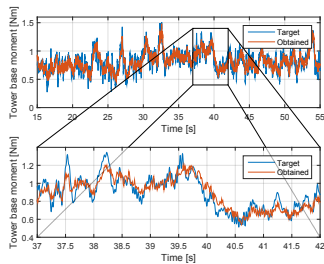


Figure 7. Time series of tower base moment with correctly scaled top mass.

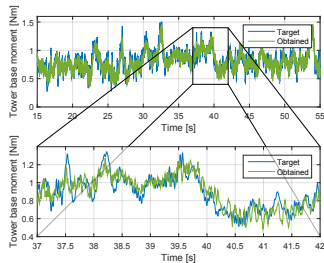


Figure 8. Time series of tower base moment without additional RNA mass.

top figure shows the performance on a longer time scale, and the lower highlights the fit when taking a closer look. A good overall agreement is seen between the targeted and obtained loads. Though the expected difficulties of reaching the target at sudden peaks is also evident. These load spikes and drops originate from the turbulence of the simulated wind field and these gusts results in the emulation system experiencing sudden and steep load changes.

In an attempt to better match the short load spikes the same loads time series was tested with the lower inertia setup system without the extra tower top mass. Increased performance is seen in the zoomed view of Fig. 8 where the load spikes in the first part of the signal are matching the target data slightly better. The better match of the obtained load time series have to be compared to the trade off of not including the correctly scaled tower top mass. This trade off can be made for the investigation of fixed wind turbines, but will not be ideal for floating wind turbine applications.

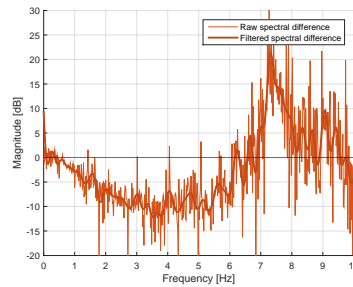


Figure 9. Magnitude of system amplification between obtained and targeted loads found in load time series with heavy RNA setup.

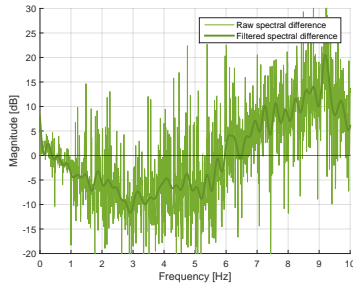
#### 4. Analysis

From the experimental data of the time series it is difficult to quantify the difference between the heavy and the light RNA setups. Fig. 9 shows the difference between the spectral power of the target and obtained signals. This is in a sense depicting the same system behavior as the magnitude part of the bode diagram. The key difference is that this information is extracted from time series data and not from discrete frequency samples. The spectral difference plot expectedly shows the same trend as the bode diagram, but a higher amplification is detected at the natural frequency. This is due to the fact that there is almost no energy in the target signal above 6 Hz.

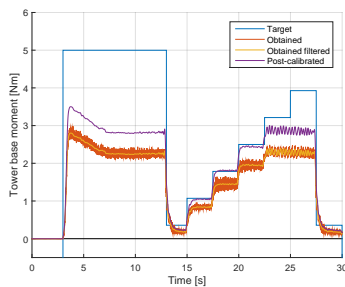
For the system with lesser inertia the match is approximately the same. From Fig. 10 it can be observed that the noise level is slightly higher, but the trend of the result is comparable to that from the discrete sweep tests. The difference at the natural frequency can be explained by two phenomena. Firstly, the fairly short cycles of each different frequency in the sweep tests may have limited the ramp up of the modal amplitude of the tower. Secondly, the low energy content of the target signal at the higher frequencies also adds to the apparently large difference. This second issue could possibly be circumvented by testing the performance over a more evenly distributed time series generated on the basis of a white noise signal.

#### 4.1 Discussion

Fig. 11 shows a calibration of the fan controller using an insufficient power source. The test was conducted while the battery power source had been drained to the point where the voltage output had dropped by approximately 20%. Since the voltage has a direct relationship to the RPM of the BLDC motor it is clear that the obtained thrust will decrease proportionally.



**Figure 10.** Magnitude of system amplification found in load time series with light RNA setup.



**Figure 11.** Adjusted calibration of execution with lower voltage power supply.

The post-calibrated results show that results obtained can be salvaged as long as the voltage drop is detected/monitored. For the lowest working area of the fan in Fig. 11 (around 12.5-15 s), the voltage drop has caused the fan to idle, and hence this part of the data cannot be salvaged via post-calibration. To avoid the issues with the voltage drop off, the setup can be improved with a tachometer feeding the RPM back into the MC. In this way the control signal can directly aim for a RPM setting which is more directly linked to the fan thrust than the PWM duty cycle.

A practical approach on how to build a scaled thrust emulation system has been presented. The first part of the paper covers the scaling of the wind turbine, and the parts, schematic and scripts needed to emulate it. This is achieved with purely off-the-shelf parts in the hopes that similar systems will spread for further testing and refinement. The system is presented from both a hardware and software perspective. The physical

layout of the system is quite straight forward, but the communication between host PC and the MC/ESC is non-trivial. Insights in how the different parts of the system accepts and handles inputs are given. This is done in the scope of emulating wind turbine thrust loads, but the approach can be easily applied to any field of non-invasive dynamic system excitation.

Two distinct configurations are presented. One with a correctly scaled RNA mass of the NREL 5MW turbine, and one lighter without any other mass at the tower top than the crucial parts. This was done in an effort to see if the inertia of the RNA would impact system performance. A clear shift of natural frequency is seen, and even a higher order mode is observed due to the more evenly distributed mass along the tower length. These natural frequencies are taken into consideration when interpreting the other results from the system performance.

Calibration methodology and results are presented. The blade length and pitch of the blade have a direct impact on the calibration, but the biggest influences on the calibrated performance of the system is the choice of power supply. The power supply have to strike a balance between output voltage, temporal stability and maximum discharge rate. The discharge rate is limiting the current at higher motor torques. This is why the maximum stable tower base moment obtained is around 3.4 Nm, or at a command value of 117. This limit is well above the desired peak of 1.5 Nm, and hence is acceptable. In this work a lead-acid battery was chosen over a LiPo battery due to the better temporal stability of the larger lead-acid pack. Even though a voltage regulated power supply could provide a 100% stable input voltage, a battery was still preferable due to the limited maximum effect of the available regulated power supplies. The calibration could be improved by going from control signal/load-calibration to RPM/load-calibration. This would detach the performance of the power supply from the calibration, and hence the small strong LiPo cell batteries would be more suitable. The RPM could easily be monitored by a brushless RPM sensor. These a cheap, widely available and would fit directly into the presented setup with a small configuration to the control in Listing 1.

The sweep test was conducted in order to understand the system behavior in the frequency domain. At lower frequencies the system reproduced the amplitudes and phases of loads in a very satisfactory way. An amplification is expectedly seen around both systems' natural frequencies. The low number of cycles at each frequency could be increased to gain a more reliable representation of the amplitude, but to the largest extent the phases.

### 5. Conclusion

The aim of the load emulation is to represent the load time series of the trust experienced by a running wind turbine. The scaled load time series of a 5MW turbine in 18 m/s turbulent winds were presented. The system captures the main dynamics of the turbine loading very well. The fan system falls short at the most sudden load changes. This is due to the inability to spin up and slow down rapidly enough.

Improved performance could be obtained in multiple simple ways. One would be going up in scale to have a lesser time compression in the load time series. With the parts presented, a scale of around 1:60 could be obtained by only adjusting the system voltage from the 6V of the lead-acid to the 7.4V of the LiPo 2 cell battery. This would cause a higher battery drain for which should be accounted. This leads to the other main contributor to system performance; the power source. In this work a battery is chosen because it delivers a suitable stable DC output. By monitoring the RPM of the BLDC the need for stable DC is removed. When including the RPM feed-back in the fan control a better instant performance and especially temporal stability could be achieved.

All in all this work presents a practical approach of building an inexpensive system capable of emulating scaled wind turbine thrust loads. Performance of the controlled fan is acceptable at lower frequencies, and a good overall fit is seen in thrust time series. The practicality and low costs of a system like this enables researchers and designers to do dynamic system testing at a much earlier state of development. For floating wind turbines this means that testing can be conducted at wave basin facilities without the capabilities of producing scaled wind fields, and alleviates the need for aerodynamic scaling.

### References

- [1] EWEA. *Wind Energy - The Facts: A guide to the technology, economics and future of wind power*. Earthscan, 2009.
- [2] Fraunhofer IWES. Wind monitor. <http://windmonitor.iwes.fraunhofer.de>, 2013. Accessed: 2016-05-03.
- [3] Heather R Martin, Richard W Kimball, Anthony M Viselli, and Andrew J Goupee. Methodology for wind/wave basin testing of floating offshore wind turbines. *Journal of Offshore Mechanics and Arctic Engineering*, 136(2):020905, 2014.
- [4] José Azcona, Faisal Bouchotrouch, Marta González, Joseba Garciandía, Xabier Munduate, Felix Kelberlau, and Tor A Nygaard. Aerodynamic thrust modelling in wave tank tests of offshore floating wind turbines using a ducted fan. In *Journal of Physics: Conference Series*, volume 524, page 012089. IOP Publishing, 2014.
- [5] C Wright, K O'Sullivan, J Murphy, and V Pakrashi. Experimental comparison of dynamic responses of a tension moored floating wind turbine platform with and without spring dampers. In *Journal of Physics: Conference Series*, volume 628, page 012056. IOP Publishing, 2015.
- [6] Jason M Jonkman, Sandy Butterfield, Walter Musial, and George Scott. Definition of a 5-mw reference wind turbine for offshore system development, 2009.
- [7] Subrata Kumar Chakrabarti. *Offshore structure modeling*, volume 9. World Scientific, 1994.
- [8] Peter Frigaard and Thomas Lykke Andersen. Analysis of waves: Technical documentation for wavelab 3. Technical report, Department of Civil Engineering, Aalborg University, 2014.
- [9] Jason M Jonkman and Marshall L Buhl Jr. Fast user's guide. *National Renewable Energy Laboratory, Golden, CO, Technical Report No. NREL/EL-500-38230*, 2005.
- [10] Jason M Jonkman. The new modularization framework for the fast wind turbine cae tool. preprint. In *51st AIAA Aerospace Sciences Meeting and 31st ASME Wind Energy Symposium, Grapevine, Texas*, 2013.

---

# Paper H

## Fan Actuated Loading on Scaled Floating Offshore Wind Turbines

Morten Thøtt Andersen  
Fancesco Ferri

The draft paper is to be submitted to  
*Journal of Marine Science and Engineering*, ISSN:2077-1312, 2016.





# Fan Actuated Loading on Scaled Floating Offshore Wind Turbines

Morten Thøtt Andersen<sup>1\*</sup> and Francesco Ferri<sup>1</sup>

## Abstract

The field of floating offshore wind turbines is still at a relatively adolescent stage. This means that extensive work is still being done in developing numerical models. A significant tool in investigation of novel concepts and verification of numerical models is the scaled experimental testing in wave basins. The conflicting scaling laws of inertia dominated hydrodynamics and drag dominated aerodynamics pose a challenge in designing the scaled setups. Even when having a correctly scaled wind turbine, the task of obtaining a representative wind field over a wave basin can be demanding. This paper presents a practical and inexpensive way of removing the need for a wind field generation and complex geometric scaling of the wind turbine. This is done by mounting a remotecontrolled fan on a floating wind turbine, and using this to excite the structure by a pre-determined correctly scaled thrust time series. This ensures an equal scaling of all dominating forces and thus correct motions can be expected.

## Keywords

Aerodynamic Thrust; Fan Excitation; Floating Offshore Wind Turbines; Experimental Testing; Concept Verification

<sup>1</sup>Dept. of Civil Engineering, Aalborg University, Aalborg, Denmark  
\*e-mail: mta@civil.aau.dk

## Contents

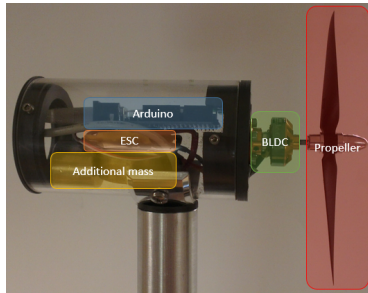
1	Introduction	1
2	Methods	2
2.1	Load Cases	2
3	Results	3
4	Discussion	4
5	Conclusion	4
	References	4

## 1. Introduction

The growing energy need of the world along with the political decision to migrate away from the fossil fuels are putting the spotlight on academia as well as the industry to solve the global energy needs by means of renewable sources [1]. One of the largest and most proven industries is the wind energy sector. Though the majority of wind turbines are still placed onshore, more and more projects are moving offshore. In 2015, 24% of all installed wind energy capacity in the EU was installed offshore - the largest share to date [2]. The benefits from installing wind turbines offshore range from more contextual topics like less public resistance due to the absence of the visual and audible nuisance caused by onshore wind turbines, to the more direct benefits of higher and steadier winds resulting in a greater energy resource [3, 4].

While most open water locations provide a good wind resource, the feasibility of a wind turbine park relies heavily on the cost of the foundation which itself is directly dependent on the water depth. The need for more elaborate foundation designs hereby limits the possible locations for new wind energy projects. The bulk of European wind energy projects are still placed in shallow to intermediate waters where the depth rarely exceeds 30 m [5, 6]. Some countries have vast territorial waters that fall under this limitation, while some have close to none. The significant growth within the offshore wind energy sector have started to influence the feasibility of projects locations due to the demand for a good combination of shallow water and relatively short distance to shore for grid connection. This has prompted the development of foundation concepts able to transition into even deeper waters. One of the newer and promising concepts is the idea of floating offshore wind turbines (FOWTs).

A floating wind turbine is a complex dynamic system excited by a plethora of various forces. Due to this, numerical models are constantly being improved to include more and more effects. One of the most cost-efficient ways of validating these models are by comparing them to experimental data where excitation and response can be investigated in a scaled environment. This approach is heavily investigated and well proven for determining the hydrodynamic behavior of floating structures. The task of correctly scaling the inertia dominated hydrodynamic loads and viscous drag dominated aerodynamic loads is far from trivial [7]. The correct scaling



**Figure 1.** RNA including control components constructed to emulate wind turbine thrust load time series [11].

of inertial loads entails a constant Froude number, while the conservation of viscous forces is done by ensuring equality in Reynolds number. This is not possible if the structure is equally scaled by a single set of factors. The present work aims to bypass this issue by substituting the need for correctly drag dominated loads on the wind turbine by a pre-determined thrust time series. This thrust can be Froude scaled and hence only a single scaling law is required.

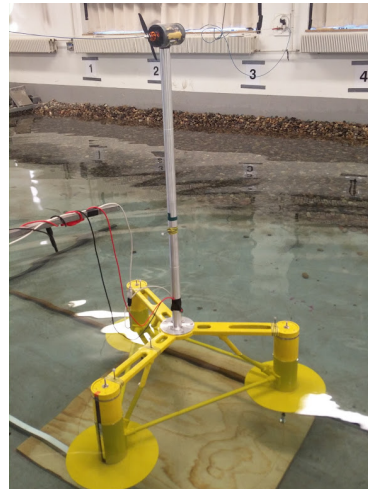
The thrust force excitation needs to be noninvasive on the dynamic response and movement range of the system in question. Hence, tactile excitation is not an option. Instead the excitation is generated by a fan mounted at the position of the turbine, blowing wind away from the structure and hereby generating an emulated thrust force. The amount of exhausted air is scaled to match the thrust force experienced of the chosen wind turbine/wind condition configuration. The idea of generating thrust by a fan is new, but not novel as explained and applied in [8, 9]. This paper will show a practical and inexpensive way of generating correctly scaled time series of aerodynamic thrust forces on a FOWT. The force time series are found from simulations of the NREL 5 MW wind turbine, and scaled down and applied to a 1:80 scaled model [10].

## 2. Methods

The thrust emulation system used for the experimental testing in this work have been thoroughly described in [11]. The layout of the components used can be seen in figure 1.

The foundation used for the investigation is a generic semi-submersible foundation as shown in figure 2. This floating foundation shares basic principles for stability with other semi-submersibles and is hence deemed to be comparable to these in behavior. The setup is tested in condition corresponding to 50 m water depth in full scale.

Usually a semi-submersible foundation would utilize cate-



**Figure 2.** Floating semi-submersible foundation with tower and thrust emulations system mounted.

nary mooring, but in this investigation taut mooring is used. The mooring is per definition a tension-leg layout, but is constructed to be highly compliant and elastic to allow for foundation motions without slack line concerns. This approach is chosen to eliminate influence of non-linear behavior and hysteresis originating from catenary cables resting on the seabed.

The motion of the structure has been assumed follow a rigid body behavior. This motion is monitored and recorded by means of optical tracking to use for comparison with a numerical model describing the same system.

### 2.1 Load Cases

To be able to assess the performance of the thrust emulation concept, the investigations carried out in this paper revolves around wind load cases only. Once this methodology is sufficiently established other load cases of combined wind and wave loads is to be investigated. This means that the extent of the hydrodynamic behavior is in this paper mainly linked to the radiation damping. As mentioned above all load simulations are pre-simulated in FAST and then the tower base bending moments are reconstructed by executing the resulting thrust force time series at hub height. The load cases investigated are as follows:

1. Constant wind speed in order to investigate steady state conditions.
2. Turbulent wind on a bottom-fixed wind turbine.

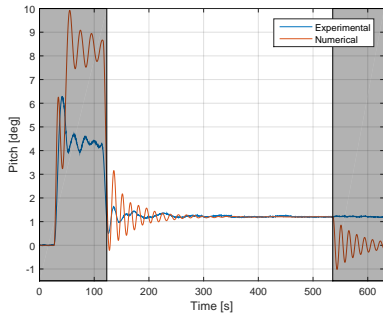


Figure 3. Pitch angle of system under steady state loads.

3. Turbulent wind on a floating offshore wind turbine (OC4 semi-submersible used for comparable behavior)

All load time series are initiated with a load significantly higher than the motor and propeller are able to produce. This is not an optimal strategy, but necessary to ensure sufficient heat-up of the motor to obtain stable behavior over the following load time series. This will be visible in the results displayed in the following, but should not be attributed as an error, but instead as a natural physical limitation of the presented layout. In the experimental tests the load time series were looped in succession. This is not the case for the numerical model, and hence the results from the numerical model will appear to change rapidly in the end of the simulation when to load time series abruptly goes to zero. Both the discrepancies in the start and the end of the comparisons will be presented, but greyed out not disturb the interesting parts of the model comparison.

3. Results

To compare the results of the numerical model with the experimentally recorded behavior of the physical system, the pitch angle of the structure is considered. This is due to the fact that this is one of the main, if not the most, excited degree of freedom.

Some discrepancies were initially found between the numerical and experimental models. The pitch angle of the systems under steady state loads did not align. The load emulation system is quite sensitive to careful calibration, but other factors might have influenced this error as well. Mainly the transformation between integer control signals at model scale to the requested loads at full scale is under suspicion to have been cause of the error, though this have not been clarified yet. To alleviate this discrepancy, the loads in the numerical model have been tuned to match the steady state pitch angle excursion of the experimental model. Figure 3 shows the steady

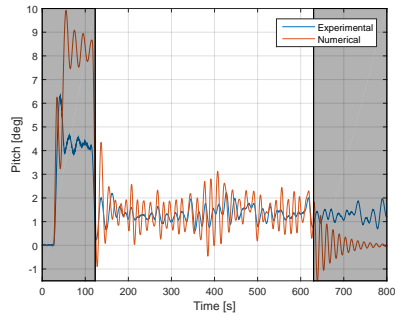


Figure 4. Pitch motions observed after excitation of fixed turbine tower base moments.

state calibrated behavior, as well as model differences in the both the first and last part of the simulations. Note that the pitch damping and natural frequency of the system have been tuned via decay tests, but the sudden change in system loads excited multiple degrees of freedom and hence the decay does not appear to be comparable.

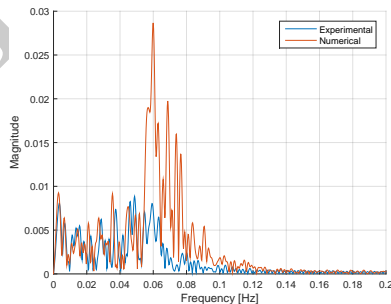
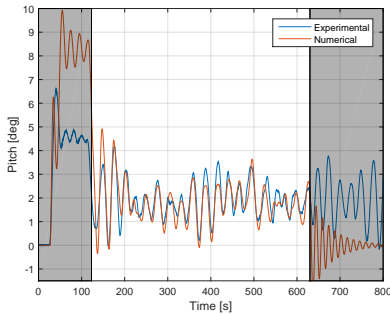


Figure 5. Frequency domain representation of the pitch motions observed after exciting the models with fixed turbine loads.

When observing the behavior excited by the moment simulated at the tower base of a fixed wind turbine some discrepancies are seen. The main dynamics of the systems compare to some extent, but the experimental setup fails at obtaining the larger pitch amplitude as expected from the numerical model as shown in figure 4. The fact that the load time series

## Fan Actuated Loading on Scaled Floating Offshore Wind Turbines — 4/5



**Figure 6.** Time domain comparison between the models when excited by loads simulated from a comparable floating system.

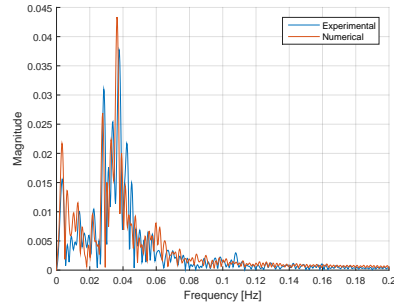
originate from a bottom fixed structure entails that more high frequency loads are to be expected due to the relative higher rigidity of such a system. The thrust emulation system is physically limited in speeding up and slowing down in order to reach these high frequency load components. This is mainly an issue due to the fact that the 1:80 scale leads to a significant compression of time during experimental testing. Figure 5 shows exactly that most of the energy if the motions are numerically expected to reside at a higher frequency than can be correctly excited with the current physical system layout.

To obtain a more comparable load time series, simulations have been conducted on the OC4 semi-submersible floating system. The inherently more compliant pitch motions of a system like this will expectedly yield a more comparable loads at the tower base between the tower and foundation. This is exactly what can be seen in figure 6 and 7. The lower dominating frequencies allows for the physical thrust emulation system to achieve good load approximations and hence a good accordance in pitch motions between the systems. Still some peak loads are still not in full compliance between the models, but in an investigation of main system dynamics the model similarity seems promising.

#### 4. Discussion

A satisfactory agreement is seen between the numerical and experimental models as long as the high frequency content of the loads time series is fairly limited. This is an expected limitation of a thrust emulation system like this and can be alleviated by e.g. increasing the scale of the physical models.

The detailed design and calibration of the thrust emulation system can be seen in [11]. With a more stable calibration



**Figure 7.** Frequency domain comparison between the pitch motions of the systems excited by lower frequency dominated load time series.

approach of the fan/motor layout, the need for system heat-up could be removed, and hence limiting the amount of transients bleeding into the simulations. A RPM based calibration would also allow for longer simulations without concern for force drift due to power supply limitations.

#### 5. Conclusion

The aim of this paper was to show the validity and possibility of using smaller fan systems for simple non-tactile thrust emulation on floating offshore wind turbines. Though the physical models and loads cases investigated have been simplified and reduced in order to limit the sources of error, the results still seem promising. The pitch measured in the physical models match well with the numerical model simulations, though more precision at peak loads would be preferred. This might somewhat solved by a RPM based fan calibration, but to be sure to capture higher impact loads the pre-simulated loads might not be sufficient. A software-in-the-loop approach might be appropriate for some extreme cases, but this will also increase the complexity of the system configuration significantly.

The concept is still adolescent in technical maturity, but the fact that relatively good model comparisons can be found with such a simple and fairly crude system implies that this approach of load emulation might be of great value to tank testing of floating wind turbines where scaling laws pose threatening uncertainties in approximations.

#### References

- [1] David MacKay. *Sustainable Energy-without the hot air*. UIT Cambridge, 2008.

- [<sup>2</sup>] EWEA. Wind in Power - 2015 European statistics. Technical report, The European Wind Energy Association, 2016.
- [<sup>3</sup>] EWEA. *Wind Energy - The Facts: a guide to the technology, economics and future of wind power*. Earthscan, 2009.
- [<sup>4</sup>] EWEA. Deep Water - The next step for offshore wind energy. Technical report, The European Wind Energy Association, 2013. ISBN: 978-2-930670-04-1.
- [<sup>5</sup>] Fraunhofer IWES. Wind monitor. <http://windmonitor.iwes.fraunhofer.de>, 2013. Accessed: 2016-05-03.
- [<sup>6</sup>] EWEA. The European Offshore Wind Industry - Key trends and statistics 2015. Technical report, The European Wind Energy Association, 2016.
- [<sup>7</sup>] Heather R Martin, Richard W Kimball, Anthony M Viselli, and Andrew J Goupee. Methodology for wind/wave basin testing of floating offshore wind turbines. *Journal of Offshore Mechanics and Arctic Engineering*, 136(2):020905, 2014.
- [<sup>8</sup>] José Azcona, Faisal Bouchotrouch, Marta González, Joseba Garciandía, Xabier Munduate, Felix Kelberlau, and Tor A Nygaard. Aerodynamic thrust modelling in wave tank tests of offshore floating wind turbines using a ducted fan. In *Journal of Physics: Conference Series*, volume 524, page 012089. IOP Publishing, 2014.
- [<sup>9</sup>] C Wright, K O'Sullivan, J Murphy, and V Pakrashi. Experimental comparison of dynamic responses of a tension moored floating wind turbine platform with and without spring dampers. In *Journal of Physics: Conference Series*, volume 628, page 012056. IOP Publishing, 2015.
- [<sup>10</sup>] Jason M Jonkman, Sandy Butterfield, Walter Musial, and George Scott. Definition of a 5-mw reference wind turbine for offshore system development, 2009.
- [<sup>11</sup>] Morten T Andersen and Francesco Ferri. Practical low cost aerodynamic thrust emulation for froude scaled wind turbines. *Under review: Experimental Mechanics*, 2016.



---

# Appendix I

## Auxiliary Publications

### **I.1 Laboratory Testing and Energy Production of Scale 1: 35 Sigma Energy WEC**

by Andersen, M. T. and Ferri, F. (2014).

DCE Contract Report No. 104  
*Not included due to confidentiality.*

### **I.2 Hydraulic Evaluation of Joltech's GyroPTO for Wave Energy Applications**

by Kramer, M. M., Pecher, A. F. S., Guaraldi, I., Andersen, M. T., and Kofoed, J. P. (2015).

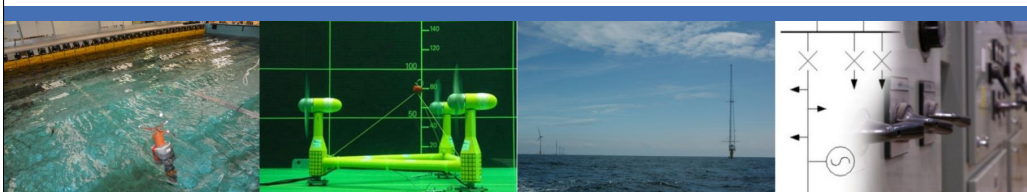
DCE Technical Report No. 178, ISSN 1901-726X  
*Not included in full length. Can be accessed via [vbn.aau.dk](http://vbn.aau.dk).*

### **I.3 The Inter Facility Testing of a Standard Oscillating Water Column (OWC) Type Wave Energy Converter (WEC)**

by Andersen, M. T. and Thomsen, J. B. (2016).

DCE Technical Report No. 180, ISSN 1901-726X





## Comparative Testing Report

# The Inter Facility Testing of a Standard Oscillating Water Column (OWC) Type Wave Energy Converter (WEC).

[The Round Robin Programme]

Facilities:

***ECN;***

***Plymouth University;***

***HMRC @ UCC;***

***Edinburgh University;***

***Aalborg University;***

***Strathclyde University.***



EC FP7 "Capacities" Specific Programme  
Research Infrastructure Action





## ABOUT MARINET

MARINET (Marine Renewables Infrastructure Network for emerging Energy Technologies) is an EC-funded network of research centres and organisations that are working together to accelerate the development of marine renewable energy - wave, tidal & offshore-wind. The initiative is funded through the EC's Seventh Framework Programme (FP7) and runs for four years until 2015. The network of 29 partners with 42 specialist marine research facilities is spread across 11 EU countries and 1 International Cooperation Partner Country (Brazil).

MARINET offers periods of free-of-charge access to test facilities at a range of world-class research centres. Companies and research groups can avail of this Transnational Access (TA) to test devices at any scale in areas such as wave energy, tidal energy, offshore-wind energy and environmental data or to conduct tests on cross-cutting areas such as power take-off systems, grid integration, materials or moorings. In total, over 700 weeks of access is available to an estimated 300 projects and 800 external users, with at least four calls for access applications over the 4-year initiative.

MARINET partners are also working to implement common standards for testing in order to streamline the development process, conducting research to improve testing capabilities across the network, providing training at various facilities in the network in order to enhance personnel expertise and organising industry networking events in order to facilitate partnerships and knowledge exchange.

The aim of the initiative is to streamline the capabilities of test infrastructures in order to enhance their impact and accelerate the commercialisation of marine renewable energy. See [www.fp7-marinet.eu](http://www.fp7-marinet.eu) for more details.

### Partners

	<b>Ireland</b> University College Cork, HMRC (UCC_HMRC) <i>Coordinator</i>		<b>Netherlands</b> Stichting Tidal Testing Centre (TTC)
			Stichting Energieonderzoek Centrum Nederland (ECNeth)
	Sustainable Energy Authority of Ireland (SEAI_OEDU)		
-----			
	<b>Denmark</b> Aalborg Universitet (AAU)		<b>Germany</b> Fraunhofer-Gesellschaft Zur Foerderung Der Angewandten Forschung E.V (Fh_IWES)
	Danmarks Tekniske Universitet (RISOE)		Gottfried Wilhelm Leibniz Universität Hannover (LUH)
	<b>France</b> Ecole Centrale de Nantes (ECN)		Universitaet Stuttgart (USTUTT)
	Institut Français de Recherche Pour l'Exploitation de la Mer (IFREMER)		
-----			
	<b>United Kingdom</b> National Renewable Energy Centre Ltd. (NAREC)		<b>Portugal</b> Wave Energy Centre – Centro de Energia das Ondas (WavEC)
	The University of Exeter (UNEXE)		<b>Italy</b> Università degli Studi di Firenze (UNIFI-CRIACIV)
	European Marine Energy Centre Ltd. (EMEC)		Università degli Studi di Firenze (UNIFI-PIN)
	University of Strathclyde (UNI_STRATH)		Università degli Studi della Tuscia (UNI_TUS)
	The University of Edinburgh (UEDIN)		Consiglio Nazionale delle Ricerche (CNR-INSEAN)
	Queen's University Belfast (QUB)		
	Plymouth University (PU)		<b>Brazil</b> Instituto de Pesquisas Tecnológicas do Estado de São Paulo S.A. (IPT)
-----			
	<b>Spain</b> Ente Vasco de la Energía (EVE)		<b>Norway</b> Sintef Energi AS (SINTEF)
	Tecnalia Research & Innovation Foundation (TECNALIA)		Norges Tekniske-Naturvitenskapelige Universitet (NTNU)
	<b>Belgium</b> 1-Tech (1_TECH)		
-----			

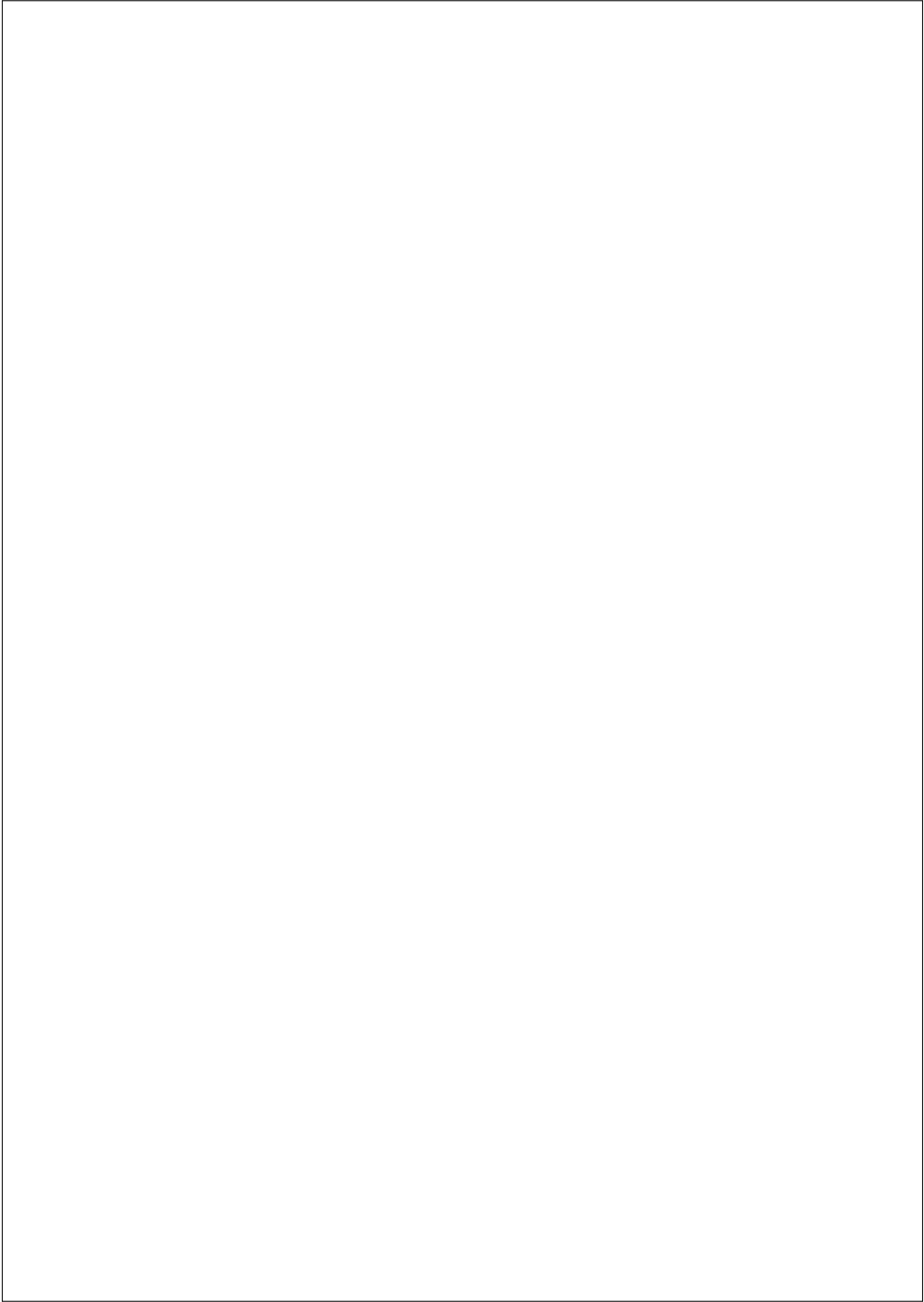
# **The Inter Facility Testing of a Standard Oscillating Water Column (OWC) Type Wave Energy Converter (WEC)**

**Morten Thøtt Andersen  
Jonas Bjerg Thomsen**

ISSN 1901-726X  
DCE Technical Report No. 180



**DEPARTMENT OF CIVIL ENGINEERING**  
AALBORG UNIVERSITY



Aalborg University  
Department of Civil Engineering  
Wave Energy Research Group

**DCE Technical Report No. 180**

**The Inter Facility Testing of a Standard  
Oscillating Water Column (OWC) Type  
Wave Energy Converter (WEC)**

by

Morten Thøtt Andersen  
Jonas Bjerg Thomsen

December 2014

© Aalborg University

### **Scientific Publications at the Department of Civil Engineering**

**Technical Reports** are published for timely dissemination of research results and scientific work carried out at the Department of Civil Engineering (DCE) at Aalborg University. This medium allows publication of more detailed explanations and results than typically allowed in scientific journals.

**Technical Memoranda** are produced to enable the preliminary dissemination of scientific work by the personnel of the DCE where such release is deemed to be appropriate. Documents of this kind may be incomplete or temporary versions of papers or part of continuing work. This should be kept in mind when references are given to publications of this kind.

**Contract Reports** are produced to report scientific work carried out under contract. Publications of this kind contain confidential matter and are reserved for the sponsors and the DCE. Therefore, Contract Reports are generally not available for public circulation.

**Lecture Notes** contain material produced by the lecturers at the DCE for educational purposes. This may be scientific notes, lecture books, example problems or manuals for laboratory work, or computer programs developed at the DCE.

**Theses** are monographs or collections of papers published to report the scientific work carried out at the DCE to obtain a degree as either PhD or Doctor of Technology. The thesis is publicly available after the defence of the degree.

**Latest News** is published to enable rapid communication of information about scientific work carried out at the DCE. This includes the status of research projects, developments in the laboratories, information about collaborative work and recent research results.

Published 2014 by  
Aalborg University  
Department of Civil Engineering  
Sofieldalsvej 9-11,  
DK-9200 Aalborg SV, Denmark

Printed in Aalborg at Aalborg University

ISSN 1901-726X  
DCE Technical Report No. 180

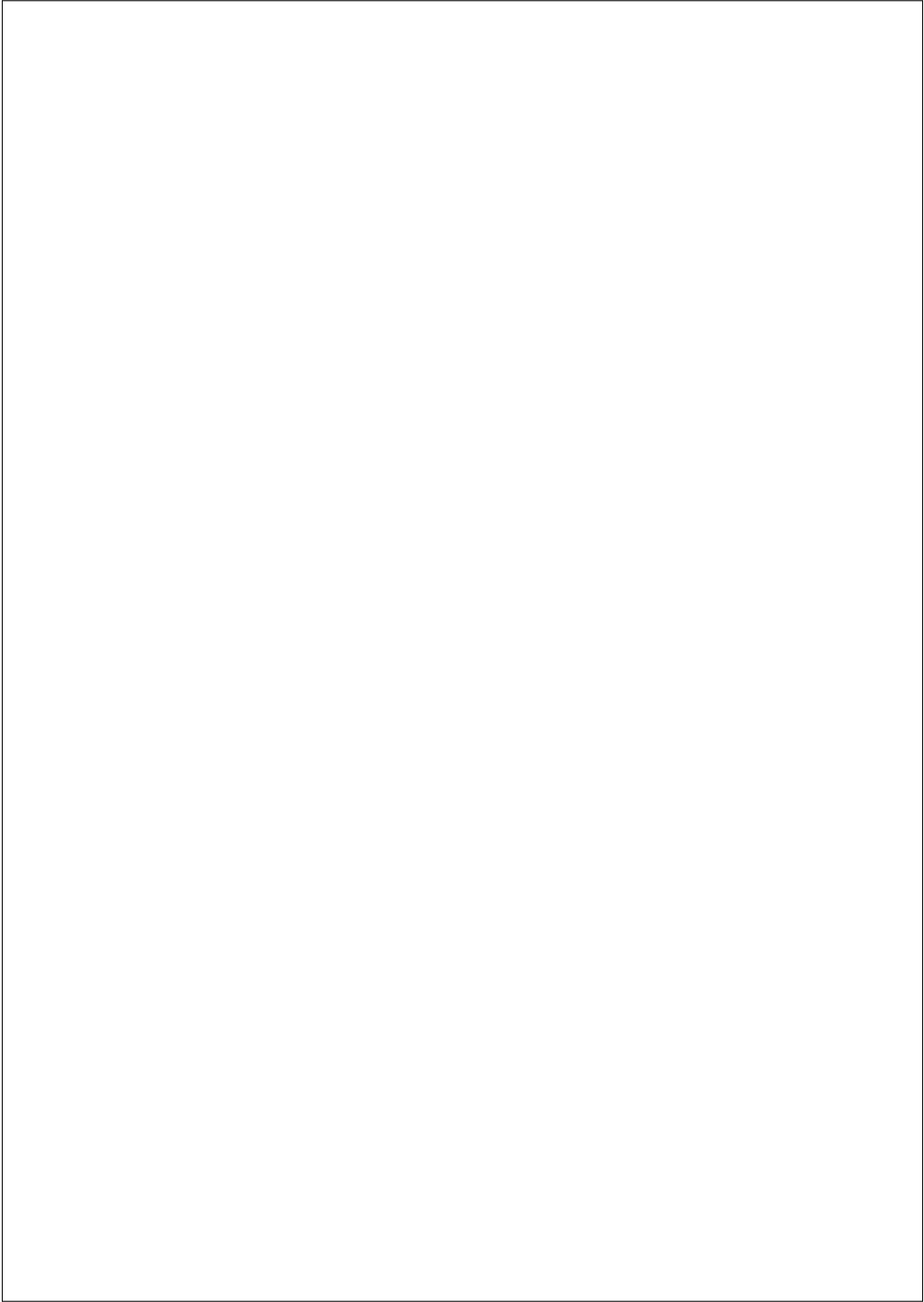
## Preface

This report describes the behavior and preliminary performance of a simplified standard oscillating water column (OWC) wave energy converter (WEC). The same tests will be conducted at different scales at 6 different test facilities and the results obtained will be used for comparison. This project will be refereed to as The Round Robin Programme. The rationale for the work is based on the MaRINET proposal:

A key aspect of the standardisation of device testing is that results from independent trials will be compatible between different test centres. Even when similar procedures are followed this may not be guaranteed. A specially selected test programme will, therefore, be implemented at certain MaRINET facilities to investigate this matter. Due to budget restrictions only laboratory scale centres can be considered but the open water operators will be consulted continuously during the formalisation of the programme to ensure scale similitude of the plan as well as the procedures. The expectation would then be that when the successful devices reach prototype size trials the previous stage results will be compatible.

The experiments have been conducted in the Hydraulics and Coastal Engineering Laboratory at Aalborg University, Sohngaardsholmsvej 57, DK-9000 Aalborg. For further information regarding the content of this report please contact Morten Thøtt Andersen (mta@civil.aau.dk) or Jonas Bjerg Thomsen (jbt@civil.aau.dk) from the Department of Civil Engineering.

Aalborg University, December 12, 2014





# Contents

Preface	vii
<b>1 Introduction</b>	<b>1</b>
1.1 Concept	1
1.2 Modelling	1
<b>2 Model Construction</b>	<b>3</b>
2.1 Scaling	3
2.2 Model description	3
2.3 Sensors	7
2.4 Power Production	9
<b>3 Model Verification</b>	<b>11</b>
3.1 Motion Response Tests	11
3.1.1 Natural Periods	11
3.1.2 Damping	12
3.2 Static Mooring Test	13
<b>4 Wave Details</b>	<b>17</b>
4.1 Scatter diagrams	17
4.2 Wave quality	17
<b>5 Raw Data Time Histories</b>	<b>19</b>
5.1 Power Production	19
5.2 Mooring Loads	20
<b>6 Avg. Value Graphs &amp; Charts</b>	<b>27</b>
6.1 Power Production	27
6.1.1 Model Scale	27
6.1.2 Full Scale	28
6.2 Mooring Loads	29

x	Contents
<b>7</b>	<b>Summary Statistics Tables</b> <b>31</b>
7.1	Wave details . . . . . 31
7.2	Power production . . . . . 31
	<b>Bibliography</b> <b>33</b>
<b>A</b>	<b>Definition of Wave States</b> <b>35</b>
<b>B</b>	<b>List of Executed Tests</b> <b>37</b>

# 1 | Introduction

The following tests are based on standard operation procedures at the Hydraulics and Coastal Engineering Laboratory at Aalborg University. It should however be noted that when working in the laboratory each project will always be treated individually in both setup and execution.

## 1.1 Concept

The Round Robin WEC (wave energy converter) is a FOWC-type (floating oscillating water column). This concept utilizes the wave elevation to drive a compression/expansion of and internal air chamber, which in turn drives a turbine/generator. The system uses a slack catenary mooring system for station-keeping.

## 1.2 Modelling

Since the correct scaling of a turbine PTO (power take-off) is not practically achievable, the PTO will instead be modeled by an orifice cap. The absorbed power of the system is then modeled as the product of the flow through the orifice and the relative chamber pressure. This will be described in detail in section 2.3. The report presents the construction and verification of the WEC itself as well as the mooring system in chapter 2 and 3.



## 2 | Model Construction

The OWC WEC model was constructed at Aalborg University, based on the prescribed full scale values. Because of the test facility at AAU it was determined to construct the model in scale 1:70. The construction of the model is described in the following sections.

### 2.1 Scaling

For scaling of the model Froude's scaling law was used.

$$x_M = \lambda x_F \quad (2.1)$$

Where  $x$  is the parameter to be scaled, subscript M indicates model scale and subscript F indicates full scale. The multiplication factor  $\lambda$  is seen in Table 2.1.

Parameter	Multiplication factor $\lambda$
Length [m]	$\lambda_L = L_M/L_F$
Time [s]	$\lambda_T = \lambda_L^{0.5}$
Mass [kg]	$\lambda_m = \lambda_L^3$
Force [N]	$\lambda_f = \lambda_L^3$
Effect [W]	$\lambda_E = \lambda_L^{3.5}$

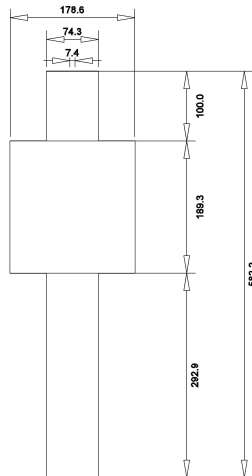
**Table 2.1:** Multiplication factors used in Froude scaling of relevant parameters.

### 2.2 Model description

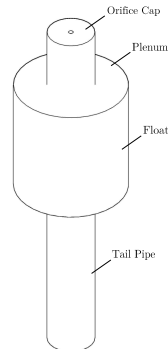
Using the scaling law, the 1:70 model was constructed with dimensions shown in figure 2.1. Materials were chosen to provide the smallest deviation between prescribed and constructed parameters. This is shown in Table 2.2.

	Model	Full Scale	Prescribed	Deviation [%]
Mass [kg]	2.35	806050	810333.01	0.53
Center of Gravity [m] (above keel)	0.286	20.02	21.14	5.28
Plenum int. diameter [m]	0.0743	5.201	5.200	0.02
Float height [m]	0.1893	13.251	13.250	0.01
Orifice diameter [m]	0.0074	0.518	0.520	0.38

**Table 2.2:** Physical properties and dimensions of constructed model together with deviation from prescribed full scale values. Cf. Figure 2.2 for definitions.



**Figure 2.1:** Dimensions of constructed model.



**Figure 2.2:** Definition of components in model.

The constructed model can be seen in Figure 2.3.



**Figure 2.3:** Photo of constructed model.

The model was placed in the wave basin in a water depth  $h = 0.7$  m. A three-legged catenary mooring system was used in order to keep the model on station. Three bottom anchors were installed and connected to three surface buoys through catenary chains with weight equal to 0.053 kg/m. The surface buoys were connected to the model through three light lines. The mooring system is illustrated in Figure 2.4-2.6.

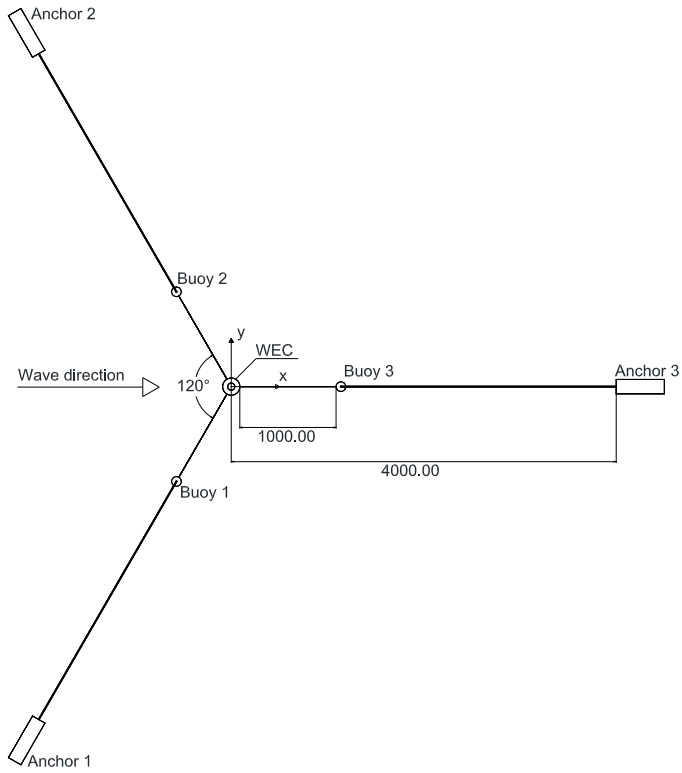


Figure 2.4: Top view of laboratory test set-up. All dimensions are in mm.



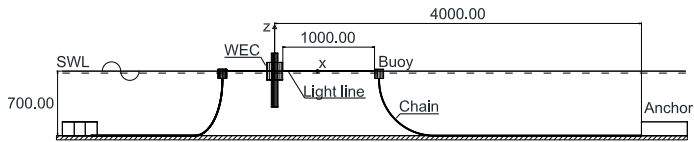


Figure 2.5: Side view of laboratory test set-up. All dimensions are in mm.

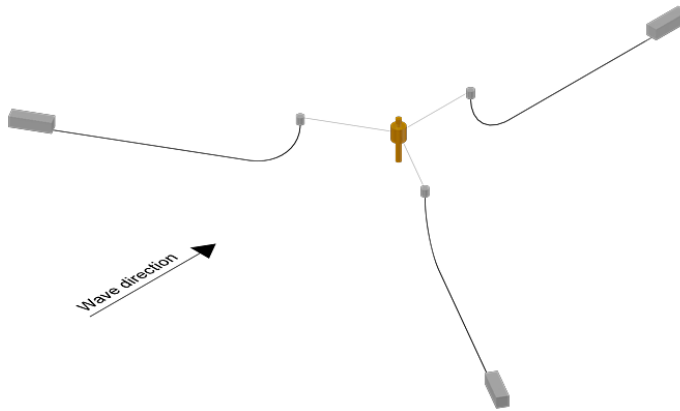
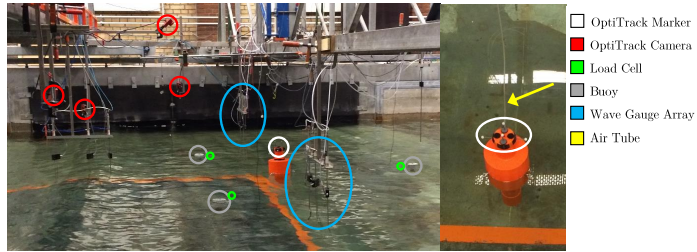


Figure 2.6: 3D model of constructed WEC.

## 2.3 Sensors

In order to measure incident waves, a total of six resistant type wave gauges were used, located beside the model, cf. Figure 2.7. Acquisition of measured data was done by the software package WaveLab 3 (Andersen and Frigaard [2014]).

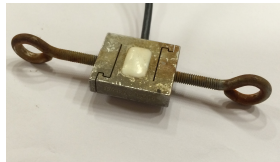


**Figure 2.7:** Laboratory set-up with used equipment.

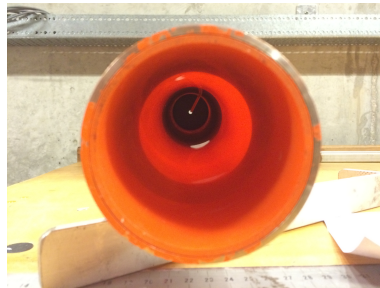
To measure the motions of the model during tests, the motion tracking system OptiTrack was used. A total of 4 OptiTrack Flex 13 cameras were installed, together with 5 reflective markers on the model. The software Motive 1.7.1 was used to track the motions. Cf. Figure 2.7 for set-up.

Mooring loads were measured at the connection point between the buoys and the light lines. Load cells of the type FUTEK LSB210 25, 50 and 100 lb was used, cf. Figure 2.8.

For calculation of the absorbed power of the waves, the pressure difference over the orifice relative to the atmospheric pressure was measured, using an installed air tube in the model, as shown in Figure 2.9.



**Figure 2.8:** Load cell FUTEK LSB210.



**Figure 2.9:** Installed air tube in model used for measuring of pressure difference over orifice.

## 2.4 Power Production

Calculation of the absorbed power is based on equation (2.2).

$$P_{abs}(t) = \Delta P(t)Q(t) = k (|\Delta P(t)|)^{1.5} \quad (2.2)$$

$$k = c_d A_d \sqrt{\frac{2}{\rho_{air}}} \quad (2.3)$$

Where  $P_{abs}$  is the absorbed wave power,  $\Delta P$  is the pressure difference over the orifice,  $Q$  is the air flow,  $t$  is the time,  $\rho_{air}$  is the air density,  $A_d$  is the orifice area and  $c_d$  is the discharge coefficient. The applied value of  $c_d$  is 0.64, which was also determined by previous tests by Nielsen et al. [2013]. For the present test it was attempted to validate this value, but AAU do not have proper equipment for these kind of tests, which resulted in unreliable results. A  $c_d$  of 0.64 was therefore used in calculation of the absorbed power. It should be noted that theoretical limits are available for the discharge coefficient. When going from a sharp orifice to a truncated cylinder the  $c_d$  raises from 0.62 to 0.88 Joachim [1926]. Since the used orifice is much closer to the sharp case, this applies even more confidence in the applied value of 0.64.

10

Chapter 2. Model Construction

## 3 | Model Verification

This chapter serves as a verification of the setup explained in chapter 2.

### 3.1 Motion Response Tests

As seen in appendix B, multiple decay tests are carried out to test if the response of the WEC matches the prescribed behavior. These tests have been conducted on different setups ranging from free-floating body to a fully hooked up system with connected air pressure tube and anchors. This is done to observe the auxiliary systems effect on the response. In the following, only two setups will be presented; the free-floating body, and the fully hooked up system on which all production tests were run. These will be referred to as *body* and *system* respectively.

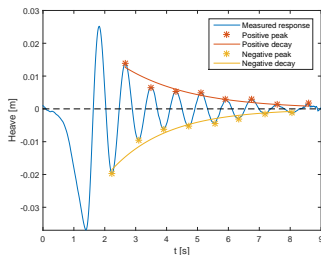


Figure 3.1: Heave response of body.

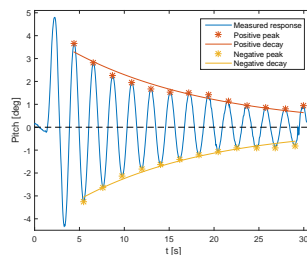


Figure 3.2: Pitch response of body.

#### 3.1.1 Natural Periods

Firstly the eigenperiods of the system is determined from and average distance between the peaks of the decays tests shown in Figure 3.1-3.4. The heave and

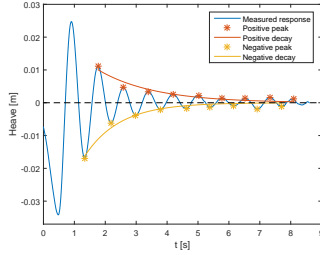


Figure 3.3: Heave response of system.

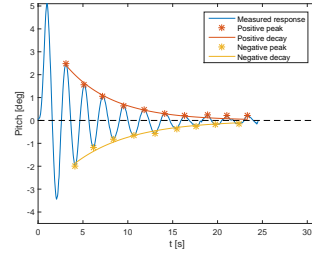


Figure 3.4: Pitch response of system.

pitch period can be seen in Table 3.1. As desired, the heave period of the system matches with the prescribed value. However, it can be seen that the mass distribution is too narrow and hence the 30% lower pitch period. Note: Only the damped periods are shown. The undamped natural periods have been calculated from (3.2), but results vary by less than 0.5% and is therefore neglected in this report.

	Body [s]	System [s]	Full scale [s]	Prescribed [s]	Deviation [-]
Heave	0.86	0.84	6.99	7	1.00
Pitch	2.17	2.06	17.24	25	0.69

Table 3.1: Measured natural periods compared to prescribed values.

### 3.1.2 Damping

The exponential decay of any single degree of freedom motion can be described from (3.1). Only the decay of the amplitudes are of interest in this report, and hence only the enveloping curve  $x = ae^{-\gamma t}$  is calculated.

$$x = ae^{-\gamma t} \cos(\omega_d t - \alpha) \quad (3.1)$$

$$\omega_d = \sqrt{\omega_0^2 - \gamma^2} \quad (3.2)$$

The average of the positive and negative envelope in Figure 3.1-3.4 have been used to describe the given decay. The first two peaks in each run have not been considered in order to remove some of the inevitable nonlinear effects of manually excited single degree of freedom decay tests. In Figure 3.5 the initial

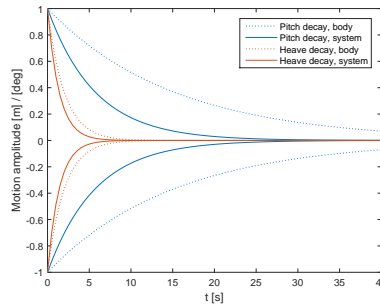
amplitudes have been normalized in order to compare the different responses. The enveloping curve is then described as:

$$\pm x = \pm e^{-\gamma t} \quad (3.3)$$

The damping coefficient,  $\gamma$ , can be seen in Table 3.2. Here the calm-down time,  $t_{0.01}$ , is also shown. The calm-down time is a more tangible measure that describes the time at which only 1% of the motion amplitude remains.

	Body		System	
	Heave	Pitch	Heave	Pitch
$\gamma$ [-]	0.50	0.07	0.72	0.18
$t_{0.01}$ [s]	9.2	69.5	6.4	26.2

**Table 3.2:** Damping coefficients and corresponding calm-down times.



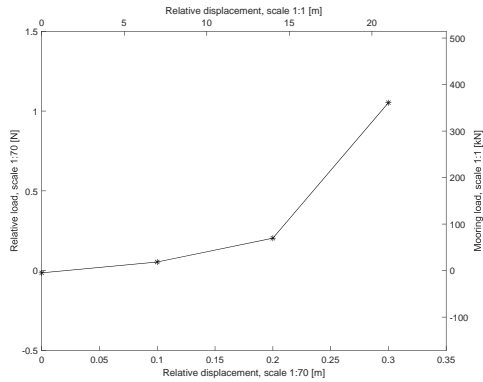
**Figure 3.5:** Normalized amplitude decay.

From the results it is obvious that the changes to damping is much more evident than the changes in stiffness when going from body- to system-setup. This is to be expected and the behavior of the full system is asserted as acceptable.

### 3.2 Static Mooring Test

Characterization of the mooring of the OWC WEC is illustrated in the following figures. The characterization was done by a static test, applying a displacement and measuring the resulting load.

Figure 3.6 illustrates the force-displacement curve for a single mooring line, hence the displacement was applied in the direction of the mooring line.



**Figure 3.6:** Force-displacement curve for single mooring line in scale 1:70 and 1:1.

The force-displacement curve for the total system was determined by applying a displacement in the x-direction (cf. Figure 2.4), measuring the loads in the mooring line and determine the applied load. The following figure illustrates the changes in mooring line loads and the applied horizontal load during the test.



3.2. Static Mooring Test

15

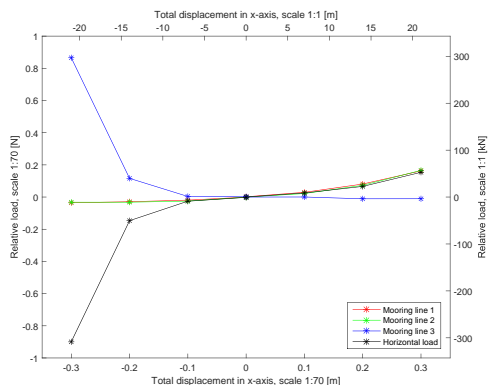


Figure 3.7: Force-displacement curve for total system in the x-direction (cf. Figure 2.4) in scale 1:70 and 1:1.

Finally a displacement was applied in the y-direction, resulting in a curve as illustrated in Figure 3.8.

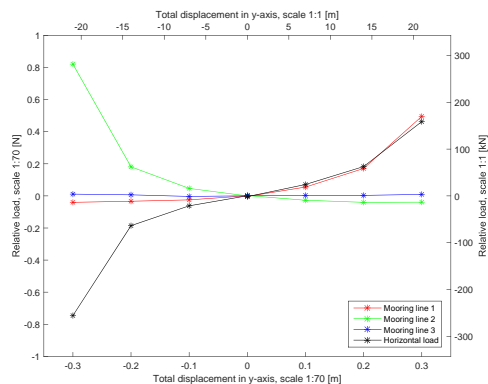


Figure 3.8: Force-displacement curve for total system in the y-direction (cf. Figure 2.4) in scale 1:70 and 1:1.



## 4 | Wave Details

This chapter serves to highlight the desired and tested sea states and the discrepancies between the two. The quality of the generated waves will be addressed.

### 4.1 Scatter diagrams

In appendix A a scatter diagram of chosen wave parameters can be seen. The requested waves are defined by  $H_{m0}$  and  $T_E$ . Since the inputs for the Brestschneider spectrum in the local wave generation software AwaSys 6 (Meinert et al. [2011]) are  $H_{m0}$  and  $T_p$ , all model scale wave parameters will be presented as such. Note that  $T_E = \frac{m-1}{m_0}$  as stated by e.g. Cahill and Lewis [2014].

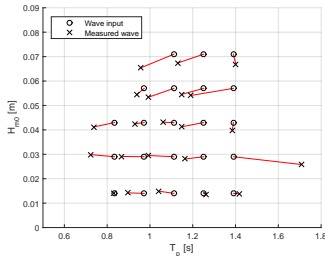


Figure 4.1: Model scale scatter diagram.

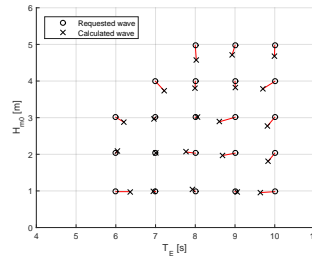
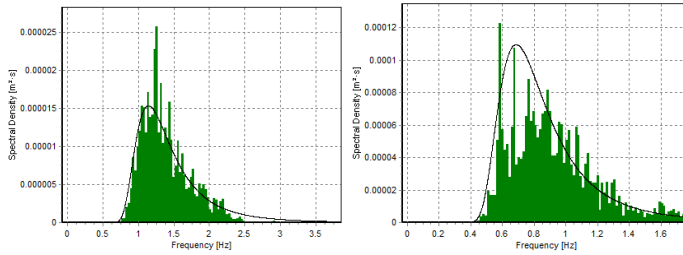


Figure 4.2: Full scale scatter diagram.

### 4.2 Wave quality

As seen in Figure 4.1 there are some discrepancies between the wave input and the generated wave in the basin. Lower wave height can be due to breaking of

the heights waves in the spectrum, lower periods can be caused by cross-modes in the basin and higher periods can be caused by insufficient calm-down time between two runs. As long as only the measured waves are used for analysis, this does not compromise the final results. In Figure 4.2 it is evident that  $T_E$  and hence the full scale results are less sensitive to the accuracy of wave periods.



**Figure 4.3:** Best spectral fit of generated waves. **Figure 4.4:** Worst spectral fit of generated waves.

In Figure 4.3 and 4.4 two measured spectra are shown alongside the requested theoretical spectra. The figures represent the best and worst  $H_{m0}/T_p$ -fit obtained in the wave basin, cf. Figure 4.1. Best fit is obtained at  $H_{m0} = 0.014$  m and  $T_p = 0.834$  s, and worst fit at  $H_{m0} = 0.029$  m and  $T_p = 1.390$  s. All wave conditions have been generated with a duration of 500 waves. This implies that all tests should be able to converge closely to the desired spectral form, but discrepancies can be expected due to reasons stated earlier. The duration necessary to produce 500 waves can be found in appendix A.

## 5 | Raw Data Time Histories

This chapter aims at illustrating the measurements performed during the test series. Examples of time series will be presented showing power production, mooring loads and motions.

### 5.1 Power Production

To illustrate the measured pressure difference and the calculated power production, a timeseries for a test with measured wave height and period,  $H_{m0} = 0.054$  m and  $T_p = 0.938$  s, is shown in Figure 5.1 and a 30 s sample of the test is shown in Figure 5.2.

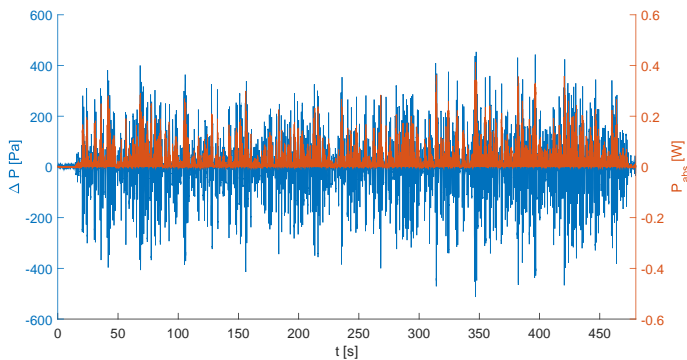


Figure 5.1: Example of time series for power production.

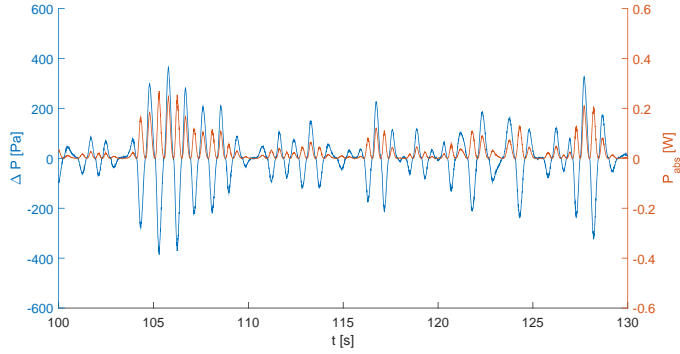
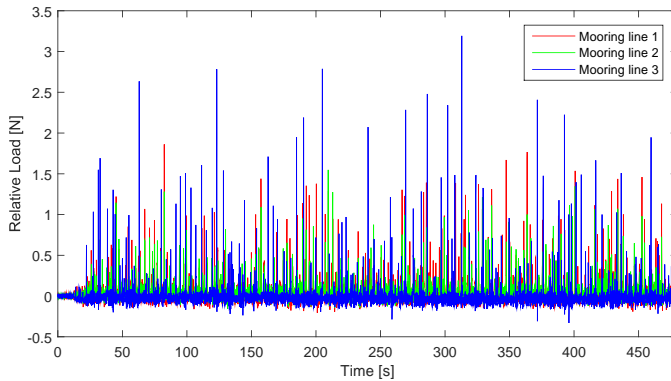


Figure 5.2: Sample of the time series in Figure 5.1

## 5.2 Mooring Loads

Mooring loads in the three lines were measured throughout all tests. An example of the timeseries from the same test as in the previous section, can be seen in Figure 5.3. In the figure the loads are presented as variations from the initial loads in the test.



**Figure 5.3:** Example of mooring load time series.

As seen from the time series, mooring line 3 was exposed to many distinct peak loads, meaning that the highest loads were observed in this line. It was suspected that this was a result of the construction of the buoys, for which reason three additional tests were performed with wave inputs similar to three of the already performed tests, but with a modification of the buoys. An example from the new test with wave input similar to the test in Figure 5.3 can be seen in the following figure. For this test  $H_{m0} = 0.056$  m and  $T_p = 1.168$  s was measured.

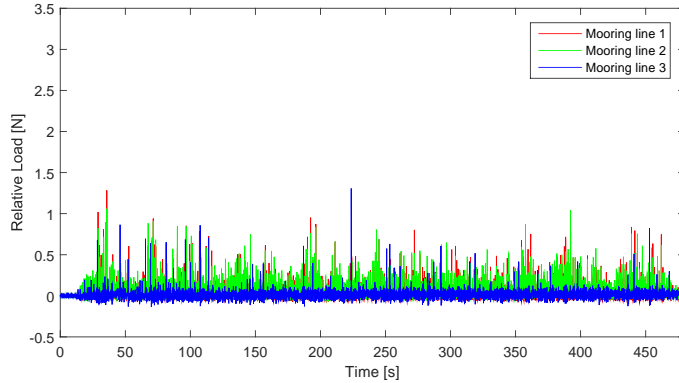


Figure 5.4: Example of mooring load timeseries with modified buoys.

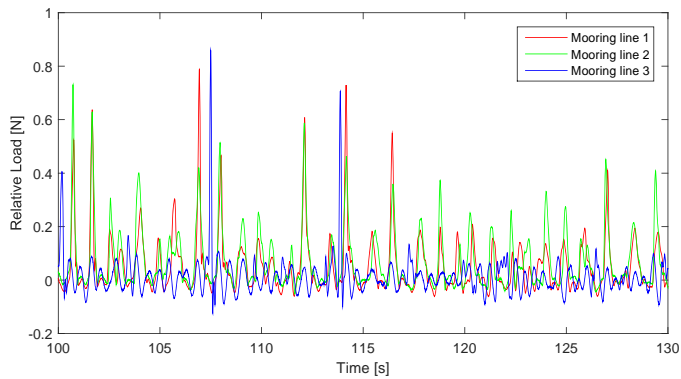
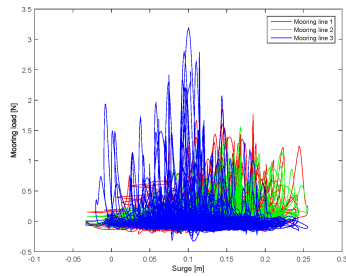


Figure 5.5: Sample of timeseries in Figure 5.4.

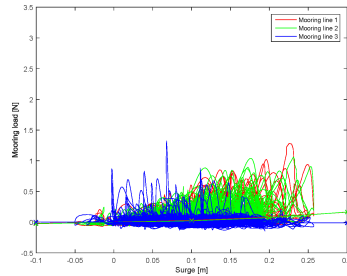
The modification of the buoys resulted in much lower loads in mooring line 3 and lower loads in line 1 and 2, which were though not as affected as line 3. Comparing the measured load-surge curve the influence of the modified buoys is clear, cf. Figure 5.6 and 5.7. Most tests were though performed with the



unmodified buoys.

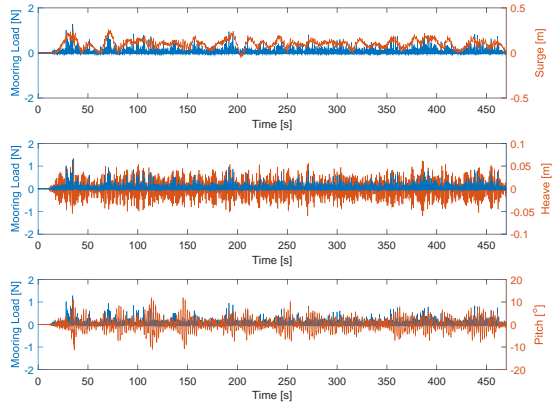


**Figure 5.6:** Example of measured load-surge curve.



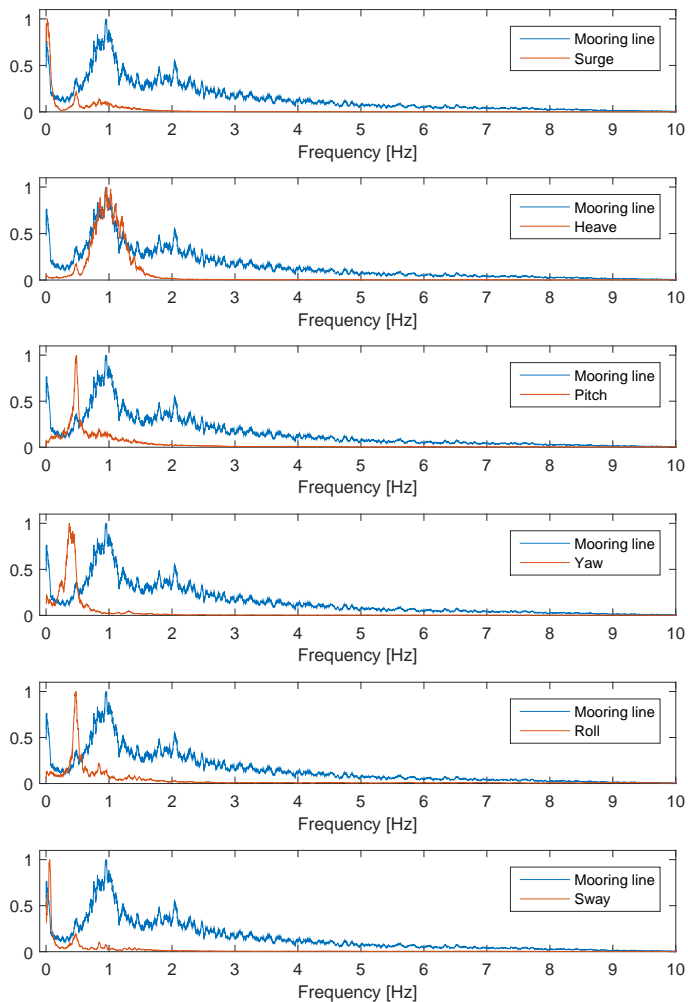
**Figure 5.7:** Example of measured load-surge curve for a test with modified buoys, together with result from static test.

In figure 5.7 the previously measured static force-displacement curve is shown, illustrating that much higher loads, are observed than in the static tests. This might be a result of the dynamic behaviour of the device under wave attack, and the other motions that it induces. Comparing the load time series with the time series from the motions, a significant correlation is seen. Figure 5.8 illustrates the load together with surge, heave and pitch motions for mooring line 1.



**Figure 5.8:** Timeseries for the mooring load in line 1 compared to timeseries for measured motions.

By observing the loads and motions in the frequency domain, cf. Figure 5.9 it is clearly seen that the different motions affects the mooring line loads. In chapter 3 the pitch frequency was found to 0.49 Hz and the heave frequency to 1.19 Hz. These corresponds to the frequencies where peaks are observed for the mooring line loads. Similar can be seen for other of the motions.



**Figure 5.9:** Frequency domain analysis of loads and motions. For illustrative purpose each time series is divided with its own maximum value.



## 6 | Avg. Value Graphs & Charts

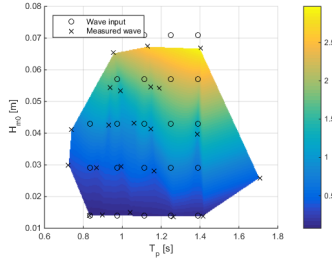
This chapter presents the relevant results from the test series as average values of power production and mooring loads. Results are found in both model and full scale values.

### 6.1 Power Production

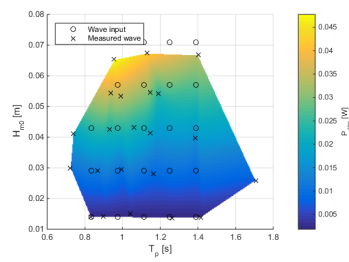
The power production is in the following described in terms of the requested full scale scatter diagram and the model scale scatter diagram. The desired data points are marked by  $\circ$ , but the data user for interpolation is placed at the corrected position marked by  $\times$ . The incident wave power,  $P_W$ , is obtained from WaveLab 3 by Andersen and Frigaard [2014] and based on the wave celerity. The absorbed power,  $P_{abs}$  is calculated as stated in (2.2). Finally the CWR (capture width ratio) is presented for both model and full scale. Note that the CWR does not change in magnitude between the scales since it is a unit-less measure of efficiency, but it is still presented to portrait the efficiency in the same scatter diagram as the other results.

#### 6.1.1 Model Scale

In Figure 6.1 a surface plot of the incident wave power in the conducted tests can be seen. Figure 6.2 shows the measured mean absorbed power.

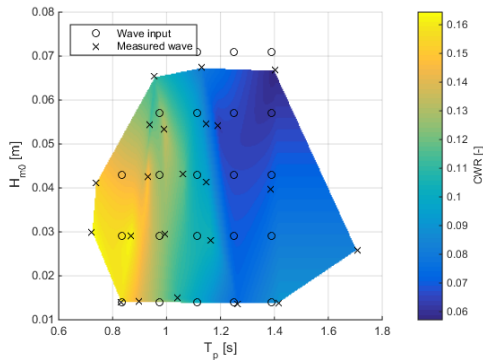


**Figure 6.1:** Incident wave power in model scale.



**Figure 6.2:** Mean absorbed power in model scale.

The CWR presented in Figure 6.3 shows some nonlinearities and a few local maxima and minima, this is due to the attempt of smoothing the surface over data points with varying internal distance.



**Figure 6.3:** CWR in model scale.

### 6.1.2 Full Scale

Full scale incident wave power is shown in Figure 6.4. The mean absorbed power upscaled to prototype scale can be seen in Figure 6.5.

6.2. Mooring Loads

29

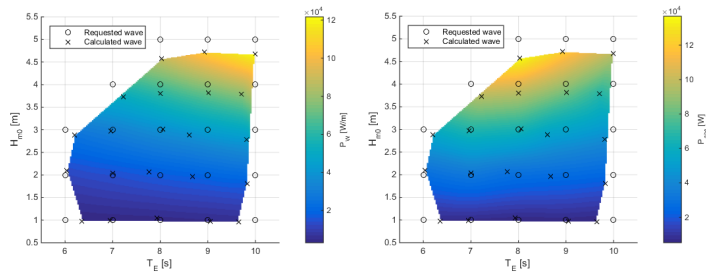


Figure 6.4: Incident wave power in full scale. Figure 6.5: Mean absorbed power in full scale.

In Figure 6.6 the CWR of the full scale system can be seen. The more even distribution of data points results in a smoother representation of the CWR over the area covered by the scatter diagram.

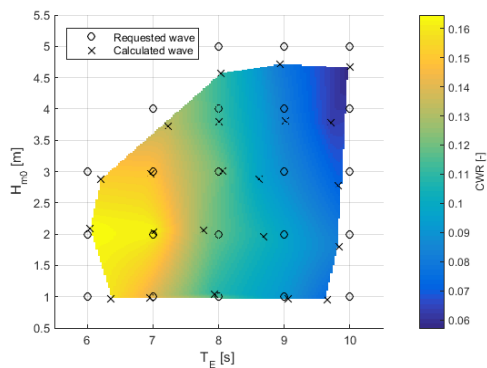
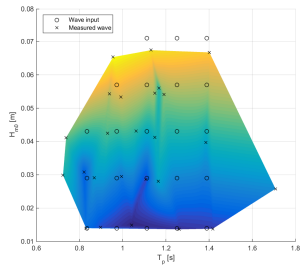


Figure 6.6: CWR in full scale.

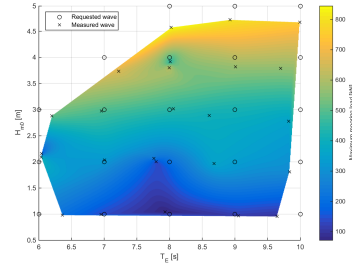
6.2 Mooring Loads

Mooring loads are in the following described in the same way as for power production.

The maximum measured mooring loads during tests, when disregarding line 3, are shown in figure 6.7 and 6.8, dependent on the wave height and period.

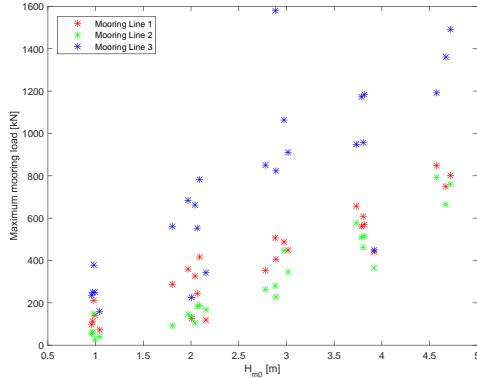


**Figure 6.7:** Maximum measured load in mooring line 1 and 2.



**Figure 6.8:** Full scale values of maximum mooring load in mooring line 1 and 2.

As seen the mooring loads are highly dependent on the wave height and less dependent on the wave period. Comparing the measured loads in each mooring line (cf. Figure 6.9), the dependency is shown. In the figure maximum loads in mooring line 3 is also stated, showing the much higher peak loads.



**Figure 6.9:** Maximum measured mooring loads in the three mooring lines.



## 7 | Summary Statistics Tables

As some of the surface plots in the prior sections of this technical report can be difficult to read with sufficient precision, this chapter presents some of the key values in tables. All values presented are for the full prototype scale, and hence ready for comparison with the other partners in The Round Robin Programme.

### 7.1 Wave details

Due to the slight offset of the wave parameters, as presented in chapter 4, the observed wave properties are presented again in Table 7.1 and 7.2. When comparing the production values one should not refer to the wave matrix, but instead take these specific wave details into consideration.

-	-	4.57	4.72	4.67	-	-	8.03	8.93	9.99
-	3.73	3.80	3.82	3.79	-	7.22	8.00	9.01	9.70
2.88	2.97	3.02	2.89	2.78	6.20	6.96	8.06	8.61	9.82
2.09	2.04	2.07	1.97	1.81	6.03	7.01	7.76	8.68	9.83
0.98	0.99	1.04	0.97	0.95	6.36	6.95	7.93	9.05	9.64

**Table 7.1:**  $H_{m0}$  [m].

**Table 7.2:**  $T_E$  [s].

### 7.2 Power production

One of the key comparison points of The Round Robin Programme is expected to be the power production. The mean effect of the system in prototype scale is previously presented as a surface in Figure 6.5. In Table 7.3 the values used for the interpolated surface can be seen.

Due to the uncertainties in the discharge coefficient,  $c_d$ , used for the calculation of the power production in (2.2) and (2.3) the true production might vary significantly. The theoretical limits of 0.62-0.88 are presented in section

-	-	137.3	121.3	97.3
-	96.9	97.0	83.0	68.6
55.3	66.2	64.9	52.5	42.3
30.5	34.1	30.4	26.4	20.6
6.8	6.9	7.0	5.8	5.0

**Table 7.3:** Estimated effect of WEC [MW].

2.4. When this lower and upper limit is applied, the range of production effect is as shown in Table 7.4.

-	-	133-189	118-167	94-134
-	94-133	94-133	80-114	66-94
54-76	64-91	63-89	51-72	41-58
30-42	33-47	29-42	26-36	20-28
7-9	7-10	7-10	6-8	5-7

**Table 7.4:** Theoretical ranges of effect for WEC [MW].

## Bibliography

- Andersen, T. L. and Frigaard, P. (2014). *WaveLab 3*.
- Cahill, B. and Lewis, T. (2014). Wave period ratios and the calculation of wave power. In *Proceedings of the 2nd Marine Energy Technology Symposium, METS2014*.
- Joachim, W. (1926). *An Investigation of the Coefficient of Discharge of Liquids through Small Round Orifices*. National Advisory Committee for Aeronautics.
- Meinert, P., Andersen, T. L., and Frigaard, P. (2011). *AwaSys 6 User Manual*.
- Nielsen, K., Jacobsen, F. P., Simonsen, M., and Scheijgrond, P. (2013). *Attenuator development phase I*. Infrastructure Access Report: KNSWING. Marinet.

34

Bibliography

## **A | Definition of Wave States**

This appendix includes a brief overview of desired sea states and the actual parameters used for inputs in the laboratory tests.

0,0143

0,1195

Full scale

Requested

H_m0	4	5	6	7	8	9	10	T_E
5								
4								
3								
2								
1								

Model 1:70

Requested

H_m0	0,4781	0,5976	0,7171	0,8367	0,9562	1,0757	1,1952	T_E
0,071								
0,057								
0,043								
0,029								
0,014								

Model 1:70

To be run

H_m0	0,556	0,695	0,834	0,973	1,112	1,251	1,390	T_p
0,071	501	502	503	504	505	506	507	
0,057	401	402	403	404	405	406	407	
0,043	301	302	303	304	305	306	307	
0,029	201	202	203	213	204	205	215	206
0,014	101	102	103	104	105	106	107	

Drop:

Under 0.8s Tp  
Steepness > 4%

#waves	500	277,96	347,45	416,94	486,43	555,92	625,41	694,9	sec
startup	0	4,6327	5,7908	6,949	8,1072	9,2653	10,424	11,582	min

## **B | List of Executed Tests**

On the following pages an overview of executed tests can be found.

## Appendix I. Auxiliary Publications

Test #	H_m0 [m]	T_p [s]	Wavelab File name	Optitrack File name	Comment	Done
101	0.014	0.556	-	-	Omitted: Basin period limit	X
102	0.014	0.695	-	-	Omitted: Basin period limit	X
103	0.014	0.834	103	103	OptiTrack time-error	X
104	0.014	0.973	104	104		X
105	0.014	1.112	105	105		X
106	0.014	1.251	106	106		X
107	0.014	1.390	107	107		X
201	0.029	0.556	-	-	Omitted: Steepness > 4%	X
202	0.029	0.695	-	-	Omitted: Basin period limit	X
203	0.029	0.834	203	203	OptiTrack time-error	X
204	0.029	0.973	204	204		X
205	0.029	1.112	205	205		X
206	0.029	1.251	206	206		X
207	0.029	1.390	207	207		X
213	0.029	0.834	213	213		X
215	0.029	1.112	215	215		X
301	0.043	0.556	-	-	Omitted: Steepness > 4%	X
302	0.043	0.695	-	-	Omitted: Steepness > 4%	X
303	0.043	0.834	303	303	OptiTrack time-error	X
304	0.043	0.973	304	304		X
305	0.043	1.112	305	305		X
306	0.043	1.251	306	306		X
307	0.043	1.390	307	307		X
401	0.057	0.556	-	-	Omitted: Steepness > 4%	X
402	0.057	0.695	-	-	Omitted: Steepness > 4%	X
403	0.057	0.834	-	-	Omitted: Steepness > 4%	X
404	0.057	0.973	404	404	h=0.9	X
405	0.057	1.112	405	405		X
406	0.057	1.251	406	406		X
407	0.057	1.390	407	407		X
415	0.057	1.112	415	415		
501	0.071	0.556	-	-	Omitted: Steepness > 4%	X
502	0.071	0.695	-	-	Omitted: Steepness > 4%	X
503	0.071	0.834	-	-	Omitted: Steepness > 4%	X
504	0.071	0.973	-	-	Omitted: Steepness > 4%	X
505	0.071	1.112	505	505		X
506	0.071	1.251	506	506		X
507	0.071	1.390	507	507		X
901	-	-	901	-	Load cell 1 2 3 calibration. 0g 100g 500g 1000g	X
902	-	-	902	-	Anchor system. 1,2,3,+X,-Y,+Y [0,10,20,30,20,10,0]	X
903	-	-	903	-	System mean test	X
904	-	-	904	-	Load cell 1 re-calibration. 0g 100g 500g 1000g	X
905	0.02	1.4	905	-	Test of mooring response	X
911	-	-	-	911	Heave decay, unmoored, no tube	X



I.3. The Inter Facility Testing of a Standard Oscillating Water Column (OWC) Type Wave Energy Converter (WEC)

912	-	-	-	912	Pitch decay, unmoored, no tube	X
913	-	-	-	913	Heave decay, moored, no tube	X
914	-	-	-	914	Heave decay, moored, tube	X
915	-	-	-	915	Pitch decay, moored, tube	X
920	-	-	-	920	Surge,sway,heave,roll,pitch,yaw	X
921	-	-	-	921	Heave decay, unmoored, no tube	X
922	-	-	-	922	Pitch decay, unmoored, no tube	X
923	-	-	-	923	Heave decay, moored, no tube	X
924	-	-	-	924	Heave decay, moored, tube	X
925	-	-	-	925	Pitch decay, moored, tube	X

---

---

---

---

*Floating Foundations for Offshore Wind Turbines*  
by Morten Thøtt Andersen



## SUMMARY

The concept of harnessing the power of the wind dates all the way back to the first ships traversing the seas. Later, windmills enabled the use of wind power for industrial purposes. Since then, technology has allowed the production of clean renewable energy through the use of wind turbines. These turbines have traditionally been placed on land, but several factors have urged a move to offshore locations. Now the boundaries are being pushed into deeper and deeper waters, where the idea of floating offshore wind turbines has emerged. In less than a decade, these have gone from scattered small-scale prototypes to full-scale pre-commercial wind parks.

This thesis explores different aspects of numerical and physical modeling of floating offshore wind turbines. Numerical investigations, validated by physical test data, are used to highlight some of the implications of modeling these highly coupled aero-hydro-servo-elastic systems. The proper dynamic numerical modeling of floating offshore wind turbines is one of the key aspects in increasing the feasibility of the sector. For experimental testing and development, a novel system for thrust load emulation has been designed and presented. This system enables cheaper early-stage physical prototype testing in wave basins without wind generating capabilities, and hence allows testing of a wider range of concepts.